Processes Responsible for the Mitigation of IASCC Susceptibility Following the Post-Irradiation Annealing of Austenitic Stainless Steels

by

Justin Ryan Hesterberg

A dissertation submitted in partial fulfillment
of the requirements for the degree of
Doctor of Philosophy
(Materials Science and Engineering)
in The University of Michigan
2019

Doctoral Committee:

Professor Gary S. Was, Chair
Dr. Jesse Carter
Professor Fei Gao
Associate Research Scientist Zhijie Jiao
Dr. Richard Smith
Professor Lumin Wang

Justin R. Hesterberg

jhesterb@umich.edu

ORCID ID: 0000-0002-6038-0055

ACKNOWLEDGEMENTS

My advisor, Professor Gary Was, deserves much appreciation for the numerous hours of guidance, the support, and the facilities necessary to complete this thesis work. The experience I have gained as a member of his research group has benefitted me immensely and will serve as the cornerstone for the rest of my research career. I would also like to thank the members of my dissertation committee, Dr. Jesse Carter, Prof. Fei Gao, Dr. Zhijie Jiao, Dr. Richard Smith, and Prof. Lumin Wang, for their assistance and insight.

Many thanks are due to my colleagues in the Was research group for their encouragement, assistance, and valuable discussion through the many years. The friendship and help offered by my fellow group members: Anne Campbell, Cheng Xu, Mike McMurtrey, Tyler Moss, Kale Stephenson, Shyam Dwaraknath, Stephen Raiman, Elizabeth Getto, Anthony Monterrosa, Tai Ni Yang, Stephen Taller, Drew Johnson, David Woodley, Gerrit Vancoevering, Rigel Hanbury, Rajan Bhanbroo, Samara Levine, Katey Thomas, and Connor Shamberger was paramount to my progress and experience. Thanks also to the many research scientists who provided much assistance and guidance through the years: Dr. Zhijie Jiao, Dr. Peng Wang, Dr. Wenjun Kuang, Dr. Miao Song, Dr. Mi Wang, and Dr. Donghai Du. A special appreciation is given to Dr. Zhijie Jiao for his assistance in the characterization of the irradiated microstructure for the materials used in this study. Finally, a thanks to Alex Flick for the countless favors and hours of assistance in the Irradiated Materials Testing Laboratory. Many other colleagues at the University of Michigan are also deserving of thanks. Members of the Radiation Safety Services division of the Occupational Safety and Environmental Health department including Rob Blackburn, Phil Simpson, Phil Keavey, and Dr. Joe Miklos provided much assistance.

Credit is also due to many professionals at the Oak Ridge National Laboratory for their cooperation and guidance with this project. Dr. Jeremy Busby, Dr. Maxim Gussev, and Dr. Phil Edmundson have been excellent mentors, providing both assistance and meaningful discussion.

Thanks also to the LAMDA laboratory staff (Alta Marie Williams, Patricia Tedder, and many others) and hot cell staff member Mark Delph for their assistance with sample handling, preparation, and shipment.

Finally, an appreciation is also needed for members of the Naval Nuclear Laboratory who greatly assisted in the completion of my practicum, during which the groundwork for the molecular dynamics simulation portion of this research was completed. This could not have been done without the assistance of Dr. Richard Smith, Dr. Jesse Carter, Dr. Thomas Webb, and my laboratory mentor, Dr. Denise Paraventi, as well as many others.

Support for this project was provided by funding from the Nuclear Energy University Programs (project number 12-3430) and under appointment to the Rickover Fellowship Program in Nuclear Engineering sponsored by Naval Reactors Division of the U.S. Department of Energy.

TABLE OF CONTENTS

LIST OF TABLES

LIST OF FIGURES

ABSTRACT

Post-irradiation annealing (PIA) was conducted on a 304L stainless steel irradiated to 5.9 dpa in the Barsebäck-1 boiling water reactor (BWR), to investigate its effect on the irradiated microstructure and the mitigation of irradiation-assisted stress corrosion cracking (IASCC) susceptibility. Evolution of irradiated microstructure including faulted dislocation loops, radiation-induced solute clusters and radiation-induced segregation (RIS) at the grain boundary was investigated in the as-irradiated condition and following thermal annealing at 500°C and 550°C for times up to 20 h. IASCC susceptibility was measured for the as-irradiated and four PIA conditions (500°C: 1 h and 550°C: 1, 5, and 20 h) via interrupted constant extension rate tensile and four-point bend experiments under simulated BWR normal water chemistry (NWC) conditions. While the faulted dislocation loop size did not change significantly after annealing up to 550°C: 5 h, the loop number density decreased steadily with increased annealing treatments, and faulted loops were fully removed after annealing at 550°C: 20 h. The average size of Ni-Si and Al-Cu clusters increased while the number density decreased with increased annealing. RIS of various elements progressively decreased with extent of annealing but were not fully removed by 550°C: 20 h. The annealing treatments were also observed to progressively reduce IASCC susceptibility, as measured by the final intergranular fracture fraction (tensile) and crack length per unit area (four-point bend), with full removal of IASCC susceptibility being observed following annealing at 550°C: 1 h for tensile specimens and 500°C: 1h for four-point bend specimens. Among the microstructure and mechanical property parameters measured as a function of PIA, the changes in the average dislocation channel spacing was observed to most closely relate to the mitigation of IASCC; decreasing by ~25% and ~40% from the as-irradiated condition after annealing at 500°C: 1 h and 550°C: 1 h, respectively. The mitigation of IASCC susceptibility correlated well with the decrease in the average dislocation channel spacing and is consistent with

a process in which crack initiation is controlled in part by the high normal stress at discontinuous dislocation channel-grain boundary intersections.

CHAPTER 1 - INTRODUCTION

Nuclear energy is a major contributor to the United States, accounting for 20% (805 TWh in 2017) of U.S. domestic electricity production [1]. Despite the many benefits of light water reactors (LWRs): density of energy production, safety, and carbon-free emissions, few new reactors have been constructed in recent years and the number operating in the U.S. has been diminishing since the 1990s [1]. Due to the aging population of LWRs in the U.S. and the exorbitant cost of constructing new plants, many plants are seeking reactor lifetime extensions to allow the continued generation of abundant, moderate-cost, and clean electricity.

Continued safety is the primary factor when considering lifetime extensions, and a major concern for existing LWRs is irradiation-assisted stress corrosion cracking (IASCC); a degradation phenomenon observed in a variety of reactor designs, materials, components, and operating water chemistries as shown in Table 1.1 [2]. The likelihood of IASCC increases with reactor age and could eventually cause safety concerns or lead to diminishing profits due to the high cost of reactor downtime for maintenance procedures. Therefore, understanding the mechanisms responsible for IASCC and establishing mitigation strategies are of high priority. Like stress corrosion cracking (SCC), IASCC has three primary requirements: a corrosive environment, a susceptible material, and an applied stress. Within a LWR, however, an intense radiation field increases both material susceptibility (through the formation of radiation-induced defects) and the corrosive nature of the environment (through radiolysis). This leads to an increased susceptibility of core structural materials, often resulting in the initiation and subsequent growth of IASCC cracks on the water-side of components until eventual replacement or failure [2].

Austenitic stainless steels are commonly used as structural components in operating LWR cores, due to their high corrosion resistance to cost ratio, but this positioning causes them to receive high levels of radiation exposure during their lifetime. Under irradiation, the microstructure of austenitic stainless steels will evolve through the formation of dislocation loops, precipitates, and

voids. These materials will also experience radiation-induced segregation (RIS) of solute elements at grain boundaries and other sinks. Due to their formation under irradiation, these micro-scale changes are believed to be responsible for the increased susceptibility to intergranular cracking, but isolating the precise mechanism is difficult due to their simultaneous evolution under irradiation. Post-irradiation annealing (PIA) is a technique that can be utilized to incrementally remove the irradiation defect populations. Due to both kinetic and thermodynamic considerations, these defects are removed at different rates as compared to simultaneous evolution. As such, PIA may be used to separate the individual effects of defect-types on IASCC susceptibility.

Irradiation also causes a transition in the deformation mode of austenitic stainless steels, moving from homogeneous to a highly localized deformation that is confined to narrow slip bands called dislocation channels. Cracks have been observed to preferentially initiate where dislocation channels intersect grain boundaries [3–7], and a study by Jiao and Was [8] showed that the relative strain in channels (as measured by average height of dislocation channel steps on the surface) of proton-irradiated stainless steels had a stronger correlation with IASCC susceptibility than a wide range of other variables. Closer examination has also revealed that grain boundaries unable to transmit dislocation channels into adjacent grains accumulate higher local stresses and are more susceptible to intergranular crack initiation [5,6,9].

This study aims to understand the processes responsible for the mitigation of IASCC susceptibility following post-irradiation annealing (PIA) treatments. To determine these interlinked processes, a thorough analysis of the evolution of the irradiated microstructure, localized deformation, and IASCC susceptibility with PIA treatments must be undertaken. Unfortunately, measurements of dislocation channeling in neutron-irradiated stainless steels are quite limited [10–12], as the brittle nature of neutron-irradiated stainless steel causes any crack initiation to quickly propagate to failure. Consequentially, the usual metrics used to describe IASCC susceptibility is percentage of intergranular fracture (%IG), total elongation, and reduction in area. Therefore, a four-point bend experiment was also utilized to provide more information on the IASCC initiation process [13]. The bend test creates a stress gradient through the sample thickness such that cracks would grow into a progressively decreasing tensile stress, thus slowing crack propagation and preserving the sample beyond the initiation of the first crack. The observations of IASCC initiation sites created by the four-point bend test, coupled with the changes

in irradiation defects populations following PIA treatments, have helped to create a clearer view of factors affecting IASCC susceptibility.

This study utilizes a 304L stainless steel alloy from a control rod blade, which was irradiated in the service in the Barsebäck 1 BWR in Sweden to a dose of 5.9 dpa. Following the irradiation, varying PIA treatments were applied to adjust the irradiation defect populations present in the as-irradiated material. To assess susceptibility to IASCC initiation, constant extension rate tensile (CERT) tests and 4-point bend experiments were performed in a simulated BWR-NWC environment. The results determined which variables affected IASCC initiation, including irradiation hardening, residual defect populations, grain boundary composition, and localized deformation. Chapter 2 presents background information including an overview of austenitic stainless steels, irradiation effects, IASCC, and post-irradiation annealing. Chapter 3 provides the research objective and experimental approach. Chapter 4 describes the experimental techniques and analytical methods employed to achieve the objective, while Chapter 5 provides the experimental results that were obtained. Chapter 6 provides an interpretation and discussion of the results and correlations, whereas the conclusions of this study are summarized in Chapter 7. Finally, suggestions for future research on expanding the resulting conclusions from this thesis are presented in Chapter 8.

Table 1.1. Component failures by IASCC in nuclear reactor service [2].

Component	Material	Reactor type	Possible sources of stress
Fuel cladding	304 SS	BWR	Fuel swelling
Fuel cladding	304 SS	PWR	Fuel swelling
Fuel cladding*	20% Cr/25% Ni/Nb	AGR	Fuel swelling
Fuel cladding ferrules	20% Cr/25% Ni/Nb	SGHWR	Fabrication
Neutron source holders	304 SS	BWR	Welding & Be swelling
Instrument dry tubes	304 SS	BWR	Fabrication
Control rod absorber tubes	304/304L/316L SS	BWR	B_4C swelling
Fuel bundle cap screws	304 SS	BWR	Fabrication
Control rod follower rivets	304 SS	BWR	Fabrication
Control blade handle	304 SS	BWR	Low stress
Control blade sheath	304 SS	BWR	Low stress
Control blades	304 SS	PWR	Low stress
Plate type control blade	304 SS	BWR	Low stress
Various bolts**	A-286	PWR & BWR	Service
Steam separator dryer bolts **	A-286	BWR	Service
Shroud head bolts **	600	BWR	Service
Various bolts	X-750	BWR & PWR	Service
Guide tube support pins	X-750	PWR	Service
Jet pump beams	X-750	BWR	Service
Various springs	X-750	BWR & PWR	Service
Various springs	718	PWR	Service
Baffle former bolts	316 SS Cold Work	PWR	Torque, differential swelling
Core shroud	304/316/347 /L SS	BWR	Weld residual stress
Top guide	304 SS	BWR	Low stress (bending)

*Cracking in AGR fuel occurred during storage in spent fuel pond. **Cracking of core internal occurs away from high neutron and gamma fluxes.

CHAPTER 2 - BACKGROUND

An understanding of the effects of radiation damage and the development of IASCC susceptibility in austenitic stainless steels requires a discussion of the properties and behavior of unirradiated austenitic stainless steel under relevant conditions. The effects of radiation damage will then be discussed, including the evolution of microstructural features and segregation, macro-scale mechanical properties, and the deformation mode. The current research regarding IASCC will then be introduced, including the effects of varying factors on the cracking susceptibility. Finally, the known effects of PIA treatments on the irradiated microstructure and IASCC susceptibility are conferred.

2.1 Austenitic Stainless Steels

Austenitic stainless steels are the most utilized type of stainless steel and are most easily identified by their non-magnetic property. These steels are easily formable and weldable, as well as having high temperature stability enabling their use in applications ranging from cryogenic temperatures to high-temperature furnaces. Austenitic stainless steels also have a high corrosion resistance due to high concentrations of chromium and nickel, though these same alloying elements also contribute to their relatively high cost [14]. These same properties of corrosion resistance and temperature stability prompted the early usage of austenitic stainless steels as structural materials in nuclear reactor cores. However, these steels have shown a clear susceptibility to intergranular cracking in that environment following exposure to irradiation [2,3,15].

2.1.1 Alloy Composition

Austenitic stainless steels are generalized as having a chromium content of 16-25%, with a corresponding concentration of nickel to stabilize the austenitic matrix. The composition ranges

required to maintain an austenitic structure can be seen on a Schaelffler-Delong diagram, as shown in Figure 2.1 [14]. In general, the addition of face-centered-cubic (FCC) elements will stabilize the austenitic structure, while adding body-centered-cubic elements (BCC) will stabilize the ferritic structure. Most austenitic stainless steels produced, including the subject material for this research, 304L, are 'lean' alloys. This unofficial categorization is for alloys with less than 20% chromium and 14% nickel, and are known for their sufficient corrosion resistance, easy weldability and formability, and work hardening capability. A list of popular lean alloys with their respective compositions are shown in Table 2.1 [14]. Due to their general-purpose nature, austenitic stainless steels may also be given other alloying elements to increase their usability in a specific environment. Chromium and molybdenum are added to improve oxidation and corrosion resistance, respectively. Silicon can be added to promote resistance to oxidizing acids, while copper may be added for resistance to sulfuric acid. Niobium may be used to creep resistance; sulfur and selenium additions can increase machinability [14].

2.1.2 Sensitization

Carbon may often be considered as an undesirable impurity in austenitic stainless steels, despite its strengthening effects and its role in stabilizing the austenitic structure; hence the high usage of low-carbon austenitic alloys such as 304L and 316L. The primary reason for this undesirability is the high thermodynamic affinity of carbon with chromium, and its low solubility in austenite. These factors lead to the formation of chromium carbides, $Cr_{23}C_6$, when the supersaturation of carbon occurs [16]. Due to the effect of temperature on supersaturation, the formation of these chromium carbides can vary greatly with temperature and carbon content as shown in Figure 2.2 [14]. As carbon diffusion at a grain boundary is much faster than the bulk, grain boundaries will often serve as the nucleation sites for these chromium carbides through the easier supersaturation of carbon. Furthermore, as the diffusion of carbon is several orders higher than chromium, the carbon will rapidly diffuse and combine with the chromium, essentially depleting the region around the grain boundary of chromium in solution. This chromium depletion around the grain boundary is visualized in Figure 2.3 [14]. In fact, this chromium depletion will often continue to such a level that the local area around the grain boundary will no longer be resistant to corrosion, leading to a preferential attack at the depleted grain boundaries when

exposed to a corrosive environment. This entire process is often referred to as sensitization, as the grain boundaries become much more sensitive to an intergranular corrosion. As such it is desirable to avoid annealing austenitic stainless steels at temperatures relevant to sensitization after fabrication.

2.1.3 Mechanical Properties

Unsurprisingly, the mechanical properties of an austenitic stainless steel will be highly dependent on the concentrations of alloying elements. Compilations have shown that the tensile properties of a stainless steel can be accurately predicted based on their composition:

$$\begin{aligned}\sigma_{YS}\,(\mathrm{MPa}) = 15.4\Big[&4.4 + 23(\%\mathrm{C}) + 32(\%\mathrm{N}) + 0.24(\%\mathrm{Cr}) + 0.94(\%\mathrm{Mo}) \\ &+ 1.3(\%\mathrm{Si}) + 1.2(\%\mathrm{V}) + 0.29(\%\mathrm{W}) + 2.6(\%\mathrm{Nb}) + 1.7(\%\mathrm{Ti}) \\ &+ 0.82(\%\mathrm{Al}) + 0.16(\%\mathrm{Ferrite}) + 0.46(d^{-1/2})\Big]\end{aligned} \quad (2.1)$$

where the compositions of the alloying elements are provided in wt.% and *d* is the grain diameter in mm, as predicted by the Hall-Petch grain size strengthening effect [14]. For most solution-annealed austenitic stainless steels, this yield strength will be in the range of 120-250 MPa, though these steels do not typically display a clear yield point, showing deformation as low as 40% of the 0.2% yield strength. This quasi-elastic behavior is a feature of the active slip systems in the FCC structure of austenite [14]. Elongations are generally in the range of 40-60%, though this will depend heavily on the processing of the steel [17,18], while the ultimate tensile strength (UTS) will typically be between 500-700 MPa, depending on the precise conditioning of the steel. Due to this high increase in strength with strain, strain hardening exponents are generally measured in the range of 0.3 – 0.5 [18]. Owing to their exceptional tensile strengths and elongations, austenitic stainless steels are also known for their high toughness. Lean austenitic stainless steels can also be highly cold-worked, leading to very robust mechanical strengths, often greater than 1000 MPa, due to the transformation of unstable austenite into martensite at high levels of shear deformation [14]. A mechanical weakness of austenitic stainless steels is their low fatigue endurance limit, ~30% of the tensile strength. Combined with their relatively high thermal coefficient of expansion, these steels can be particularly susceptible to thermal fatigue when exposed to temperature cycles [14].

2.1.4 Deformation Behavior

As discussed before, austenite has an FCC lattice structure, thus dislocation slip will occur in the $\langle 110 \rangle$ directions along the {111} planes, allowing for 12 different variations. The Burgers vector for FCC is $a/2\langle 110 \rangle$, connecting a corner atom with the neighboring face-centered atom. Figure 2.4a displays the atom arrangement on the (111) plane, with b_1 being the primary Burgers vector of $a/2(10\bar{1})$ [19]. In FCC the Burgers vector direction is a high-energy pathway, thus the slip will dissociate into two easier pathways: b_2 and b_3, which are referred to as partial dislocations. Figure 2.4b shows a vector diagram for the dissociation of $b_1 \rightarrow b_2 + b_3$, $a/2(10\bar{1}) \rightarrow a/6(2\bar{1}\bar{1}) + a/6(11\bar{2})$ [19]. The combination of these two partial dislocations may be referred to as an extended dislocation, which will both move together to maintain an equilibrium width. This width between the two partial dislocations is called the stacking fault, and its size is determined by the stacking fault energy (SFE) of the alloy, which is often heavily dependent on composition. The dissociation into partial dislocations can also severely limit cross slip as the partials must recombine before cross slip can occur [19]. Austenitic stainless steels often have a low SFE (<20 mJ/m^2), thus limiting cross-slip due to the larger spacing [20].

Due to the active slip systems and relatively low stacking fault energy, a variety of deformation microstructures are possible in austenitic stainless steels, varying with material condition, test temperature, and the applied strain rate [21]. Wide stacking faults (partial spacings >1 μm) and twin bands are formed after deformation at low temperatures and high strain rates [21,22]. As temperature increases up to 450^{o}C, stacking faults become increasingly narrower, allowing cross-slip from perfect dislocations to dominate. This results in an equiaxed dislocation cell structure at low strain [21], followed by dislocations becoming progressively more tangled at higher strains [21,23]. The deformation microstructure in austenitic stainless steels is also closely related to the equivalent applied stress: dislocation tangles are dominant below 400 MPa, whereas isolated stacking faults (<1 μm) can form between 400-600 MPa, and large stacking faults/twin bands (> 1 μm) dominate at stresses higher than 600 MPa [24]. The equivalent stress level may be increased by many forms of strengthening: increasing the strain level, decreasing the deformation temperature, or through irradiation [24]. Note that there also are various stress-induced phase transformations that may occur in austenitic stainless steels, thus leading to further complexity in development of the deformation microstructure [25,26].

Polycrystallinity complicates deformation, as deformation in a single grain must be accommodated by deformation in adjacent grains. It is typically assumed that if all grains undergo the same deformation as the bulk material, the activation of at least five of the possible twelve slip systems in an FCC crystal is required [27]. Deformation is further influenced by grain boundaries, which limit the slip transfer between grains; this leads to non-uniform local stresses when a polycrystalline material is subject to a uniform bulk stress. In particular, model results have shown that the highest stress concentrations will result at grain boundaries inclined perpendicularly to the bulk stress direction as well as near triple points (the location where three adjacent grains meet), due to the deformation constraints of adjacent grains [28]. As expected, the Hall-Petch relationship has shown that as the average grain size becomes smaller, the overall material strength increases due to the increase in relative grain boundary surface, which acts as a barrier to dislocation motion.

2.2 Effects of Irradiation on Austenitic Stainless Steels

Before one can fully understand the development of IASCC in reactor core internals, the precise methods by which irradiation can influence both the austenitic stainless steel and the water environment must be first understood. There are two primary manners in which irradiation can affect materials: through direct atomic manipulation, such as radiolysis or transmutation, and by collision, physically creating excess vacancies and interstitials, which can further influence the microstructural evolution and material properties. In general, the effects of irradiation on austenitic stainless steels can be broadly separated into two areas: microchemical and microstructural.

2.2.1 Microchemical Effects

Under the neutron irradiation present in a nuclear reactor there are multiple microchemical changes that can be induced in a material; where ‘microchemical change’ is used to refer to the localized adjustment or redistribution of the atomic composition of the material. There are two primary methods by which these changes can be induced: transmutation and radiation-induced segregation (RIS).

2.2.1.1 Transmutation

Transmutation simply refers to the conversion of an element or isotope into another. In reactor conditions this will often occur through a nuclear reaction in which an energetic neutron collides with a nucleus. In relation to IASCC, the transmutation into helium is considered particularly important due its likelihood of occurring and possible embrittlement or swelling effects [2]. Under neutron irradiation, there are two common transmutation reactions that can create helium in stainless steels:

$$^{10}\mathrm{B} + \mathrm{n} \rightarrow {}^{7}\mathrm{Li} + {}^{4}\mathrm{He} \tag{2.2}$$

$$^{58}\mathrm{Ni} + \mathrm{n} \rightarrow {}^{59}\mathrm{Ni} + \gamma\,;\ {}^{59}\mathrm{Ni} + \mathrm{n} \rightarrow {}^{56}\mathrm{Fe} + {}^{4}\mathrm{He} \tag{2.3}$$

The boron transmutation will produce helium at low fluence, however, due to its low concentration in stainless steels, the ^{10}B will often be fully consumed within a few dpa. Due to its higher concentration, nickel is a larger contributor to helium production, however, as the reaction is a two-step process through the initial production of ^{59}Ni, helium generation through this process is quite limited until 5-10 dpa [2]. The possible effects of helium generation via transmutation on IASCC will be further discussed.

2.2.1.2 Radiation-Induced Segregation

Radiation-induced segregation (RIS) refers to the redistribution of both major alloying and impurity elements at point defect sinks; grain boundary segregation has been historically more well studied in relation to IASCC [29–34]. Different from both thermal segregation and elemental depletion due to the formation of grain boundary precipitates, i.e. sensitization [32], RIS is driven by the flux of irradiation-produced point defects: interstitials and vacancies. These point defects are created in concentrations several magnitudes higher than those present at thermal equilibrium. These defects create an enhanced diffusion rate within the material and the unequal participation of a solute in the vacancy and interstitial fluxes at the sink will lead to either enrichment or depletion of the solute [2]. In general, undersized solutes will enrich, while oversized solutes will deplete [35], though the precise magnitude and rate of this enrichment/depletion process is dependent on multiple factors, including: defect migration bias, binding energy between solutes, total dose, dose rate, and temperature [33]. At high temperatures the back segregation of vacancies

to the sink is increased, while at low temperatures, the lower mobility allows for the recombination of interstitials and vacancies; as such segregation is only dominant at intermediate temperatures such as those present within LWRs. For higher dose rates, the greater defect concentration will increase recombination, thus the intermediate temperature at which segregation occurs will increase with dose rate, due to the need for a higher mobility of defects to prevent recombination [2].

For austenitic stainless steel alloys, RIS at grain boundaries will often induce depletion of chromium and iron, while enriching nickel and most impurity concentrations including silicon, phosphorous, and sulfur. It is important to note that the segregation profiles created by RIS are narrow, often confined to 5-10 nm from the grain boundary due to the back diffusion of the resulting concentration gradient at the sink [36]. Figure 2.5 illustrates a typical grain boundary segregation profile for an austenitic stainless steel. The segregation of iron has been observed to either deplete or enrich according to the magnitude of nickel and chromium segregation [33,37].

Minor alloying elements and impurities have also been observed to segregate under irradiation. As molybdenum and manganese are oversized elements they deplete at grain boundaries [34,36,38,39]. Silicon has been observed to enrich heavily at grain boundaries [34,38,39], whereas phosphorus was observed to moderately segregate to boundaries [36,38,40]. Note that phosphorus has also been observed to thermally segregate to grain boundaries, thus making the contribution solely due to irradiation difficult to determine [36]. Sulfur has also been observed to enrich under irradiation [15,36]. Minor elements of carbon, boron, and nitrogen should theoretically enrich to grain boundaries due to being undersized elements; however, their small size makes their segregation difficult to measure using standard transmission electron microscopy (TEM) techniques. However, atom probe tomography (APT) examinations of the grain boundary segregation in austenitic stainless steels have shown a clear segregation of boron under proton-irradiation, though there was little evidence of carbon segregation [40]. While helium has a low mobility in steel at common reactor temperatures [2], due to its formation by the transmutation of boron, it has a potential to be enriched at the grain boundary due to prior boron segregation [36]. Overall, the segregation behavior of minor elements under irradiation is not well understood, and further complicated by the difficulty of measurement and possible coupling effects between large and small elements [2,36,37].

It should be noted that while a majority of the available research focuses on the segregation effects at grain boundaries, RIS can be induced at any sink, including voids and dislocation loops [39–47], an example of which is shown in Figure 2.6 [42]. Due to locally enhancing the solute element concentrations, this RIS can drastically influence phase stability during irradiation by acting as precursor sites for the later formation of precipitates, such as γ' [40,43–50]. Prior to transforming into a precipitate these clusters of enhanced solute concentration may still act as weak barriers to dislocation movement through solid solution hardening [51–53], thus leading to a significant hardening of the material.

2.2.2 Microstructural Effects

In addition to microchemical adjustments in a material, irradiation can also induce various microstructural changes. The microstructure of austenitic stainless steels have been observed to change rapidly under irradiation [15,54,55], and the resulting microstructure is heavily dependent on the irradiation temperature [36]. The evolution of the irradiated microstructure with temperature in austenitic stainless steels can be seen in Figure 2.7 [36]. At the typical operating temperatures of a LWR, point defect clusters, often referred to as "black dots," will begin forming at very low doses, with dislocation loops and network dislocations evolving over further dose, followed by the possible formation and growth of helium cavities and bubbles, and precipitates in locations exposed to higher temperatures and dose [2,25,48–50,54,56]. In most common stainless steels, these defects will lead to extensive hardening and strengthening, reaching yield strengths up to four times the unirradiated value after just 7-10 dpa, as shown in Figure 2.8 [36].

2.2.2.1 Small Defect Clusters (Black Dots)

The terminology of "small defect cluster" refers to the development of vacancy and interstitial clusters during the recombination of the damage cascade from the initial collision event, and as such are one of the most common defect structures created under LWR conditions. These clusters were often originally called "black dots" due to the inability of electron optics to resolve their details when they were first observed [2]. Due to their fast creation rate, similar in relation to the rapidity of IASCC susceptibility at low damage doses, these defects are presumed to greatly influence the hardening process and IASCC susceptibility of materials [57]. In austenitic stainless

steels, these small defect clusters are traditionally thought to be predominately faulted interstitial dislocation loops and vacancy clusters [58]; but more recent experiments have indicated the presence of both vacancy and interstitial faulted loops [59]. Further experiments on austenitic stainless steels have suggested that the density of the vacancy faulted loops is much higher than previously thought, possibly even greater than that of the faulted interstitial loops [60]. In austenitic stainless steels, the small size of these small defect clusters, approximately 0.5 nm in diameter, makes them near impossible to examine under traditional TEM techniques, but hardness measurements after low-temperature (<100°C) irradiations have predicted the density of these features to saturate around 10^{24} m^{-3} by 0.1 dpa [48,60]. However, as their stability would decrease with temperature, the saturation density of small defect clusters is expected to be much lower under LWR conditions. Nevertheless, while small defect clusters are very small, they are still effective blockades to dislocation movement, thus they significantly contribute to the increased hardness of a material subjected to irradiation.

2.2.2.2 Dislocation Loops

Much like small defect clusters, dislocation loops form during the recombination of the damage cascade of the initial radiation event. These are predominately faulted interstitial loops and nucleate and grow due to the higher mobility of interstitials over vacancies. For FCC metals, such as austenitic stainless steels, the dislocation slip is along the {111} planes, thus the faulted dislocation loops will form on the {111} planes [19]. These dislocation loops are prismatic, or perfect loops if the Burgers vector is $a/2\langle 110\rangle$ and Frank, or faulted loops with a Burgers vector of $a/3\langle 111\rangle$. As faulted dislocation loops can continue to grow by adsorbing interstitials, the density and size of the faulted loop population will continue to grow until the adsorption of both interstitials and vacancies equalize [57]. The theoretical evolution of the loop density and size with temperature for an austenitic stainless steel can be seen in Figure 2.9 for a nominal dose of 10 dpa [61]. It is observed that small dislocation loops will dominate at low temperatures, while large dislocation loops will become more dominant as temperature increases. This estimation can also be compared to the Figure 2.10, which shows the theoretical evolution of dislocation loops in an austenitic stainless steel with increased dose, all at a nominal temperature of 288°C [61]. Under these conditions it is seen that the population and size of small dislocation loops will saturate by 1

dpa, whereas the density and size of large interstitial loops will continue to increase until about 5 and 10 dpa, respectively. Figure 2.11 shows the experimentally measured dislocation loop size and density for several LWR irradiated austenitic stainless steels [36]. The experimental results show that the loop density saturates quickly, around 1 dpa, whereas the size continues to increase until about 5 dpa; this is quite similar to the theoretical behavior [61]. While the specific size and density of the resulting loop population is dependent on multiple factors, including irradiation condition and alloying elements [62–64], but under typical LWR conditions, the loop size is generally saturated to a diameter of 20 nm with densities on the order of 10^{23} m^{-3} for austenitic stainless steels [36]. This observed saturation in size is due in part to the unfaulting of faulted loops into perfect loops, as this unfaulting reaction becomes more energetically favorable at larger loop sizes [57].

2.2.2.3 Voids, Cavities, and Bubbles

The formation of voids, cavities, and bubbles may begin to form during the irradiation of austenitic stainless steels, particularly at temperatures above 300°C, due to the increased mobility of point defects with temperature. As for terminology, "void" refers to the formation of stable coalescence of vacancies, a "cavity" is essentially a gas-containing void, whilst a "bubble" contains enough gas to be in a mechanical equilibrium with the matrix. Under reactor conditions irradiation-induced cavities and bubbles are most prevalent; generally being filled with helium, generated from transmutation, or hydrogen, which is adsorbed from the water environment. In general, the existence of these gases has been observed to synergistically lead to nucleation and growth, through the stabilization of void embryos [65]. While the temperatures for void nucleation and growth are often above the operating temperatures of most LWRs, gamma heating within thicker core internals can substantially increase the local temperature of a material [66], thus raising it above the nucleation threshold. As such, cavities and bubbles have been observed in a variety of stainless steels after operation in LWR reactor conditions, especially at high dose levels [65,67–72]. The development of cavities and their subsequent growth causes a volume increase in the material, thus causing it to swell. Figure 2.12 demonstrates the evolution of cavities and bubbles, through the measured swelling, with increased temperature and dose for several austenitic stainless steels from a pressurized water reactor (PWR) reactor [71]. The nucleation and growth

of cavities is highly dependent on temperature with baffle bolts from operating PWRs, made from several austenitic stainless steel alloys, displaying an increase from 0.0% to 0.029% swelling when the temperature was increased from 290^{o}C to 329^{o}C, over a dose range of 7.5 to 25 dpa [71]. Void growth can be influenced by a myriad of factors: dose rate, applied stresses, both external and internal, material processing, precipitation [66], and material composition [71,72]. Despite the various factors that can influence cavity growth, the dislocation loop microstructure will continue to be a more dominant defect in austenitic stainless steels over the operation temperatures for BWRs, i.e. < 300^{o}C [2].

2.2.2.4 Irradiation-Influenced Phase Stability

Irradiation has been observed to actively accelerate or retard the precipitation of second phases in austenitic stainless steels, in addition to modifying the stability of existing precipitates. This leads to the development of irradiation-induced phases, which are not formed under thermal treatments [36,43,48,49]. The formation of precipitates during irradiation is largely controlled by solute segregation, which is adjusted under irradiation through RIS. RIS induces a buildup of undersized elements at sinks, particularly nickel and silicon [48]. Irradiation effects the stability of different phases to varying degrees and its effects can be broadly be defined into three categories: enhanced/retarded, modified, and induced. Radiation-enhanced/retarded refers to phases which exist in the same composition and structure as their thermally aged equivalents, however, the relative abundances are changed as an effect of irradiation. Radiation-enhancement applies to phases which undergo either increased growth or nucleation, or that form at lower temperatures, due to irradiation. Conversely, radiation-retarded refers to phases which see a reduced abundance or are shifted to higher formation temperatures due to irradiation [48]. Note that as these phases are present under thermal conditions, and their growth is simply either enhanced or retarded by irradiation, these phases will not disappear or change composition under subsequent thermal treatments [73]. Radiation-modified phases are those which also exist under thermal conditions, however, their phase composition is changed during irradiation. Note that these compositional changes generally conform to RIS, i.e. more nickel and silicon, less chromium and molybdenum [48,74]. Radiation-induced phases are unique to the irradiation environment, as they are not formed under thermal aging at any temperature. These phases are often the result of RIS

modifying the local composition around a sink to levels such that a new phase can be formed [36,43,48,49,66]. Table 2.2 shows the classes of radiation-influenced phases common in austenitic stainless steels [48].

As radiation-enhanced/retarded and radiation-modified precipitates exist under thermal aging conditions, albeit under different quantities and compositions, their contribution to the irradiated microstructure is less than that of radiation-induced phases. For austenitic stainless steels, the irradiation-induced phases consist of G ($M_6Ni_{16}Si_7$), γ' (Ni_3Si), and several phosphides (MP, M_2P, M_3P) and their evolution seems to be heavily reliant on RIS, particularly the enrichment of nickel, silicon, and phosphorus. As such, the development of these radiation-induced phases is heavily influenced by alloy composition, thermo-mechanical pretreatment, and irradiation temperature. It has also been observed that under certain irradiation conditions, austenite can be transformed into ferrite and/or martensite [49].

The formation of phosphide phases in austenitic stainless steels following irradiation were first observed in the early 1970s. These phosphides are often needle-shaped, and come in several compound forms: M_3P, M_2P, and MP, in which the M is iron, chromium, or titanium. Phosphides are often observed in standard austenitic stainless steels in irradiations from 400-650^{o}C and 5-30 dpa; however, they appear to be quite unstable with dose, often dissolving by 30 dpa. Likewise, their stability also appears to be drastically reduced by the presence of helium [49], which is expected to present in irradiated alloys due to transmutation reactions. Due to the high formation temperatures and helium instability, the formation of phosphide precipitates is not expected under LWR conditions.

Radiation-induced G-phase precipitates in austenitic stainless steels were first observed in the late 1970s; the compound is a complex silicide, $M_6Ni_{16}Si_7$, in which the M can be manganese, titanium, niobium, or chromium, (though manganese is predominately observed to enrich) and has an FCC structure [49]. In austenitic stainless steel alloys, the formation of G phase precipitates has been observed in a narrow temperature regime around 500^{o}C, and preferably in solution-annealed over cold worked conditions. The addition of titanium and niobium appears to increase its abundance, as well as widen the temperature regime to 400-650^{o}C. Furthermore, G phase are often single, coarse particles (20-250 nm) and are frequently associated with voids [49]. Due to its high formation temperature, G phase precipitates are not expected due to irradiation under LWR conditions.

The γ’ phase was also first observed in the late 1970s, and takes form as Ni_3Si, an intermetallic compound with an ordered FCC ($L1_2$) crystal structure. The formation of γ’ precipitates has been observed to regularly develop in austenitic stainless steels over the temperature range of 270-550ºC [49,75], and thus have been observed to form under LWR conditions [43,76–78]. The abundance of γ’ precipitates is very sensitive to alloy composition and thermo-mechanical pretreatment; the formation kinetics appear to be faster in cold-worked materials, as compared to solution annealed. γ’ precipitation occurs at doses less than 5 dpa [75], and increase with dose. Unlike G-phase, γ’ precipitates form as fine particles or clusters (5 – 50 nm) and are often associated with the dislocation network and loops, and only rarely with voids [49]. With increased irradiation temperature, the γ’ precipitates tend to increase in size and decrease density [75]. Furthermore, γ’ formation appears to be sensitive to changes in helium levels, thus creating differences between the formation kinetics in reactor conditions and laboratory irradiations. Particularly the in-reactor helium generation appears to initially amplify the γ’ formation sensitivity, but then destabilize the phase at higher doses [49]. As γ’ precipitates are the only irradiation-induced phases observed to develop under LWR conditions, they will be the focus of later studies regarding IASCC susceptibility and the effects of PIA.

2.2.3 Mechanical Behavior

The evolution of the defect microstructure under irradiation will also create changes in the mechanical behavior of an austenitic stainless steel, including radiation hardening and localized deformation. Radiation hardening represents the subsequent increase in hardness and strength following irradiation; this results from the formation of dislocation loops, precipitates, voids, and defect clusters, all of which impede dislocation movement. Localized deformation describes the loss of homogeneous deformation in irradiated materials with increasing dose, turning instead to a more heterogeneous deformation with the formation of dislocation channels.

2.2.3.1 Radiation Hardening

As previously discussed, the microstructures of austenitic stainless steels have been observed to change rapidly under irradiation [15,54,55], and the resulting microstructure is observed to be heavily dependent on temperature [36]. In most austenitic stainless steels, these

defects will lead to extensive hardening and strengthening, reaching yield strengths up to five times the unirradiated value after just 7-10 dpa, as shown in Figure 2.8 [36]. Overall, the formation of these irradiation defects will increase the hardness and yield strength of the material in proportion to their density and size as predicted by the dispersed barrier hardening model [79]:

$$\Delta\sigma_{y,x} = \alpha_x M\mu b\sqrt{N_x d_x}, \tag{2.4}$$

where $\Delta\sigma_y$ represents the increase in yield stregth resulting from barriers of strength, α, size, d_x, and density, N_x [79]. α_x is oft referred to as the obstacle strength and varies from 0-1, where 1 is a perfectly hard barrier. M, μ, and b are material parameters: Taylor factor, shear modulus, and magnitude of Burgers vector, respectively. For a fully isotropic FCC material, such as a solution-annealed austenitic stainless steel, the average Taylor factor of 3.06 ± 0.01 is expected [80,81], as irradiation does not induce texturing this value should not change. As the hardening in irradiated materials is oft the result of multiple different defect types, it is necessary to expand the dispersed barrier hardening model to combine the impact from the individual defect types [82]. There are two generally accepted methods to combine the separate hardening contributions: linear superposition:

$$\Delta\sigma_y = \alpha_A M\mu b\sqrt{N_A d_A} + \alpha_B M\mu b\sqrt{N_B d_B}\,, \tag{2.5}$$

and square superposition:

$$\left(\Delta\sigma_y\right)^2 = \left(\alpha_A M\mu b\sqrt{N_A d_A}\right)^2 + \left(\alpha_B M\mu b\sqrt{N_B d_B}\right)^2. \tag{2.6}$$

Usually, linear superposition is more accurate when combining defects of vastly different obstacle strengths, while square superposition may provide a better fit when the varying defects have similar obstacle strengths [19]. Depending on the literature source, fits to dislocation loops will usually give an obstacle strength between 0.2 - 0.5 [77,78,83,84], the obstacle strength of a precipitate heavily depends on its misorientation and structure, but γ' precipiates have values of ~0.4 [77,78], while solute clusters are lower, between 0.1 – 0.3 [43,78,83,84]. While the dispersed barrier hardening model has been used for many years to determine the effect of irradiation defects on hardening, the wide range in obstacle strength for specific defects, such as dislocation loops, between different materials reveals some of its deficiences. Efforts have thus been put into more accurately predicting the obstacle strengths of various defects based on their respective shapes, i.e. spherical, disc-like, rod-like, and their effect on the free energy of the system [82,85,86], as

opposed to the generalization of the dispersed barrier hardening model. While these newer methods have shown some reliability in predicting the obstacle strengths of specific defects, the dispersed barrier hardening model still remains the most widely used method for its simplicity and accuracy.

2.2.3.2 Localized Deformation

Localized deformation describes the loss of homogeneous deformation in irradiated materials with increasing dose, upon which the defect microstructure has evolved such that it effectively impedes dislocation motion [36,87]. Due to the difficulty in moving dislocations through this microstructure, there are very few active dislocation sources, almost exclusively at grain boundaries [88], often located on widely-separated slip planes [89]. Dislocations released from these sources will glide along their respective slip planes either annihilating or assimilating any defects in their path [89,90], a process confirmed by in-situ TEM studies [91–93]. This clearing will create a narrow dislocation path, or channel, through which subsequent dislocations from the same source can easily pass. As such subsequent deformation in the material will occur heterogeneously, constrained to these dislocation channels in which prior dislocation gliding has dissolved the defect structure [90,94]. As the strain level in the dislocation channels is often >100% for just a few percent bulk strain [9,89], localized necking of the shear bands results and hence a sharp reduction in uniform elongation is observed [36]. The localized stresses and strains from these channels cannot always be accommodated by the grain boundary, where these dislocation channels both originate and terminate leaving clear steps proportional to the strain in the channel [9], thus leading to grain boundary deformation and possible cracking [4,8,9,95–98].

The development of localized deformation is directly dependent of the irradiated microstructure, as these defects produce the resistance to dislocation movement. As such the transformation from the homogeneous deformation observed in unirradiated austenitic stainless steels to the heterogenous deformation in dislocation channels can be closely related to the irradiation dose that the material has received [23,99,100]. This transformation has been closely studied by Byun *et al.* where the deformation mode in irradiated 316 and 316L steels was observed in response to irradiation dose, as seen in Figure 2.13 [99]. This research, which has been supported by other work as well [22,23,88,90,100–102], clearly illustrates that the primary deformation mode

in these austenitic stainless steels changes from dislocation tangles, to stacking faults, to a mixed twinning and dislocation channel regime as dose increases [99]. In fact, it appears that dislocation channeling and twinning is the main deformation mode for steels that have reached an irradiation dose greater than 0.1 dpa. Similarly, not only will the primary deformation mode change with increased irradiation, but also the degree of localized deformation may change, with both larger and more widely spaced dislocation channels being observed with higher dose levels [23,100,103]. It is important to note, however, that while Figure 2.13 shows that dislocation channeling cannot occur below the true yield stress, this is not synonymous with the bulk yield strength of a material. Due to variable grain orientations, many grains may individually deform prior to the bulk yield strength of the material; and in the case of irradiated steels this deformation can certainly be in the form of dislocation channels. For irradiated stainless steels, dislocation channels will typically begin to develop around 65-70% of the bulk yield strength [88], though this is likely to vary slightly based on material conditions [104].

There are several research studies that have examined the effects of both irradiation dose and strain on the physical features of localized deformation in irradiated austenitic stainless steels, specifically the average channel height, the width of, and spacing between dislocation channels [8,23,89,100–103,105]. Farrell *et al.* showed that for low dose 316 stainless steel, the average channel spacing almost doubled from 284 to 535 nm at an irradiation dose of 0.17 and 0.78 dpa, respectively [89]. Meanwhile, the channel width also increased from 10 to 24 nm between the conditions; the bulk strain was comparable at 6 and 5% strain for the 0.17 and 0.78 dpa conditions, respectively. For the 0.78 dpa condition a slight decrease in the average channel spacing was observed with increasing strain: 622, 535, and 588 nm at strains of 2, 5, and 32% respectively [89]. Miura *et al.* [23] examined the dislocation channel spacing at 2% strain following the He^+ ion irradiation of a 304 and 316 stainless steel to doses of 0.1, 0.5, 1, 2, 4, and 20 dpa. Miura observed an increase in the channel spacing from 1.2 to 2.3 μm with dose for the 316 alloy and 1.5 to 2.2 μm with dose for the 304 alloy [23]. Jiao and Was examined the effect of alloy, strain, and dose on the development of localized deformation following the proton irradiation of austenitic stainless steels; this analysis focused primarily on the weighted average of the channel height, though some dislocation channel spacing measurements were under taken [100]. The dislocation channel spacing was observed to vary with alloy but increase with dose at a bulk strain of 3%: ranging

between 4.5 and 8.0 μm for 1 dpa and 7.8 and 10.0 μm for 5 dpa. The weighted average channel height increased with increases in either strain and/or irradiation dose. The variation in channel height between alloys also appeared to be correlated with the stacking fault energy (SFE), though this was suggested to be due the effect of SFE on the resultant irradiated microstructure [8,100]. Nishioka *et al.* examined the localized deformation following the neutron irradiation of a cold-worked 316 stainless steel at doses of 4, 35 and 73 dpa [103,105]. In this study the spacing between dislocation channels was measured following the straining to 2-3% at 300^{o}C. The average channel spacing was observed to increase from 1.3 to 2.2 μm from 4 to 35 dpa [103], but remain constant at an average spacing of 2.2 μm at a dose of 73 dpa [105]. While there appears to be a degree of variability in the characterization of dislocation channels between institutions, alloy, and irradiation the results for individual conditions are comparable in that the localized deformation becomes more significant in austenitic stainless steels with increases in dose and strain.

2.3 Irradiation-Assisted Stress Corrosion Cracking

Irradiation-assisted stress corrosion cracking (IASCC) describes the premature cracking and later failure of materials in a corrosive environment which is either induced or accelerated by the presence of ionizing irradiation [106]. The occurrence of this phenomenon has been most prevalent in the structural components of LWRs, where it has been shown that irradiation, even to dose as low as 1 dpa, can significantly alter the mechanical properties and microstructures of austenitic stainless steels, as seen by Figure 2.8 and Figure 2.11, and increase the susceptibility of these alloys to intergranular stress corrosion cracking. Table 2.3 lists a history of environmentally-assisted cracking incidents in BWRs [107], where it can be seen that early on failures were limited to very susceptible regions, i.e. fuel cladding and sensitized components, whereas in current times IASCC failures are observed in un-sensitized core internals. Despite the number of incidents that have occurred during reactor service, initially corrosion was not considered as a serious problem during the design of LWRs. Austenitic stainless steel, the primary structural material used in LWRs, was expected to have a low rate of general corrosion, due to the formation of a strongly passive oxide film. Furthermore, it is likely that initial laboratory experiments underestimated the high stress environment in nuclear reactors, as well as the factor of time, as crack initiation can take up to 25 years [108]. Due to the importance of IASCC-related failures in limiting the

operational lifetimes of the current LWR fleet, it is imperative to understand the processes through which IASCC develops in response to the environment and material parameters.

2.3.1 Environmental Effects

Environmental effects play an important role in the initiation and propagation of cracks in LWRs; the role of the environment can be broadly separated into two categories: water chemistry and radiolysis. The water chemistry refers to the prepared chemistry of the feed water to the reactor and varies primarily based on reactor type. Radiolysis is the primary influence of irradiation on the water chemistry and includes the dissociation of water into several new molecular, ionic and radical products [2,109–112]. Many of these products are either oxidizing or reducing, and hence their relative concentrations can influence the corrosion potential of materials in the environment [109,110,112].

2.3.1.1 Water Chemistry

Water chemistry refers to the prepared chemistry of the feed water that is used within the nuclear reactor. Currently there are three distinct environments that are used in commercial reactors: BWRs use one of two chemistries referred to as normal water chemistry (NWC) and hydrogen water chemistry (HWC), while PWRs use a third distinct water chemistry. While the specific chemistry used may vary from plant to plant, Table 2.4 outlines the main parameters of the individual chemistries [113]. Across these chemistries the primary differences are varying concentrations of dissolved oxygen and hydrogen, which are interlinked. Furthermore, the PWR chemistry operates at higher temperatures and pressures, and has boron and lithium additions. It is also seen that the electrochemical corrosion potential (ECP) varies for each environment; while there are several parameters that change the corrosion potential [114] the most important contributor is the dissolved oxygen content, which is seen to increase ECP with increasing concentration [112,114–116], this effect can be seen in Figure 2.14. It has been observed that lowering the ECP is a key factor in reducing the IASSC susceptibility of stainless steels in high temperature water, as seen in Figure 2.14. One effective method of reducing the ECP, is through the addition of hydrogen to the feed water. Increased hydrogen content promotes the recombination: $2H_2 + O_2 = 2H_2O$, effectively decreasing the oxygen concentration and lowering

the ECP [109,114–116]. However, it takes a large amount of hydrogen additions to effectively reduce the oxidants, which increases expense, as well as initiating several side effects, including adjusting the oxide structure and increasing radiation fields [113–115]. As PWRs run high concentrations of hydrogen, boric acid is added to act as a neutron absorber and reduce the radiation field. As this addition creates an acidic environment, lithium hydroxide (LiOH) is added to balance the pH and maximize the lifetime of steam generators, which is optimized in a slightly alkaline environment. LiOH is chosen over other basic solutions due to its low solubility and presumed negligible effects on corrosion [113]. While these additions are effective in reducing the increased radiation fields from hydrogen additions, the specific effects on how they may influence corrosion has not been well studied.

It is observed that water chemistry is a critical factor in determining the susceptibility of austenitic stainless steels to intergranular corrosion [117], in both irradiated and unirradiated states. Generally, the susceptibility of an environment can be most fully predicted by its resultant ECP [112–116]; which in turn is influenced by a wide range of parameters. Perhaps the most effective method in decreasing the ECP of an environment is to increase hydrogen content, which in turn reduces the dissolved oxygen through the recombination to water; this method has been proven to reduce the intergranular susceptibility in both HWC and PWR water chemistries [112–114]. However, this increased hydrogen concentration can introduce additional factors not accounted for through the ECP, such as altering oxide formation and increasing radiation fields [113]. To combat some of these additional factors, boron and lithium additions are added to PWR chemistry, which can possibly lead to further problems regarding crack initiation and oxide stability [118–120]. Furthermore, the concentration of additional solutes in the feed water, such as sodium, chloride, and even lead, can have wide ranging effects and lead to enhanced cracking susceptibility, though initially present in very small concentrations [113]. Nevertheless, new developments such as the use of zinc additions to the feed water and Noblechem have recently proven useful in reducing ECP and cracking susceptibility [121,122] thus reducing the effect of the water environment on cracking susceptibility and decreasing the lifetime limitations of current reactors due to IASCC.

2.3.1.2 Radiolysis

Radiolysis creates new oxidizing and reducing species through the dissociation of water under irradiation, as such these new products can increase the ECP and hence influence the cracking susceptibility of an environment [109]. While the amount of radiolytic species created by irradiation varies on multiple factors, their concentrations can be estimated as proportional to the square root of the radiation flux for pure water [2]. While these radiolytic products can potentially increase the ECP, the production of oxidizing products is severely limited by the hydrogen content in the feed water [109]. Thus the production of radiolytic products is not considered a major issue in PWR and HWC, as the ECP is effectively unchanged from equilibrium [2,109]. However, these radiolytic products do tend to increase the ECP of NWC due to the low concentration of reducing agents, thus the potential for corrosion in NWC environments can be further enhanced by irradiation. Overall, the effect of radiolysis on corrosion appears to be captured by its effect on ECP, which is negligible in environments containing H_2, but further increases the ECP of oxidizing environments [2].

The effect of irradiation on the localized environment present in the crack tip has also been considered; however, due to the complete oxygen consumption at the crack tip [123], the ECP at the crack tip is reduced from the bulk water chemistry, thus the increased ECP from radiolysis products is minor in comparison. Some radiolytic products, H_2O_2 in particular, have been proposed to have a direct effect on corrosion at the crack tip, i.e. one not fully captured by ECP, but crack initiation or crack propagation data has not yet been found to support this theory [3]

2.3.2 Microchemical Effects

Microchemical effects entails the effect that alloying and solute additions can have on the susceptibility of a material to IASCC. These effects can be broadly divided into three areas: first the initial composition of the material, and secondly the irradiation effects of transmutation and radiation-induced segregation.

2.3.2.1 Material Composition

The initial composition of an austenitic stainless steel can have a wide ranging effect on the specific susceptibility of a material to IASCC [8,33,124–126]. However, it is somewhat difficult to compare directly the specific effect of alloy composition across varying studies as this contribution may be lost in other differences, such as irradiation condition and testing environment. A study by Jiao and Was [8] compared the cracking susceptibilities of several different alloys under the same irradiation conditions and environment. Their results showed two trends: first, that commercial purity alloys, such as CP 304, have higher cracking susceptibility than high purity alloys; second, that as the chromium and nickel content of the alloy increases, its cracking susceptibility appears to be reduced [8]. These trends have been observed in other literature as well, with intergranular cracking being observed to decrease at high chromium contents [2,36] and with high purity alloys having less cracking susceptibility than their commercial purity counterparts [12,124–126]. Note that the effect of material composition can also be dependent on the water environment, for example increasing chromium content is more important in reducing the cracking susceptibility in highly oxygenated environments, and less so under hydrogenated conditions [117]. In summary, it can be seen that increasing the nickel and chromium content [2,8] and removing excess impurity concentrations [12,124–126] from an alloy will decrease its IASCC susceptibility, though there have been exceptions [127,128]. It must be noted that these changes may simply increase the resistance to IASCC, for example, requiring a higher threshold dose to initiate cracking, but do not entirely remove the IASCC susceptibility.

2.3.2.2 Transmutations

The irradiation-induced transmutation of elements describes the conversion of an element or isotope into another. In reactor conditions this will often occur through a nuclear reaction in which an energetic neutron collides with a nucleus. In relation to the IASCC susceptibility, transmutation is of interest due to its production of helium, which may cause embrittlement, as well as encourage void and bubble nucleation [2,65,109]. Transmutation reactions also often generate hydrogen as well; however, as hydrogen is highly mobile in stainless steels at LWR temperatures, this generation is quite minor in comparison to the flux of hydrogen through the

exposure of the material to the reactor coolant. As discussed earlier, void nucleation occurs predominately at temperatures higher than that of LWRs, making the stabilization of void embryos from helium an important issue during weld repair operations, during which both voids and bubbles may form in the heat-affected zone. As such at LWR operation temperatures, the effects of helium and hydrogen cannot be linked directly to an increased IASCC susceptibility of the materials, though their presence will cause embrittlement, leading to an increased yield strength and hardness, as well as reducing the fracture toughness of the material [2,109]. While helium is relatively immobile at LWR temperatures, boron has been known to thermally segregate to grain boundaries [2,35,36], thus the helium will also tend to be located close to the grain boundary upon transmutation, thus enhancing the embrittlement of the material at the grain boundary, leading to an increased probability of intergranular fracture [109].

In addition to the production of helium and hydrogen, there are several secondary effects of transmutation that may influence IASCC susceptibility. Lithium can be produced from boron transmutation in addition to helium; existing as a liquid at LWR temperatures, lithium can decrease the cohesive strength of grain boundaries [129] or enhance crack growth rate through an exothermic, hydrogen-producing reaction with water at the crack tip [55]. Furthermore, transmutation reactions of manganese can lead to the dissolution of MnS precipitates thus releasing sulfur back into the matrix, increasing IASCC susceptibility [55].

2.3.2.3 Radiation-Induced Segregation

Radiation-induced segregation involves the redistribution of both solute and primary alloying elements, thus creating localized changes in composition at point defects, including grain boundaries. As IASCC involves the failure of a material through intergranular cracking and as RIS adjusts the localized composition at those same boundaries, it would not be unreasonable to suggest a correlation. However, as RIS involves both the enrichment and depletion of multiple elements simultaneously, it can be difficult to attribute a change in IASCC susceptibility to the RIS of a specific element, and synergistic effects between the segregation of different elements can lead to even more complex behavior. Despite these complexities, radiation–induced segregation is perhaps the most studied irradiation induced phenomenon in austenitic stainless steels [31–39,117,130–132].

For austenitic stainless steels, chromium will deplete from the grain boundary and point defect sinks under irradiation. As chromium is the most important alloying element in creating the passivating film that leads to the well-known corrosion resistance of stainless steels, its depletion from the grain boundary under irradiation has traditionally been considered the primary reason for the increased susceptibility of these alloys to intergranular cracking. This is largely due to prior studies involving the chromium depletion from the grain boundary during sensitization, through the formation of grain boundary carbides under high temperature annealing, which has been historically linked to excessive grain boundary corrosion [32,36,133]. However, an important difference between radiation-induced chromium depletion and that from sensitization is the width of the depleted zone: under RIS the depleted zone is on the order of 10-20 nm [36], as seen in Figure 2.5, whereas the depleted zone is between 200-300 nm following sensitization [2,16,36,133]. Due to this difference, the dependence of IASCC on grain boundary chromium depletion is much different from that observed from sensitization studies on non-irradiated materials, as seen in the lack of correlation between the amount of cracking and grain boundary chromium content shown in Figure 2.15. Almost no correlation can be drawn regarding the interdependence of chromium depletion and IASCC susceptibility, aside from the fact that there appears to be a maximum chromium content of ~18 wt.% above which the alloy is not susceptible [2], while there is not a corresponding minimum content below which a material will have a guaranteed susceptibility to IASCC. Another argument against the effect of chromium depletion on IASCC susceptibility is the influence of pre-irradiation heat treatments; these treatments can be designed to enrich the grain boundary chromium content prior to irradiation, thus lessening the impact of the subsequent chromium depletion under irradiation. However, even though the materials that received the pre-irradiation heat treatment showed less chromium depletion following irradiation, they actually exhibited a higher IASCC susceptibility [130]. Thus it can be said that while chromium depletion likely influences the IASCC in austenitic stainless steels, it alone is not sufficient to cause IASCC [54]; except in cases of highly oxygenated water, in which chromium depletion has been directly correlated to increased IASCC [117].

Silicon is observed to heavily segregate to the grain boundary under irradiation, and as a solute addition it appears to have a mixed effect on an alloy's IASCC susceptibility by simultaneously enhancing the segregation of chromium and nickel, lowering the yield strength, and increasing elongation [124,126]. However, it has more recently been observed that silicon

segregation appears to continue increasing with dose, as seen in Figure 2.16, up to ten times the initial concentration [54]; this is different from other solute elements which appear to reach a maximum threshold of segregation [36]. This continued segregation is expected to enhance the formation of silicon-type precipitates (γ' and G-phase) [2,45,50] and further increase the susceptibly of silicon-containing alloys, particularly at higher dose levels [2,54]. The increase in the grain boundary segregation of silicon is observed to have a detrimental impact on the grain boundary oxidation under exposure to a high temperature water environment in many studies [134–136]. This has been linked to both the enhanced grain boundary oxidation, as silicon has a lower oxidation free energy than other common alloying elements in austenitic stainless steels [134], and the fact that silicon oxide preferentially dissolves in high temperature water environments [136] by the oxidation reaction:

$$\mathrm{Si} + 2\mathrm{H_2O} = \mathrm{SiO_2} + 4\mathrm{H^+} + 4\mathrm{e^-}\,, \tag{2.7}$$

which is described by a Nerst equation at 288ºC of:

$$E_o = E^o - 0.111\,pH - 0.0278\log(a_{\mathrm{Si}}), \tag{2.8}$$

where E_o is the equilibrium potential, E^o is the standard electrode potential (-1.08 V), and a_{Si} is the atomic concentration of silicon [137]. The equilibrium potential for a typical stainless steel alloy at 288ºC is less than the corrosion potential of both NWC and HWC environments, verifying that silicon is expected to oxidize into SiO_2, which would subsequently dissolve in exposure to high temperature water. The silicon oxide dissolution kinetics should be heavily dependent on the overpotential between the environment and equilibrium potential, thus increasing with both silicon concentration and the corrosion potential of the environment. Interestingly, the role of silicon segregation in enhancing IASCC susceptibility, is most evident in reducing environments, i.e. HWC or PWR, with minimal effects in oxidizing environments, i.e. NWC [135]. Nevertheless, the possible role of an enhanced grain boundary silicon in increasing IASCC susceptibility cannot be dismissed.

While chromium depletion and silicon enrichment are perhaps the most studied elements regarding the response of IASCC to RIS, it is well known that other minor solute elements also segregate under irradiation. Manganese additions are seen to deplete rapidly from the grain boundaries during irradiation, but the effect on IASCC seems to be negligible. Sulfur enriches under irradiation, and appears to enhance IASCC susceptibility [124], particularly at high doses

[138]. The effect of this sulfur segregation appears to be mitigated at low doses by high relative concentrations of carbon and manganese [138]. Phosphorus seems to enrich under irradiation, but is relatively minor in comparison to thermal segregation; due to the prior thermal enrichment and its low bulk concentration, changes are difficult to detect [54]. As a synergistic effect the presence of phosphorus has been observed to decrease the grain boundary enrichment of nickel under irradiation [31]. Molybdenum depletes from the grain boundary during irradiation, but should have little impact on IASCC, though it may increase susceptibility in certain corrosive environments. Helium has low mobility under reactor conditions, but it will likely be enriched at grain boundaries due to the transmutation of boron [54]; this presence of helium should increase IASCC susceptibility [109], but its actual effect is difficult to measure. Boron, carbon, and nitrogen are believed to enrich under irradiation, however, their low bulk concentration and small atomic size make their effects on IASCC difficult to characterize [36,54]. These minor elements are s to suspected to have a more pronounced effect on IASCC susceptibility via coupling mechanisms with the larger elements [36,54]. Thus, while the presence and segregation of various minor elements may either enhance or mitigate IASCC susceptibility, the occurrence of IASCC cannot be directly linked to any single element. As such, while radiation-induced segregation may certainly influence the IASCC susceptibility of a material; RIS alone is not responsible for the phenomenon.

2.3.3 Microstructural Effects

Microstructural effects entail the effect that physical treatments and irradiation-induced changes can have on the susceptibility of a material to IASCC. These effects can be broadly divided into three areas: conditioning of the steel prior to irradiation, irradiation hardening, including defect populations, and change in the deformation mode.

2.3.3.1 Steel Conditioning

During the manufacturing of austenitic stainless steel products there are various treatments which may be undertaken to adjust the mechanical properties of the material. Two common treatments used in the industry are cold-working and annealing, both of which have the propensity to adjust the behavior of the steel under irradiation, and hence influence its IASCC susceptibility.

It should be noted that these effects are most evident as lower doses before the irradiated microstructure saturates, after which both cold worked and annealed steels exhibit similar microstructures [2] as observed in Figure 2.17 [48]. Note that Figure 2.17 shows data from fission neutron irradiations at ~400^{o}C, thus this saturation of the dislocation microstructure would be expected to occur at a higher dose under LWR conditions.

Cold-working is a process generally used to increase the hardness and yield strength of steel, and is undertaken through the deformation of the material, commonly by rolling, which introduces a dislocation network. This dislocation network in turn strengthens the material by resisting the movement of dislocations under further stress. It has been shown in unirradiated steels that increased amounts cold working can lead to enhanced crack growth rates in simulated BWR water tests at 288^{o}C [54]; however, under irradiation cold work has been shown to suppress the formation of radiation defects, particularly voids [2,139], as the dislocation network acts as a sink for the radiation-induced vacancies and interstitials, hence promoting their recombination [123]. It has also been observed that under irradiation to high doses the dislocation network created by cold working is replaced by an irradiated microstructure dominated by loops and small defect clusters [2,48,140]. Furthermore, some types of cold work, particularly surface grinding, can lead to enhanced crack initiation and thus IASCC susceptibility [123,141]. Nevertheless, recent experiments have shown that cold working may still influence IASCC susceptibility, even at higher doses, whereas the IG% of the fracture surface is seen to decrease with increasing unirradiated yield strength, which is representative of the level of cold work [12].

Annealing treatments are often performed on steels after the initial manufacturing to normalize the grain structure and remove residual dislocations; in general, these treatments lead to increased elongation, but decreased yield strength. As was seen in Figure 2.17, annealed steels exhibit a very strong hardening response to irradiation, even at small doses, i.e. <1 dpa, this is primarily because these materials have few sites for vacancy and interstitial recombination, leading to a fast buildup of irradiation defects. As compared to cold-worked materials, annealed materials typically show higher IASCC susceptibility, particularly at low doses, and a greater inclination for the formation of irradiation defects and swelling [123]. Furthermore, excessive heat treatments, particularly those which induce sensitization in the material, have been linked to increased IASCC susceptibility under irradiation [130].

2.3.3.2 Hardness and Yield Strength

As shown by Busby *et al.* the change in yield strength under irradiation for an austenitic stainless steel can be linearly correlated to the increase in hardness, such that:

$$\Delta\sigma_y = 3.03\ \Delta H_v\ , \tag{2.9}$$

wherein $\Delta\sigma_y$ is in MPa and ΔH_v is in kg/mm^2 [142]. Henceforth the effect of an increased hardness and yield strength from irradiation will be considered identical. Under irradiation, austenitic stainless steels undergo hardening in response to the formation of irradiation defects, predominately dislocation loops, in accordance with the dispersed barrier hardening model [54,79], as described previously. The effect of this increased hardening on IASCC susceptibility can be seen in Figure 2.18 in which IASCC susceptibility (%IGSCC) is seen to increase with yield strength [61]. Note that this correlation only seems valid at both very low values (< 400 MPa) and high values (> 800 MPa), wherein the data at the intermediate yield strengths shows a large amount of scatter [54]. However, there is clear evidence to suggest that a high hardness alone is not responsible for an increased IASCC susceptibility. Hash *et al.* performed a comparison of several CP 304 tensile samples with the same nominal hardness, but different contributions from cold work and irradiation; these samples ranged from 35% cold work and no irradiation damage to 0% cold work and 1.7 dpa of damage [141], as represented in Figure 2.19. After testing in a simulated NWC environment at 288ºC, only the samples that received the highest irradiation dose displayed cracking, suggesting that microstructure and not hardness is responsible for enhancing IASCC susceptibility [54,141]. It can be further noted that annealing experiments have further confirmed the lack of an exact correlation between IASCC and hardness [54,78,132,143], though these results will be discussed later.

2.3.3.3 Defect Populations

It has been shown on numerous occasions that the hardening of a material under irradiation is due to the formation of various defect clusters, including: dislocation loops, cavities/voids, solute clusters, and precipitates [12,36,40,42,45,59,78,132,144]. In general, the formation of these defect clusters is related to the hardening by the dispersed barrier hardening law [79], which has been shown to accurately relate the resultant hardening from a particular microstructure [12,132].

The development of the defect populations under irradiation can be seen in Figure 2.8, whereas the increasing defect population is represented by the increasing yield strength [54]; it can be seen that the defect population continues to develop up to ~5 dpa at which point it appears to stabilize. Due to this relation between the radiation hardening and the defect population, the dependence of IASCC susceptibility on the defect population can be viewed as identical to the dependence of IASCC susceptibility on the hardness/yield strength. While there may be specific effect of different defect types on IASCC susceptibility, these relations cannot currently be drawn as the differing defects develop simultaneously under irradiation, thus making their separation exceedingly difficult.

2.3.4 Localized Deformation Effects

As previously discussed, the deformation mode of austenitic stainless steels can change significantly with irradiation [21,90,99,145]. The homogeneous deformation in the unirradiated state is replaced by a heterogeneous deformation at higher doses as the irradiated microstructure impedes dislocation movement. The plasticity becomes localized to narrow channels (< 100 nm) that have been cleared of defects by preceding dislocations, thus providing a preferred path for the movement of subsequent dislocations [2,92–94,146]. This dislocation channeling can cause localized necking and a sharp reduction in the uniform elongation [2]. Of particular interest to IASCC susceptibility is that there are also many possible interactions between dislocation channels and grain boundaries, as shown in Figure 2.20 [10]. These dislocation channels act as a pathway to feed dislocations into a localized portion of the grain boundary, which will pile-up and develop an additional stress field at the grain boundary intersection if they are unable to transmit across the grain boundary [9,146–149]. This pile-up stress has been both shown by both simulation and experiment to be up to twice the applied stress [95,148,149]. The extent of localized deformation, as defined by the channel height, has also been closely related to a material's IASCC susceptibility, shown in Figure 2.21. This study by Jiao and Was found that the dislocation channel height best defined an alloy's susceptibility; much better than several other parameters, including: stacking fault energy (SFE), hardness, and grain boundary chromium RIS [8]. Jiao's results confirmed earlier modeling results that predicted that larger dislocation channels would produce larger normal stresses at the channel intersection, thus making the material more sensitive to intergranular

cracking [97]. More recent studies have more directly linked crack initiation to the pile-up stress present at discontinuous channels [5,7,9,147,148], with discontinuous channel-grain boundary interaction sites being much more likely to initiation cracks, as shown in Figure 2.22 [7]. However, while it has been widely shown that an increased degree dislocation channeling is linked to an increased cracking susceptibility, the exact relationship between dislocation channeling and IASCC are connected has not yet been conclusively proven.

2.3.5 Current State of IASCC Knowledge

IASCC is a major problem for the current generation of nuclear reactors as the cracking susceptibility of the structural materials, predominately austenitic stainless steels, increases maintenance costs and reduces reactor safety, limiting the capability of the commercial reactors to obtain an operational lifetime extension. As such it is imperative that the basic mechanisms of IASCC be understood such that the problem can be better managed and that materials with lower cracking susceptibility can be developed [150–152]. Perhaps the difficult part of understanding the IASCC phenomenon is the difficulty in separating the contributions of varying effects, which develop concurrently under irradiation, as shown in Figure 2.23 [3]. Under irradiation, the water chemistry is adjusted due to radiolysis [110,111], the microchemical state of the material is changed through transmutation [2,109] and RIS [31,38]. Simultaneously, the microstructure is transformed due to the formation of defect clusters [59], dislocation loops [36], solute clusters [42–44], precipitates [74,153], and voids [69]. These microstructural changes lead to localized deformation in dislocation channels becoming the dominant deformation mode [8]. Furthermore, not only is the phenomenon of IASCC complicated by the concurrent development of these irradiation effects, as shown in Figure 2.24 [123], but also by the additional complexity of each effect individually, for example the synergy of hydrogen and helium in void formation [65] or the dependence of precipitate stability on RIS [50]. Due to these complexities, the defining mechanism behind IASCC susceptibly has not yet been determined, though recent research has indicated an inclination towards the fault of dislocation channeling [2,4,8,11,95,104,148], at least with regard to crack initiation. Nevertheless, while correlations have indicated this relationship, there has been limited definitive proof towards the responsibility of localized deformation in determining a material's IASCC susceptibility.

2.4 Post-Irradiation Annealing

As previously discussed, radiation damage in nuclear reactor core internals, and the resulting IASCC, is a major problem threatening the effective lifetime of the current reactor fleet [151]. There are several methods designed to reduce the effect of irradiation and the resulting susceptibility to IASCC, such as new advanced materials [131,150–152,154,155] as well as material treatments such as grain boundary engineering [152,156]. However, there is currently a desire to extend the operating licenses of US reactors beyond their operational lifetimes of 40 years, which for most of the current US reactor fleet will be ending in the next few years. For the operational license extensions to be made, the reactor vessel and core internals must be structurally safe and dependable. The primary factor in lowering the lifetime of nuclear reactors is IASCC, thus finding a way to eliminate, or at least mitigate, IASCC is a key ingredient in improving the lifetime and reliability of the LWR fleet. As such an in-core mitigation technique is desired, using the existing structural materials, predominately 300-series stainless steel, that are being employed in the current commercial reactors. One such method of mitigating IASCC is PIA, a low-temperature annealing process which can remove radiation-induced defects. Low temperature annealing treatments are preferred to prevent the sensitization of the steels [14]. PIA has been shown to reduce the irradiation defect populations, recover the ductility and work-hardening of irradiated structural materials, and reduce or remove the IASCC susceptibility in laboratory tests [47,54,57,78,143,157–168]; and while PIA has not been yet utilized for the treatment of reactor core internals, i.e. austenitic stainless steel components, thermal annealing has been utilized for reducing the radiation embrittlement in many VVER 440-type reactor pressure vessels, constructed of low-alloy steel, from 1987 – 1993 [169].

2.4.1 Removal of Defects

During post-irradiation annealing, the removal of unstable radiation defects, such as defect clusters and dislocation loops [170], and compositional gradients such as those caused by RIS at grain boundaries and solute clusters, will be determined by the equilibrium vacancy concentration and the corresponding diffusion rate [163]. Furthermore, there will be a competition between the removals of opposing defects based on the concentration of vacancies around each defect type. The concentration of vacancies around each defect type will be based on the thermodynamic

considerations, i.e. how much the defect increases the free energy of the system, while the removal rate of a defect type will depend on kinetic considerations, referring to the relative size and placement of the defects. While complete simulations of these processes are available in literature [57,132,163,170], the main points will be outlined.

The vacancy supersaturation around a defect, C_d, will primarily depend on the effect of the defect on the free energy of the system. For dislocation loops, this will be in relation to the dislocation line energy, U, dislocation loop radius, r_{loop}, and the stacking energy, Γ, such that:

$$C_d = C_{eq} * \exp\left[-\left(\frac{U}{br_{loop}} + \frac{\Gamma}{b}\right) b^3/kT\right]. \quad (2.10)$$

Where C_{eq} is the equilibrium vacancy concentration, b is the Burgers vector, k is the Boltzmann constant, and T is the annealing temperature [170]. The segregation of solutes to sinks, whether this be in the formation of solute clusters or RIS at grain boundaries, does not significantly affect the free energy of the overall system, hence the removal of these defects under annealing is largely driven by solute diffusion in accordance with Fick's laws of diffusion [57]. As the dislocation loop formation increases the free energy of the system more than segregation profiles, there will be a larger driving force for the removal of dislocation loops under annealing as compared to that of solute clusters or grain boundary RIS [57].

While thermodynamics are certainly an important part in the removal of defects during an annealing treatment, kinetics must also be considered. These kinetic considerations refer to the overall size of the defects, i.e. how many thermal vacancies are required to fully remove the defect, as well as the distance that the vacancy travels before it encounters a radiation defect. Continuing with the earlier comparison between dislocation loops and segregation profiles, it is seen that dislocation loops not only require less vacancies per volume to be removed in comparison to RIS, but that they are also more evenly dispersed throughout the material, meaning that they have an increased likelihood of encountering thermal vacancies [163]. As such, dislocation loops are also kinetically more likely to be removed than segregation profiles during an annealing treatment. Figure 2.25 shows the simulation for the removal of both dislocation loops and RIS based on both thermodynamic and kinetics, with respect to temperature [163]. Here it is observed that the grain boundary chromium segregation is reduced by ~40%, by the time the dislocation loop population is fully removed, regardless of annealing temperature [57]. This behavior is expected for most radiation defects; defect clusters and dislocation loops will be removed preferentially to their larger

and more stable counterparts, such as grain boundary RIS, solute clusters, precipitates, and larger voids under annealing treatments [60,132,159].

2.4.2 Effects of Post-Irradiation Annealing

While simulations have shown that annealing treatments will reduce the irradiation defect populations, and thus somewhat restore the material to its unirradiated state, quantitative experiments must also be performed to better understand the evolution of these radiation defects under annealing, as well as comparing the reduction of these defects to the IASCC susceptibility of the material. To attain this understanding, data from various literature sources was compiled [43,77,78,132,143,161,164–168,171] and analyzed. Before getting to the data, it is important to note that the various sources utilized different annealing treatments regarding both temperature and time, thus to normalize these parameters, they will be compared based on iron diffusion distance:

$$d = \sqrt{Dt}, \tag{2.11}$$

where D is the iron self-diffusion coefficient and t is the annealing time. D is given by:

$$D = D_o e^{-Q/kT}, \tag{2.12}$$

where Q is the migration energy (2.95 eV), D_o is the pre-exponential term (4.9×10^{-5} m^2/s), and T is the annealing temperature [78]. All later comparisons will be made based on iron diffusion distance, which henceforth represents the severity of the annealing treatment, as calculated with the above listed values.

2.4.2.1 Mitigation of IASCC Susceptibility

Perhaps the most important change to first examine with respect to the annealing treatment is the change in the IASCC susceptibility, as indicated by the intergranular crack fraction (%IG). The results for several cracking experiments for neutron irradiated specimens are shown in Figure 2.26, whereas the % remaining of the as-irradiated IG fracture surface is used to measure the recovery of the IASCC susceptibility. Note that although these materials have different material compositions and levels of irradiation dose, as well as being tested in different water environments, all the materials individually showed a decrease in IASCC susceptibility with increased iron

diffusion distance. However, the rate at which the IASCC susceptibility was recovered, as well as the total amount of the recovery seems to be dependent on the individual material and their respective irradiations. Nevertheless, these results are indicative of the recovery of a material's IASCC susceptibility after a PIA treatment. However, it is also important to note that PIA can also be used as a technique for separating the effects of different radiation effects due to the differing recovering rates of defects under annealing, as was discussed earlier for the case of dislocation loops and segregation profiles. As such it may be useful to examine the change in both microstructural and microchemical features under annealing and compare those changes to the corresponding adjustments in IASCC susceptibility. Thus, if the IASCC susceptibility recovers at the same rate as the recovery of a specific irradiation effect, a possible relation would be highly suggested.

2.4.2.2 Evolution of Irradiation-Induced Microstructure

Changes in the bulk material properties suggest an adjustment of irradiated microstructure during the annealing treatment. Due to the impact of the irradiated microstructure on the material properties, the recovery of these defects is expected to lead to a decreased hardness and yield strength, as well as adjustments to the radiation-induced precipitates and the overall method of deformation. As such these changes can be divided into four general categories: bulk hardness, dislocation loops, solute clusters and precipitates, and deformation mode.

Under an annealing treatment the irradiation hardening of the material is reduced due to the annealing of radiation defects, particularly dislocation loops and small defect clusters. The change in the irradiation hardening with respect to the severity of the annealing treatment can be viewed in Figure 2.27. Overall the data demonstrates a clear reduction in irradiation hardening with increased annealing, indicating the recovery of the irradiation defects. However, it can also be seen that a good correlation is not present between the mitigation of IASCC susceptibility and the recovery of hardening. Though both are recovered with increased iron diffusion distance, the IASCC susceptibility is fully recovered before the hardening; thus confirming the early observations that irradiation hardening alone cannot be responsible for IASCC susceptibility [2].

As explained earlier, dislocation loops are expected to be removed quite rapidly under annealing treatments [132]. This expected reduction of dislocation loops with PIA has been

confirmed by TEM analysis of the microstructure [77,78,132,143,160]. As most of the dislocation loops present in an irradiated austenitic stainless steel are interstitial loops, the primary method of their removal under PIA is the recombination reaction of the interstitials in the loop with thermally-induced vacancies in the matrix. This will lead to a decrease in the average loop size and density with annealing [132]. The simplest method to measure the reduction in the dislocation loop sizes and densities is to examine the overall reduction in the dislocation loop line length that is the circumference of the average dislocation loop multiplied by the density. Figure 2.28 compares the reduction in the dislocation loop line length and the reduction in irradiation hardening following PIA for several neutron-irradiated austenitic stainless steels [77,117]. Overall, the dislocation loop line length and irradiation hardening are reduced at relatively similar rates, however, there is some residual hardening remaining after the dislocation loops have been fully removed. This correlation seems to indicate that the dislocation loop populations contribute to most, but not all the irradiation hardening.

While solute clusters and precipitates both certainly play a role in the overall hardening of a material under irradiation, the stability of a precipitate is generally higher, as well as being a more effective barrier to dislocation movement [78]. This increased stability seems to suggest precipitates may be a primary contributor to the residual irradiation hardening observed after PIA. Unfortunately, as γ' precipitates only form under specific conditions during LWR irradiation, the influence of post-irradiation annealing on γ' precipitates have not been widely studied. However, there are two recent literature references which studied the dependence of both γ' precipitates and nickel-silicon solute clusters on annealing [43,78]. Both papers investigated samples irradiated under similar conditions: a PWR environment to a dose of ~25 dpa; however, the materials and techniques used were different. Toyama *et al.* studied the γ' precipitates in 304 stainless steel using atom probe tomography (APT) [43], while Fukuya *et al.* studied cold-worked 316L using TEM. The primary difference is that APT measures clusters of enriched silicon and nickel concentrations, thus observing both solute clusters and precipitates, while TEM is only able to identify precipitates with a specific γ' lattice structure. While the populations are expected to be similar due to the similarity in irradiation, the results showed wide variations in γ' precipitate size and density, as well as different responses to post-irradiation annealing. In general, the APT showed much higher densities and sizes; whereas the TEM analysis was lower in size and density. Furthermore, as shown in Figure 2.29, the APT analysis demonstrated a large change in size and density under

PIA, with the clusters both dissolving and becoming more diffuse. The TEM analysis showed relatively little change with annealing, seeming to indicate that nickel and silicon-enriched clusters that have formed a lattice structure, i.e. becoming γ' precipitates, are much more stable than their cluster brethren. While the recent literature reports seem to indicate a difference in annealing behavior of nickel and silicon-enriched clusters and true γ' precipitates, more experiments are required before the annealing behavior can be fully understood.

2.4.2.3 Localized Deformation

As discussed earlier, the level of localized deformation in an irradiated specimen has been closely linked to its IASCC susceptibility [4,8,12]; however, despite this correlation there have not been any definitive observations of the change in the localized deformation with respect to annealing. The primary reason for this discrepancy lie in the timings of the studies: the effects of PIA was predominantly studied more than 15 years ago, whereas the correlation between IASCC and localized deformation has only been examined more recently. As such there is not currently any data available to assess the change in localized deformation with respect to annealing, though a recent resurgence in PIA research may change this in the near future [47,143,157]. For example, recent work by Jiao *et al.* has indicated, at least qualitatively, that both the channel heights and densities appear to decrease with annealing [143]. Thus, while annealing data correlating the change in IASCC susceptibility and localized deformation is not currently available, it is expected within the next few years.

2.4.2.4 Microchemistry

As was discussed earlier, there are three major microchemical effects that seem to have an influence on the IASCC susceptibility of a material: the starting composition, transmutations under irradiation, and RIS. Of these three, only RIS will possibly be adjusted under PIA; with the RIS of chromium being the most widely studied. Thus, it is important to examine how the level of RIS of solute elements changes under annealing, particularly regarding the changes in IASCC susceptibility. Figure 2.30 compares the change in the as-irradiated chromium segregation and IASCC susceptibility with respect to the iron diffusion distance [77,78,168,171]. It is easily seen that while the chromium segregation remains relatively constant, only significantly decreasing at

high iron diffusion distances, the IASCC susceptibility is removed rather rapidly. This reduction of RIS being limited to high iron diffusion distances matches the earlier modeling of thermodynamic and kinetic considerations [163], which suggested that the reduction of RIS would only be preferred once most of the other irradiation defects are removed. However, it must be noted that RIS of more minor solute elements, such as silicon, will be de-segregated more rapidly under PIA treatments, due to their faster diffusion rates. Despite the improved diffusion rates, full recovery of silicon segregation is still achieved after the full IASCC mitigation of the material has been achieved under PIA treatments [78,132]. Overall, this correlation further indicates that IASCC susceptibility is not dependent on the chromium grain boundary concentration [132], though the role of more minor solutes is more inconclusive.

2.4.3 Annealing Characteristics

Annealing characteristics is meant to refer to the effect that changing the various annealing parameters may affect the overall IASCC recovery of the target material. For this purpose, the primary parameters are the annealing temperature and the annealing time. Perhaps the best source for solely examining the effect of annealing temperature is Fukuya *et al.* which performed annealing experiments at temperatures of 450^{o}C, 500^{o}C, 550^{o}C, and 600^{o}C all for a time period of one hour [78]. The effect of these varying temperatures on the irradiated microstructure and microchemistry, as well as cracking behavior, can be seen in Figure 2.31 and Figure 2.32. As seen in Figure 2.31, annealing at an increased temperature typically leads to a lower defect density, indicated by a higher removal rate; this is expected due to the increased concentration of thermal vacancies that would be present at higher temperatures. Furthermore, Figure 2.32 demonstrates that the IASCC susceptibility and irradiation hardening are also more rapidly removed during higher temperature annealing treatments, whereas the increased temperature is indicated by the increased iron diffusion distance. The effect of annealing time is even more straightforward as increased annealing time leads to an increased removal of defects. However, recent work by Jiao *et al.* has indicated that there may be a limit on the total amount of irradiation damage that can be removed at a specific annealing temperature, as seen in Figure 2.33 [143]. This set of annealing experiments indicates that the maximum hardness recovery for 500^{o}C is approximately 40% of the as-irradiated, 550^{o}C annealing can reduce the hardness to 20% of the as-irradiated state and

annealing at 600^{o}C can lead to full recovery of the hardness. These results seem to indicate that there may be specific irradiation defects which are more stable, such as precipitates, and hence require a higher annealing temperature to be dissolved. It should be noted, however, that due to the exponential dependence of the iron diffusion distance on the annealing temperature, this effect is not unexpected. Iron diffusion distance remains as the best method to normalize annealing treatments at different times and temperatures.

2.4.4 Summary of Post-Irradiation Annealing

It has been shown that PIA treatments are extremely effective in reducing the IASCC susceptibility, irradiation hardening, and, to a lesser extent, chromium RIS of neutron-irradiated austenitic stainless steels. While the data shown thus far has been exclusively from neutron-irradiated material, it is important to note that similar PIA studies on proton-irradiated material shows an excellent comparison, as shown in Figure 2.34. Due to its increased ease in production and handling, proton-irradiations have been effective in expanding the available data set, allowing for a clearer examination of the trends with increased PIA treatments. Overall, IASCC susceptibility is observed to decrease quite rapidly with annealing, while the removal of irradiation hardening decreases more evenly with increased iron diffusion distance. Finally, the amount of segregation of chromium to grain boundaries remains relatively constant, until most of the irradiation-induced defects have been removed. PIA is an effective method of in removing the IASCC susceptibility of irradiated austenitic stainless steels, as well as separating out the individual impact of specific microstructural and microchemical features.

Table 2.1. Common alloys of lean austenitic stainless steels [14].

Alloy	Designation	C	N	Cr	Ni	Mo	Mn	Si	Other	Other	Other
201	S20100	0.08	0.07	16.3	4.5	0.2	7.1	0.45	0.001 S	0.03 P	0.2 Cu
201 drawing	S220100	0.08	0.07	16.9	5.4	0.02	7.1	0.5	0.001 S	0.30 P	0.6 Cu
201LN	S20153	0.02	0.13	16.3	4.5	0.2	7.1	0.45	0.001 S	0.03 P	0.5 Cu
301 tensile	S30100	0.08	0.4	16.6	6.8	0.2	1.0	0.45	0.001 S	0.03 P	0.3 Cu
301 drawing	S30100	0.08	0.04	17.4	7.4	0.02	1.7	0.45	0.007 S	0.03 P	0.6 Cu
304	S30400	0.05	0.05	18.3	8.1	0.3	1.8	0.45	0.001 S	0.03 P	0.3 Cu
304 drawing	S30400	0.05	0.04	18.4	8.6	0.3	1.8	0.45	0.001 S	0.03 P	0.3 Cu
304 extra drawing	S30400	0.06	0.04	18.3	9.1	0.3	1.8	0.45	0.001 S	0.030 P	0.4 Cu
304L tubing	S30403	0.02	0.09	18.3	8.1	0.3	1.8	0.45	0.013 S	0.030 P	0.4 Ci
305	S30500	0.05	0.02	18.8	12.1	0.2	0.8	0.60	0.001 S	0.02 P	0.2 Cu
321	S32100	0.05	0.01	17.7	9.1	0.03	1.0	0.45	0.001 S	0.03 P	0.4 Ti
316L	S31603	0.02	0.0	16.4	10.5	2.1	1.8	0.50	0.010 S	0.03 P	0.4 Cu

Table 2.2. Common phases formed in austenitic stainless steel separated by class of radiation-influenced development [48].

Radiation-enhanced/retarded	Radiation-modified	Radiation-induced
M_6C, MC, $M_{23}C_6$, Laves, σ, χ	M_6C, M_2P, Laves	$M_6Ni_{16}Si_7$ (G), Ni_3Si (γ'), MP, M_2P, M_3P

Table 2.3. Component failures by IASCC or IGSCC including reactor location, alloy, and failure date [2].

Component and mode of failure	Alloy	Failure Date
Fuel cladding, IASCC	304	1960s ↓
Furnace-sensitized safe ends, IGSCC	304, 182, 600	
Weld-sensitized small diameter piping, IGSCC	304	
Weld-sensitized large diameter piping, IGSCC	304	
Furnace-sensitized weldments and safe ends, IGSCC	182/600	
Crevice-induced cracking	304L/316L	1980s ↓
Jet pump beams, IGSCC	X750	
Cold work induced IGSCC of "resistant" alloys	304L	
Irradiated core internals, IASCC	304, 316	
IGSCC/IASCC of low-carbon and stabilized stainless steels	304L, 316L, 321, 347	2000s

Table 2.4. Water chemistry parameters for commercial reactors: BWR-NWC, BWR-HWC, and PWR [113].

Environmental Parameters	BWR-NWC	BWR-HWC	PWR
Coolant Temp (^{o}C)	288	288	320
Coolant Pressure (psig)	1020	1020	2420
pH (at 25^{o}C)	6.0	6.0	7.0-7.2
Oxygen (ppb)	300-2000	<10	<5
Hydrogen (ppm)		0.4-3	3-5 (35 cc/kg)
ECP (mV_{SHE})	+150	<-230	-770
Conductivity (μS/cm)	<0.1	<0.1	20.5
B content (ppm)			1000
Li content (ppm)			2-3
SO_{4-} content (ppb)	<3	<3	<3
Cl^{-} content (ppb)	<1	<1	<1

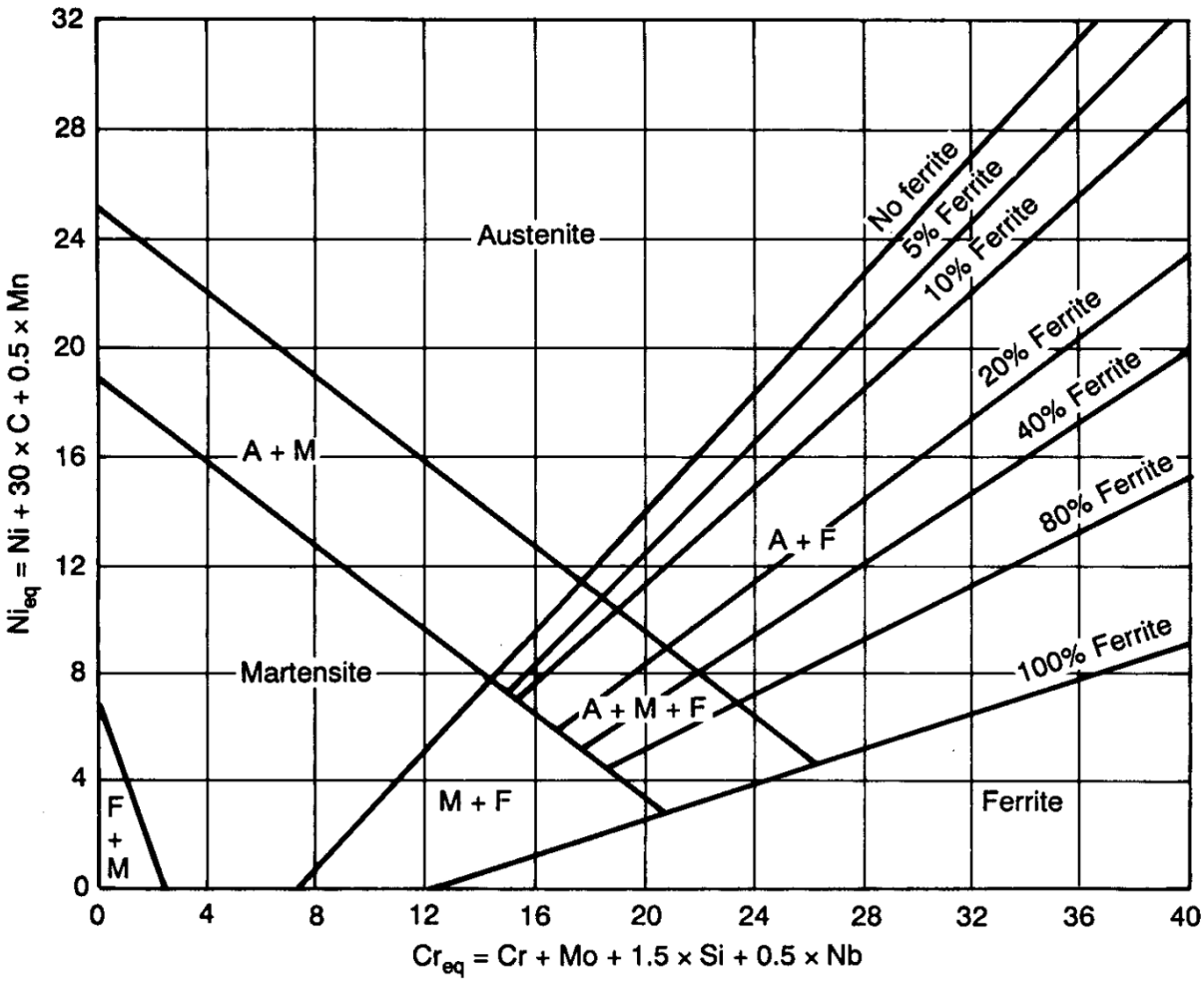

Figure 2.1. Schaeffler-Delong stainless steel constitution diagram, showing the equivalent nickel and chromium concentrations and effect on the resulting phase [14].

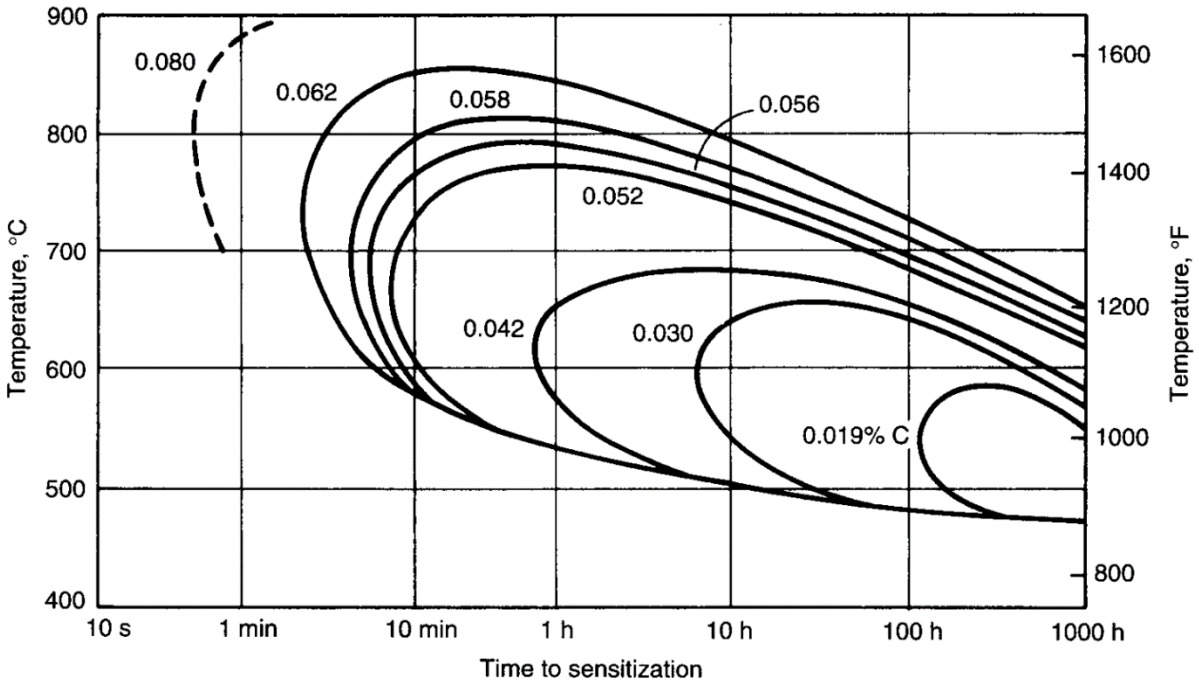

Figure 2.2. Time-temperature-sensitization curves for $Cr_{23}C_6$ as a function of carbon content [14].

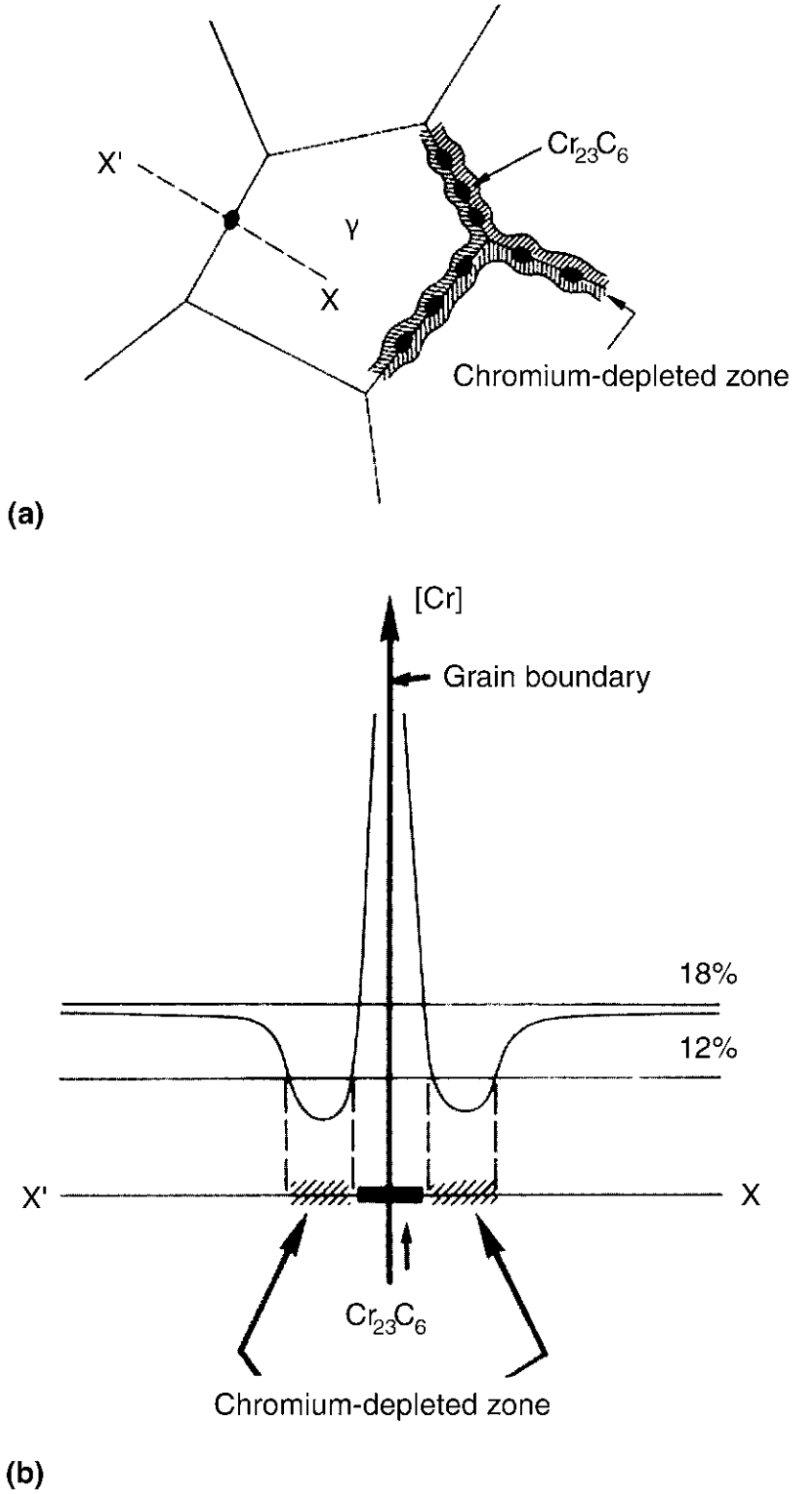

Figure 2.3. Representation of chromium depletion through sensitization [14].

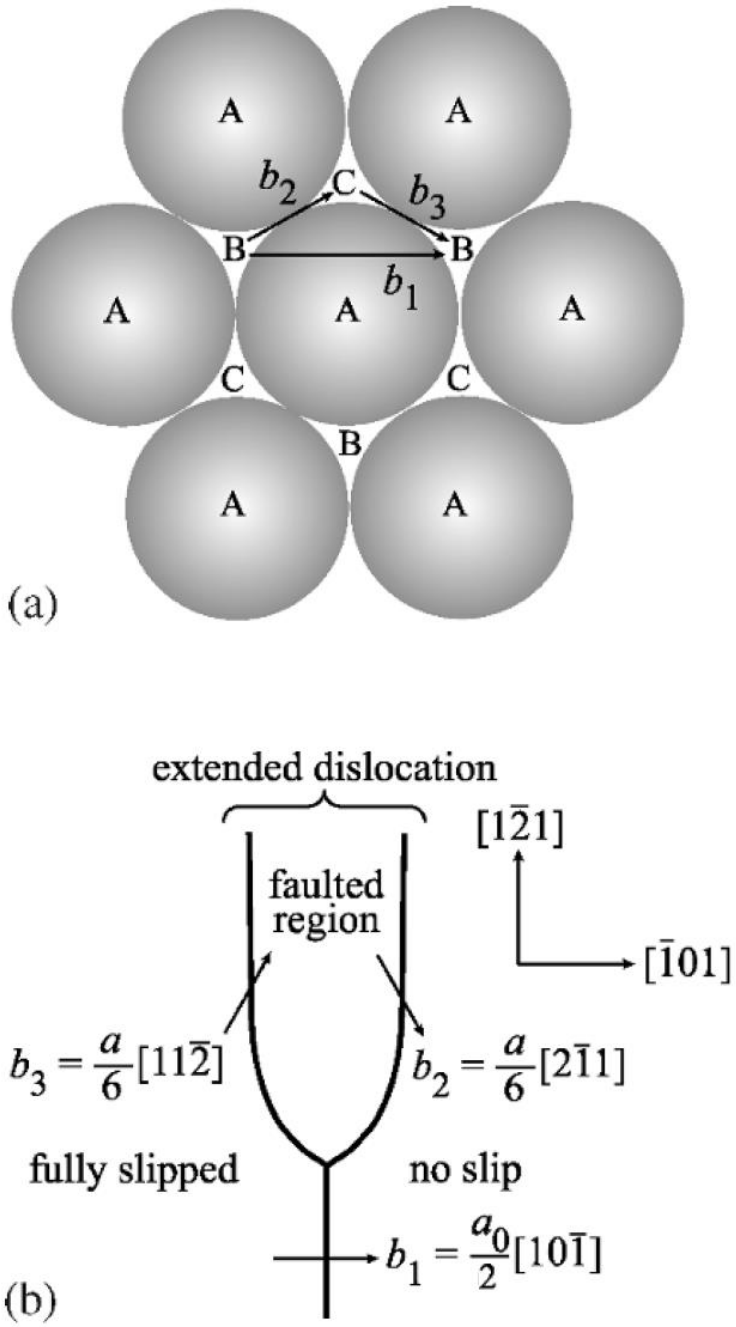

Figure 2.4. a) Dissociation of an edge dislocation (b_1) into two partial dislocations (b_2, b_3) on a {111} plane in an FCC lattice structure. b) dissociation reaction showing the separation of the partial dislocations by a stacking fault [19].

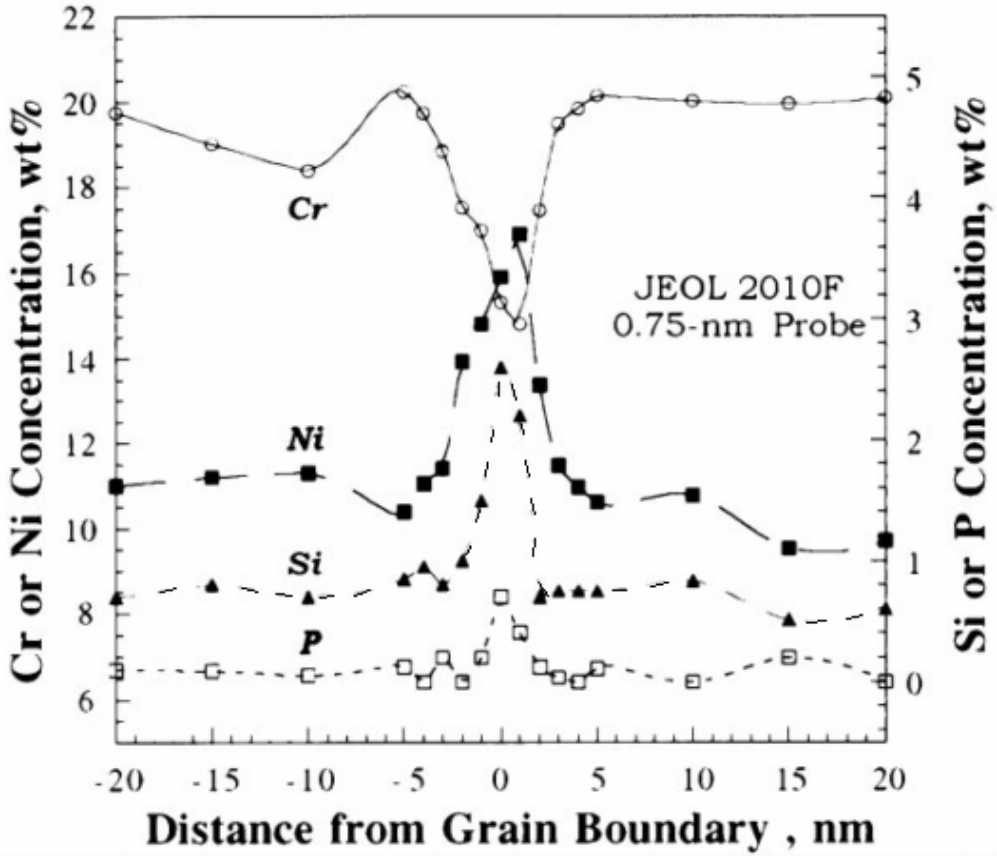

Figure 2.5. Typical radiation-induced segregation profile at a grain boundary for an austenitic stainless steel [36].

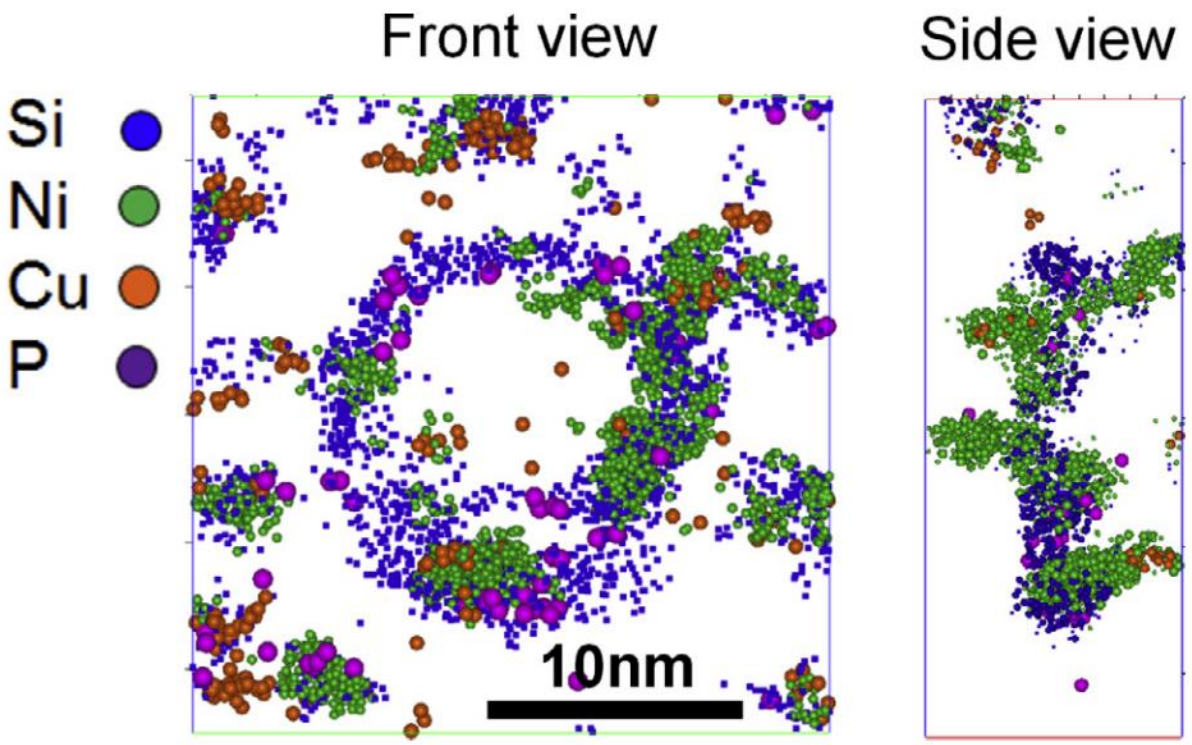

Figure 2.6. Close-up image of a solutes segregated to a dislocation loop. Only atoms that exceed a specified local concentration are displayed: Si, 6.3 at.%; Ni, 23.0 at.%; Cu, 3.0 at.%; P, 2.0 at.% [42].

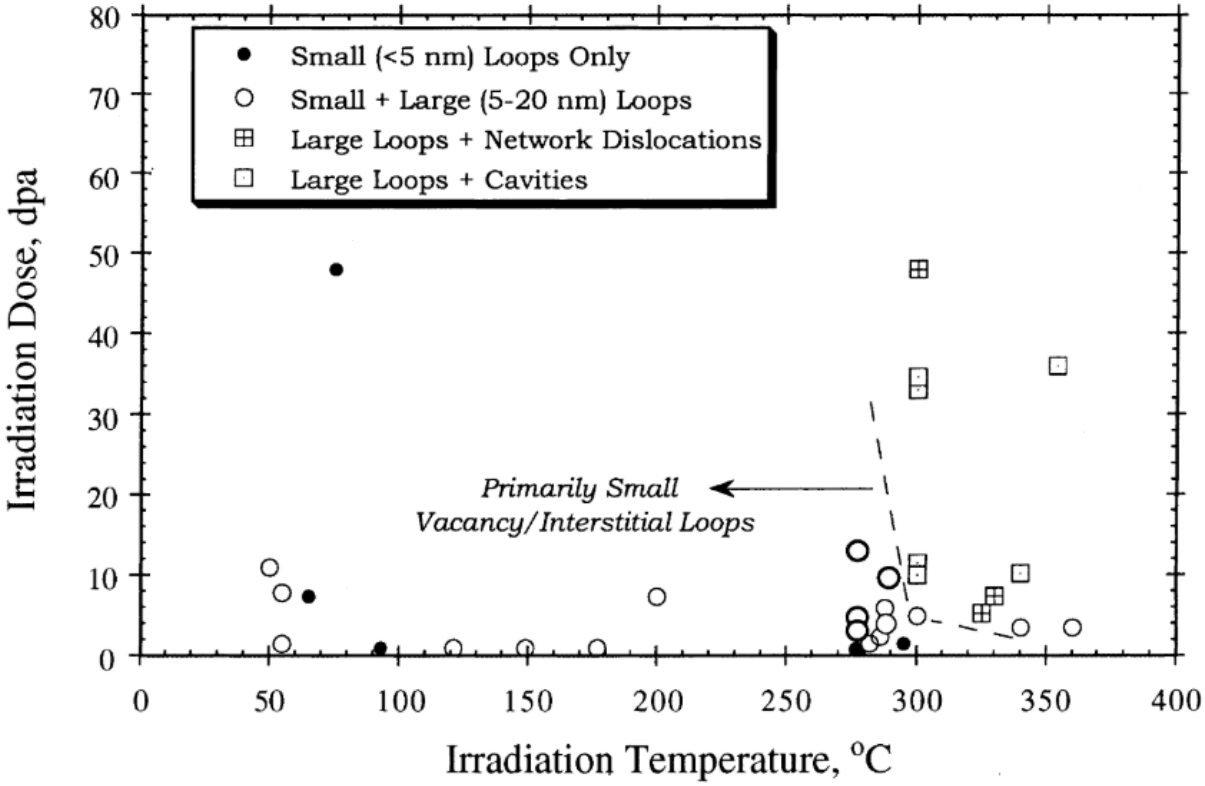

Figure 2.7. Dependence of the irradiated microstructure on the irradiation temperature and dose. 300°C is generally considered to be an important transition temperature, below which only small dislocation loops and defect clusters will form [36].

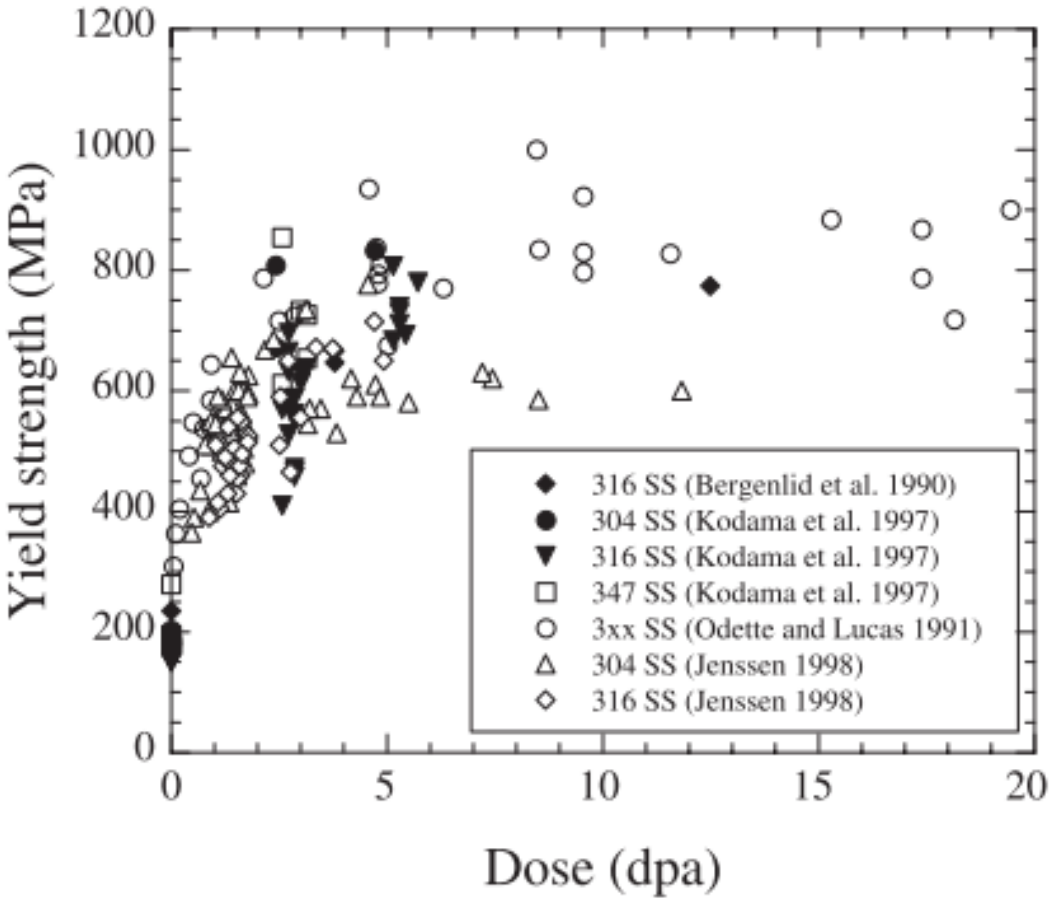

Figure 2.8. Increasing yield strength with respect to dose. The data shows a sharp increase in yield strength by a factor of four once a dose of 5 dpa is reached, after which the yield strength appears to saturate [54].

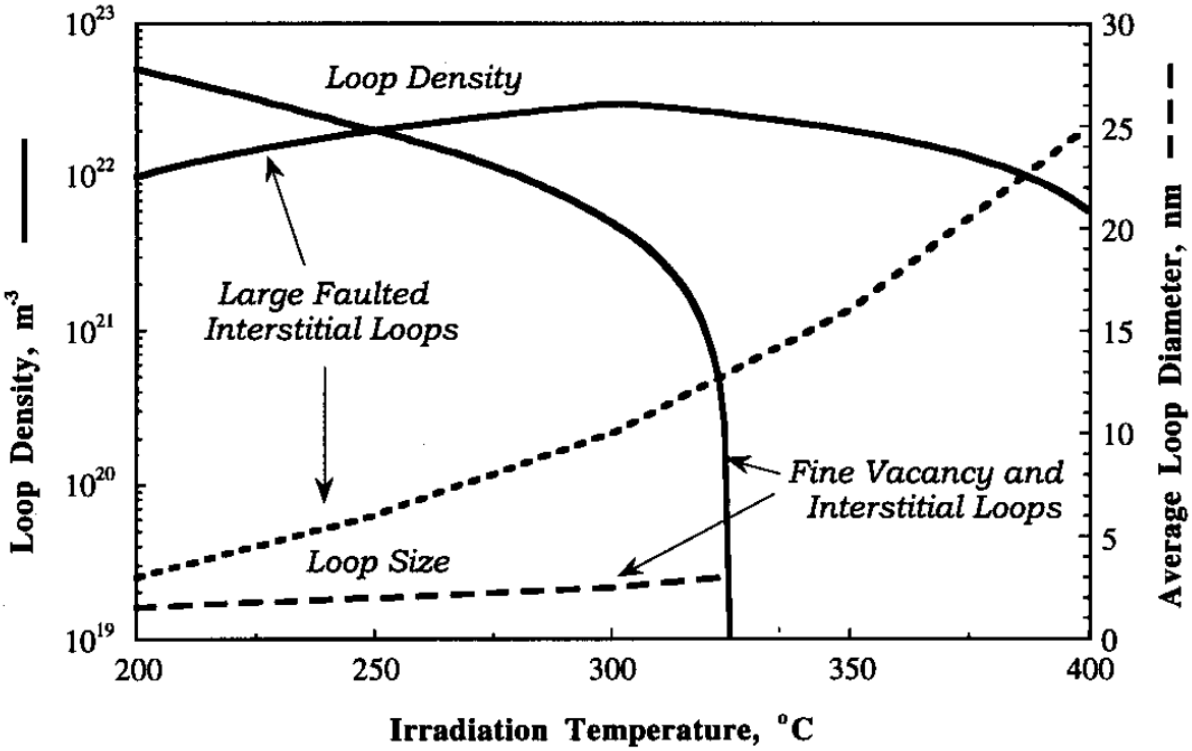

Figure 2.9. Estimated dislocation loop size and density as a function of temperature at a dose of 10 dpa for austenitic stainless steels [61].

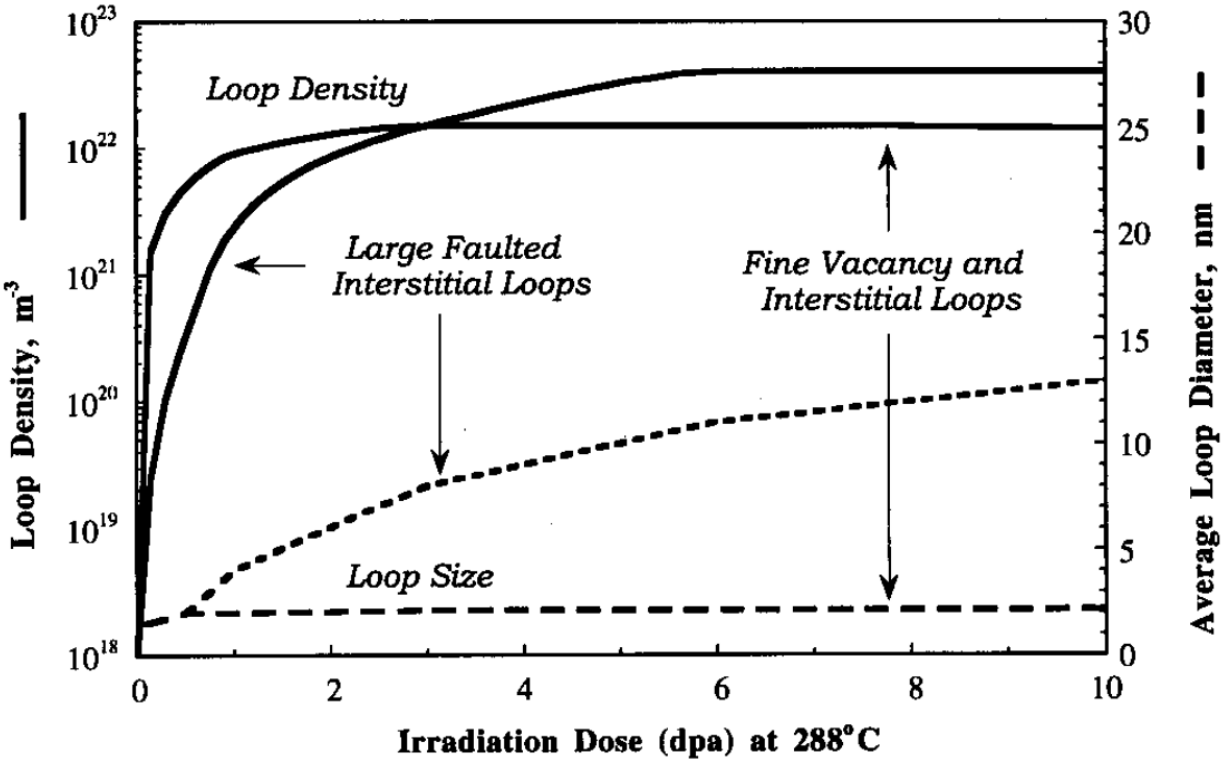

Figure 2.10. Evolution of the loop density and size with respect to dose at a temperature of 288ºC. The density saturates quite quickly (~1 dpa) whereas the size does not appear to saturate [61].

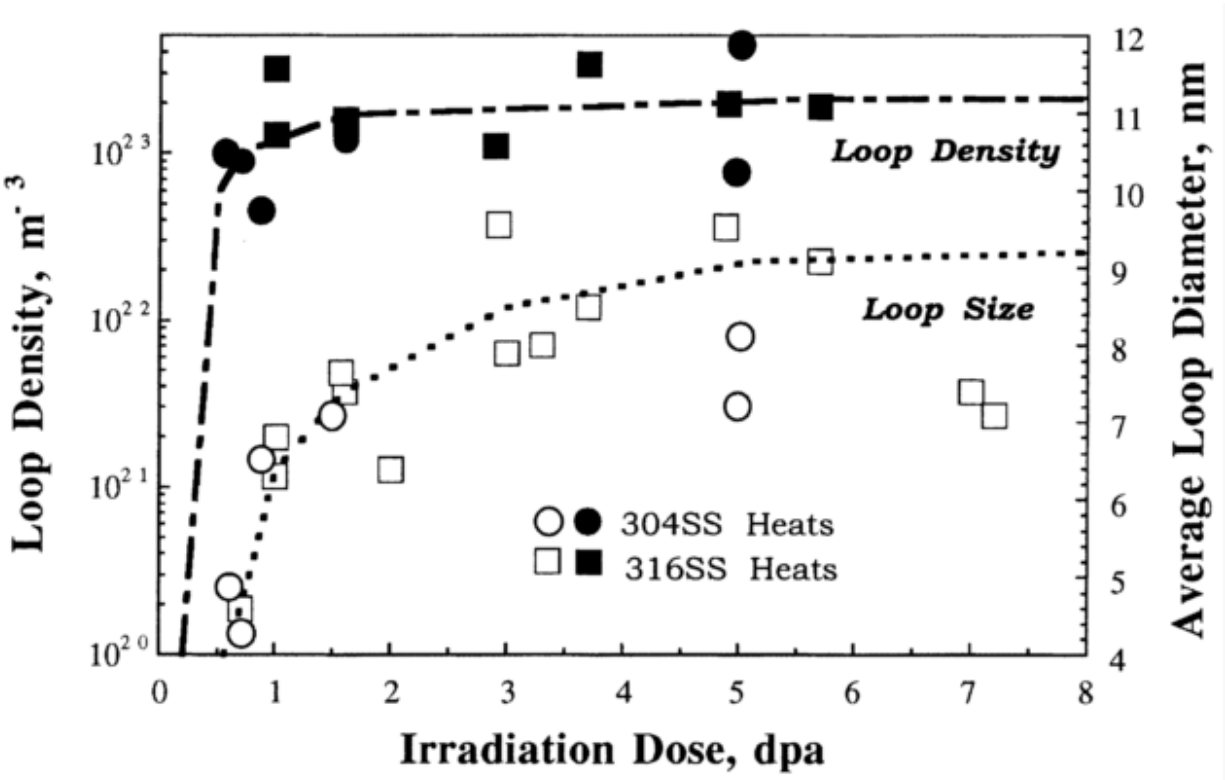

Figure 2.11. Evolution of the loop density and size with respect to dose. The density saturates quite quickly (~1 dpa) whereas the size does not appear to saturate until (~5 dpa) [36].

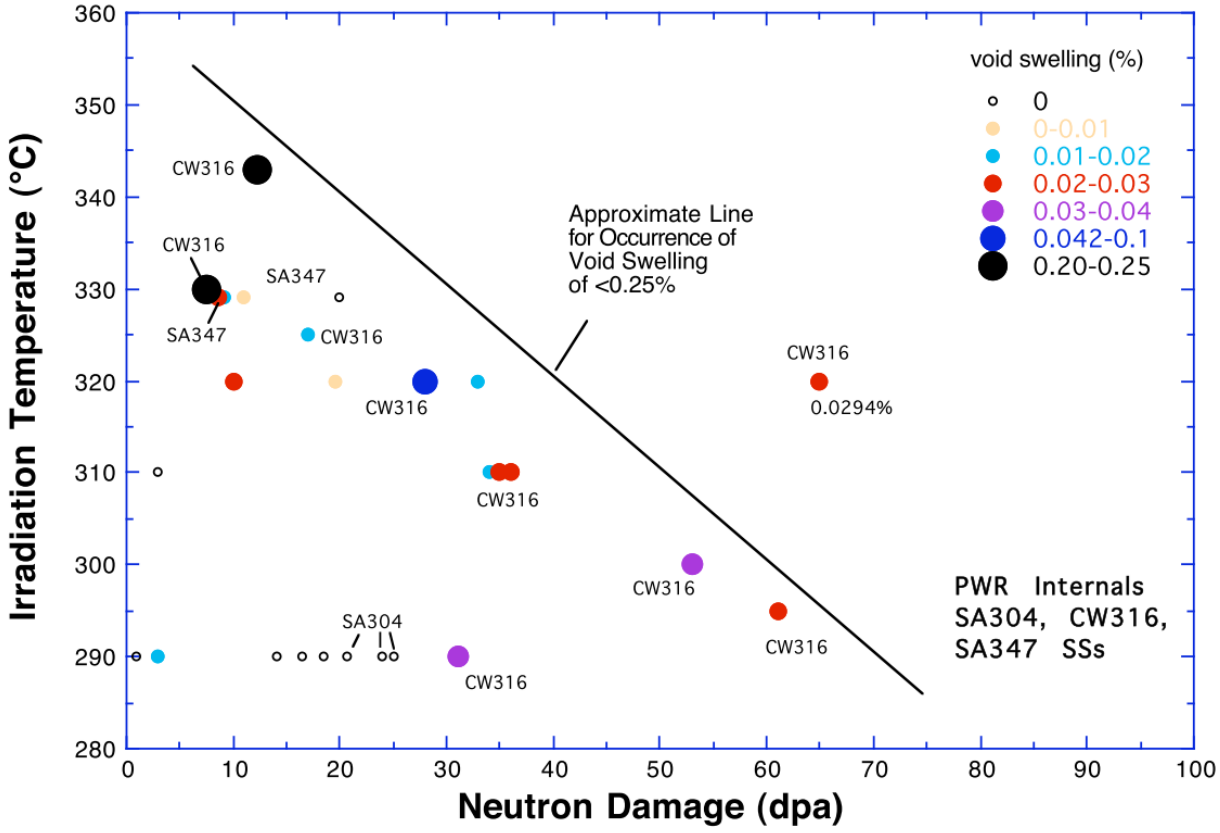

Figure 2.12. Evolution of swelling in austenitic stainless steels with regards to dose and temperature [71].

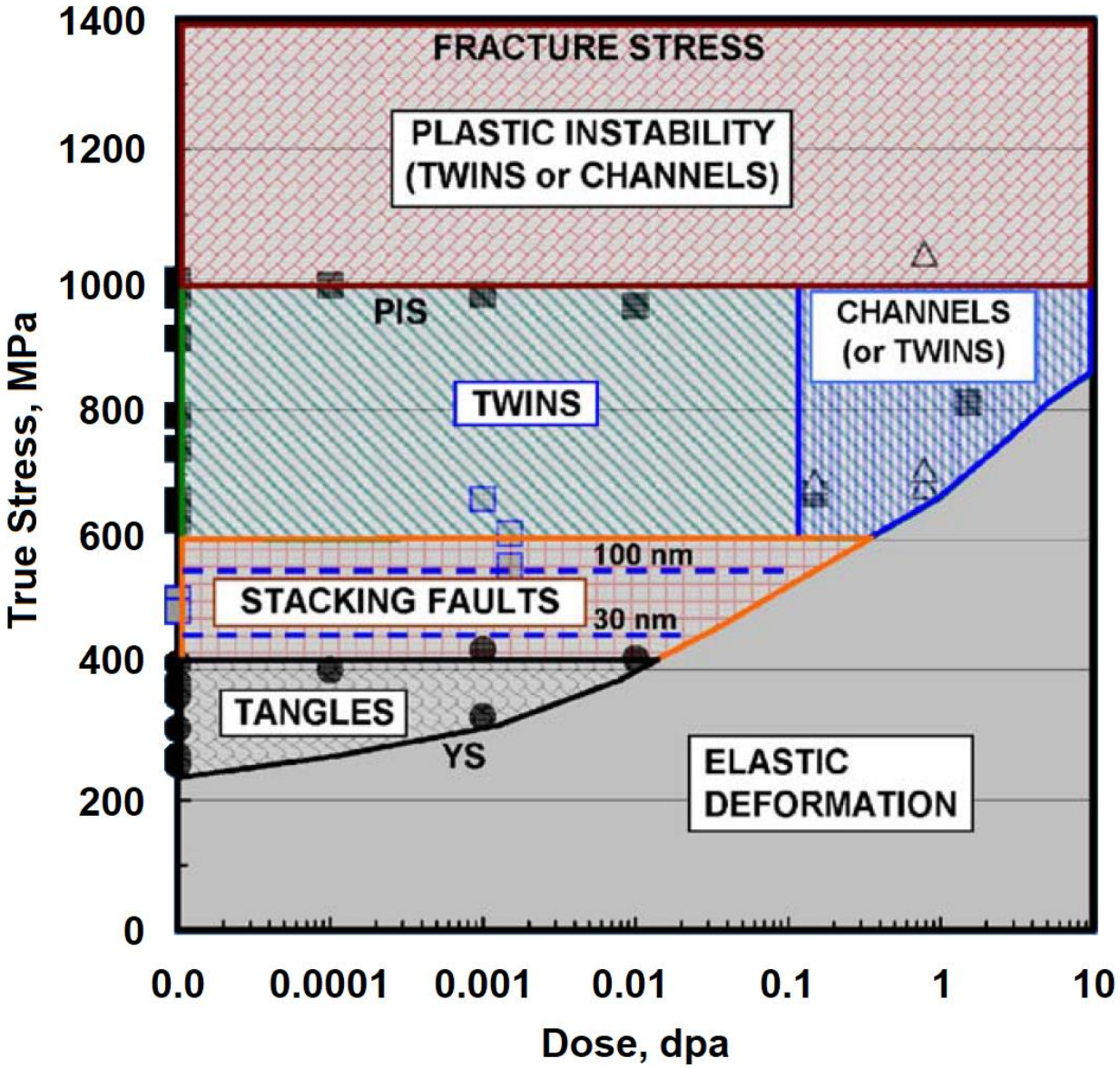

Figure 2.13. Deformation mode map for irradiated 316 and 316L austenitic stainless steels in true stress-dose space. Dislocation channeling is the primary deformation at high stresses and doses greater than 0.1 dpa [99].

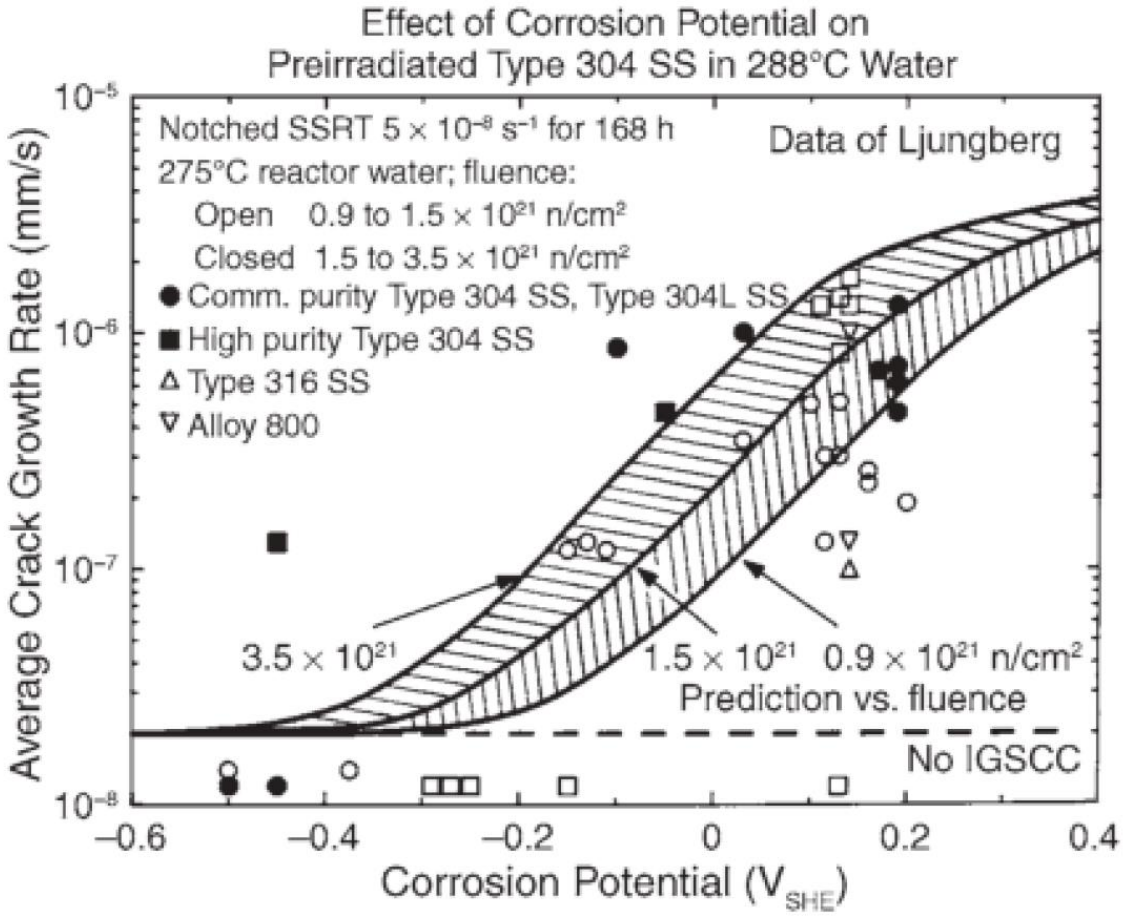

Figure 2.14. Dependence of crack propagation rate on ECP, note the ECP regions for NWC and HWC and their respective crack growth rates [123].

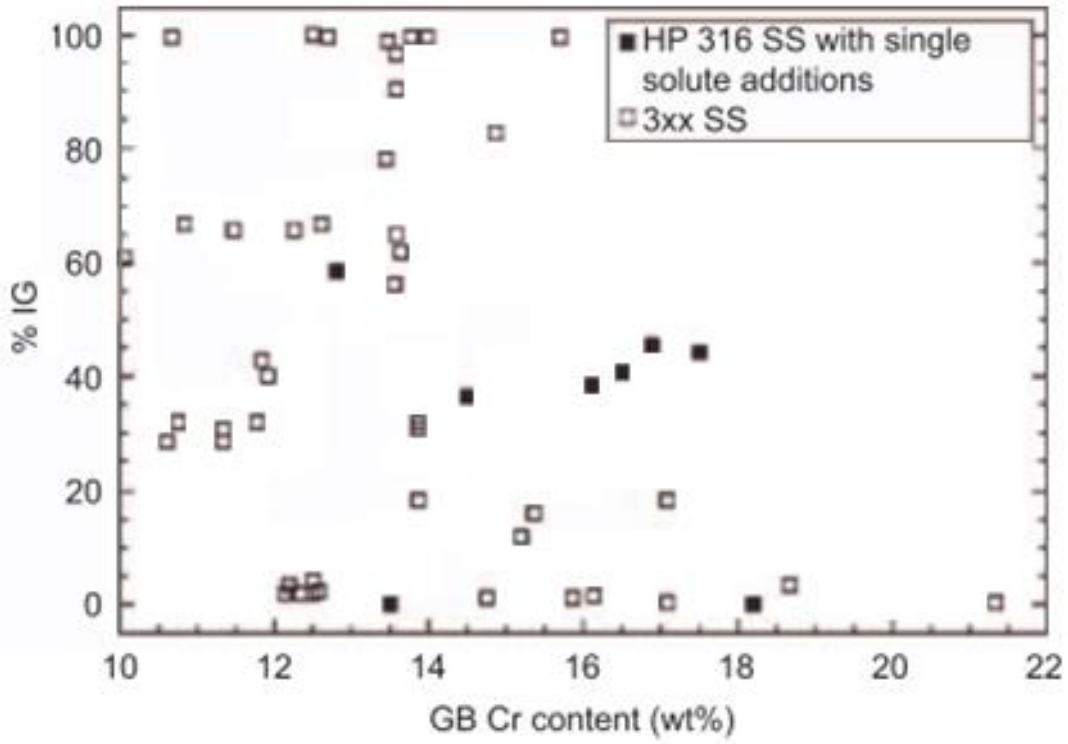

Figure 2.15. Comparison of intergranular cracking with the grain boundary chromium content. Overall, there is not a clear correlation though there does appear to be a threshold maximum (18 wt.%) above which cracking does not occur [2].

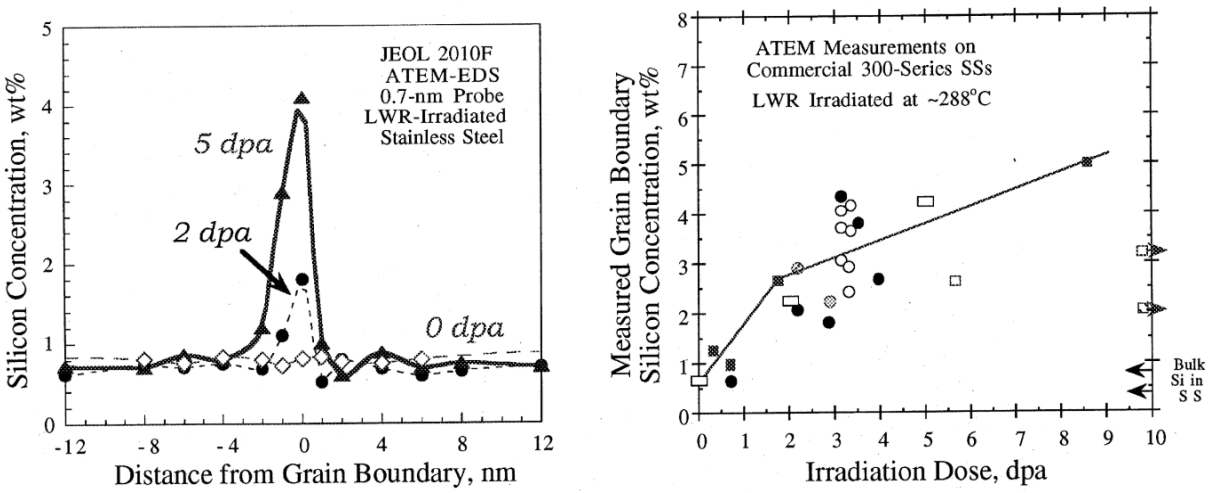

Figure 2.16. Demonstration of the increase in the segregation of silicon under irradiation as a function of dpa [36].

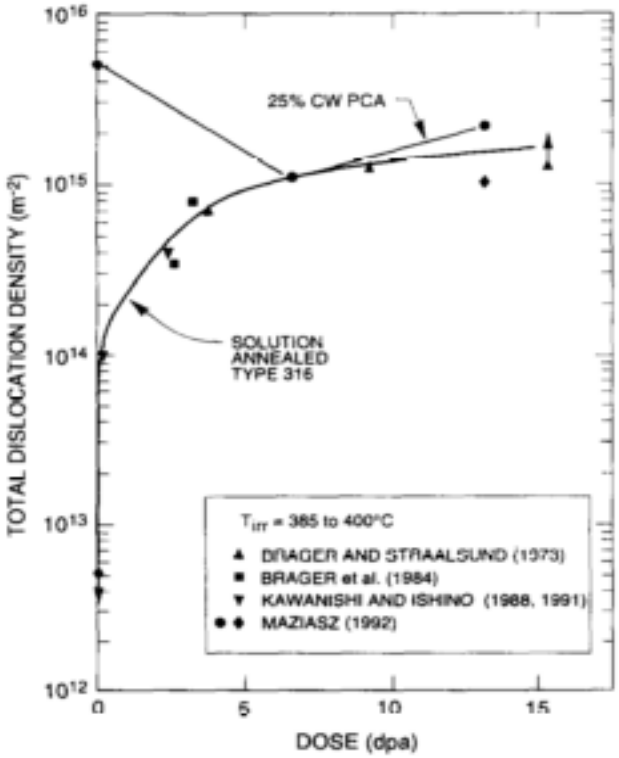

Figure 2.17. Change in the total dislocation density as a function of dose at 400ºC for both cold worked and annealed 316 stainless steel; note that both have similar densities above 5 dpa [48].

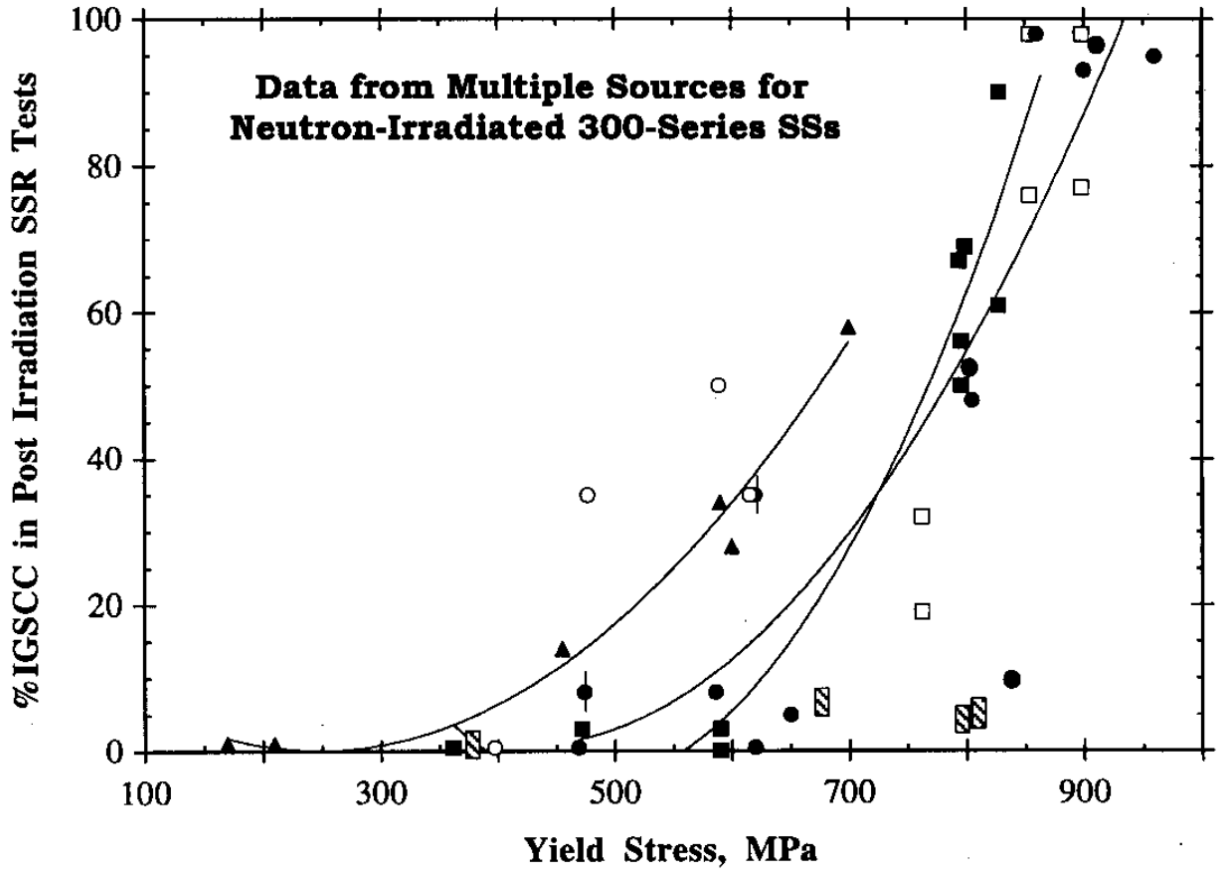

Figure 2.18. Distribution of the as-irradiated yield strength of several austenitic stainless steels in comparison to the IG% of the fracture surface [61].

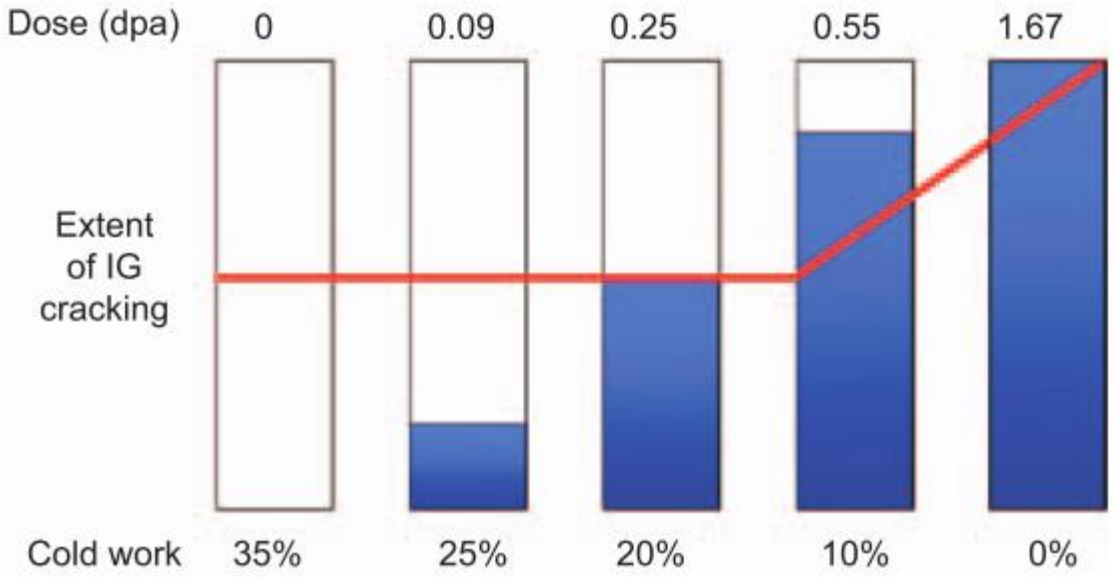

Figure 2.19. Illustration of the dependence of cracking on irradiation hardening and cold work. Hardening alone is insufficient in enhancing the IASCC susceptibility of an alloy [2,141].

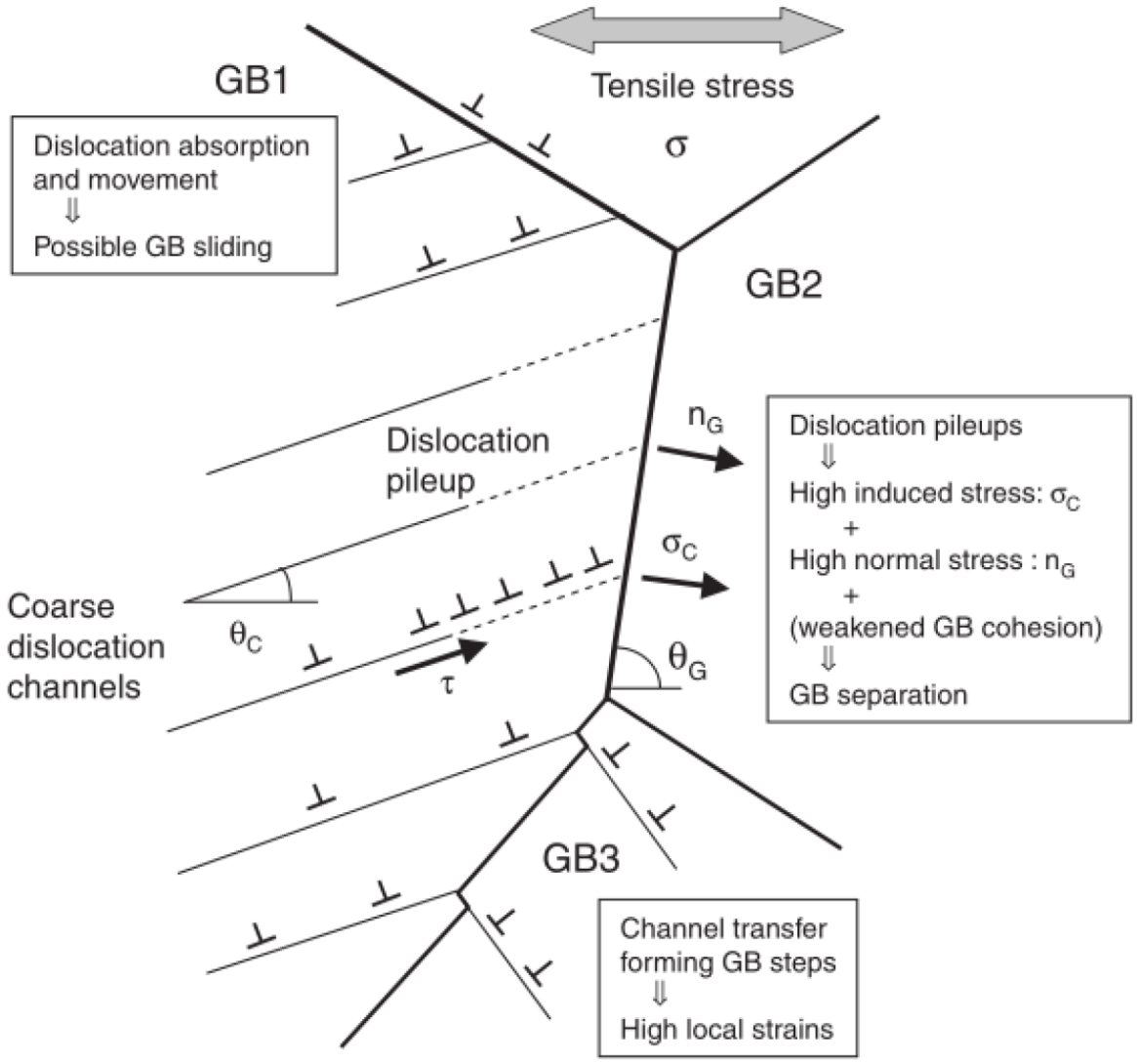

Figure 2.20. Schematic demonstrating several possible dislocation channel-grain boundary interactions, and the possible impact on enhancing IASCC susceptibility [10].

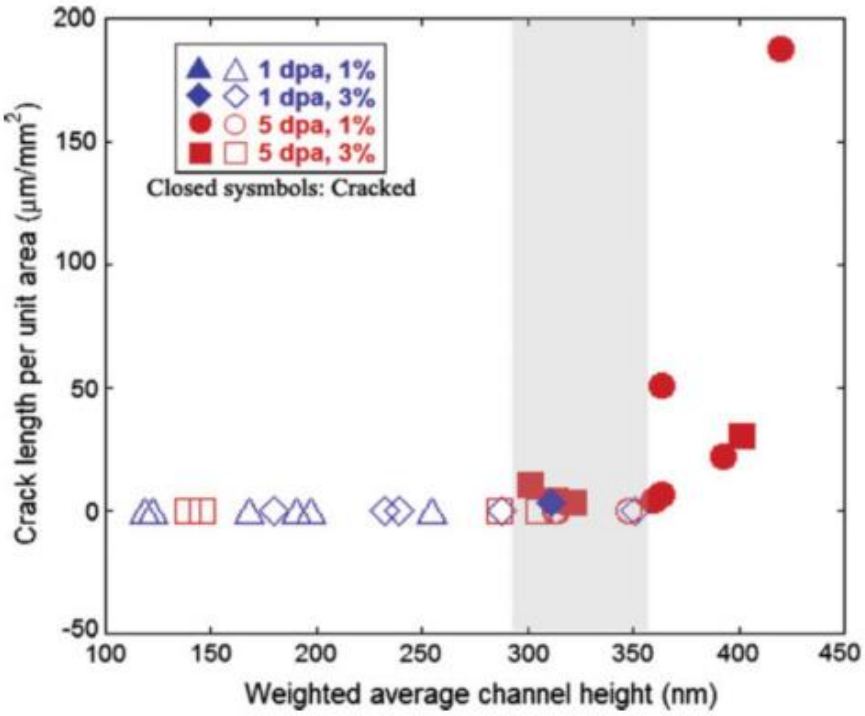

Figure 2.21. Comparison of the channel height of several irradiated alloys and the IASCC susceptibility (crack length per unit area) [8].

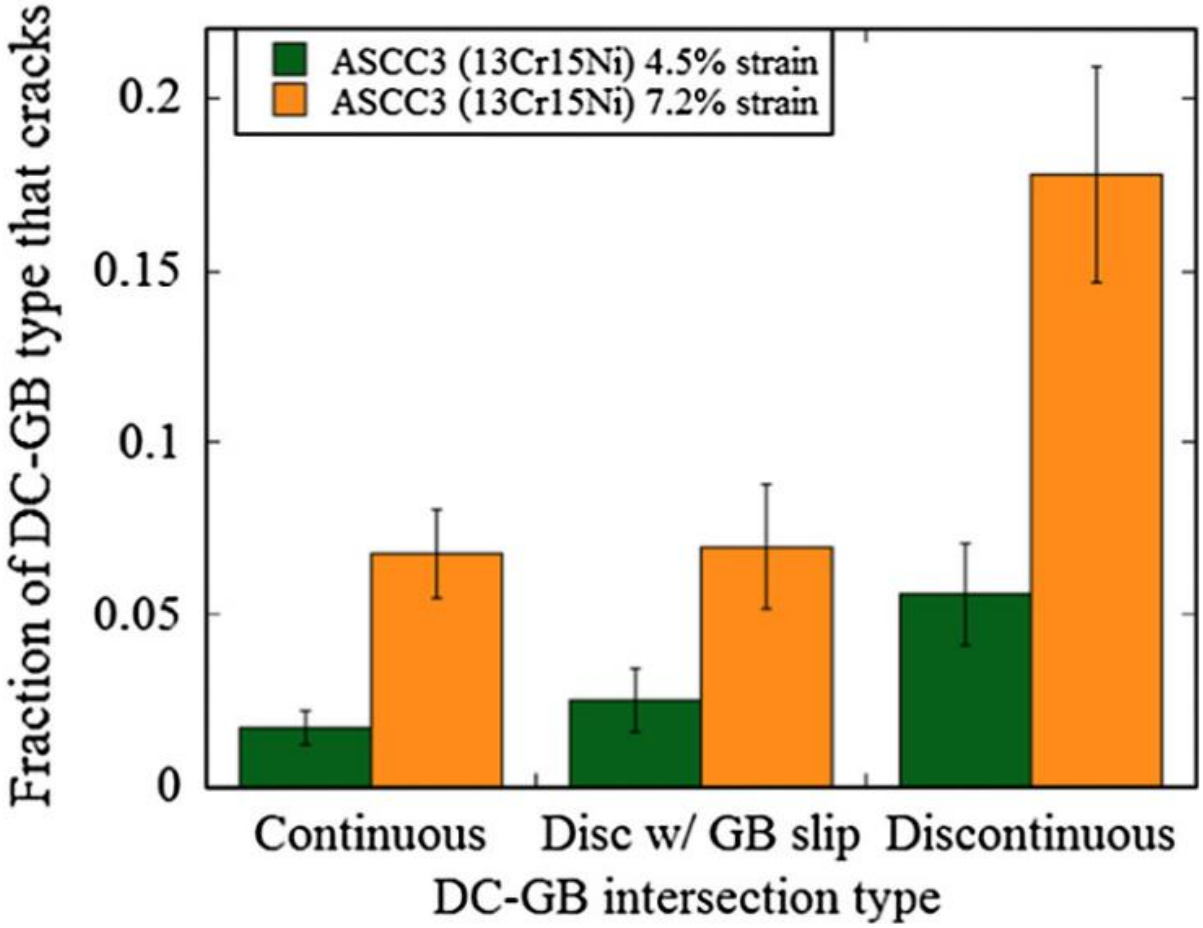

Figure 2.22. Comparison of the cracking fraction for various types of dislocation channel-grain boundary interaction sites. Discontinuous interaction sites without grain boundary slip showed the highest cracking fraction [7].

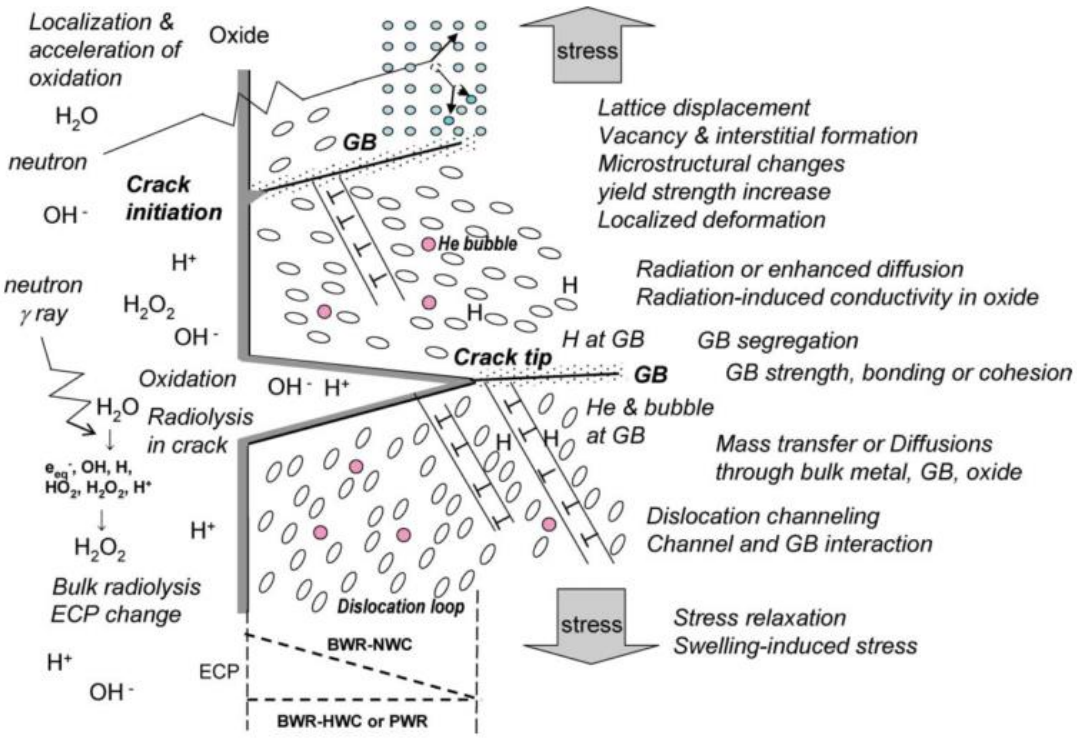

Figure 2.23. Schematic illustrating the various different factors that may affect the IASCC susceptibility of a structural material within a nuclear reactor [3].

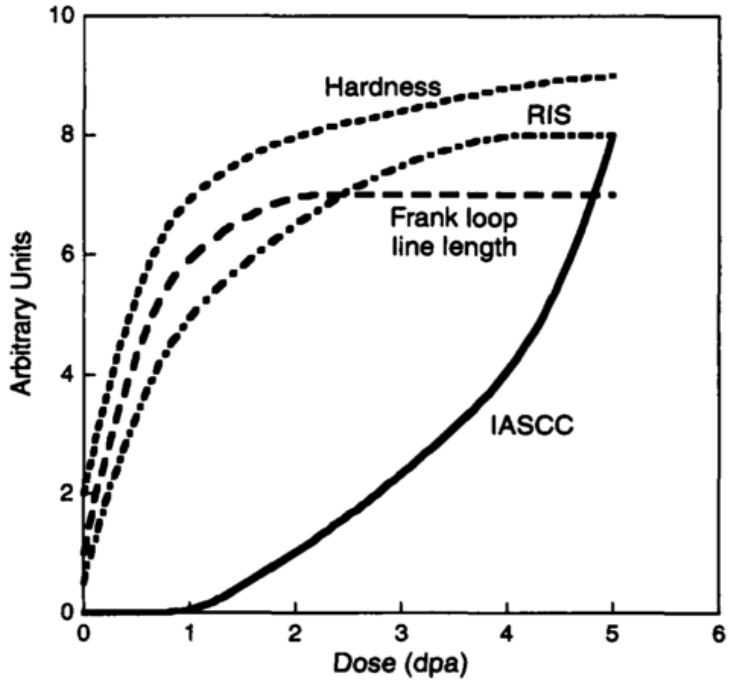

Figure 2.24. Demonstration of the difficulty in separating the differing effects of hardness, RIS, and loop formation with respect to IASCC susceptibility due to the concurrent evolution [123].

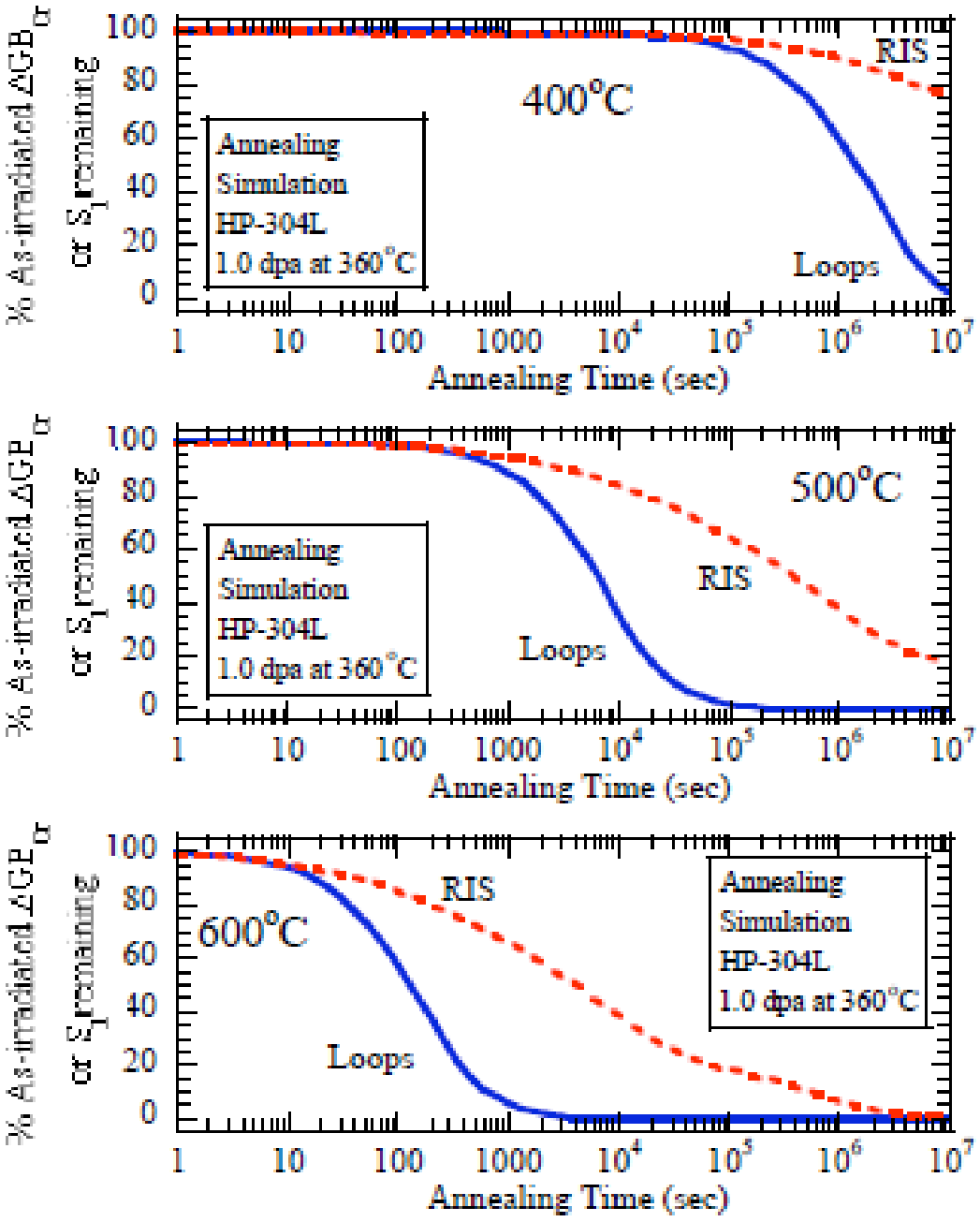

Figure 2.25. Simulation of the removal of both chromium RIS and dislocation loop line length during annealing at different temperatures. The dislocation loops are favorably removed as compared to the RIS [163].

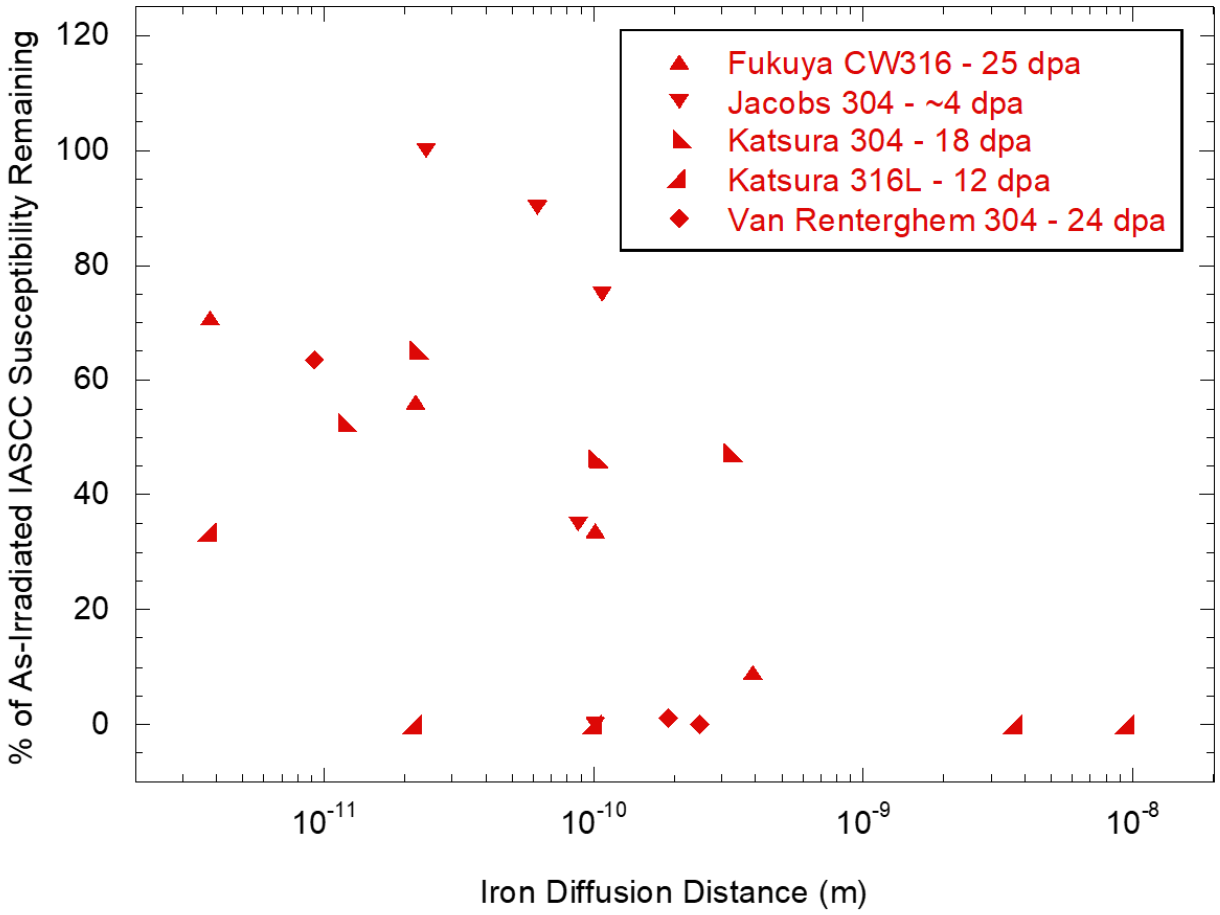

Figure 2.26. Change in intergranular fracture percentage for neutron-irradiated specimens with post-irradiation annealing time. Overall, IASCC susceptibility decreases with increased iron diffusion distance, however, the rate and value of the decrease varies based on materials and irradiation conditions [77,78,167,168,171].

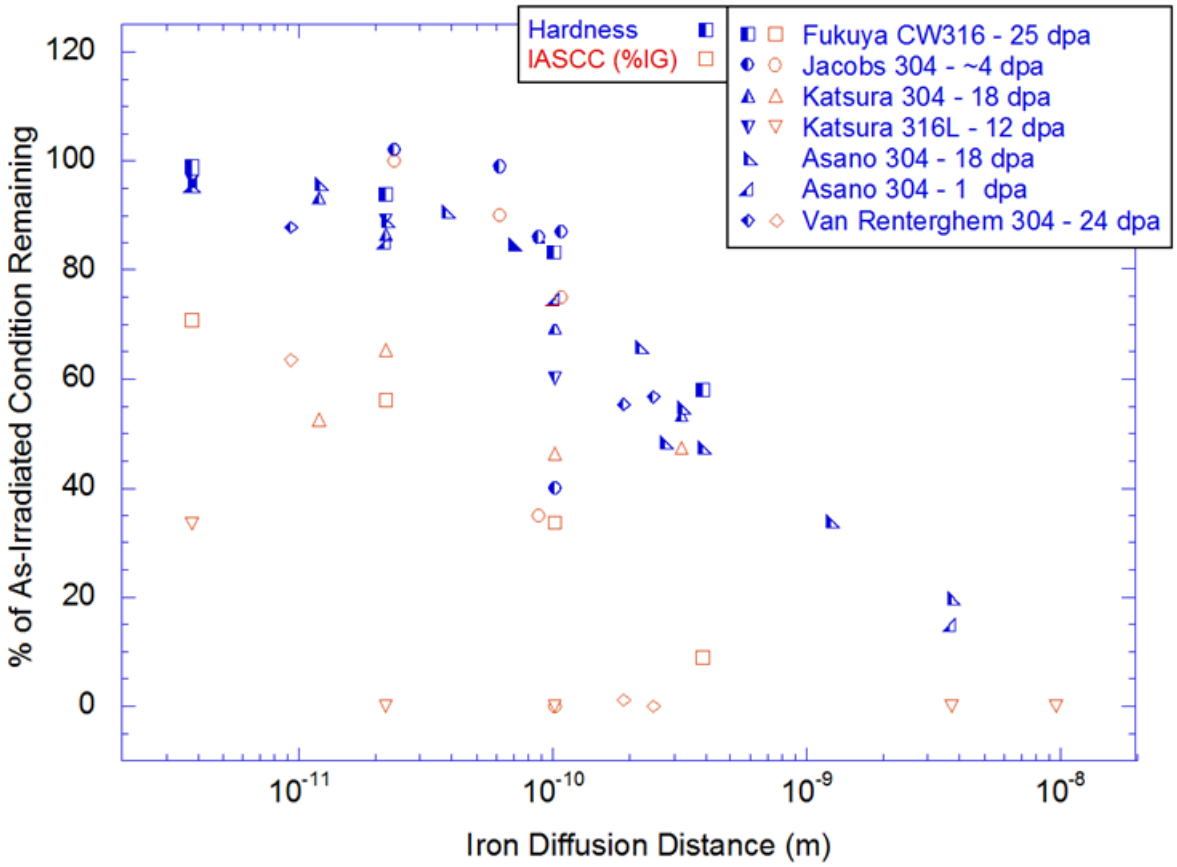

Figure 2.27. Recovery of the as-irradiated hardness for various neutron-irradiated materials, with respect to the iron diffusion distance. A compilation of data representing the recovery of IASCC susceptibility is also shown [77,78,166–168,171].

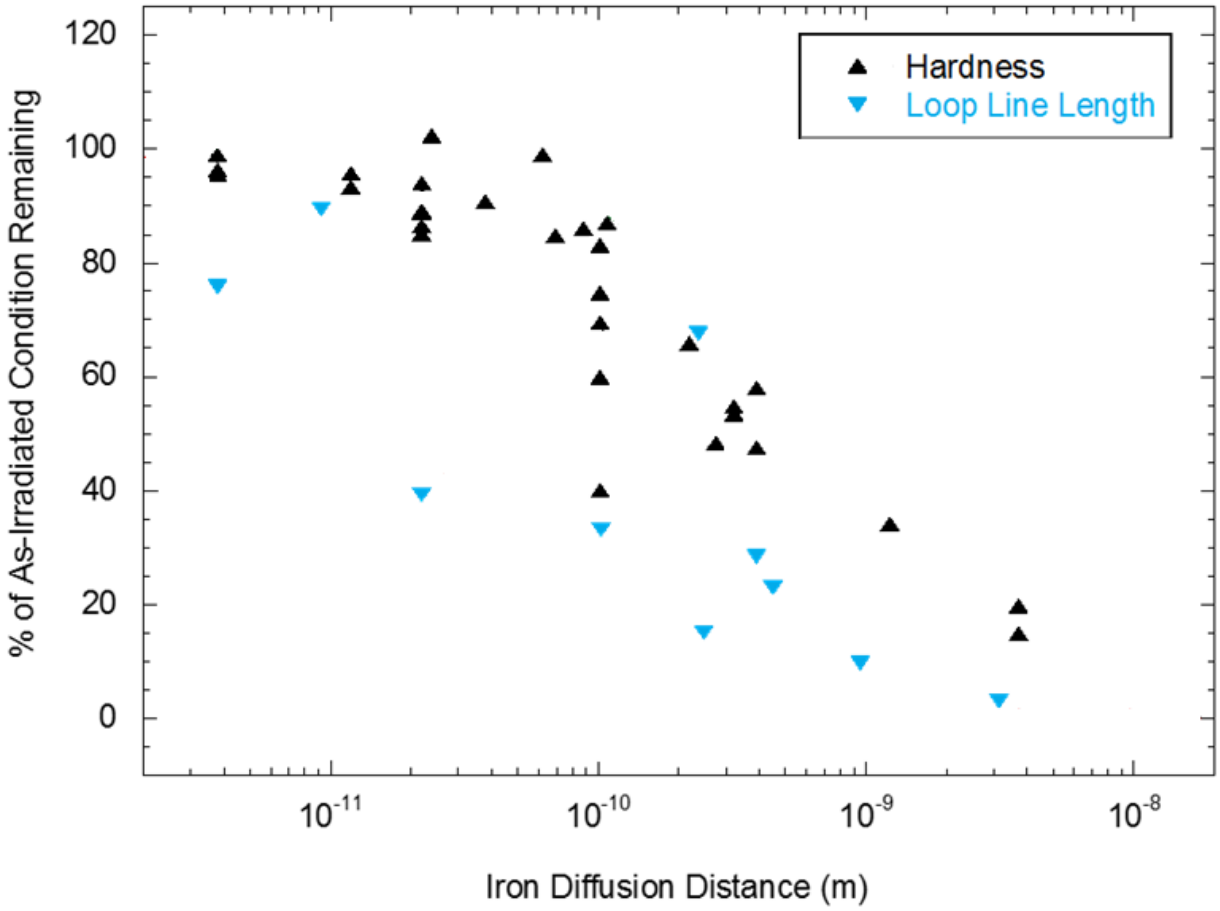

Figure 2.28. Recovery of the as-irradiated hardness for various neutron-irradiated irradiations, with respect to the iron diffusion distance, as compared to the reduction in the total dislocation loop line length [77,78,166–168,171].

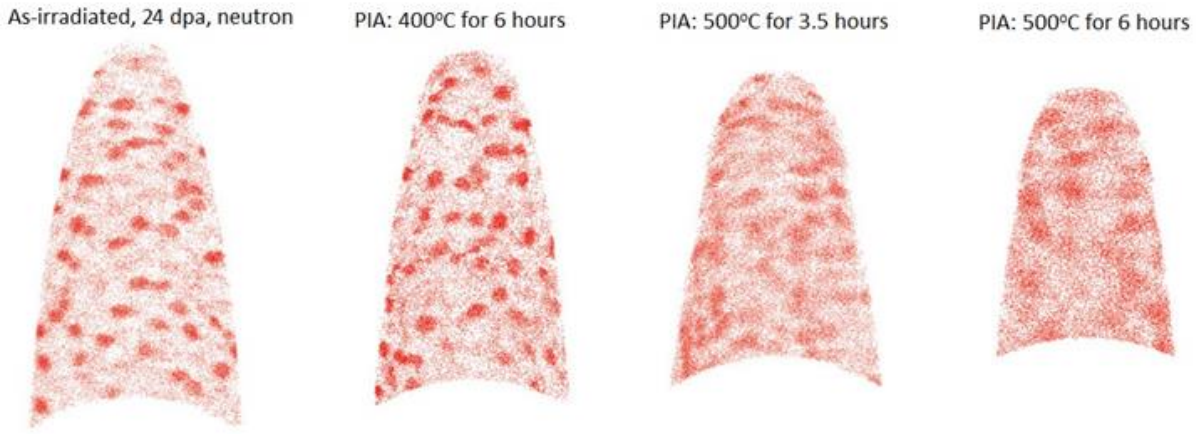

Figure 2.29. Change in the silicon distribution, with increasing iron diffusion distance (left to right). Initially the clusters appear to be quite densely concentrated, however, with increased annealing temperature and time they become larger and more diffuse [43].

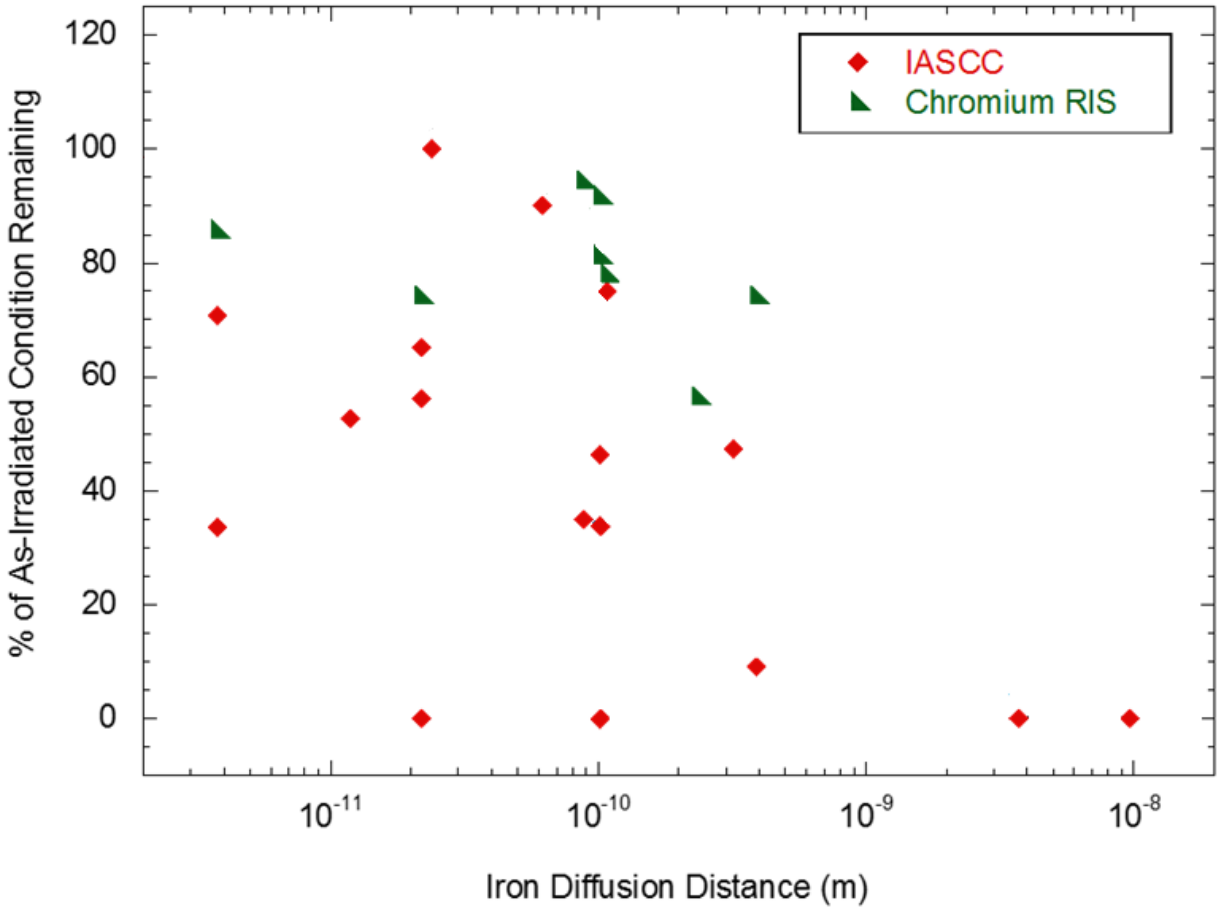

Figure 2.30. Change in the grain boundary chromium concentration for neutron-irradiated stainless steels with increasing iron diffusion distance. It is relatively clear that the chromium RIS remains quite high (>60%) when the IASCC susceptibility is fully removed [77,78,167,168,171].

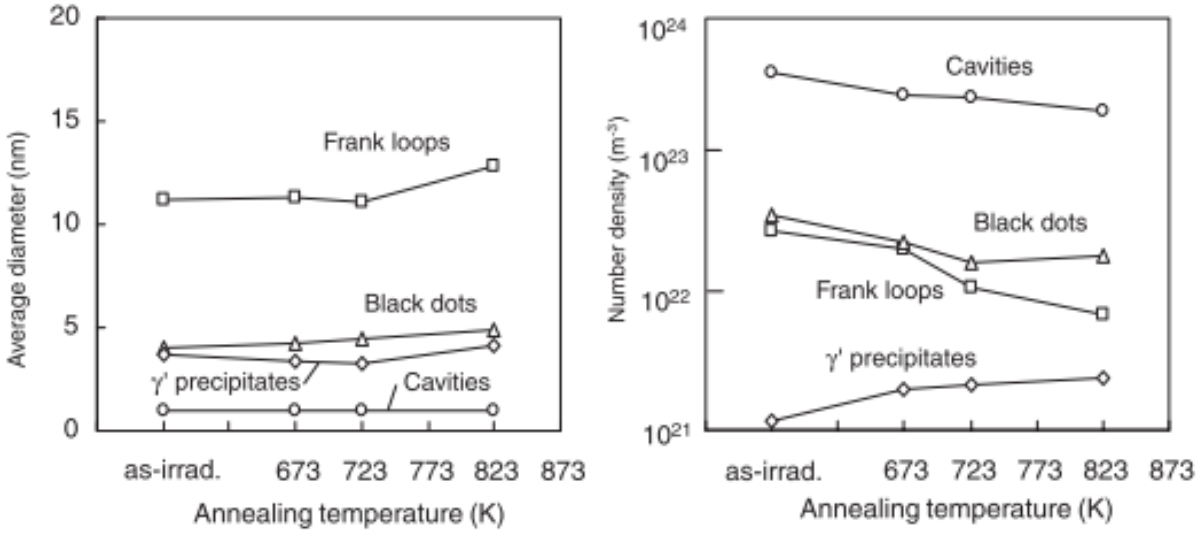

Figure 2.31. Adjustment in the irradiation defects, both average size and density, at different annealing temperatures. In general, the average density is reduced with increased temperature [78].

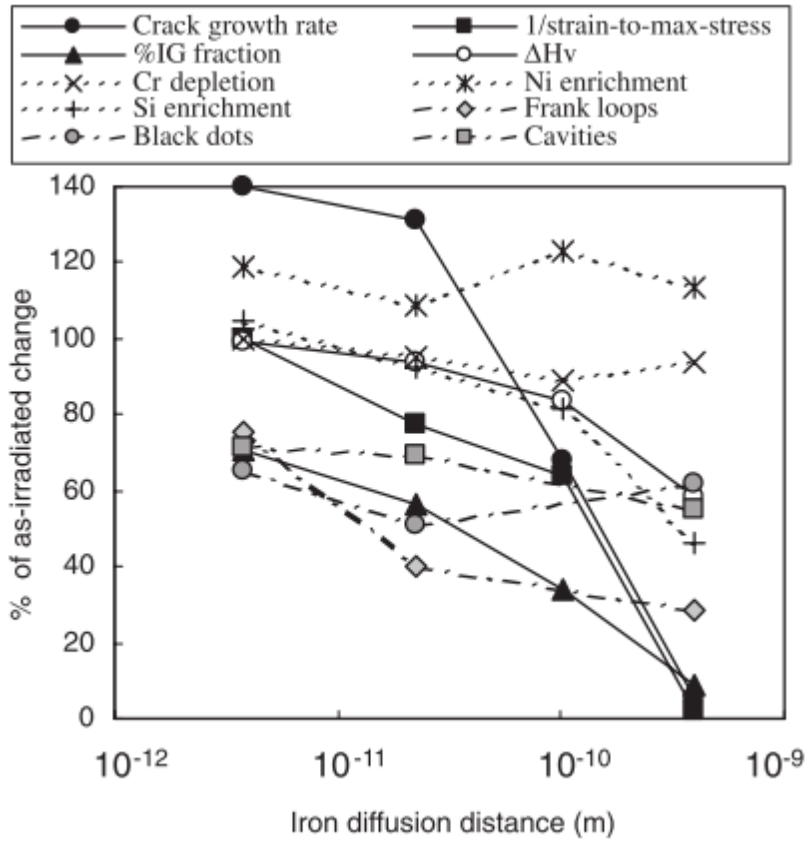

Figure 2.32. Adjustment in several irradiation effects with increased annealing temperature, which correlates with an increased diffusion distance [78].

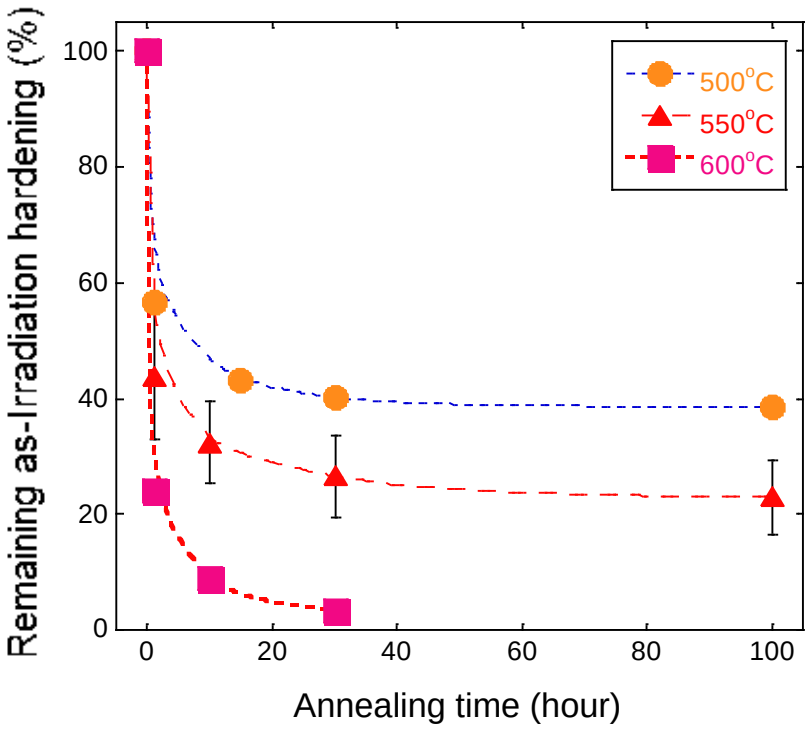

Figure 2.33. The dependence of the as-irradiated hardness recovery on both annealing temperature and time for a proton-irradiated austenitic stainless steel [143].

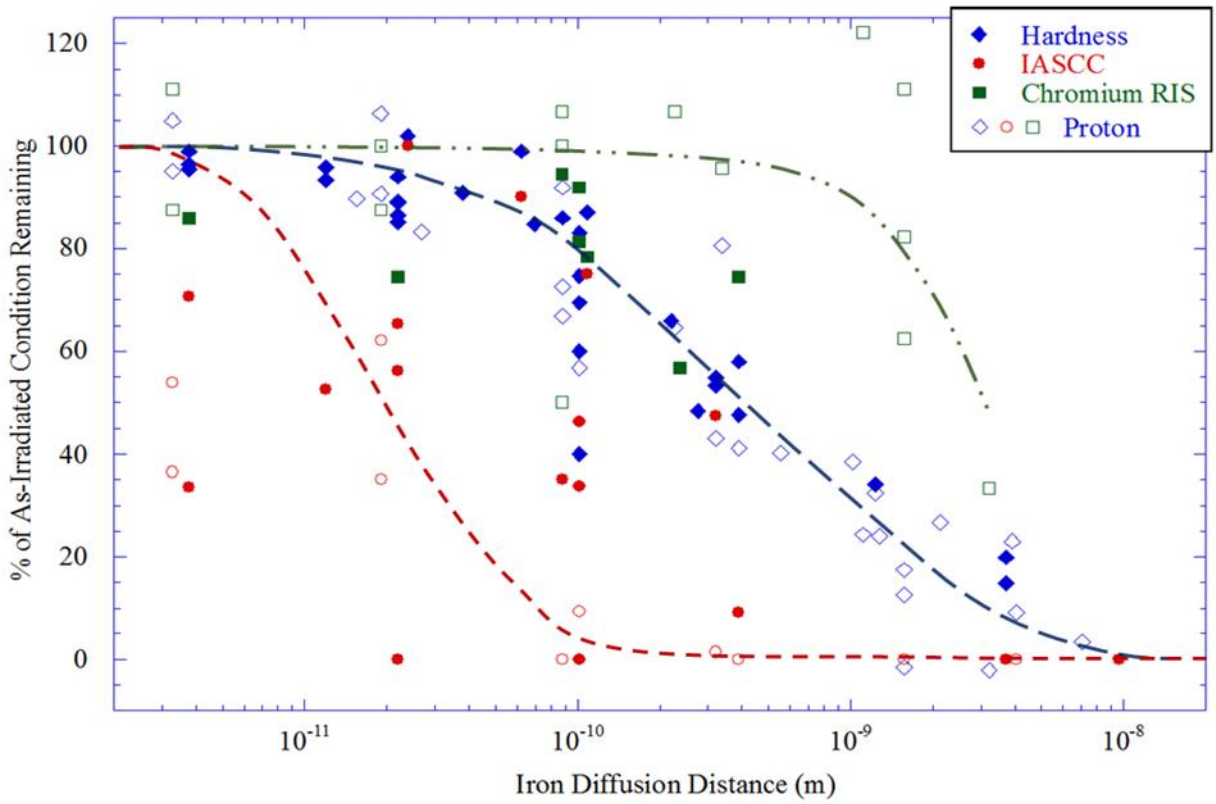

Figure 2.34. The recovery of various irradiation effects with increasing iron diffusion distance. Neutron-irradiated data is shown in solid data points, while proton-irradiated material is shown with open data points [77,78,132,143,161,166–168,171].

CHAPTER 3 - OBJECTIVE AND APPROACH

The objective of this thesis is to determine the processes responsible for the mitigation of IASCC susceptibility following PIA for a BWR-irradiated austenitic stainless steel. A hypothesis for the responsible processes for the mitigation of IASCC susceptibility is presented as follows:

Post-irradiation annealing treatments will remove a significant portion of irradiation defects, thus increasing the homogeneity of deformation through a reduction in the degree of dislocation channeling. This change will reduce the localized stress at grain boundary-channel intersections, and thus lower the overall IASCC cracking susceptibility.

To determine these interlinked processes, a thorough analysis of the irradiated microstructure and its evolution with PIA treatments is necessary. Secondly, the relationship between the irradiated microstructure and the localized deformation must be unveiled. Finally, the relation between the strain homogeneity and IASCC susceptibility will be determined.

To identify the influence of the PIA treatments on the irradiated microstructure, it is necessary to characterize both the as-irradiated state and that following significant annealing treatments. This analysis would monitor the evolution of dislocation loops, precipitates, and solute segregation, both at grain boundaries and within solute clusters. As the irradiated microstructure influences the overall mechanical properties of the material, closely examining the progression of both the dislocation loops and solute clusters over a broad range of annealing treatments will lead to new insights. Additionally, through modelling the dislocation interaction of various irradiation-induced defects a more fundamental understanding of their barrier strengths will be determined; the association between solute clusters and dislocation loops will be closely examined. Identifying the evolution of the irradiation-induced defect microstructure after post-irradiation annealing will be critical in understanding the later changes in the mechanical deformation and IASCC susceptibility.

To determine the impact of the evolved microstructure, the IASCC susceptibility of the as-irradiated and annealed conditions will be determined. This will be accomplished through tensile

straining the as-irradiated and PIA conditions in a susceptible environment: simulated BWR-NWC. To fully encompass the mitigation of the IASCC susceptibility following annealing treatments, the analysis will consist of three factors: strain till crack initiation, final strain to failure, and final intergranular fracture surface, i.e. %IG. To better understand the initiation phenomena, stress corrosion cracking experiments will also be performed on 4-point bend specimens, whose unique geometry limits the surface area for crack initiation as well as retarding crack growth. The completion of these straining experiments in a simulated reactor environment will provide the baseline IASCC susceptibility of the as-irradiated condition and the effectiveness of the PIA treatments in mitigating IASCC susceptibility.

Due to the previously observed relations between localized deformation and the IASCC susceptibility of a material, understanding how the deformation evolves with post-irradiation annealing treatments is critical. The strain homogeneity can be identified through incremental straining experiments, thereby directly relating the specific microstructure of a PIA condition to the result degree of localized deformation. Of an equally critical importance is the specific degree of localized deformation that may result in IASCC susceptibility; by precisely characterizing the channeling near crack initiation sites, new insights may be identified.

The study and analysis of these three focuses will result in a thorough understanding of the modification to the irradiated microstructure, localized deformation, and IASCC susceptibility due to the post-irradiation annealing treatments. Furthermore, this systematic study will seek to highlight the compounding relations of the irradiated microstructure on the strain homogeneity and the threshold limits between strain homogeneity and IASCC susceptibility. Understanding the processes responsible for the mitigation of IASCC susceptibility will provide insight into the underlying processes and causes of IASCC.

CHAPTER 4 - EXPERIMENTAL PROCEDURES

4.1 Materials and Specimen Preparation

The specimens used for this research were obtained through Studsvik Nuclear AB, having been originally irradiated during the operation of the Barsebäck 1 BWR in Sweden as Control Rod #1690, from 1975 to 1999 [172]. This section outlines the composition and irradiation history of the as-received material, as well as the post-irradiation annealing treatments used for this research. Also described are the individual specimen geometries and preparation methods utilized for this research.

4.1.1 Alloy Composition, Irradiation, and Mechanical Properties

Control Rod #1690 was manufactured by ASEA-ATOM (now Westinghouse Electric Sweden AB) of 304L stainless steel, heat number C47576, by Vereinigte Edelstahlwerke AG and was delivered in a solution-annealed condition; no other heat treatments were performed during the fabrication of the control rod. The mechanical properties of the unirradiated material were examined at both room temperature and 300^{o}C, as shown in Table 4.1; the measured mechanical properties are typical of a solution-annealed 304L austenitic stainless steel. The chemical composition of the material is shown in Table 4.2, in which the compositions are given in weight percent (wt. %). The chemical composition was determined both by ladle analysis of the non-irradiated material during fabrication [172] and by an APT characterization of the irradiated material [173]. The two chemical compositions are quite comparable, except for trace concentrations of both aluminum and copper observed by the APT analysis, elements which were not examined in the original ladle analysis.

Control Rod #1690 was used in the operation of the Barsebäck 1 BWR in Sweden but was withdrawn from the core for the entirety of its use, from 1975 to 1999. As such, the material was

exposed to a lower neutron irradiation flux than normal for a commercial reactor, eventually receiving an equivalent dose of 5.9 dpa. A summary of the irradiation history is shown in Table 4.3; the neutron flux was calculated by Barsebäck personnel using in-core fuel management code POLCA [172]. Following the irradiation of Control Rod #1690, two tensile experiments at 288°C were completed at Studsvik Nuclear AB on duplicate specimens, the results of which are shown in Table 4.4. As compared to Table 4.1, a large increase in yield stress from the irradiation is observed.

4.1.2 Post-Irradiation Annealing Treatments

PIA treatments were conducted in an air furnace at varying times and temperatures: 450–600°C for 1-20 h; a total of twelve different time-temperature combinations were performed. These times and temperatures were selected to examine the full spectrum of the hardening recovery under annealing, based on prior literature results [166]. The furnaces used for the annealing treatments demonstrated a high temperature stability and displayed a good agreement between the built-in and secondary thermocouple used to monitor the interior temperature. To limit the oxidation of the specimens during the annealing treatment, they were first loaded into a small folder constructed of a stainless steel foil, which would act as an oxygen getter. These folders were inserted into the furnace once it was stabilized to the desired temperature, and the annealing time was recorded to begin at the point at which the internal temperature returned to 95% of the desired temperature after closing the furnace door, which generally took 3-5 minutes. After the desired annealing time was reached, the furnace was opened, and the stainless steel folders were then removed and allowed to air cool back to room temperature. All annealed specimens were removed from the furnace within ±2 min of their desired timing. Table 4.5 outlines the entire list of irradiated specimens that were utilized for this research as well as their applied annealing treatments.

4.1.3 Tensile Bar Specimens and Preparation

Studsvik Nuclear AB provided documentation detailing the initial fabrication of the irradiated tensile specimens [172]. A total of 12 tensile samples were delivered, 6 of which were used for this research. The tensile samples were machined by wire-cut electro discharge machining (EDM) in accordance with the design, shown in Figure 4.1, with final dimensions shown in Table 4.6. Note that methods to remove the recast surface layer resulting from the EDM process were

not attempted prior to shipment [172]. To ensure the later success of crack initiation testing on the constant extension rat test (CERT) tensile specimens for this project, multiple preparation steps were first required. Due to the high dose rates of the tensile specimens, all preparation work was completed at the Oak Ridge National Laboratory (ORNL) hot cell facilities, largely using manipulators. The difficultly of completing the preparation work is exponentially increased within the hot cell facilities.

Prior to the annealing treatment of the designated tensile specimens, it was necessary to complete several cutting operations on the heads of the tensile specimens. The goal of these cutting operations was three-fold: first, the cutting removes ~50% of the specimen mass, thereby reducing the total dose rate; second, the cutting operation creates several small specimen slices that can be used to analyze the pre- and post-annealed hardness of the tensile specimens. Third, these slices cut from the ends of the tensile specimens can later be fabricated into specimens for 4-point bend experiments, as later described in Section 4.1.5. This cutting operation was completed using a Buehler™ slow speed saw with an abrasive diamond blade, to cut slices 1-2 mm thick perpendicular to the tensile bar length. Due to the requirement of completing this cutting operation in the ORNL hot cells with manipulators, there was a large degree of variation in the thickness of the cut slices.

Following the cutting operations on the tensile specimens, the required annealing treatments were performed using the procedure described earlier in Section 4.1.2. Note that one of the cut slices was included in the stainless steel folder with the tensile specimen to match the exact annealing conditions and later measure the reduction in material hardness. The specific heat treatment that each tensile specimen received is recorded in Table 4.5.

During the original machining of the tensile specimens, EDM was used to cut the parallel flats on opposing sides of the gauge section. EDM leaves a thin, amorphous recast layer, which may affect the cracking behavior in a simulated BWR-NWC environment. As such, the gauge section flats were mechanically polished to remove the EDM recast layer. Due to the use of manipulators, both tensile heads were first clamped in a small vice, to prevent any possible bending, and a polishing paper was carefully moved across the gauge flats. An 800-grit sandpaper was first utilized to remove the EDM layer, while a 1200-grit paper was utilized to prepare the surface for a later electropolishing. The removal of the EDM layer was monitored by the usage of an in-cell camera.

Electropolishing was completed on the tensile specimens to create a final surface finish satisfactory for CERT testing in a simulated BWR-NWC environment. The electropolishing operation was completed in the hot cell fume hood. The electropolishing setup was quite simple, consisting of a power supply, a grid cathode, and a beaker of electrolyte. The electropolishing was completed at a potential of 30 V at 20^{o}C in a Struers A2™ solution. A single electrochemical polishing step was applied for 15 seconds, and each tensile specimen underwent at least 4 steps, rotating the specimen each time to apply an even electropolish. This entire procedure was expected to remove roughly 20 µm of material based on prior experiments. After electropolishing, each specimen was observed via an optical microscope to verify a good surface quality.

4.1.4 Sample Blank Specimens and Preparation

Studsvik Nuclear AB provided documentation detailing the initial fabrication of the irradiated sample blank specimens [172]. During the initial fabrication of the tensile specimens, blanks with a width of 3.5 mm were cut from the full width of the control rod blade, which had a thickness of 8 mm, as shown in Figure 4.2. When these blanks were machined to the proper thickness for the tensile specimens, two thin plate-like specimens were left over from each tensile head (four per tensile specimen), with a thickness as shown by the red highlighted areas in Figure 4.2. When these plate-like specimens were cut from tensile blanks they fell to the bottom of the water reservoir of the EDM machine and were not retrieved until the EDM was completed for all the tensile specimens. As such, it is not possible to determine the origin specimen for these sample blank specimens; furthermore, several of the specimens were flushed out with the effluent water and were not retrievable [172].

As these specimens were cut from the sides of the tensile blanks, their approximate dimensions were: 3.5 x 8.5 x 0.7 mm, as the EDM process removes roughly 0.3 mm of material. After shipment to the ORNL Low Activation Materials Development and Analysis (LAMDA) laboratory, seven of the highest quality sample blank specimens were cut in half using a Buehler™ slow speed saw, with one half given an ‘A’ suffix identifier. These specimens underwent preparation for micro-hardness measurement as later described in Section 4.2.1, followed by annealing treatments as outlined in Section 4.1.2. Following the annealing treatments, the residual

micro-hardness was measured once again. The specific heat treatment that each sample blank specimen received is recorded in Table 4.5.

4.1.5 Four-Point Bend Specimens and Preparation

Four-point bend samples were created from the earlier cut slices from the ends of the tensile bars (as described in Section 4.1.3) in the ORNL LAMDA facility. Being cut from the tensile heads, the 4-point bend specimens had length and width dimensions of 6.0 mm and 3.5 mm, respectively, as shown in Figure 4.1. Large variations in the thickness were present due to the inaccuracy inherent in cutting the specimens in the hot cell facilities, ranging from 0.9 – 2.5 mm. Slices thinner than 0.9 mm were not able to be converted for use as a 4-point specimen. These slices were first mechanically polished in preparation for micro-hardness measurement as described in Section 4.2.1, to confirm the effects of the annealing treatments. After micro-hardness testing samples were mechanically thinned to a target thickness of 800 μm using a Buehler Mini-met 1000™ grinding and polishing tool. Incremental polishing of 120, 180, and 340 grit SiC grinding paper as applied to each side to achieve a uniform thickness (final thickness variations were less than 20 μm). One side of each sample was given a final mechanical polish with a 3 μm nylon pad in the Mini-met™ and subsequently electrochemically polished in a Struers LectroPol-5™ system. One electrochemical polishing step was applied for 15 seconds at a potential of 30 V at 20^{o}C in the Struers A2™ solution. Note that the slice specimen from the parent T5 tensile specimen (annealing condition 500^{o}C: 1 h) was too thin for conversion into a 4-point bend specimen, so an as-irradiated slice 9C was annealed in LAMDA for 500^{o}C: 1 h in accordance with Section 4.1.2. All other 4-point bend specimens were annealed in the ORNL hot cell facilities with their parent tensile specimen. Bend sample ID, parent tensile bar ID, annealing condition, and pre-electropolishing thickness are presented in Table 4.7.

4.2 Microstructure Characterization

This section outlines the preparation procedure and analysis techniques used for the microstructural characterization of the material for this research project, including micro-hardness, TEM, including both rel-rod and segregation analysis, and APT analysis. Table 4.8 shows a list of

the microstructural characterization that was completed for each annealing condition. Special thanks are required for Dr. Zhijie Jiao's contribution to the microstructure characterization, including his work in completing the necessary TEM microscopy for the dislocation loops and RIS analysis, as well as the FIB lift out and atom evaporation required for the APT solute cluster characterization.

4.2.1 Micro-Hardness Measurement

Micro-hardness measurements were made to evaluate the bulk changes in the irradiated microstructure; all preparation and measurements were completed at the ORNL LAMDA facility. Prior to the measurements, specimens were mechanically polished with a succession of finer grits (using 120, 180, and 340 grit SiC grinding paper), ending with a 3 μm diamond polish, using a Buehler Mini-met 1000™ grinding and polishing tool. The specimens were then electropolished using a Struers LectroPol-5™ system at 30 V at 20°C for 15 seconds using a commercial Struers A2™ solution. After electropolishing, provided no defects or scratches were observed, the specimens were measured using a Wilson Instruments' Knoops/Vickers 402MVD™ micro-hardness indenter. Each specimen was measured at a load of 200 gf, with at least 30 independent indents.

4.2.2 Transmission Electron Microscopy Analysis

TEM foils were prepared from an electropolished 3-mm disk, cut from the earlier prepared sample blank specimens as described in Section 4.1.4, at LAMDA at ORNL. TEM foils for dislocation loop analysis were prepared by jet thinning using a Struers TenuPol-5™ system at 30 V at 20°C with a commercial Struers A2™ solution. Dislocation loops were examined with rel-rod technique using JEOL 2100 STEM™ at ORNL. Dislocation loops were imaged at different locations under the [110] zone axis. The faulted loop density, ρ, was calculated as:

$$\rho = \frac{N}{V} = \frac{N}{A*\delta}, \tag{4.1}$$

where N is the number of faulted loops counted in the TEM micrograph, and V is the volume as calculated from the surface area over which the loops were counted, A, and the foil thickness, δ. The foil thickness was measured using the EELS zero loss technique on the JEOL 2100 STEM™,

with values generally around 100 nm. The average faulted dislocation loop diameter, D_{ave}, was calculated as:

$$D_{ave} = \frac{1}{N}\sum_{i=1}^{N} D_i \,, \tag{4.2}$$

where D_i is the individual faulted diameter of a measured faulted dislocation loop. The error in the average loop diameter of each condition was taken as the standard error: $\sigma/\sqrt{N}$, where σ is the standard deviation of the measurement. The error in the average faulted dislocation loop density, ε_ρ, was calculated as:

$$\varepsilon_\rho = \rho\sqrt{\left(\frac{\varepsilon_N}{N}\right)^2 + \left(\frac{\varepsilon_\delta}{\delta}\right)^2} \,, \tag{4.3}$$

where ε_N is the counting error, i.e. $\sqrt{N}$, and ε_δ is the error in the thickness measurement, which was assumed to be 10% of the measured thickness [174]. The number of loops characterized is dependent on the number density of each annealing condition, but multiple images were taken to ensure statistical validity.

RIS at the grain boundaries was also assessed. Energy-dispersive X-ray Spectroscopy (EDS) maps were taken from random high angle boundaries, after being tilted to the edge-on position, using the FEI F200X S/TEM™ instrument equipped with ChemiSTEM™ at the LAMDA laboratory at ORNL using a map size of 1024x1024 pixels with a resolution of ~0.23 nm/pixels with a probe full width half max of ~1.5nm. Each scan had a duration of one hour with more than 100,000 counts/sec with dead times from 1-6%. The qualitative x-rays counts were converted to quantified weight percentages using the Bruker Esprit© 1.9 software package, which uses the Cliff-Lorimer calculations for each pixel. Due to the limitation of available grain boundaries for RIS analysis, only one grain boundary was measured for each condition, but multiple EDS maps were obtained from different segments of the grain boundary.

4.2.3 Atom Probe Tomography Analysis

Precipitates/solute clusters were analyzed using the APT. Needle-shaped APT specimens were prepared by the standard lift-out method and focused-ion beam (FIB) milling using a Quanta 3D™ FIB in LAMDA at ORNL. These APT specimens were prepared from the electropolished 3-mm disks, prior to their jet thinning for TEM analysis. Prior to the lift-out procedure, platinum

was deposited to protect the material from ion beam damage. A final 5 kV clean-up procedure was utilized to minimize the gallium-damaged regions and reduce the tip radius to ~50 nm. About 6 APT tips were made for each condition for APT analysis; however, during transportation from ORNL multiple APT tips were damaged leading to less available data for several conditions. APT specimens were analyzed using a LEAP-4000XHR™ microscope at the University of Michigan operated in electrical mode with a voltage pulse fraction of 20%. Specimen temperature was maintained at 50K and detection rate was kept constant at 0.005 atom/pulse.

Reconstruction of the relative atom positions from the raw data was performed using the commercial software, IVAS 3.6.4 from CAMECA™. Solute clusters were analyzed using the maximum separation method. The nickel-silicon solute clusters were defined by the tenth-order spacing of silicon atoms, whereas a suitable d_{max} (the maximum separation of tenth-order silicon atoms) was selected to best separate the clustered and randomized silicon atoms based on the spacing distribution. The aluminum-copper solute clusters were defined by the fourth-order spacing of aluminum atoms, whereas a suitable d_{max} (the maximum separation of fourth-order aluminum atoms) was selected to best separate the clustered and randomized aluminum atoms based on the spacing distribution for each APT tip. For both cluster types the value of N_{min}, the minimum accepted cluster size by atom number of selected type (i.e. silicon or aluminum), was chosen equal to the maximum cluster size observed for a randomized set of experimental APT data.

For each APT tip a respective IVAS cluster analysis output file was produced; this file included various parameters about the APT tip such as the cluster number, coordinate-specific radii of gyration for each cluster, the total atom count of each element, both in the matrix and within each cluster. From this data, various properties of the solute clusters can be calculated. The volume of each APT tip, V_{APT}, was first calculated:

$$V_{APT} = \frac{\sum_i N_i V_i}{\epsilon}, \tag{4.4}$$

where N_i is the number of atoms of element i, V_i is the atomic volume of element i, and ϵ is the detector efficiency: 37% for the LEAP-4000XHR™. The cluster number density, ρ_c, for each examined condition is calculated:

$$\rho_c = \frac{\sum N_{c,i}}{\sum V_{APT,i}}, \tag{4.5}$$

where $N_{c,i}$ and $V_{APT,i}$ are the number of clusters of a specified type and volume of the *i*th APT tip of that condition, respectively. The volume fraction of the clusters, f_v, is determined as:

$$f_v = \frac{\sum N_{sol} V_{sol}}{\sum_i N_i V_i} \ , \tag{4.6}$$

where N_{sol} and V_{sol} is the number and atomic volume of the solute atoms, i.e. nickel and silicon for the nickel-silicon clusters, located within clusters and $\sum_i N_i V_i$ is the total sum from all of elements in the APT tip. Finally, the Guinier diameter, D_G, of each cluster was measured:

$$D_G = 2\sqrt{\frac{5}{3}}\, R_g \ , \tag{4.7}$$

$$R_g = \sqrt{R_{gx}^2 + R_{gy}^2 + R_{gz}^2} \ , \tag{4.8}$$

where R_g is the overall radius of gyration for the cluster as calculated from the respective radius in each coordinate direction [175,176]. From this the average diameter of the cluster for each condition was determined, with the error in the average diameter assumed to be standard: $\sigma/\sqrt{N}$.

4.3 CERT Test System and Experimental Procedures

4.3.1 CERT Test System

The CERT experiments required for this project were performed using the IM1 autoclave system in the Irradiated Materials Testing Laboratory (IMTL) at the University of Michigan. The IM1 autoclave system is constructed of an Inconel 625 pressure vessel and is capable of supercritical water experiments. A full schematic of the IM1 autoclave system is displayed in Figure 4.3. The IM1 loading system can strain up to four tensile bar samples simultaneously, while the application of load is controlled using an Interactive Instruments Model 5K Servo motor. An Omega LDG21-15 linear variable differential transformer (LVDT) is mounted on the crosshead to measure displacement. Four pull rods connect each sample to the crosshead, and load is measured on each by a Transducer Techniques TLL-1K load cell. Each of the pull rods are sealed at the feed-through into the autoclave with a self-energizing graphite seal with an internal spring that expands under pressure. Each pull rod is connected to an Inconel 625 sample loading fixture, in which the tensile specimen is shoulder-loaded as shown in Figure 4.4. Electrical insulation of the loading fixture from the vessel is provided by zirconia washers located in loading fixture connections to

the pull rods. Due to the crosshead arrangement, non-irradiated type 304L SS tensile bar specimens were used to occupy empty loading locations and provide load balance at the system crosshead. These specimens were selected such that they have a similar yield stress as the neutron-irradiated specimen currently being examined. After specimen loading, the autoclave body is sealed to the autoclave head, thus preventing any leakage during the experiment.

4.3.2 CERT Test Procedure

All CERT tests were conducted in increments in a simulated boiling water reactor normal water chemistry (BWR-NWC) environment. During each straining, system water pressure was maintained at 9.7 MPa and temperature at 288ºC, while the outlet dissolved oxygen and conductivity were maintained at 2000 ppb and 0.2 µS/cm, respectively. After pressurizing and achieving the desired temperature for the intended environment, the system was stabilized until the conductivity had dropped below 0.2 µS/cm. During this stabilization period, a gas mixture of 95% argon/ 5% oxygen was bubbled into the primary water column to control the concentration of dissolved oxygen in the water; the target concentration was achieved by regulating the main column gas overpressure pressure with a back-pressure regulator. Conductivity control was initiated once the vessel outlet water conductivity again dropped below 0.2 µS/cm. Conductivity was controlled by adding small amounts of dilute H_2SO_4 to the primary water column with the peristaltic pump, which was automated to operate whenever conductivity would decrease below the target value. Once the target levels of outlet dissolved oxygen concentration and outlet conductivity were achieved the system was maintained for at least four hours to ensure stability, after which the straining experiment would commence.

Directly prior to each straining increment, a preload of 20 MPa was applied to each specimen. At the end of the stabilization period, straining was initiated by moving the crosshead with the servo motor. This displacement was completed at a rate of 4.19×10^{-6} mm/s for all experiments, which corresponds to a strain rate of 3.5×10^{-7} s^{-1}. This strain rate was selected to both allow sufficient time for corrosion processes to occur and to be comparable to prior literature. Throughout the stabilization period and straining, all environmental and stress-strain data were recorded every 30 seconds using the LabView™ data acquisition program. Recorded data includes

inlet and outlet water pressure, inlet and outlet water conductivity, outlet dissolved oxygen, vessel internal and preheater temperature, LVDT displacement, and load cell readings.

4.3.3 Stress-Strain Analysis

Plots of engineering stress vs. engineering strain were created to measure several mechanical properties of each condition. Before measurement, the load and crosshead displacement data were adjusted to account for system pressure and compliance, respectively. These steps are necessary because direct measurements on the specimens are not possible in a high temperature environment.

The tensile load measured for each specimen must be adjusted, as a tare load is added to each of the specimens by the system water pressure through the pull rod. The added tare load can be directly converted to a tare stress based on the specimen cross sectional area. Due to the direct dependence of tare stress on the cross-sectional area of the specimen and vessel water pressure, this value was calculated *in situ* and directly recorded every 30 seconds using the LabView™ data acquisition program. With a typical specimen cross section, a tare stress of ~60.0 MPa is applied to the specimen through the 4.76 mm diameter pull rod and the 9.7 MPa system pressure.

For the purposes of this research, the term, system compliance, is used to refer to extension in the load train during a CERT experiment due either to elastic deformation or elimination of slack. As the displacement of the specimen is not directly measured and is instead inferred through a crosshead LVDT, this additional deformation is added to the effective displacement of the specimen, leading to an apparent elastic modulus that is much lower than literature would suggest. To correct for system compliance, the raw stress-strain curve was plotted to determine the apparent modulus, which is generally between 10-13 GPa. Crosshead displacement values are converted to strain by dividing the change in displacement as measured by the crosshead LVDT by the original specimen gage section length (12 mm). The apparent modulus was determined by fitting a linear trend line in the elastic region of the curve. This apparent modulus was then divided by reported modulus values for 304 stainless steel at 300^{o}C: 166.3 GPa [104]. The resulting ratio was multiplied by the apparent strain up to the measured yield point, effectively correcting the elastic behavior to that observed in literature. Plastic strain data was continued from the yield point by subtracting the difference in strain between the original strain and the compliance corrected strain;

no compliance correction was applied during plastic elongation. A comparison between raw and compliance corrected stress-strain curves is shown in Figure 4.5.

After applying the corrections for system pressure and compliance, several mechanical properties were determined from the stress-strain curve. If strain hardening was observed, the yield stress was recorded as the 0.2% offset yield stress. Yield stress was instead taken as the maximum stress, if strain softening occurred. Uniform elongation was recorded as the strain at which the maximum stress occurred, whereas total elongation was the strain at the point of failure.

4.3.4 SEM Characterization of Tensile Specimens

As previously discussed, increased localized deformation has been closely correlated with increasing cracking susceptibility [100], however, the change in localized deformation following PIA treatments has never been measured for a neutron-irradiated material. Furthermore, more recent studies [5,6,9], have indicated that dislocation channels that are discontinuous at grain boundaries have a higher propensity of crack initiation. For this study, the tensile straining experiments were completed in small increments to more precisely identify point of crack initiation and study the development of the localized deformation with stress/strain. After each stress/strain increment the tensile specimen was removed from the autoclave were examined using a JEOL JSM-6480^{TM} scanning electron microscope (SEM). This examination was used to measure plastic strain through fiducial markings, as well as record any sites of crack initiation and changes in the localized deformation. Following each stress/strain increment both the gage flats were fully imaged at 500x magnification. This magnification allowed for a balance of both image quality and imaging time, while the large-scale imaging also allows for a spatial correlation of images following each additional strain increment.

Most of the tensile specimens in this study showed a clear necked region during straining, where failure later occurred. As cracking susceptibility and localized deformation may depend on the applied strain, it is imperative that the strain in these necked regions be estimated, as it is likely to vary significantly from the bulk tensile strain. Images from each tensile specimen were used to define the total extent of the necked region for the increment prior to failure. Fiducial marks on the specimen were then used to identify the necked region on each of the preceding strain increments until reaching an increment which was strained below the yield stress. This increment

below the yield stress was presumed to have no significant plastic deflection and thus was used to determine the starting length of the necked region. The engineering strain was then calculated for each increment, based on the change in the length of the necked region divided by the initial length. This measurement is therefore an average over the entire necked region and may not identify the precise strain at the location where a crack initiated. Furthermore, these measurements were completed using low magnification images to encompass the entire gage area, hence the significant errors on the local strain measurements.

Due to the higher local strains in these necked regions, the measurement of the dislocation channel spacing was only conducted in the necked region. The measurement of crack initiation included both the number of independent sites, as well as the total length of cracks on the specimen surface. The measurement of the localized deformation included the dislocation channel density, the average dislocation channel spacing, and the type of dislocation channel-grain boundary intersection, i.e. continuous or discontinuous.

4.3.5 Post-Failure Fractography

Fractography was performed on each fractured tensile bar following the CERT test using a JEOL JSM-6480™ SEM. Low-magnification images of the gage surface were taken to indicate the locations of IG fracture and secondary cracking, while the edges of the main IG crack and secondary cracks were imaged at higher magnification. The fracture surfaces of each specimen were also examined in detail to characterize the nature of failure by viewing the fracture surface perpendicular to the tensile axis. Regions of intergranular (IG), transgranular (TG), mixed (IG+TG), and ductile-type failure were identified. Higher magnification imaging (>500x) was performed in regions of note.

Reduction of area (RA) was calculated using the total area of the fracture surface viewed perpendicular to the tensile axis. The area of the fracture surface was determined using the Image J™ imaging software program particle analysis feature. The RA is determined by dividing the difference in area between the fractured surface (viewed parallel to the tensile direction) and the original cross-sectional area by the original cross-sectional area.

Regions of IG, mixed, TG, and ductile fracture were characterized by area and expressed as an area-based percentage of the total fracture surface. Using the Image J™ program, separate

fracture regions were cut from the overall view of the fracture surface and their area was measured using the particle analysis feature of the software. The sum of these areas divided by the total fracture surface area yielded the percentage for each fracture type.

4.4 Four-Point Bend Test System and Experimental Procedures

The 4-point bend test procedure was utilized to perform smaller-scale experiments to examine the initiation of IASCC in a more controlled area, as compared to CERT of larger tensile specimens. A 4-point bend test creates a region of uniform uniaxial strain on the lower surface [177], with a gradient of tensile to compressive stress through the thickness of the specimen. This arrangement allows for a similar surface strain as in the tensile experiment, while simultaneously limiting crack propagation by the stress gradient. Early efforts in benchmarking and utilizing irradiated 4-point bend specimens was pioneered in part by Kale Stephenson [13,104], many of whose methodologies was adopted for this research, though some improvements were added.

4.4.1 Four-Point Bend Test System

The 4-point bend experiments required for this project were performed using the IM2 autoclave system in the Irradiated Materials Testing Laboratory (IMTL) at the University of Michigan. The IM2 autoclave system is very similar in design to the earlier described IM1 system, but it is instead constructed of a 316 stainless steel pressure vessel. The IM2 loading system also only has a single, central pull rod, thus allowing for the straining of one specimen at a time. This single pull rod is connected to a heat-treated Inconel 718 4-point bend loading fixture, as shown in Figure 4.6. Electrical insulation of the loading fixture from the vessel is provided by zirconia washers located in loading fixture connections to the pull rod.

4.4.2 Four-Point Bend Test Procedure

All 4-point bend experiments were conducted in a simulated boiling water reactor normal water chemistry (BWR-NWC) environment. During each straining, system water pressure was maintained at 9.7 MPa and temperature at 288^{o}C, while the outlet dissolved oxygen and conductivity were maintained at 2000 ppb and 0.2 µS/cm, respectively. After pressurizing and achieving the desired temperature for the intended environment, the system was stabilized until

the conductivity had dropped below 0.2 µS/cm. During this stabilization period, a gas mixture of 95% argon/ 5% oxygen was bubbled into the primary water column to control the concentration of dissolved oxygen in the water; the target concentration was achieved by regulating the main column gas overpressure pressure with a back-pressure regulator. Conductivity control was initiated once the vessel outlet water conductivity again dropped below 0.2 µS/cm. Conductivity was controlled by adding small amounts of dilute H_2SO_4 to the primary water column with the peristaltic pump, which was automated to operate whenever conductivity would decrease below the target value. Once the target levels of outlet dissolved oxygen concentration and outlet conductivity were achieved the system was maintained for at least four hours to ensure stability, after which the straining experiment would commence.

Directly prior to straining, a preload of 50 N was applied to each specimen. At the end of the stabilization period, straining was initiated by moving the crosshead with the servo motor. This displacement was completed at a rate of 3.05×10^{-6} mm/s for all experiments, which corresponds to a strain rate of 3.5×10^{-7} s^{-1} in the central region of the bend specimen. This strain rate was selected to be identical to the prior tensile experiments. Throughout the stabilization period and straining, all environmental and stress-strain data were recorded every 30 seconds using the LabView™ data acquisition program. Recorded data includes: inlet and outlet water pressure, inlet and outlet water conductivity, outlet dissolved oxygen, vessel internal and preheater temperature, LVDT displacement, and load cell readings.

4.4.3 Bend Stress Approximation

The difference in the geometry between 4-point bend and tensile experiments, makes it more convenient to examine straining experiments in 4-point bend in terms of bend load vs. deflection, rather than the comparison of stress vs. strain commonly used in tensile experiments. However, when completing strain increments below yield conditions, it is more useful to load to percentages of the yield stress, as was done with the tensile experiments. A relationship between the bend yield load in 4-point bend and the tensile yield stress was formed utilizing previous experimental data on neutron-irradiated 304 stainless steel specimens by Kale Stephenson [104] and benchmarking experiments utilizing a heat of 316 stainless steel cold-worked to varying degrees, as shown in Figure 4.7. While there is some variability, this comparison allowed a

prediction of the bend yield load based on previous measurements of the tensile yield stress. Due to the linear relationship, it was assumed that loading to a percentage of the bend yield load in a 4-point experiment is directly comparable to loading to that percentage of the yield stress for the specimen.

As with the tensile experiments, there is a tare load applied to the bend specimen by the vessel water pressure that is not directly measured by the pull rod load cell. As described earlier in Section 4.3.3, this value was calculated *in situ* and directly recorded every 30 seconds using the LabView™ data acquisition program. With a 4.76 mm diameter pull rod and the 9.7 MPa system pressure, a tare load of ~170 N was added to the bend specimen, under simulated BWR-NWC conditions.

4.4.4 Bend Deflection Measurement

To measure the plastic strain in the central region of a 4-point bend specimen, it is first necessary to measure the plastic bend deflection. While direct sample bend deflection measurements, such as the use of a microminiature differential variable reluctance transducer (DVRT), may be possible in room-temperature air [104], they are not feasible under simulated BWR-NWC environment. While *ex situ* measurements of the plastic bend deflection can be made through measuring the side profile of a 4-point bend specimen, it is also necessary to have an *in situ* approximation of the bend deflection, such that the experiment can be halted at the correct strain level. Therefore, estimations of plastic deflection were made by subtracting a load-dependent compliance correction factor from the crosshead deflection measurement, as visualized in Figure 4.8. A compliance correction factor was determined in 288ºC BWR-NWC, by loading a ~6 mm Inconel 718 specimen with the same cross-sectional geometry as actual bend test specimens. Due to its large thickness and hardness, it was assumed, and confirmed post-loading, that no specimen deflection occurred during loading, thus any measured crosshead displacement was due to the system compliance. The thick specimen was loaded multiple times, and data was averaged for accuracy. The compliance correction factor was determined by fitting a third-order polynomial to the averaged bend load-crosshead deflection curve.

The following correction factor was determined for a simulated BWR-NWC condition:

$$CF_{NWC} = 0.00352 * P^3 - 0.36755 * P^2 + 20.228 * P - 146.27, \quad (4.9)$$

where P is the applied load in N and CF_{NWC} is the correction factor for a simulated BWR-NWC environment in μm. Subtracting the correction factor from the measured crosshead deflection will yield the specimen bend deflection. Test experiments showed a good agreement between this estimated *in situ* value for plastic bend deflection and *ex situ* measurements of the side profiles by SEM imaging.

4.4.5 Bend Strain Calculation

In a four-point bend experiment the maximum bend strain, ε_{max}, is directly related to the specimen thickness, bend deflection, and the geometry of the bend test fixture [177]:

$$\varepsilon_{max} = \frac{h}{2p} = \frac{h}{\sqrt{\frac{1}{4{y_L}^2}[La-a^2]+a^2}+h}, \tag{4.10}$$

where h is the specimen thickness, p is the radius of curvature, y_L is the bend deflection, L is the distance between the lower load points, and a is the distance between the upper load points, as shown in Figure 4.10. For small deflection, where $y_L << a$ and $y_L << L$, Equation 4.2 can be simplified to a linear relation between ε_{max} and y_L [177]:

$$\varepsilon_{max} = \frac{2hy_L}{a[L-a]}. \tag{4.11}$$

For the geometry of our 4-point bend fixture, the conditions of a small deflection would qualify for any deflections less than 35 μm. To not depend fully on theoretical calculations, an array of microhardness indents was applied to the surface of several test bend specimens of 16.9% CW 316 stainless steel prior to deformation, spaced ~100 μm apart. The indent spacings were compared before and after deformation through SEM imaging, to determine associated strain between indent locations. The average longitudinal strain in the central region, as measured by the indents, was then compared to the plastic bend deflection as measured through side profile imaging, as shown in Figure 4.11. A least squares linear fit was applied to determine the slope, forcing the fit through the origin, as only plastic strain and plastic deflection were considered, which are both assumed to be zero prior to yield:

$$\varepsilon_{xx} = 0.000748 * \delta_b, \tag{4.12}$$

where ε_{xx} is the longitudinal plastic strain and δ_b is the plastic bend deflection in μm, the calculated slope is in units of μm^{-1}. Due to the relatively small deflections, $y_R \approx 0$, and thus δ_b is equivalent to y_L. As a clear majority of the strain in the central region has been shown to be in the longitudinal direction [104], ε_{xx} is a good approximation of ε_{max}. As such, it becomes clear that Equations 4.11 and 4.12 are also equivalent. Equation 4.12 was used to calculate the bend strain in the central region at small plastic deflections (< 30 μm), while it was corrected to account for the theoretical deviation from linear behavior predicted in Equation 4.10 for larger plastic deflections (>30 μm).

4.4.6 SEM Characterization of 4-Point Bend Specimens

For this study, the straining experiments were completed in small increments, such that the point of crack initiation could be more precisely identified, as well as recording the evolution of the localized deformation with strain. Before the initial bend increment, and following each stress/strain increment, the bend specimen was imaged with a JEOL JSM-6480 SEM. Surface examination was performed with the sample oriented as shown in Figure 4.9, where strain (ε_{xx}) was along the longitudinal axis. Secondary electron (SE) imaging mode was used to record the center ~3500 μm of the sample along the entire length of the transverse axis at a low magnification setting, 500x. Additionally, the central zone of uniaxial strain (~750 μm) was recorded at higher magnification, 1000x. Areas of interest, such as crack initiation sites, were separately imaged at higher magnifications as well. The measurement of crack initiation included both the number of independent sites, as well as the total length of cracks on the specimen surface. Channeling was clearly visible when imaging the bend sample surface at 500x or higher magnification, allowing quantification of dislocation channel density, average channel spacing, and the fraction of channeled area. This dislocation channel characterization was performed in a region bounded by the center 750 μm of longitudinal axis by the central 2000 μm of the transverse axis, an area of ~1.45 mm^2.

While the method of compliance subtraction can provide an accurate approximation of the plastic bend deflection during an experiment, slight variations in the system set-up and conditions can lead to variations from the averaged correction factor, resulting in final errors in the estimated bend deflection up to 5 μm. As such, the SEM characterization of the bend specimens includes a full imaging of each of the leading side profiles at a direction parallel to the specimen surface at a

magnification of 500x. The deflection in the central 500 µm of side profiles following each strain increment was compared to the deflection in the initial condition, and the difference was measured. The final plastic bend deflection for an increment was recorded as the average of the deflection measured in both side profiles.

4.5 Modelling Dislocation – Radiation Defect Interactions

To more thoroughly understand the interaction between a dislocation and a radiation defect, and the effective barrier strengths of said defects, a simulation was developed. This simulation was developed utilizing the open-source Large-scale Atomistic/Molecular Massively Parallel Simulator, henceforth referred to as LAMMPS, which is a classic molecular dynamics (MD) code with a focus on materials modeling developed by Sandia National Laboratories [178]. This software and many similar codes have been used in recent years to closely examine the interaction between a dislocation and an irradiation-induced obstacle on an atomistic-scale [92,179–191]. Of interest to this research is the effective barrier strength of a combined solute cluster-dislocation loop, a defect that has been rarely examined in literature [188], and never for an austenitic stainless steel.

The complete and commented LAMMPS input file used for the simulations of this research is available in Appendix A, but a summary of the simulation will be provided here. The simulation cell was arranged in a style originally developed by Osetsky and Bacon [189] and commonly used in similar simulations to examine obstacle-dislocation interactions [182,183,188]. The FCC crystallite had axes oriented along $[\bar{1}10]$, $[\bar{1}\bar{1}2]$ and [111] directions and contained about 0.9M mobile atoms. Its dimensions along x, y and z directions were 24.9 x 21.5 x 18.3 nm, respectively. A lattice parameter of 3.5146 Å was selected as it had the lowest energy for the selected composition of Fe-12Ni-20Cr (at.%) using the embedded atom method (EAM) pair potentials for a ternary Fe-Ni-Cr alloy developed by Bonny *et al.* [191] which were used to complete the simulations of this study. Periodic boundary conditions were applied along the x and y directions, while atoms in a few outer ±z atomic layers were rigidly fixed in their positions. Shear deformation of $[\bar{1}10](111)$ type was created by moving the rigid top and bottom z-planes with a constant velocity of 0.2 m/s, thus resulting in a strain rate of 2.2×10^7 s^{-1}. It should be noted that this strain

rate is ~14 orders of magnitude greater than that used in the tensile and four-point bend experiments, and 3-4 orders of magnitude greater than strain rates easily achieved in macro-scale experiments. As these strain rates are necessary due to inherent time limitations in MD simulations, prior research has examined the possible effects of these increased rates in MD simulations [192–194]. The general conclusion is that high strain rates tend to limit long-range diffusion processes, hence leading to large variations when considering multi-crystal simulations. With regards to a single crystal system, as utilized in this research, the impact is considerably less, though some diffusion processes, such as dislocation climb, may be lessened, causing slightly enhanced obstacle strengths at higher strain rates [192]. This MD simulation was conducted under NVE conditions in LAMMPS, thus conserving the number of atoms, N, system volume, V, and total energy, E, at a temperature of 300K.

An edge dislocation with $b_v = 1/2[\bar{1}10]$ was introduced near the edge of the simulation cell according to the method applied by Osetsky and Bacon [189], i.e. the removal of a vertical half-plane of atoms. The created dislocation was relaxed using the minimization command in LAMMPS, after which the dislocation was dissociated into two Shockley partials located at a distance of about 10 nm from each other, which corresponds well to the value expected from the elasticity theory considerations [191]. In order to properly identify the dislocation-obstacle interactions the open-source software, OVITO [195], was utilized to subtract atoms of the FCC structure, leaving only the stacking faults around the edge dislocation and dislocation loop obstacle.

Prior to studying the interaction of the dislocation with differing obstacles, the dislocation movement in a defect-free Fe-12Ni-20Cr crystal was modeled to evaluate the friction stress, τ_f, which the dislocation experiences at the imposed strain rate. A smooth movement of the dislocation was observed at the studied temperature of 300K, and while the width of the stacking fault ribbon was seen to vary (±25% from the average value), no constrictions were seen to form on the dislocation line. The apparent friction stress, τ_f, was calculated by averaging the instantaneous resolved shear stress over the time the dislocation moves once through the simulation crystal.

Three different irradiation-induced defects and their interaction with a mobile edge dislocation were examined in this study: faulted dislocation loops, solute clusters, and combined

solute cluster-dislocation loops. All obstacles were placed in the center of the simulation cell and centered in the plane of the edge dislocation. This set-up would presumably have the strongest barrier strength, as dislocation is interacting with the widest section of the obstacle.

The faulted interstitial dislocation loops were initialized by placing a one-atom thick cylinder of the selected diameter on the one of the {111} planes. The selected diameters used in this study included 3, 5, and 7 nm, while loops oriented on the $(1\bar{1}1)$, $(\bar{1}\bar{1}1)$, and $(\bar{1}11)$ planes were examined. The (111) loop orientation lies directly in the plane of the $[\bar{1}10]$ edge dislocation, and thus is presumed to have a minimal chance of interacting with a mobile dislocation, hence it was not included in this study.

Solute clusters were initialized by selecting a spherical region of the simulation cell and changing the type of random atoms in the selected area to nickel. This process creates a spherical region of an enhanced nickel concentration, as compared to the matrix. Solute clusters were examined at diameters of 3-7 nm, in 1 nm increments, with an atomic nickel concentration of 50%. Selected diameters of 5 and 7 nm were also examined with atomic nickel concentrations of 25 and 75%.

While combined defects of a solute cluster-dislocation loops have been observed experimentally [42], their exact formation with irradiation is not fully understood. Due to the similar sizes of dislocation loops and Ni-Si solute clusters in this thesis study, it was decided to form the combined defect of a dislocation loop and solute cluster with the same diameter. The dislocation loop was first initialized, followed by the adjustment of the nickel concentration in the surrounding spherical region. To examine the impact of varying factors on the strength of the combined defect a combined defect with a loop orientation of $(1\bar{1}1)$, cluster concentration of 50% nickel, and diameter of 5 nm was chosen as the baseline condition. The effect of diameter (3 and 7 nm), solute concentration (25 and 75%), and loop orientation ($(\bar{1}\bar{1}1)$ and $(\bar{1}11)$) were specifically examined as compared to the baseline combined defect and the individual solute clusters and dislocation loops.

Following the initialization of the edge dislocation and obstacle, the energy of the cell was minimized and then brought to the simulation temperature of 300K. The dislocation motion was created through the shearing of the simulation cell, which lasted for 450 ps (450000 timesteps); this was enough time for the dislocation to move at least once through the simulation cell. The XZ

shear stress was recorded as a function of simulation time, and the maximum stress required for the first traversal of the obstacle array was recorded as the peak shear stress for the obstacle. Multiple simulation runs were completed for each defect type with a randomization of the matrix atoms for each run, and the average for each obstacle type was obtained after 6-12 simulation runs.

Table 4.1. Mechanical properties of the 304L stainless steel in the unirradiated condition [172].

Test No.	Room Temperature				300 °C			
	YS MPa	UTS MPa	ε_{tot} %	Z[1)] %	YS MPa	UTS MPa	ε_{tot} %	Z[1)] %
191	215	509	65	80	-	-	-	-
360	215	509	65	82	179	380	35	75
361	208	502	65	82	159	380	49	75
362	209	502	70	82	-	-	-	-
Mean	**212**	**506**	**66**	**82**	**169**	**380**	**42**	**75**

1) Reduction of area.

Table 4.2. Chemical composition of the 304L stainless steel both of the un-irradiated material via ladle analysis [172] and the irradiated material via APT [173] in wt%. The primary difference is the addition of Al and Cu impurities seen by APT, but which were not tested for in the ladle analysis.

Method	Fe	Cr	Ni	C	Si	Mn	Co	N	P	S	Al	Cu
Ladle (Un-irradiated)	Bal.	18.35	10.57	0.025	0.30	1.09	0.029	0.024	0.013	0.003	-	--
APT (Irradiated)	68.01	18.34	11.6	0.035	0.40	1.13	0.15	--	0.02	0.001	0.02	0.12

Table 4.3. Summary of the irradiation conditions for Control Rod #1690; as this control rod was withdrawn from the core for the entirety of its service life (1975-1999), it was exposed to a rather low neutron flux, though for an extended period, culminating in a total damage of 5.9 dpa [172].

Control Rod ID	Time (h)	Flux ($n/cm^2 \cdot s$) (E > 1 MeV)	Fluence (n/cm^2) (E > 1 MeV)	Dose (dpa)
1690	95608	$1.2 \cdot 10^{13}$	$4.16 \cdot 10^{21}$	5.9

Table 4.4. Results from tensile testing of 304L Heat SW at 288ºC following irradiation to a dose of 5.9 dpa [172].

Specimen	YS MPa	UTS MPa	ε_u %	ε_{tot} %
1	662	662	0.04	11.3
2	683	683	0.03	11.2
Mean	**672**	**672**	**0.03**	**11.2**

Table 4.5. Overview of the specimens utilized for this research, as well as their applied annealing treatments.

Specimen Type	Specimen ID	Annealing Condition
Sample Blank	5	500°C: 1 h
	5A	450°C: 20 h
	9	450°C: 5 h
	9A	450°C: 1 h
	11	550°C: 1 h
	11A	600°C: 20 h
	15	550°C: 5 h
	15A	550°C: 20 h
	16	500°C: 20 h
	16A	600°C: 5 h
	17	600°C: 1 h
	17A	600°C: 5 h
	18	500°C: 1 h
	18A	500°C: 5 h
Tensile	T4	As-Irradiated
	T5	500°C: 1 h
	T7	550°C: 5 h
	T9	550°C: 20 h
	T12	550°C: 20 h
	T13	550°C: 1 h
4-Point Bend	4-B	As-Irradiated
	7-B	550°C: 5 h
	9-C	500°C: 1 h
	10-B1	As-Irradiated
	12-B1	550°C: 20 h

Table 4.6. Dimensions of the fabricated tensile specimens in mm, with the measured dimensions corresponding to Figure 4.1.

Specimen ID	A	B	C	D	E	F
Nominal	1.7	33.0	16.0	2.0	3.5	6.0
Tolerance	±.05	±.15	±.05	±.05	±.05	±.05
T4	1.68	33.03	15.97	2.02	3.49	5.99
T5	1.66	33.06	16.08	1.99	3.49	6.00
T7	1.69	33.16	16.03	2.0	3.51	6.01
T9	1.71	33.18	16.4	1.93	3.50	5.99
T12	1.72	33.07	16.09	1.93	3.49	5.99
T13	1.71	33.05	16.07	1.93	3.45	6.01

Table 4.7. Specimen ID, parent tensile specimen, annealing treatment, and pre-electropolishing thickness of the 4-point bend specimens utilized for this research.

Specimen ID	Parent Tensile	Annealing Treatment	Thickness (μm)
4-B	T4	As-Irradiated	808
7-B	T7	550°C: 5 h	802
9-C	T9	500°C: 1 h	802
10-B1	T10	As-Irradiated	803
12-B1	T12	550°C: 20 h	798

Table 4.8. Overview of the microstructural analysis completed for each of the examined annealing conditions.

Annealing Condition	Micro-Hardness	Rel-Rod Imaging	RIS	APT
As-Irradiated	X	X	X	X
450°C: 1 h	X			
450°C: 5 h	X			
450°C: 20 h	X			
500°C: 1 h	X	X		X
500°C: 5 h	X			
500°C: 20 h	X			
550°C: 1 h	X	X		X
550°C: 5 h	X	X	X	X
550°C: 20 h	X	X	X	X
600°C: 1 h	X			
600°C: 5 h	X			
600°C: 20 h	X			

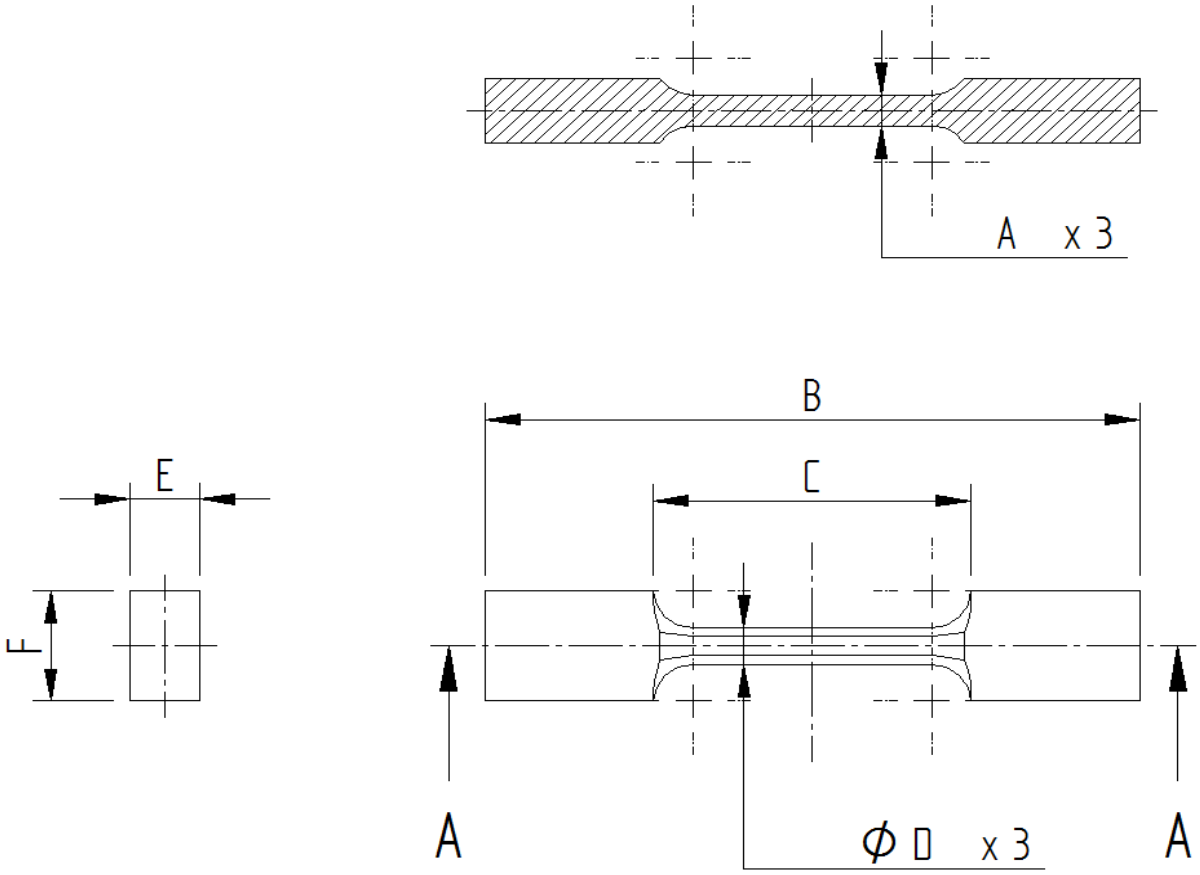

Figure 4.1. Schematic of the tensile specimens that were manufactured for this project, with the labeled dimensions that were measured for each sample as seen in Table 4.6.

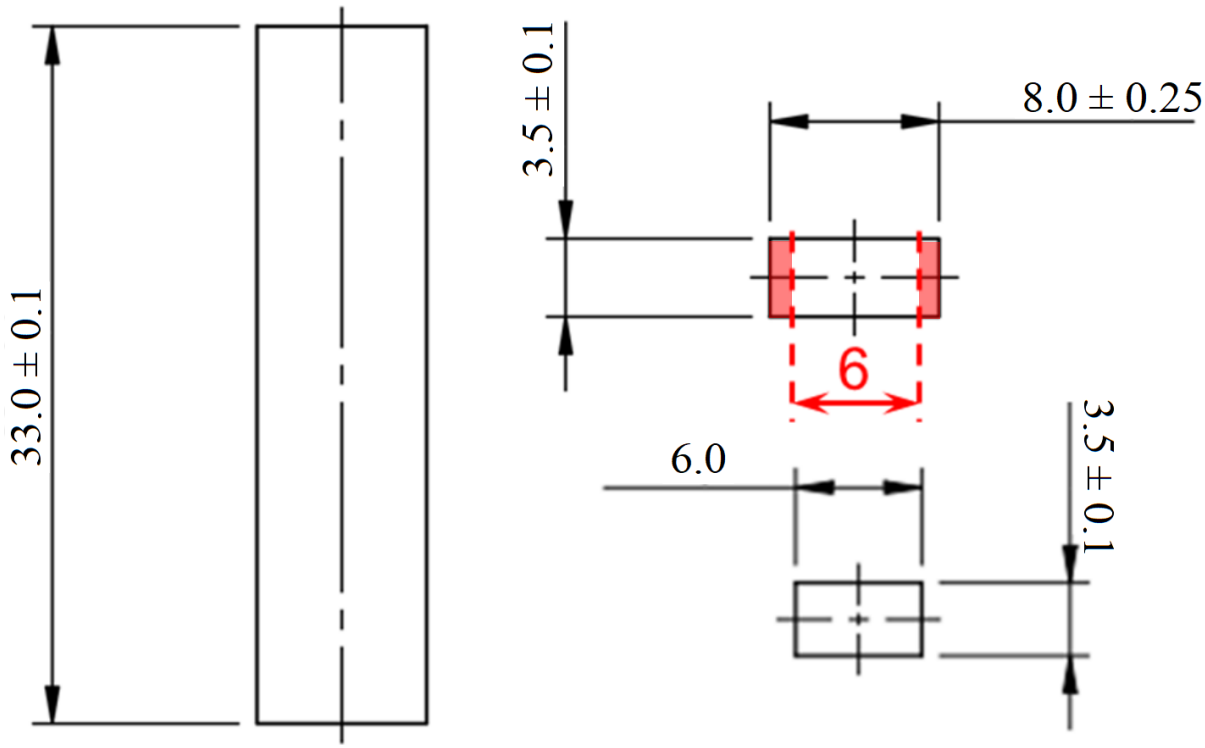

Figure 4.2. Schematic of the blanks for the tensile specimens, from which the sample blank specimens were cut; all dimensions are in mm. The residual material that became the sample blanks specimens are highlighted in red, with approximate dimensions: 3.5 x 8.5 x 0.7 mm.

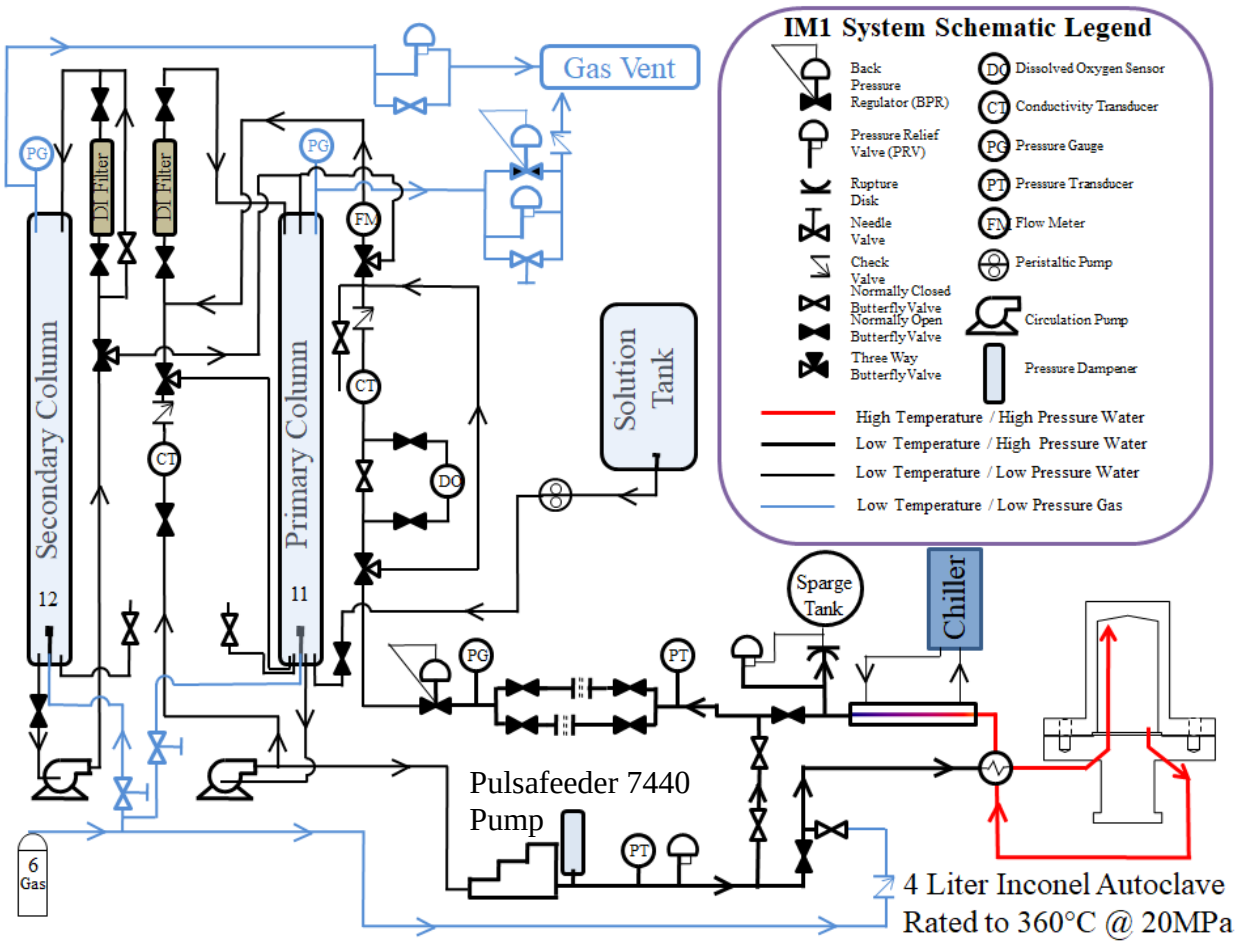

Figure 4.3. Schematic of the IM1 autoclave system.

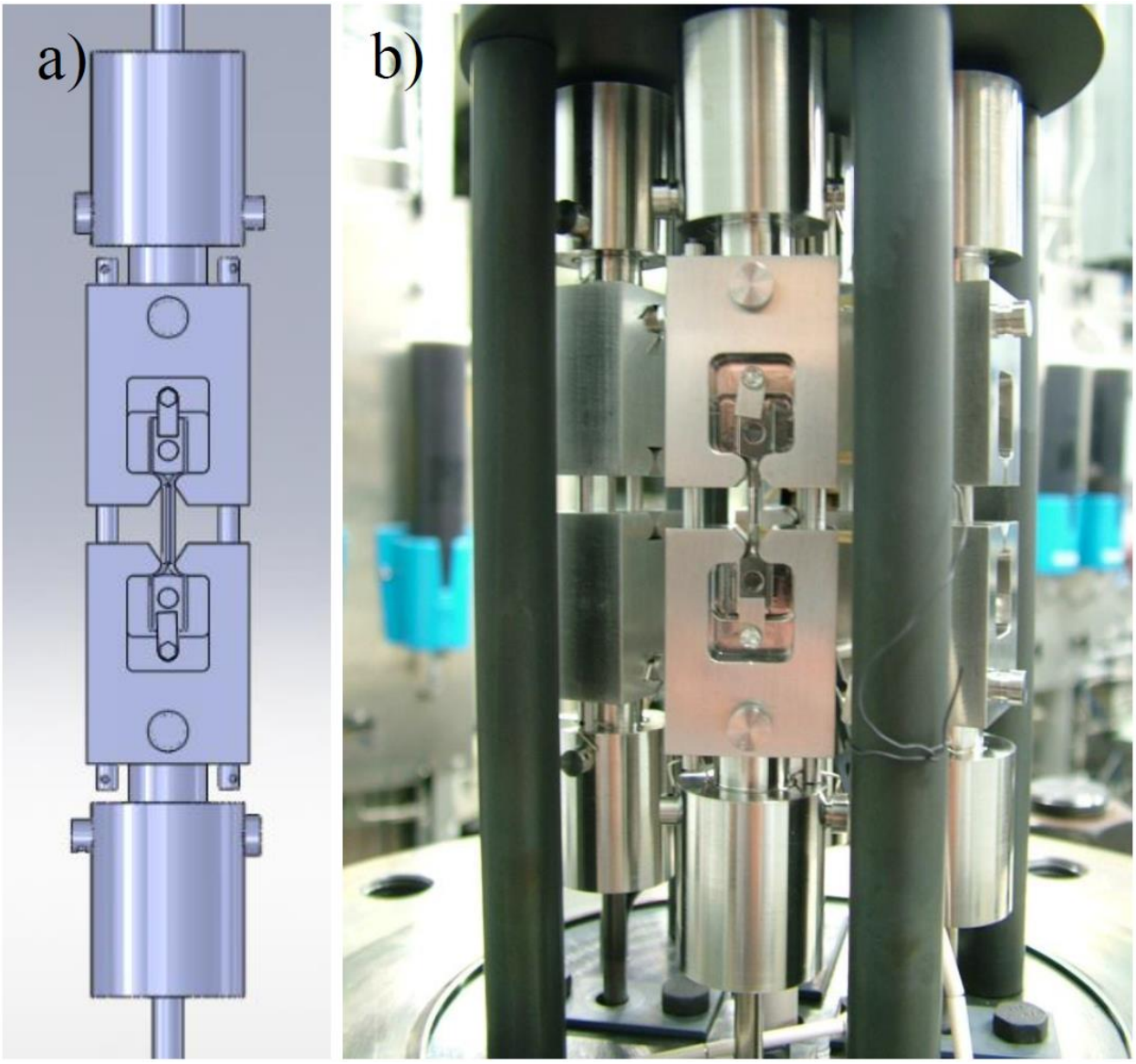

Figure 4.4. a) Schematic of CERT tensile specimen loading fixture. b) image of the four loading fixtures installed in the IM1 autoclave system [104].

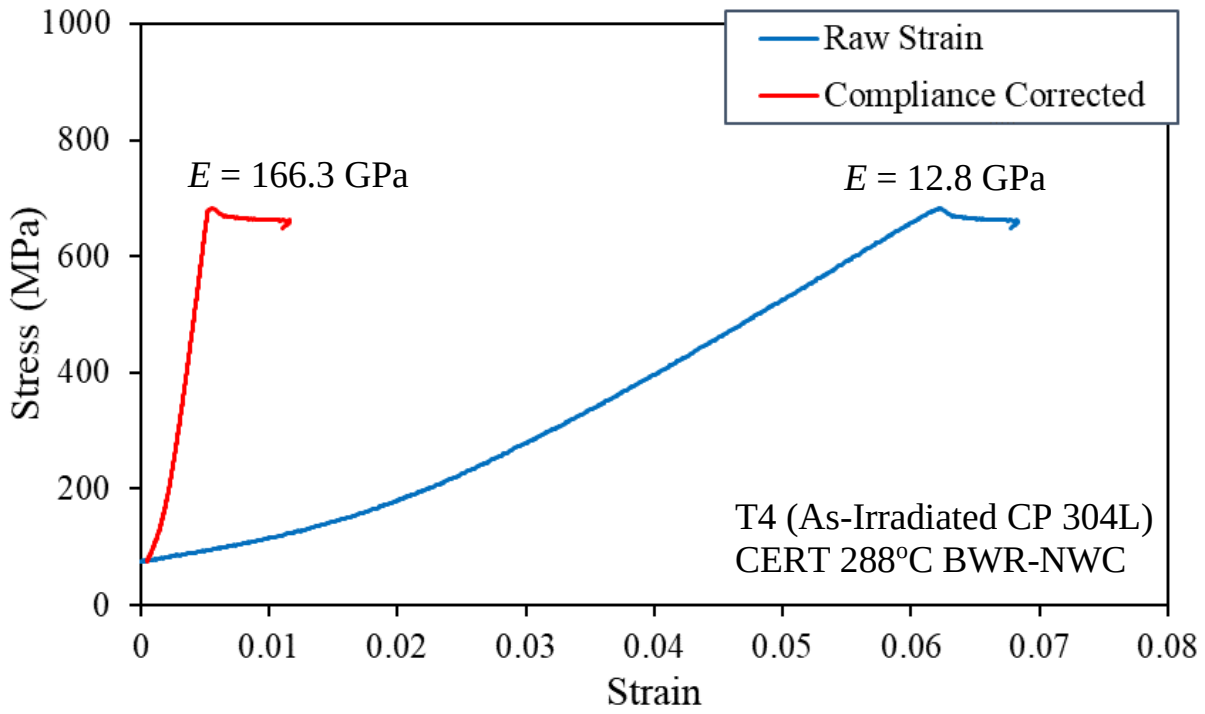

Figure 4.5. Raw and compliance-corrected stress-strain curves for a CERT experiment on specimen T4, as-irradiated condition, under simulated BWR-NWC conditions.

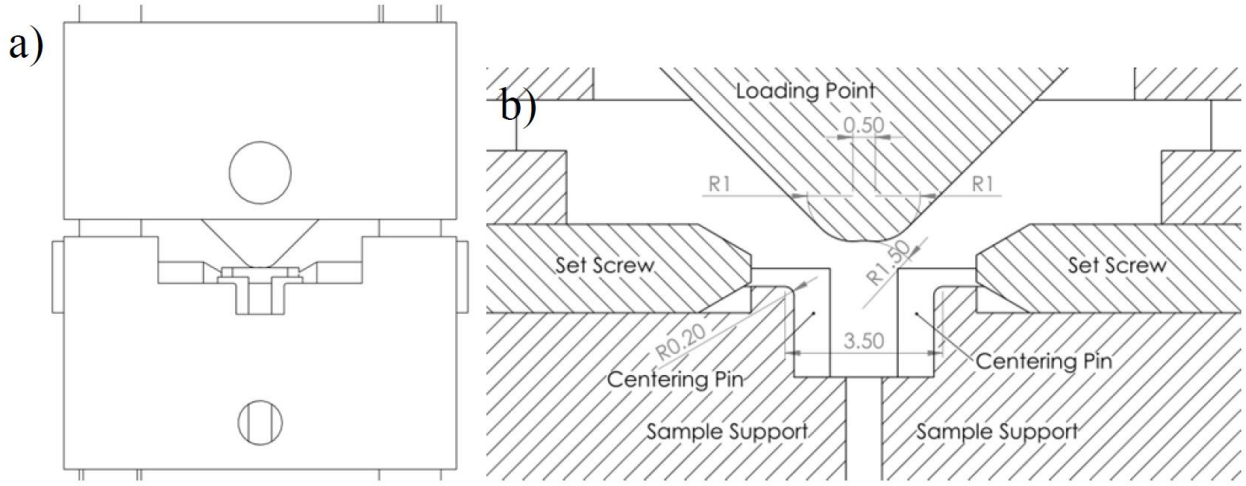

Figure 4.6. a) Schematic of 4-point bend loading fixture, with a centered bend specimen. b) cross sectional view of the loading fixture excluding the bend specimen. Included dimensions are in mm [104].

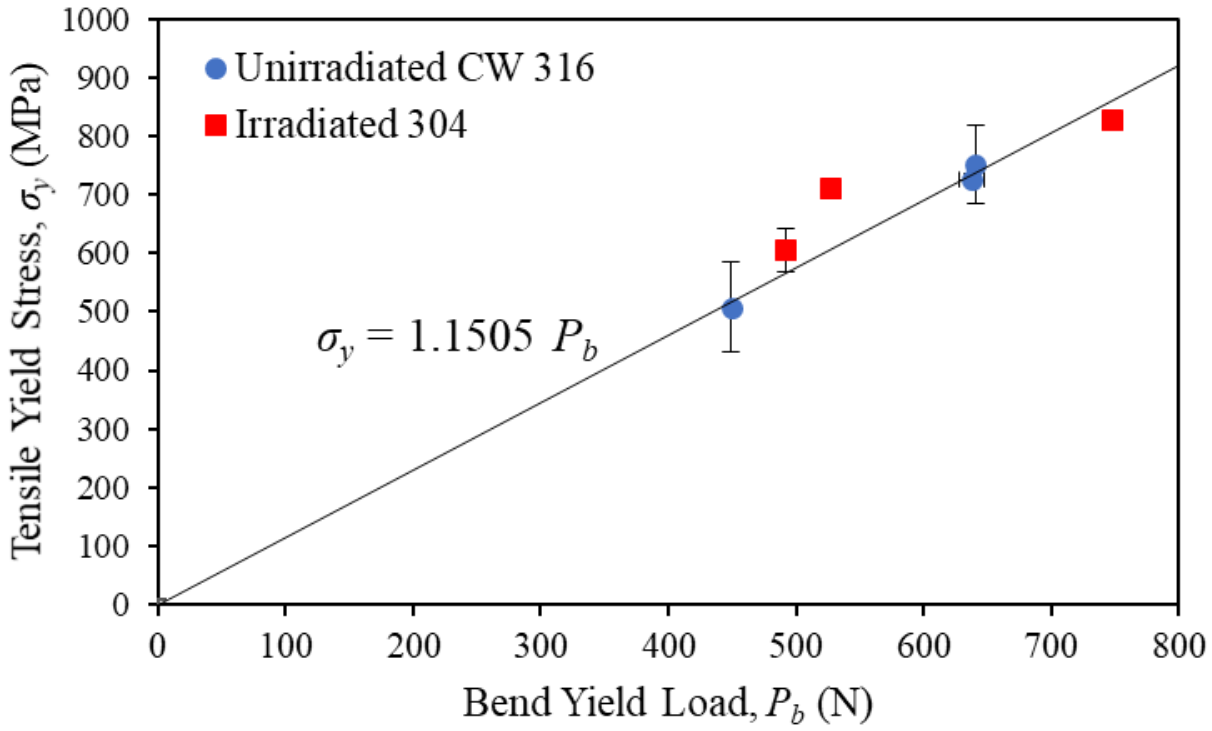

Figure 4.7. Comparison between the measured tensile yield stress and 4-point bend yield load for several specimens, both irradiated and unirradiated. The linear fit was utilized to predict the bend yield load for conditions previously strained in tensile experiments.

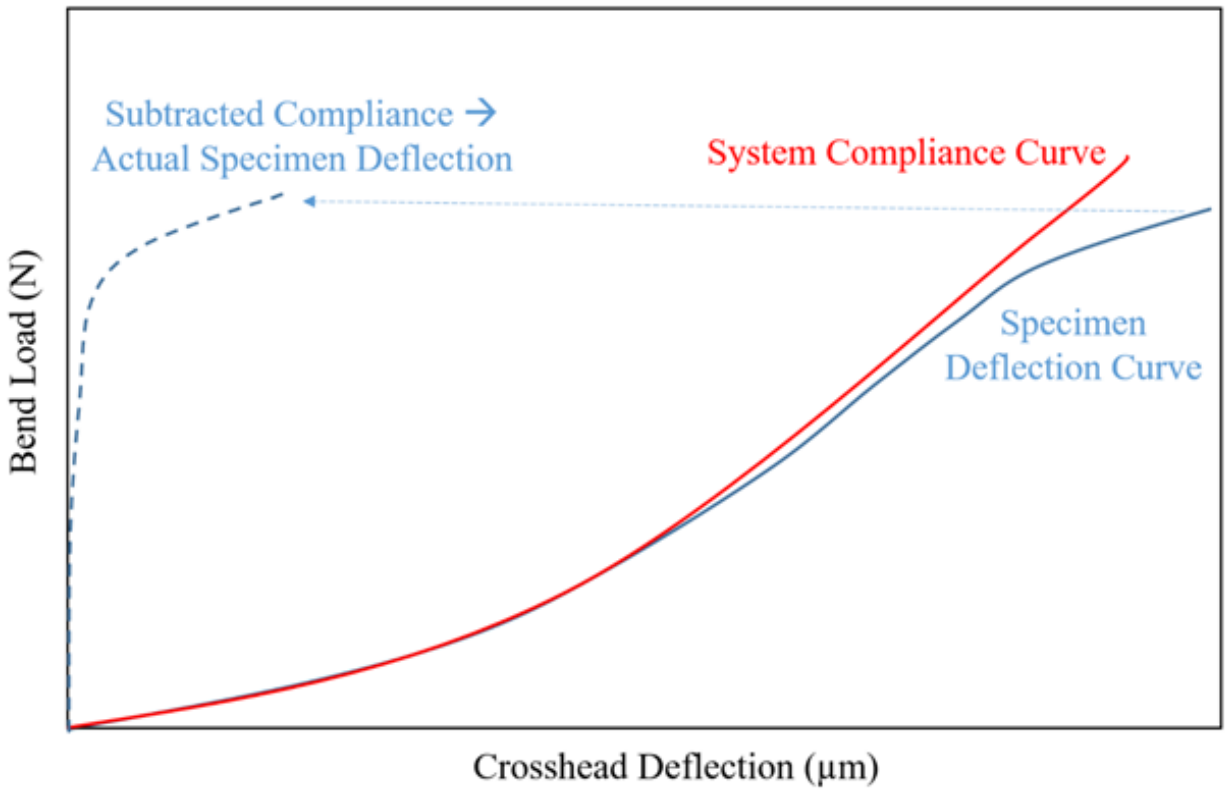

Figure 4.8. Illustration of a system compliance curve for a 4-point bend experiment and its subtraction from the specimen deflection curve to determine the physical specimen deflection.

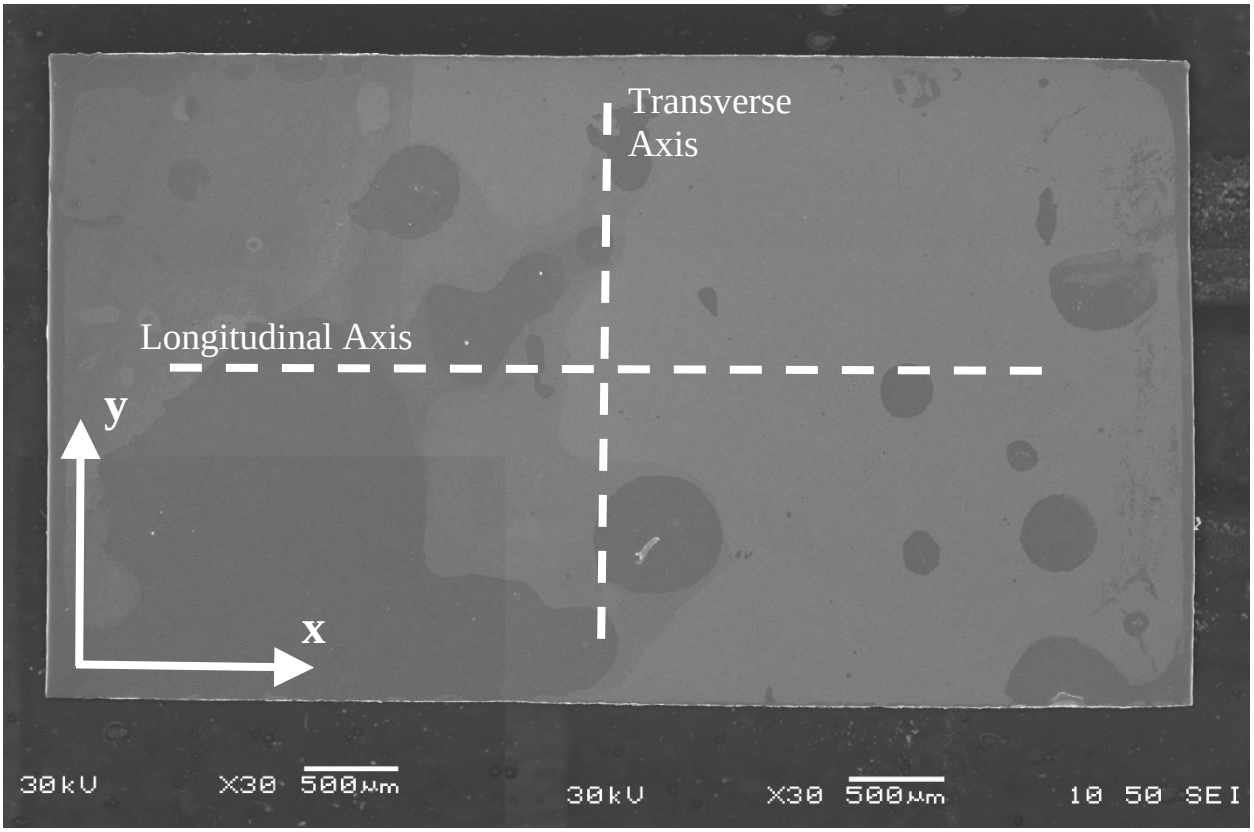

Figure 4.9. Image of electropolished 4-point bend specimen 10-B1, with a demonstration of the typical orientation and reference coordinate system. Dashed lines indicate the primary strain axes.

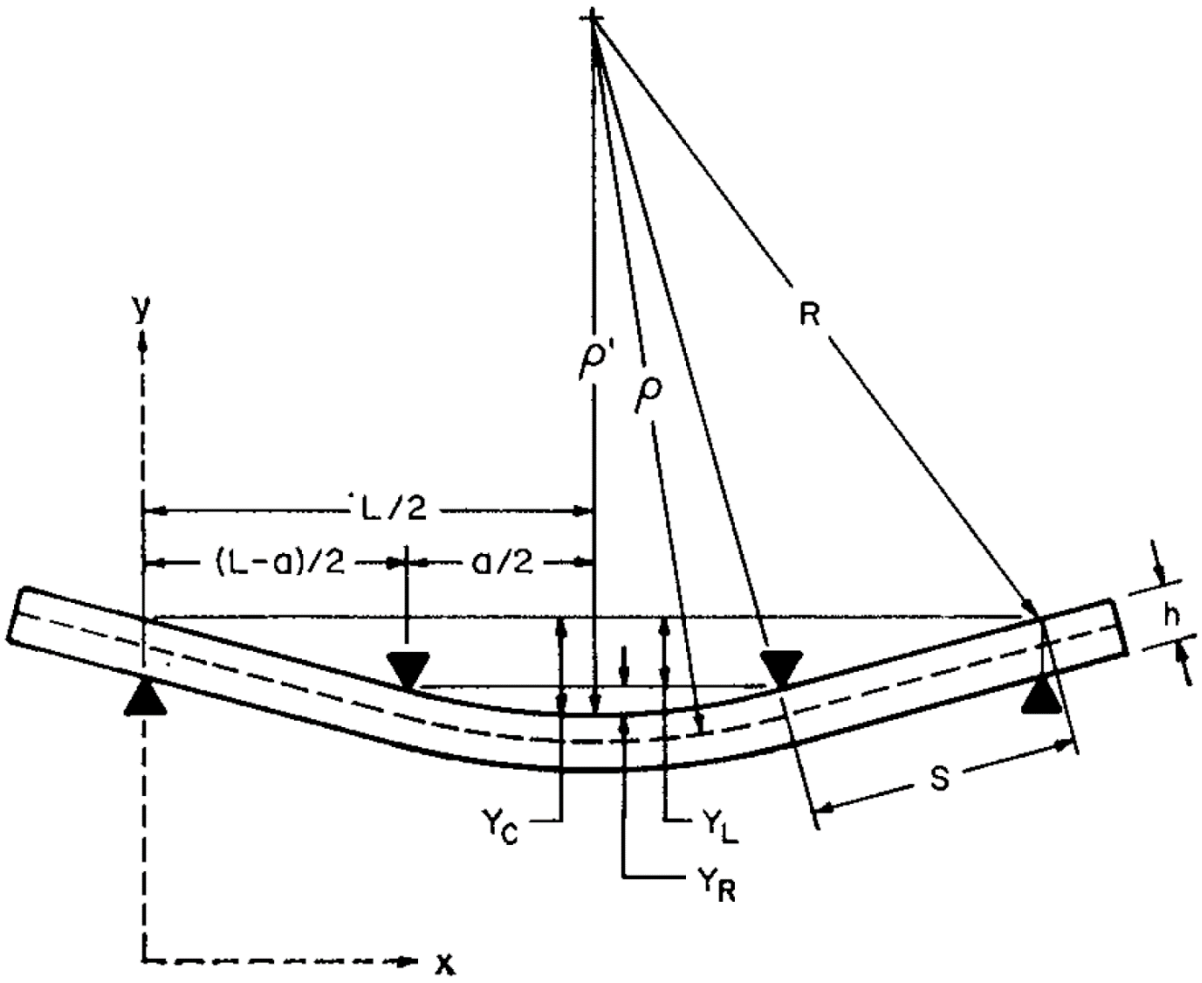

Figure 4.10. Illustration of a 4-point bend experiment and the different specimen and experimental dimensions used to calculate the maximum bend strain [177].

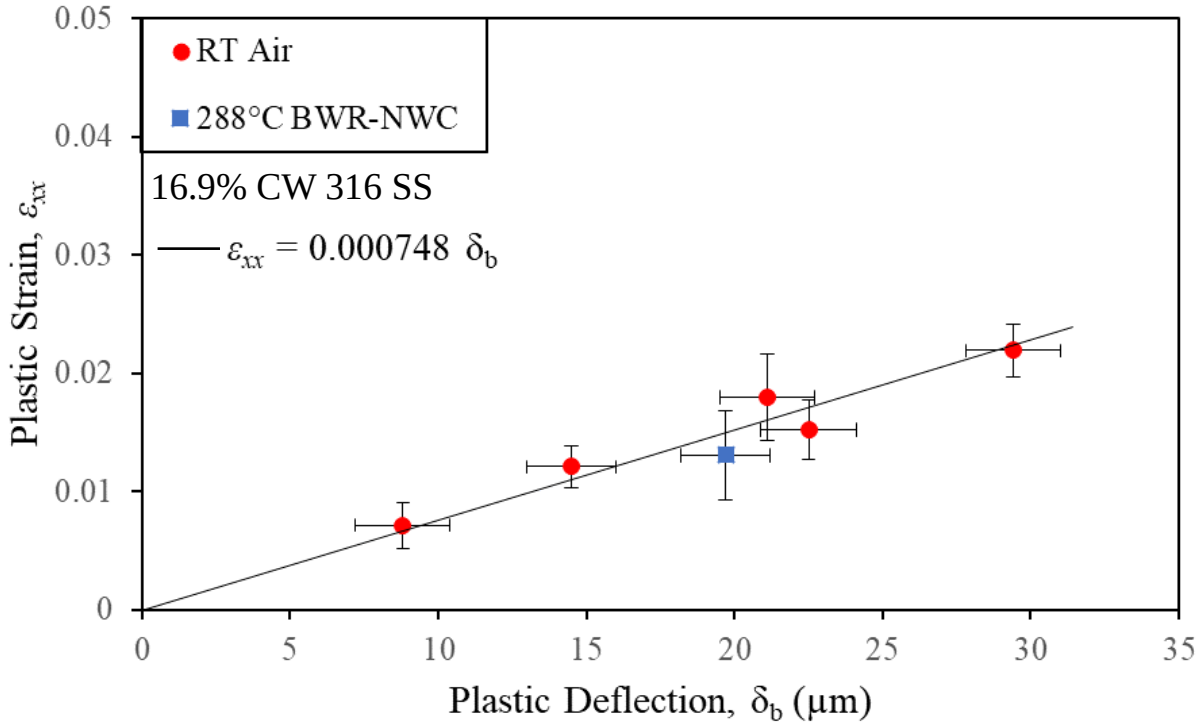

Figure 4.11. Comparison of the measured plastic strain, via a grid of fiducial indents, and the plastic deflection, via side profile measurements, for an unirradiated stainless steel. The identified linear relationship was used to predict bend strain at low deflection values.

CHAPTER 5 - RESULTS

This chapter first summarizes the characterization of the irradiated microstructure, through hardness, transmission electron microscopy (TEM), and atom probe tomography (APT). The results of the incremental CERT experiments on the as-irradiated and PIA conditions under a simulated BWR-NWC environment and evolution of the localized deformation with strain are then presented. Results of four-point bend experiments on as-irradiated and PIA specimens will further detail observations of crack initiation sites and analysis of dislocation channeling. Finally, the results of molecular dynamics (MD) simulations examining the strengthening effects of irradiation-induced defects are also presented.

5.1 Irradiated Microstructure

This section presents a summary of the results of the microstructural analysis, completed on the as-irradiated condition and multiple annealing conditions. The microstructural analysis includes the effect of annealing on the dislocation loop size and density, solute cluster size and density, grain boundary segregation, and the Vickers micro-hardness. Special thanks are required for Dr. Zhijie Jiao's contribution to the microstructure characterization, including his work in completing the necessary TEM microscopy for the dislocation loops and RIS analysis, as well as the FIB lift out and atom evaporation required for the APT solute cluster characterization.

5.1.1 Dislocation Loops

The faulted dislocation loops in the as-irradiated 304L SS and after PIA at 500°C: 1 h, 550°C: 1, 5, and 20 h were characterized using the rel-rod dark field technique as described in Section 4.2.2. TEM rel-rod images of dislocation loops are shown in Figure 5.1. The foil thickness of each TEM specimen was also measured through electron energy loss spectroscopy (EELS) zero loss technique: as-irradiated, 87 nm; 500^{o}C: 1 h, 67 nm; 550^{o}C: 1 h, 93 nm; 550^{o}C: 5 h, 75 nm.

Dislocation loops were easily confirmed in all examined PIA conditions, excepting PIA of 550^{o}C:20 hours. Annealing at 550°C: 20 h resulted in a negligible density of faulted loops, thus rel-rods were not observed. However, imaging under a bright field two-beam condition did reveal a slight population of large unfaulted loops and stacking fault tetrahedral for this annealing treatment, as shown in Figure 5.2. The population of these unfaulted loops was much less than the number of faulted loops observed in other conditions, with a number density of 0.05 x 10^{22} m^{-3}, though having a larger average diameter of 26 nm. As the population of unfaulted loops was not examined for any other conditions, the following results and discussion will focus only on the populations of faulted dislocation loops.

The average faulted dislocation loop diameter and density in 304L SS irradiated to 5.9 dpa in BWR and after various post-irradiation annealing conditions are given in Table 5.1. The initial average dislocation loop diameter after irradiation was 8.3 nm, which increased to 9.6 nm after PIA at 500°C: 1 h. The average loop size was 8.9 nm and 8.0 nm after PIA at 550°C: 1 h and 5 h, respectively. Overall, while the average loop size varied after annealing, there was no significant or systematic change in the size up to 550^{o}C: 5 h. The loop density reduced significantly from 1.1 x 10^{23} m^{-3} in the as-irradiated condition to 8.2 x 10^{22} m^{-3} after annealing at 500°C: 1 h, to 3.2 x 10^{22} m^{-3} at 550°C:1 h, to 1.3 x 10^{22} m^{-3} at 550°C: 5 h. Thus, the loop density reduced to ~75% of its initial density after PIA at 500°C: 1 h and to ~10% after PIA at 550°C: 5 h. Post-irradiation annealing at 550°C: 20 h revealed a negligible population of faulted dislocation loops. The size distribution of dislocation loops in 304L stainless steel irradiated to 5.9 dpa in a BWR environment and after various post-irradiation annealing conditions is shown in Figure 5.3. It appears that smaller dislocation loops are preferably annealed out at the 500°C: 1 h condition and in fact, the density of large loops (>13nm) shows an increase in population compared to the as-irradiated condition. This trend continued for the 550°C annealing conditions, in which the dislocation loop density was continuously decreased across most sizes, though a few large loops were observed to increase in size.

5.1.2 Solute Clusters

Two types of solute clusters were observed in 304L SS irradiated to 5.9 dpa in BWR; Ni-Si rich clusters and Al-Cu rich clusters. These clusters are shown in Figure 5.4 for the as-irradiated

condition, and their evolution after PIA is shown in Figure 5.5. The number density, average diameter, Ni-Si or Al-Cu ratio and volume fraction for Ni-Si and Al-Cu clusters are given in Table 5.2 and Table 5.3, respectively; these values were measured in accordance with Section 4.2.3.

The Ni-Si clusters are presumed to be precursors of the γ′ or G phase as the concentrations of Ni and Si have not reached that following phase formation, i.e. 75% Ni and 25% Si. The number density in the as-irradiated condition is 4.52×10^{23} m^{-3} and decreases to 3.06×10^{23} m^{-3} after PIA at 500ºC: 1 h and to 2.69×10^{23} m^{-3} after PIA at 550ºC: 1 h. The density further decreases to 1.39×10^{23} m^{-3} and 0.81×10^{23} m^{-3} after annealing at 550ºC: 5 and 20 h, respectively. The average cluster size, however, increases from ~9 nm at the as-irradiated condition to 18 nm after annealing at 550ºC: 20 h, though there is a large increase in the size variability. Due to the increase in the cluster size while decreasing number density the volume fraction does not change significantly after annealing: ~2.5% in the as-irradiated condition and ~3.0% after annealing at 550ºC: 20 h. The change in the nickel and silicon concentrations of the Ni-Si clusters following annealing treatments are plotted as radial concentration profiles in Figure 5.6, which show the diffusion of the solutes away from the core of the cluster.

The Al-Cu clusters displayed a similar trend as the Ni-Si clusters following annealing treatments. The number density in the as-irradiated condition is 3.32×10^{23} m^{-3} and it decreases to 2.87×10^{23} m^{-3} after PIA at 500ºC: 1 h and to 1.80×10^{23} m^{-3} after PIA at 550ºC: 1 h. The density further decreases to 1.04×10^{23} m^{-3} after annealing at 550ºC: 20 h, which is ~32% of the as-irradiated number density. Only a small reduction in density, to 2.99×10^{23} m^{-3}, was observed following annealing at 550ºC: 5 h; however, this is thought to be an exception to the trend as only one APT tip was examined at that condition. Meanwhile, the cluster size increased from ~5.5 nm in the as-irradiated condition to ~12.5 nm after annealing at 550ºC: 20 h. The volume fraction of Al-Cu clusters is rather small, ~0.049% in the as-irradiated condition and ~0.032% after annealing at 550ºC: 20 h.

5.1.3 Grain Boundary Segregation

RIS was examined in 304L stainless steel in the as-irradiated condition and PIA at 550°C: 5 and 20 h conditions. Figure 5.7 and Figure 5.8 are the ChemiSTEM elemental images showing segregation of Cr, Ni and Si at an edge-on grain boundary in the as-irradiated and PIA at 550°C:

20 h condition, respectively. Depletion of Cr, Fe and enrichment of Ni, Si and P are evident from composition profile across the grain boundary in the as-irradiated condition (Figure 5.9).

Table 5.4 lists the maximum/minimum grain boundary concentrations measured for Cr, Ni, and Si in wt.% for the examined conditions. In the as-irradiated condition the depletion of chromium is ~5.5% and enrichment of nickel and silicon are 13.4% and 2.2% respectively. The depletion of chromium decreases to 3.2% after annealing at 550°C: 5 h and 1.4% after annealing at 550°C: 20 h. Enrichment of nickel drops to ~3.2% after annealing at 550°C: 20 h, which corresponds to 23% of the nickel enrichment in the as-irradiated condition. There is only 0.13% of enrichment of silicon at the grain boundary after annealing at 550°C: 20 h, which is only ~6% of the silicon enrichment that was present in the as-irradiated condition. Composition profiles for Cr, Ni, Si and P for the as-irradiated and 550°C PIA conditions are shown in Figure 5.10. In addition to the decrease in the peak segregation for each of the examined elements by thermal annealing, the segregation profiles are also observed to broaden following annealing.

5.1.4 Hardness

Vickers micro-hardness has been often used in literature as a simple method to evaluate bulk changes in the irradiated microstructure following PIA treatments, as a reduction in hardening has been observed to correspond to the removal of irradiation defects such as dislocation loops and solute clusters. As such, to select the specific annealing conditions for microstructure analysis, CERT and four-point bend experiments, a wide range of annealing temperatures and times were applied to the as-received sample blanks listed in Table 4.5, and using the procedure outlined in Section 4.1.2. Four different temperatures: 450ºC, 500ºC, 550ºC, and 600ºC with times: 1, 5, and 20 hours at each temperature were utilized, as these time/temperature combinations were expected to fully bound the complete removal of irradiation hardening.

The irradiation hardening ($\Delta H_{v,\,Irr}$), is the increase in the hardness due to the presence of irradiation defects and is calculated from the following expression:

$$\Delta H_{v,Irr} = H_{v,Irr} - H_{v,Unirr}\,, \tag{5.1}$$

where $H_{v,Irr}$ is the measured hardness of the as-irradiated 304L stainless steel, and $H_{v,Unirr}$ is the measured hardness of the unirradiated 304L stainless steel. As no archive material is available, the hardness of the unirradiated material was assumed to be the same as that of a Heat SW 304L

stainless steel available at ORNL, which was measured as 157.95 H_v. Similarly, the post-PIA residual hardening ($\Delta H_{v,PIA}$) can be calculated via Equation 5.1, where the measured hardness after PIA ($H_{v,PIA}$) is substituted for the as-irradiated measurement ($H_{v,Irr}$). The percentage of as-irradiated hardening remaining is then calculated as:

$$\%\ \text{of As} - \text{Irradiated Hardening} = \frac{\Delta H_{v,PIA}}{\Delta H_{v,Irr}} \ . \tag{5.2}$$

The hardness measurements for the selected temperatures are shown in Table 5.5 and Figure 5.11, where the irradiation hardening is plotted as a percentage of the as-irradiated condition. Overall, it was observed that annealing at 450°C, had a negligible impact on the irradiation hardening up to times of 20 hours. However, temperatures of 500°C, 550°C, and 600°C showed successively greater removal of hardening with increasing time and temperature. Following annealing at 600°C: 20 h, the measured hardness had returned to a value expected for an unirradiated 304L stainless steel.

Based on the residual hardening, annealing conditions of 500°C: 1 h, 550°C: 1 h, 550°C: 5 h, and 550°C: 20 h, were selected for both more detailed microstructural analysis and application to the tensile and 4-point bend specimens. Following the annealing of the tensile samples, hardness measurements from both the tensile specimens and slices from the tensile heads, which later become the 4-point bend specimens, were used to confirm the removal of hardness, as shown in Table 5.5. There was a good agreement in hardening removal as compared to earlier data from the sample blank specimens, as shown in Figure 5.11.

5.2 CERT Experiments

This section presents a description of the incremental CERT test results obtained from the irradiated and PIA tensile bars. CERT tests were conducted at 288°C under simulated BWR-NWC conditions. The stress-strain behavior of each specimen is first presented with comments about the observed mechanical behavior. A summary of the mechanical properties is then presented followed by images of both crack initiation sites and the final fracture surface after completion of the CERT tests. The results of the dislocation channel density analysis for the tensile specimens is then presented.

5.2.1 Prediction of Yield Stress and Incremental Straining Experiments

Prior to beginning the incremental straining experiments, it was necessary to first predict the yield stress of both the as-irradiated condition and that following each annealing treatment. Previous studies have shown that the change in irradiation hardening is linearly related to the change in the yield stress as seen in Equation 3.3 [142].

$$\Delta\sigma_y = X * \Delta H_v \,, \tag{5.3}$$

where X is the linear correlation factor; prior work by Busby *et al.* found that for irradiated austenitic stainless steels, an average correlation factor of X = 3.03, best fits the available data. However, the correlation factors for individual data sets have more variability, ranging from 2.63 to 3.83 [142]. Using the average correlation factor of 3.03 and the unirradiated hardness and yield stress of 157.95 H_v and 211.5 MPa as measured from a similar Heat SW 304L stainless steel at ORNL, respectively, an initial prediction of the yield stresses for our initial two specimens, T-4 (as-irradiated) and T-9 (550ºC: 20 h) were calculated based on the hardness measurements taken after PIA treatments, previously shown in Table 5.5. Based on these predictions straining increments to 40, 60, 80, and 100% of the yield stress were made for these two specimens as listed in Table 5.6. The as-irradiated specimen T-4 showed a very close agreement between the predicted and measured yield stress. However, for the T-9 specimen, the original hardness value was incorrectly measured, thus resulting in a miscalculated yield stress prediction. As such, an additional stress increment was required to reach the correct yield stress. A remeasurement of the hardness of the T-9 specimen revealed that the correct hardness closely matched the measured yield stress.

Utilizing these measured yield stresses a new correlation factor was fit to our specific material, which was then used to predict the yield stresses of the T-5 (500ºC: 1 h), T-13 (550ºC: 1 h), T-7 (550ºC: 5 h), and T-12 (550°C: 20 h) specimens. As shown in Figure 5.12, the final correlation factor for these five specimens was calculated as X = 2.46. While this correlation factor is lower than those previously seen in literature, the difference is likely an effect of the PIA treatments, as the previous correlation factors only examined as-irradiated microstructures to different dose levels [142].

Table 5.7 shows a complete list of the incremental straining experiments that were applied to each of the examined specimens, including the target stress/strain for each increment as well as

the final value. Overall, there was a good agreement between the target and achieved stress/strain, excluding the yield stress for specimen T-9 specimen and the 0.5% ε_p increment for the as-irradiated T-4 specimen. The T-7 increment to 10% ε_p was purposely halted early for examination due to the occurrence of significant necking.

5.2.2 Stress-Strain Behavior

Engineering stress-strain curves for each of the tested conditions: as-irradiated, 500°C: 1 h, 550°C:1 h, 550°C: 5 h, and 550°C: 20 h are shown in Figure 5.13. The elastic deformation portion of each curve has been corrected to subtract system compliance by normalizing to the expected Young's modulus for an austenitic stainless steel, as outlined in Section 4.3.3.

The as-irradiated condition displayed a yield stress drop and subsequent strain softening. as is typical of the irradiated condition of a solution-annealed stainless steel, due to the increased source hardening and plastic instability after yielding [196]. Annealing at 500°C: 1 h slightly reduced the yield stress, while completely removing the yield stress drop and strain softening behavior, instead displaying neither strain hardening nor strain softening behavior. Due to the early onset of localized necking, the plastic strain in this specimen was also considered to be in the plastic instability regime. Annealing at 550°C: 1 and 5 h, further reduced the yield stress and resulted in a slight strain hardening behavior, with higher elongations and onset of diffuse necking at ~7% plastic strain, representing a return to the expected plastic deformation expected in an unirradiated stainless steel. Annealing at 550°C: 20 h caused a further drop in the yield stress and an increase in the elongation. Furthermore, one specimen, T-9, at this condition displayed a clear strain hardening behavior, indicating the return of uniform elongation, up to about 8.5% plastic strain, while the other, T-12, displayed a very rapid failure, despite having a lower yield stress.

5.2.3 Mechanical Properties

Mechanical properties of the varying annealing treatments, as determined from the CERT tests, are summarized in Table 5.8. The table is organized by annealing condition, showing the yield stress, maximum stress, uniform and total elongation. For the as-irradiated condition, uniform elongation and maximum stress both occurred at the yield point (~0.5%) because of strain softening. Overall, it was observed that the yield stress was reduced in proportion to the residual

hardening following the annealing treatments. Furthermore, it was seen that the annealing treatments also lead to a change in the mechanical behavior, from a strain softening to strain hardening, and a general increase in the ductility of the specimen, though the T-12 specimen was an exception to this trend.

5.2.4 Tensile Crack Initiation

As a part of the incremental straining experiments, the tensile specimens were examined in the SEM following each strain increment as described in Section 4.3.4. Part of this SEM examination included the investigation of crack initiation, including both the number of crack initiation sites and the total length of surface cracks on the specimen, as listed in Table 5.9. Example images of the three tensile specimens that displayed crack initiation prior to failure: T-4, T-5, and T-12 are displayed in Figure 5.14, Figure 5.15, and Figure 5.16, respectively. Note that while multiple crack initiations sites were observed in both T-4 and T-12, only one crack initiation site was observed in T-5, which then grew over additional strain increments. A representation of change in both crack number density and crack length density for the tensile specimens are shown in Figure 5.17 and Figure 5.18. Overall, both the cracking number density and crack length density appeared to decrease with increased annealing, excepting the T-12 specimen. T-4 and T-12 showed a similar level of crack length density, however, in the case of T-4 this crack length was a factor of several large cracks, while in the T-12 specimen, this crack length was largely due to the large number of crack initiation sites, ~4.5 times that observed in the T-4 specimen.

5.2.5 Tensile Fractography

Following the failure of a specimen in CERT testing, the fracture and gage surfaces were fully examined by SEM. Areas of IG or TG cracking were quantified to determine %IG, %TG, % mixed IG/TG, and % ductile failure. Examples of each type of fracture can be seen in Figure 5.19. Reduction in area was also determined based on the full area of the fracture surface. The fracture surface from each individual tensile specimen is shown in Figure 5.20 through Figure 5.25.

The results of the fractography classification and reduction of area analysis after CERT are summarized in Table 5.10 and Figure 5.26. The %IG varied between 81.0% and 0%, and it was

observed to largely decrease in response to increasing annealing time and temperature. However, while the IASCC susceptibility was fully removed for the 550°C: 1 and 5 h annealed specimens, as evidenced by the fully ductile fracture surfaces, the 550°C: 20 h specimens still displayed a very clear cracking susceptibility. Reduction of area (RA) followed a similar trend as total elongation in that it increased with increasing annealing, however, specimen T-5 (500°C: 1 h) showed a much higher reduction in area as compared to T-4 (as-irradiated), despite an only slightly higher final elongation. Meanwhile, due to its very low strain at failure, the T-12 (550°C: 20 h) specimen had a minimal RA.

5.2.6 Dislocation Channeling

As previously mentioned, the degree of localized deformation was measured via SEM following each stress/strain increment. However, due to the highly strained region that occurs during the advancement of a crack tip, measurements of the dislocation channel density were only taken for increments which displayed no significant crack growth. Furthermore, the as-irradiated material displayed an unexpected resistance to localized deformation as significant populations of dislocation channels were only observed post-yield, following the addition of bulk plastic strain. Previous literature studies for irradiated material have observed significant localized deformation below the specimen yield stress [13,87,88].

The measured dislocation channel densities, grain boundary interaction site densities, ratio of discontinuous to continuous interaction sites, and average dislocation channels spacing for each of the tensile strain increments are shown in Table 5.11. As most specimens exhibited regions of enhanced strain, where the eventual crack initiation and/or failure later occurred, the measured channel densities are taken over this region (~2-3 mm of gage length) where later failure was observed, rather than over the entire gage length, along with the respective local plastic strain measured in the necked region. Comparison of the dislocation channel density with strain for the examined conditions: as-irradiated, 500°C: 1 h, 550°C: 1, 5, and 20 h, is shown in Figure 5.27. The density of dislocation channel-grain boundary interaction sites is given in Figure 5.28. It should be noted that localized deformation was not measured for the T-12 (550°C: 20 h) specimen, due to its premature crack initiation.

It is observed that the as-irradiated (T-4), 500°C: 1 h (T-5), and 550°C: 1 h (T-13) conditions have very similar dislocation channel densities at similar strain levels, while the 550°C: 5 h (T-7) sample exhibited a slight decrease in the density. The 550°C: 20 h (T-9) had a significantly reduced density regardless of the plastic strain. The density of the interaction sites seems to change in proportion to the total dislocation channel density regardless of the annealing condition, furthermore, a relatively constant ratio of discontinuous to continuous interaction sites was maintained regardless of annealing condition. The average dislocation channel spacing appears to decrease with annealing condition and strain, but this is difficult to validate, due to the lack of data in the as-irradiated condition for the tensile specimens.

5.3 Four-Point Bend Experiments

This section presents a description of the incremental 4-point bend test results obtained from the irradiated and PIA bend specimens. 4-point bend experiments were conducted at 288°C under simulated BWR-NWC conditions. The load-deflection behavior of each specimen is first presented with comments about the observed mechanical behavior. A summary of the mechanical properties is then presented followed by example images of each cracked surface after completion of the 4-point bend increments. The results of the dislocation channel density analysis for the 4-point bend specimens is then presented.

5.3.1 Prediction of Bend Yield Load and Incremental Straining Experiments

Prior to beginning the incremental straining experiments, it was necessary to first predict the yield stress of both the as-irradiated condition and that following each annealing treatment. The yield stress for each bend specimen was predicted from the measured hardness as explained in Section 5.2.1, while the predicted yield stress was converted to a bend yield load through the linear fitting of the relationship between the tensile yield stress and the 4-point bend yield load for specimens of the same material, as explained in Section 4.4.3. This procedure provided the predicted bend yield stresses as shown in Table 5.12, along with the measured bend yield stresses from each specimen. There was a large discrepancy between the predicted and measured yield stresses. However, the trend between the measured tensile and bend yield stresses remained linear

as shown in Figure 5.29, simply having a large degree in scatter. This scatter is predominately due to the difficulty in accurately measuring the mechanical behavior of a material during the 4-point bend experiments.

Table 5.13 shows a complete list of the incremental straining experiments that were applied to each of the 4-point bend specimens, including the target stress/strain for each increment as well as the final value. Not that increments below the yield stress were only applied to the as-irradiated 4-B specimen. Overall, there was a good agreement between the target and achieved stress/strain, though there was some variability due to the inaccuracy of the *in situ* deflection measurements.

5.3.2 Stress-Strain Behavior

Unlike the tensile straining experiments, it is quite difficult to measure the stress-strain behavior of a 4-point bend specimen. This is largely due to both the inaccuracy of the compliance subtraction method, as described in Section 4.4.4, and the measured mechanical behavior of the 4-point bend specimens. During a 4-point bend experiment it was observed that the load required to bend the specimen generally increased as a function of strain, a process which would generally be referred to as strain hardening. Under subsequent increments, however, it was found that the bend yield load was not the same as final load in the prior increment, an example of which is shown for the 4-B (as-irradiated) specimen in Figure 5.30. This behavior leads to difficulty in examining the stress-strain properties of the 4-point bend specimens, thus the partial stress-strain relation was plotted in Figure 5.31, where the bend yield stress of a subsequent increment is listed as the final stress of the prior increment. Using the 4-B specimen as an example, the load at the end of the increment to a total strain of 2.88% ε_p was assumed to be the yield load of the planned strain increment to 4% ε_p, 645.5 N. Viewing the 4-point bend increments in this manner, reveals that the annealed specimens, 9-C (500^{o}C: 1 h) and 7-B (550^{o}C: 5 h) have a neutral strain hardening behavior, neither hardening or softening, much the same as the tensile specimens. The as-irradiated specimens display a more unusual behavior in that the 4-B specimen begins to display a strain softening behavior following about 3% ε_p, while the 10-B1 specimen appears to be strain hardened over the course of its straining increments. Note that the strain hardening in the 10-B1 specimen only serves to bring this specimen up to the predicted yield stress, as it originally yielded at a lower than expected stress.

5.3.3 Four-Point Bend Crack Initiation

As a part of the incremental straining experiments, the 4-point bend specimens were examined in the SEM following each strain increment as described in Section 4.4.6. Part of this SEM examination included the investigation of crack initiation, including both the number of crack initiation sites and the total length of surface cracks on the specimen, as listed in Table 5.14. Example images of the three 4-point bend specimens that displayed crack initiation during the examined straining increments: 4-B, 10-B1, and 12-B1 are displayed in Figure 5.32, Figure 5.33, and Figure 5.34, respectively. A representation of change in both crack number density and crack length density for the 4-point bend specimens are shown in Figure 5.35 and Figure 5.36. Overall, both the cracking number density and crack length density appeared to decrease with increased annealing, excepting the 12-B1 specimen. Note that the bend specimen annealed at 500^{o}C:1 h (9-C) did not display crack initiation, unlike its respective tensile specimen, T-5. The as-irradiated bend specimens (4-B and 10-B1) showed similar levels of crack length density with strain in the center of the bend specimen, while in the 550^{o}C: 20 h specimen (12-B1) the crack initiation appeared to be associated with the edges of the bend specimen.

5.3.4 Dislocation Channeling

As described in Section 4.4.6, the degree of localized deformation in the 4-point bend specimens was measured via SEM following each stress/strain increment. The measured dislocation channel densities, average dislocation channel spacing, and fraction of channeled area for each strain increment are shown in Table 5.15. Comparison of the dislocation channel density with strain for the examined conditions: as-irradiated, 500^{o}C: 1 h, 550^{o}C: 5 and 20 h, is shown in Figure 5.37. It is observed that the as-irradiated, 500^{o}C:1 h, 550^{o}C:1 and 5 h conditions have very similar dislocation channel densities, while the 550^{o}C:20 h sample exhibited an apparent decrease in the dislocation channel density.

Examining the average channel spacing with strain displays a variation between the as-irradiated and annealed conditions. While all conditions show a decrease in the average channel spacing with strain, across all strain levels that as-irradiated condition appears to have an average channel spacing roughly 3.5 μm larger than that of the annealed conditions of 500^{o}C:1 h, 550^{o}C:

5 and 20 h. However, the lack of data for the annealed conditions, makes a precise comparison difficult.

The fraction of channeled area, as shown in Figure 5.38, appears to vary in response to both changes in strain and annealing condition. For example, it is observed that the fraction of channeled area for both as-irradiated specimens, 4-B and 10-B1, is about 10% more than the annealed specimens 9-C (500^{o}C: 1 h) and 7-B (550^{o}C: 5 h). Meanwhile, the 550^{o}C:20 h specimen, 12-B1, has a much lower fraction of channeled area, though there is only a single data point. Overall the fraction of channeled area appears to increase with strain and decrease with annealing treatments.

5.4 LAMMPS Simulations

This section presents the results of the LAMMPS simulations, which were completed to examine the change in shear stress as an edge dislocation interacted with and crossed a periodic array of typical radiation-induced defects. Figure 5.39 shows the shear stress-strain curves as the edge dislocation crosses different defects of size 5 nm, as compared to the glide stress of the matrix. In general, the dislocation loop forms a large increase in shear stress as it interacts with the dislocation, while the solute cluster only forms a slight modification from the glide stress. The combined cluster-loop defect follows much of the same trend as an independent dislocation loop, though a slight stress enhancement from the cluster is also present.

The average peak shear stress for each examined type of obstacle array was determined and listed in Table 5.16, along with the standard 95% confidence interval of the average. The friction stress was measured over multiple randomized matrices and was had an average value of 181.5 MPa, a value matching with previous simulations of 300-type stainless steel with this potential [191]. The dislocation loop obstacles saw a considerable increase in peak shear stress, >150 MPa, as compared to the friction stress. Loops with an orientation of $[1\bar{1}1]$ and $[\bar{1}11]$ increased with loop size, while the peak stresses for loops at the $[\bar{1}\bar{1}1]$ orientation remained constant regardless of loop size. The peak stresses resulting from the nickel solute cluster obstacles were fairly minimal, often increasing <50 MPa from the friction stress. The peak shear stresses from the solute clusters increased with both cluster diameter and solute concentration. The combined solute cluster-dislocation loop defects often had similar peak stresses as their

independent dislocation loops, though an increase in the peak stress was measured from the additional solute atoms. The increase in shear stress for the combined defect was similar to that observed for the independent cluster and loop defects, i.e. increase with size and solute concentration, with the exception of the $[\bar{1}\bar{1}1]$ where the peak shear stress was actually observed to decrease below the independent loop as a result of the added solute atoms.

5.4.1 Edge Dislocation-Dislocation Loop Interactions

While the interaction between the edge dislocation and a solute cluster defect was a cutting of the defect by a pure shear mechanism, the interaction between a dislocation and a dislocation loop can be much more complex. In this research the edge dislocation-dislocation loop interaction was simply quantified as for whether or not the faulted dislocation loop unfaulted into a perfect loop during the interaction. The unfaulting of a dislocation loop did not seem to significantly affect the peak shear stress to bypass the barrier, but his unfaulting does effectively eliminate the barrier for following dislocations. It should be noted that earlier works by Bakaev *et al.* [182] and Terentyev *et al.* [183] more intimately studied dislocation-dislocation loop interactions in FCC, and the simulations of this research largely confirmed the same behavior.

The unfaulting of dislocation loops was primarily defined by three factors: size, orientation, and solute concentration, in the case of the combined cluster-loop defects. The effect of defect size can be seen when examining the dislocation loops at an orientation of $[1\bar{1}1]$: 60% of the examined loops were observed to unfault at a diameter of 3 nm, compared to ~17% at 5 nm, and 0% at 7 nm. Loops at an orientation $[\bar{1}\bar{1}1]$ were observed to unfault much less with only ~14% unfaulting at a diameter of 3 nm, and none were observed to unfault at larger sizes. Loops with an orientation of $[\bar{1}11]$ were not observed to unfault at any size. When examining loops at an orientation of $[1\bar{1}1]$, enhancing the Ni concentration of the spherical cluster to 50% around a 3 nm loop, was able to decrease the unfaulting to 40%. For loops with a diameter of 5 nm, enhancing the Ni concentration to 25% did not affect the unfaulting rate: ~17%, but increasing the solute concentration to 50% or 75%, reduced the unfaulting to 0%. Dislocation loops with an orientation of $[1\bar{1}1]$ were the most likely to unfault through an interaction with a $[\bar{1}10]$ edge dislocation, but stability was seen to increase with loop diameter and solute concentration in the case of a combined cluster-loop defect.

Table 5.1. Faulted dislocation loop size and number density in 304L SS irradiated to 5.9 dpa in BWR and after various post-irradiation annealing conditions.

Condition	Density (10^{22}/m^3)	% of As-Irradiated Density	Average Diameter (nm)	Loop Line Length Density (10^{15} m/m^3)	% of As-Irradiated Length Density
As-Irradiated	11.12 ± 1.19	100%	8.3 ± 0.3	2.89 ± 0.12	100%
500˚C: 1 h	8.21 ± 0.96	74.0%	9.6 ± 0.4	2.47 ± 0.10	85.5%
550˚C: 1 h	3.25 ± 0.36	29.3%	8.9 ± 0.4	0.90 ± 0.05	31.4%
550˚C: 5 h	1.27 ± 0.15	11.4%	8.0 ± 1.2	0.32 ± 0.12	11.0%
550˚C: 20 h	0.0 ± 0.0	0.0%	0.0 ± 0.0	0.0 ± 0.0	0.0%

Table 5.2. Ni-Si cluster size, density and volume fraction in 304L SS irradiated to 5.9 dpa in BWR and after various post-irradiation annealing conditions.

Condition	Density (10^{23} /m^3)	% of As-Irradiated	Diameter (nm)	Ni-Si Ratio	Volume Fraction of Ni and Si (%)
As-Irradiated	4.52 ± 0.68	100%	8.62 ± 1.24	5.13 ± 0.13	2.47 ± 0.08
500°C: 1 h	3.06 ± 0.52	67.7%	9.97 ± 1.67	5.12 ± 0.48	2.44 ± 0.21
550°C: 1 h	2.69 ± 0.13	59.5%	11.34 ± 1.60	5.43 ± 0.27	2.97 ± 0.05
550°C: 5 h	1.39 ± 0.24	30.7%	16.09 ± 4.43	7.61 ± 0.59	3.59 ± 0.62
550°C: 20 h	0.81 ± 0.09	17.9%	18.07 ± 4.57	7.95 ± 0.03	2.96 ± 0.16

Table 5.3. Al-Cu cluster size, density and volume fraction in 304L SS irradiated to 5.9 dpa in BWR and after various post-irradiation annealing conditions.

Condition	Density (10^{23} /m^3)	% of As-Irradiated	Diameter (nm)	Cu-Al Ratio	Volume Fraction of Al (%)
As-Irradiated	3.32 ± 0.68	100%	5.30 ± 0.43	0.49 ± 0.12	0.049 ± 0.009
500°C: 1 h	2.87 ± 0.11	86.4%	5.84 ± 0.34	0.46 ± 0.01	0.035 ± 0.003
550°C: 1 h	1.80 ± 0.13	54.2%	8.97 ± 0.53	0.85 ± 0.03	0.033 ± 0.004
550°C: 5 h	2.99 ± 0.24	90.1%	10.10 ± 0.50	0.88 ± 0.08	0.066 ± 0.011
550°C: 20 h	1.04 ± 0.30	31.3%	12.38 ± 0.59	0.69 ± 0.02	0.032 ± 0.001

Table 5.4. Peak grain boundary concentrations in the as-irradiated condition and after PIA at 550°C for 5 and 20 hours.

	GB Cr (wt%)	ΔCr (wt%)	% of As-Irr ΔCr	GB Ni (wt%)	ΔNi (wt%)	% of As-Irr ΔNi	GB Si (wt%)	ΔSi (wt%)	% of As-Irr ΔSi
As-Irradiated	12.83	-5.52	100	23.98	13.41	100	2.48	2.18	100
550°C: 5 h	15.11	-3.24	59	14.7	4.13	31	0.65	0.35	16
550°C: 20 h	16.92	-1.43	26	13.72	3.15	23	0.43	0.13	6

Table 5.5. Change in hardness following PIA treatments for the various specimen types: sample blanks, tensile, and four-point bend

Specimen Type	Specimen ID	PIA Treatment	As-Irradiated Hardness ($H_{v,Irr}$)	PIA Hardness ($H_{v,PIA}$)	Irradiation Hardening ($\Delta H_{v,Irr}$)	Post-PIA Irradiation Hardening ($\Delta H_{v,PIA}$)	% of As-Irradiated Hardening
Sample Blank	9A	450°C: 1 h	341.50	329.09	183.55	171.14	93.24%
	9	450°C: 5 h	341.50	310.42	183.55	152.48	83.07%
	5A	450°C: 20 h	339.75	309.81	181.80	151.86	83.53%
	18	500°C: 1 h	334.75	321.00	176.80	163.05	92.22%
	5	500°C: 1 h	339.75	308.05	181.80	150.10	82.56%
	18A	500°C: 5 h	334.75	304.81	176.80	146.86	83.07%
	16	500°C: 20 h	350.33	286.61	192.38	128.67	66.88%
	11	550°C: 1 h	341.67	287.28	183.71	129.33	70.40%
	15	550°C: 5 h	337.42	248.28	179.46	90.33	50.33%
	15A	550°C: 20 h	337.42	220.19	179.46	62.24	34.68%
	17	600°C: 1 h	371.67	228.95	213.71	71.00	33.22%
	17A	600°C: 5 h	371.67	185.38	213.71	27.43	12.83%
	16A	600°C: 5 h	350.33	184.61	192.38	26.67	13.86%
	11A	600°C: 20 h	341.67	150.42	183.71	-7.52	-4.10%
Tensile	T-5	500°C: 1 h	346.67	326.93	188.71	168.97	89.54%
	T-13	550°C: 1 h	347.53	298.53	189.57	140.57	74.15%
	T-7	550°C: 5 h	337.47	266.67	179.51	108.71	60.56%
	T-9	550°C: 20 h	340.60	247.85	182.64	89.89	49.22%
	T-12	550°C: 20 h	339.23	207.07	181.27	49.11	27.09%
Bend	9-C	500°C: 1 h	340.60	326.73	182.64	168.77	92.41%
	7-B	550°C: 5 h	337.47	261.67	179.51	103.71	57.77%
	12-B1	550°C: 20 h	339.23	203.07	181.27	45.11	24.89%

Table 5.6. Prediction of the yield stress based on changes in hardness following PIA.

Specimen	Measured Hardness (H_v)	Predicted Yield Stress (MPa)	Measured Yield Stress (MPa)
T-4 (As-Irradiated)	348.0 ± 9.6	679.8 ± 23.8	685.5
T-5 (500^{o}C: 1 h)	326.9 ± 9.5	627.8 ± 23.5	633.4
T-13 (550^{o}C: 1 h)	298.5 ± 13.9	557.9 ± 34.4	553.2
T-7 (550^{o}C: 5 h)	266.7 ± 10.2	479.3 ± 25.2	483.6
T-9 (550^{o}C: 20 h)	247.9 ± 14.2	433.0 ± 35.1	421.3
T-12 (550^{o}C: 20 h)	207.07 ± 9.3	332.5 ± 23.0	316.6

Table 5.7. List of the tensile straining increments

Specimen	Target value of stress or strain	Maximum Stress (MPa)	Fraction of Yield Stress (%)	Total Plastic Strain (%)
T-4 (As-Irradiated)	40% σ_y	270.6	39.5	0.00
	60% σ_y	401.5	58.6	0.00
	80% σ_y	539.5	78.7	0.00
	100% σ_y	685.5	100.0	0.13
	0.5% ε_p	682.8	99.6	0.74
	1.5% ε_p	657.2	95.9	1.51
	ε_f	328.5	47.9	2.00
T-5 (500^{o}C: 1 h)	80% σ_y	497.7	78.6	0.00
	100% σ_y	633.4	100.0	0.12
	1.0% ε_p	642.4	101.4	1.10
	1.5% ε_p	636.7	100.5	1.63
	2.0% ε_p	607.8	96.0	2.11
	ε_f	471.0	74.4	2.58
T-13 (550^{o}C: 1 h)	80% σ_y	446.0	80.6	0.00
	100% σ_y	553.2	100.0	0.08
	1.0% ε_p	555.1	100.3	1.07
	2.0% ε_p	558.6	101.0	2.05
	3.0% ε_p	564.0	102.0	3.11
	4.0% ε_p	565.8	102.3	4.07
	5.0% ε_p	571.1	103.2	5.10
	7.0% ε_p	569.2	102.9	7.19
	9.0% ε_p	557.7	100.8	9.35
	ε_f	515.8	93.2	11.61
T-7 (550^{o}C: 5 h)	80% σ_y	377.4	78.0	0.00
	100% σ_y	483.7	100.0	0.13
	2.0% ε_p	502.0	103.8	2.06
	4.0% ε_p	510.5	105.6	4.04
	6.0% ε_p	512.0	105.9	6.08
	10.0% ε_p	512.6	106.0	9.47
	ε_f	470.1	97.2	12.12
T-9 (550^{o}C: 20 h)	40% σ_y	130.8	31.0	0.00
	60% σ_y	196.2	46.6	0.00
	80% σ_y	261.6	62.1	0.00
	100% σ_y	341.1	81.0	0.00
	100% σ_y	415.6	98.6	0.08
	1.0% ε_p	437.7	103.9	1.06
	2.0% ε_p	454.4	107.9	2.02
	3.0% ε_p	463.6	110.0	3.22
	5.0% ε_p	478.6	113.6	5.29
	ε_f	491.5	116.7	11.43
T-12 (550^{o}C: 20 h)	100% σ_y	316.6	100.0	0.17
	ε_f	317.0	100.1	0.96

Table 5.8. Change in the mechanical properties due to specific annealing treatments: 500°C: 1 h and 550°C: 1, 5, and 20 h.

Specimen	Yield Stress (MPa)	Maximum Stress (MPa)	Uniform Elongation (%)	Total Elongation (%)	Reduction in Area (%)
T-4 (As-Irradiated)	685.5	685.5	0.00	2.00	28.6
T-5 (500°C: 1 h)	633.4	642.4	0.95	2.58	46.8
T-13 (550°C: 1 h)	553.2	559.2	6.52	11.61	83.8
T-7 (550°C: 5 h)	483.6	512.6	6.27	12.12	84.0
T-9 (550°C: 20 h)	421.3	491.5	8.71	11.43	73.0
T-12 (550°C: 20 h)	316.6	317.0	0.69	0.96	10.1

Table 5.9. Record of crack initiation prior to tensile specimen failure.

Specimen	Plastic Strain (%)	Local Plastic Strain (%)	Number of Cracks	Total Crack Length (μm)	Number Density (#/mm^2)	Length Density (μm/mm^2)
T-4 (As-Irradiated)	0.13	1.03 ± 0.72	0	0	0	0
	0.74	4.38 ± 0.72	0	0	0	0
	1.51	NM	17	5335.0	0.47	148.19
T-5 (500^{o}C: 1 h)	0.12	1.21 ± 0.73	0	0	0	0
	1.10	5.47 ± 0.73	1	40.5	0.028	1.13
	1.63	6.33 ± 0.73	1	189.8	0.028	5.27
	2.11	10.26 ± 0.73	1	957.5	0.028	26.60
T-13 (550^{o}C: 1 h)	0.08	0.11 ± 0.78	0	0	0	0
	1.07	3.29 ± 0.78	0	0	0	0
	2.05	4.84 ± 0.78	0	0	0	0
	3.11	6.58 ± 0.78	0	0	0	0
	4.07	9.06 ± 0.78	0	0	0	0
	5.10	NM	0	0	0	0
	7.19	NM	0	0	0	0
	9.35	NM	0	0	0	0
T-7 (550^{o}C: 5 h)	0.16	1.17 ± 0.88	0	0	0	0
	2.16	4.83 ± 0.88	0	0	0	0
	4.31	8.26 ± 0.88	0	0	0	0
	6.46	14.99 ± 0.88	0	0	0	0
	9.47	NM	0	0	0	0
T-9 (550^{o}C: 20 h)	0.08	0.11 ± 0.55	0	0	0	0
	1.06	0.54 ± 0.55	0	0	0	0
	2.02	0.98 ± 0.55	0	0	0	0
	3.22	1.96 ± 0.55	0	0	0	0
	5.29	5.23 ± 0.55	0	0	0	0
T-12 (550^{o}C: 20 h)	0.17	NM	76	6453.5	2.11	179.26

Table 5.10. Change in the relative areas of fracture mode for the as-irradiated and PIA treatments: 500ºC: 1 h and 550ºC: 1, 5, and 20 h.

Specimen	% IG fracture	% Mixed fracture	% TG fracture	% Ductile fracture
T-4 (As-Irradiated)	48.40	28.62	3.62	19.41
T-5 (500ºC: 1 h)	34.86	12.82	36.58	15.74
T-13 (550ºC: 1 h)	0.00	0.00	0.00	100.00
T-7 (550ºC: 5 h)	0.00	0.00	0.00	100.00
T-9 (550ºC: 20 h)	20.60	25.04	35.28	19.08
T-12 (550ºC: 20 h)	80.95	4.58	5.67	8.79

Table 5.11. Change in the dislocation channel and interaction site densities in the failure region. Also compared is the percentage of discontinuous sites. NM signifies that the value was 'not measured,' while '-' indicates that a measurement was not possible, likely due to an insufficient number of channels.

Specimen	Plastic Strain (%)	Local Plastic Strain (%)	Channel Density (#/mm^2)	Continuous Site Density (#/mm^2)	Discontinuous Site Density (#/mm^2)	Discontinuous/ Continuous Site Ratio	Average Channel Spacing (μm)
T-4 (As-Irradiated)	0.13	1.03 ± 0.72	121 ± 19	21.2 ± 7.3	139 ± 22	6.5	14.5 ± 2.5
	0.74	4.38 ± 0.72	1337 ± 169	332 ± 67	1747 ± 229	5.3	8.7 ± 0.8
T-5 (500^{o}C: 1 h)	0.12	1.21 ± 0.73	3.5 ± 2.9	0.0 ± 0.0	6.9 ± 5.8	-	-
	1.10	5.47 ± 0.73	1903 ± 246	239 ± 99	3019 ± 424	12.7	6.2 ± 0.8
	1.63	6.33 ± 0.73	2462 ± 232	307 ± 78	3454 ± 553	11.2	5.7 ± 1.0
	2.11	10.26 ± 0.73	2718 ± 297	325 ± 116	4239 ± 553	13.1	5.3 ± 0.6
T-13 (550^{o}C: 1 h)	0.08	0.11 ± 0.78	180 ± 48	42 ± 18	230 ± 66	5.5	-
	1.07	3.29 ± 0.78	2448 ± 228	398 ± 68	3540 ± 520	8.9	5.8 ± 0.5
	2.05	4.84 ± 0.78	2602 ± 153	451 ± 51	3618 ± 225	8.0	5.2 ± 0.5
	3.11	6.58 ± 0.78	2737 ± 274	417 ± 48	4010 ± 446	9.6	4.6 ± 0.4
	4.07	9.06 ± 0.78	2869 ± 206	427 ± 95	4201 ± 306	9.8	4.4 ± 0.3
	5.10	NM	2856 ± 192	405 ± 65	4105 ± 296	10.1	NM
	7.19*	NM	5099 ± 344	765 ± 115	7365 ± 498	9.6	NM
T-7 (550^{o}C: 5 h)	0.16	1.17 ± 0.88	99 ± 38	14 ± 12	151 ± 58	10.9	-
	2.16	4.83 ± 0.88	2137 ± 220	262 ± 69	3289 ± 332	12.6	5.4 ± 0.5
	4.31	8.26 ± 0.88	2617 ± 376	405 ± 132	3891 ± 579	9.6	4.7 ± 0.4
	6.46*	14.99 ± 0.88	3657 ± 494	438 ± 79	5588 ± 736	12.8	3.9 ± 0.3
T-9 (550^{o}C: 20 h)	0.09	0.11 ± 0.55	8.8 ± 5.5	0.0 ± 0.0	16 ± 10	-	-
	1.10	0.54 ± 0.55	132 ± 46	21 ± 13	190 ± 61	9.1	-
	2.02	0.98 ± 0.55	174 ± 76	44 ± 38	260 ± 81	5.9	8.6 ± 0.8
	3.22	1.96 ± 0.55	499 ± 115	100 ± 49	694 ± 132	6.9	6.4 ± 0.5
	5.29	5.23 ± 0.55	585 ± 136	107 ± 56	835 ± 156	7.8	5.8 ± 0.5

*Specimens T-7 and T-13 were observed to severely neck at ~6% ε_p, thus the sharp increase in dislocation channel density is believed to be a direct factor of the necking and does not accurately represent the changing localized deformation with strain.

Table 5.12. Prediction of the yield stress for 4-point bend specimens following PIA based on change in hardness. The yield stress was converted from the bend yield load as described in Section 4.4.3.

Specimen	Measured Hardness (H_v)	Predicted Yield Stress (MPa)	Yield Stress (MPa)
4-B (As-Irradiated)	348.0 ± 9.6	679.8 ± 23.8	726.9
10-B1 (As-Irradiated)	342.4 ± 9.7	667.3 ± 24.0	617.1
9-C (500°C: 1 h)	326.7 ± 13.7	628.5 ± 33.9	585.7
7-B (550°C: 5 h)	261.7 ± 8.7	467.9 ± 21.5	496.8
12-B1 (550°C: 20 h)	203.1 ± 7.7	323.1 ± 19.0	407.9

Table 5.13. List of the utilized four-point bend straining increments

Specimen	Target value of stress or strain	Increment Yield Load (N)	Fraction of Specimen Yield Load (%)	Plastic Deflection (um)	Total Plastic Strain (%)
4-B (As-Irradiated)	40% σ_y	231.8	36.7	-	-
	60% σ_y	351.4	55.6	-	-
	80% σ_y	469.3	74.3	1.57 ± 1.53	0.11
	100% σ_y	631.8	100.0	5.04 ± 1.48	0.38
	1.0% ε_p	627.3	99.3	16.38 ± 1.47	1.23
	2.0% ε_p	632.7	100.1	28.26 ± 1.50	2.11
	3.0% ε_p	613.6	97.1	38.53 ± 1.52	2.88
	4.0% ε_p	645.5	102.2	54.06 ± 1.60	4.04
	5.0% ε_p	593.0	93.9	69.23 ± 1.79	5.18
	6.0% ε_p	512.0	81.0	85.50 ± 1.80	6.01
	7.0% ε_p	467.5	74.0	104.6 ± 1.88	7.25
10-B1 (As-Irradiated)	1.0% ε_p	536.4	100.0	12.73 ± 1.49	0.95
	3.0% ε_p	568.2	105.9	45.42 ± 1.53	3.40
	5.0% ε_p	627.3	116.9	69.35 ± 1.63	5.19
	10.0% ε_p	636.4	118.6	162.07 ± 2.21	10.77
9-C (500^{o}C: 1 h)	2.0% ε_p	509.1	100.0	24.46 ± 1.52	1.83
	5.0% ε_p	540.9	106.3	63.75 ± 1.73	4.77
	10.0% ε_p	568.2	111.6	160.52 ± 2.48	10.68
7-B (550^{o}C: 5 h)	2.0% ε_p	431.8	100.0	31.68 ± 1.47	2.37
	5.0% ε_p	509.1	117.9	63.23 ± 1.71	4.73
	10.0% ε_p	477.3	110.5	152.80 ± 2.50	10.22
12-B1 (550^{o}C: 20 h)	2.0% ε_p	354.5	100.0	35.88 ± 1.70	2.68

Table 5.14. Four-point bend crack initiation with plastic strain and annealing treatments.

Specimen	Plastic Strain (%)	Number of Cracks	Total Crack Length (μm)	Number Density (#/mm^2)	Length Density (μm/mm^2)
4-B (As-Irradiated)	0.38	0	0	0	0
	1.23	0	0	0	0
	2.11	0	0	0	0
	2.88	0	0	0	0
	4.04	0	0	0	0
	5.18	2	40.1	1.14	22.93
	6.01	4	249.3	2.29	142.43
	7.25	9	946.4	5.14	540.82
10-B1 (As-Irradiated)	0.95	0	0	0	0
	3.40	0	0	0	0
	5.19	0	0	0	0
	10.77	15	2385.6	8.57	1363.20
9-C (500^{o}C: 1 h)	1.83	0	0	0	0
	4.77	0	0	0	0
	10.68	0	0	0	0
7-B (550^{o}C: 5 h)	2.37	0	0	0	0
	4.73	0	0	0	0
	10.22	0	0	0	0
12-B1 (550^{o}C: 20 h)	1.83	4	489.0	2.29	279.43

Table 5.15. Change in the dislocation channel density, average channel spacing, fraction of channel area with annealing condition and strain for the four-point bend specimens. NM signifies that the selected characterization was 'not measured' at that strain level.

Specimen	Plastic Strain (%)	Channel Density (#/mm^2)	Average Channel Spacing (μm)	Fraction of Channeled Area (%)
4-B (As-Irradiated)	0.38	537 ± 43	13.9 ± 1.3	51.47
	1.23	1240 ± 100	11.9 ± 1.4	68.43
	2.11	1397 ± 112	11.2 ± 1.1	77.95
	2.88	1822 ± 147	10.2 ± 1.1	78.11
	4.04	2139 ± 172	8.9 ± 0.9	79.23
	5.18	NM	8.2 ± 0.8	NM
	6.01	NM	7.8 ± 0.7	NM
	7.25	NM	7.2 ± 0.6	NM
10-B1 (As-Irradiated)	0.95	1029 ± 83	11.8 ± 1.3	72.40
	3.4	1851 ± 149	10.3 ± 1.1	82.68
	5.19	2344 ± 189	8.0 ± 0.9	84.76
	10.77	NM	7.1 ± 0.6	NM
9-C (500^{o}C: 1 h)	1.83	1062 ± 85	8.5 ± 1.0	51.45
	4.77	2113 ± 170	6.0 ± 0.8	66.68
	10.68	NM	5.6 ± 0.5	NM
7-B (550^{o}C: 5 h)	2.37	1760 ± 142	6.7 ± 0.8	72.06
	4.73	2329 ± 187	6.1 ± 0.7	76.54
	10.22	NM	4.7 ± 0.3	NM
12-B1 (550^{o}C: 20 h)	2.68	914 ± 74	7.1 ± 0.7	43.40

Table 5.16. Change in the peak shear stress for an array of various obstacles as simulated in LAMMPS.

Obstacle Type	Loop Orientation/ Cluster Shape	Diameter (nm)	Nickel (at.%)	Peak Shear Stress (MPa)
None	Friction Stress	--	12	181.5 ± 9.2
Dislocation Loop	$[1\bar{1}1]$	3	12	395.6 ± 9.7
		5	12	516.7± 16.9
		7	12	589.4 ± 15.6
	$[\bar{1}\bar{1}1]$	3	12	361.3 ± 20.5
		5	12	350.8 ± 43.8
		7	12	343.3 ± 30.4
	$[\bar{1}11]$	3	12	306.7 ± 28.0
		5	12	359.0 ± 44.8
		7	12	519.4 ± 55.9
Solute Cluster	Spherical	3	50	217.0 ± 13.0
		4	50	240.1 ± 20.7
		5	25	212.7 ± 21.2
			50	249.9 ± 23.3
			75	264.0 ± 18.8
		6	50	251.0 ± 23.3
		7	25	222.8 ± 20.8
			50	249.5 ± 13.1
			75	275.7 ± 21.2
Loop-Cluster Combined Defect	$[1\bar{1}1]$ + Spherical	3	50	441.2 ± 33.9
		5	25	530.9 ± 22.8
			50	557.0 ± 29.4
			75	567.2 ± 26.5
		7	50	638.8 ± 25.8
	$[\bar{1}\bar{1}1]$ + Spherical	5	50	309.5 ± 20.4
	$[\bar{1}11]$ + Spherical	5	50	407.0 ± 24.8

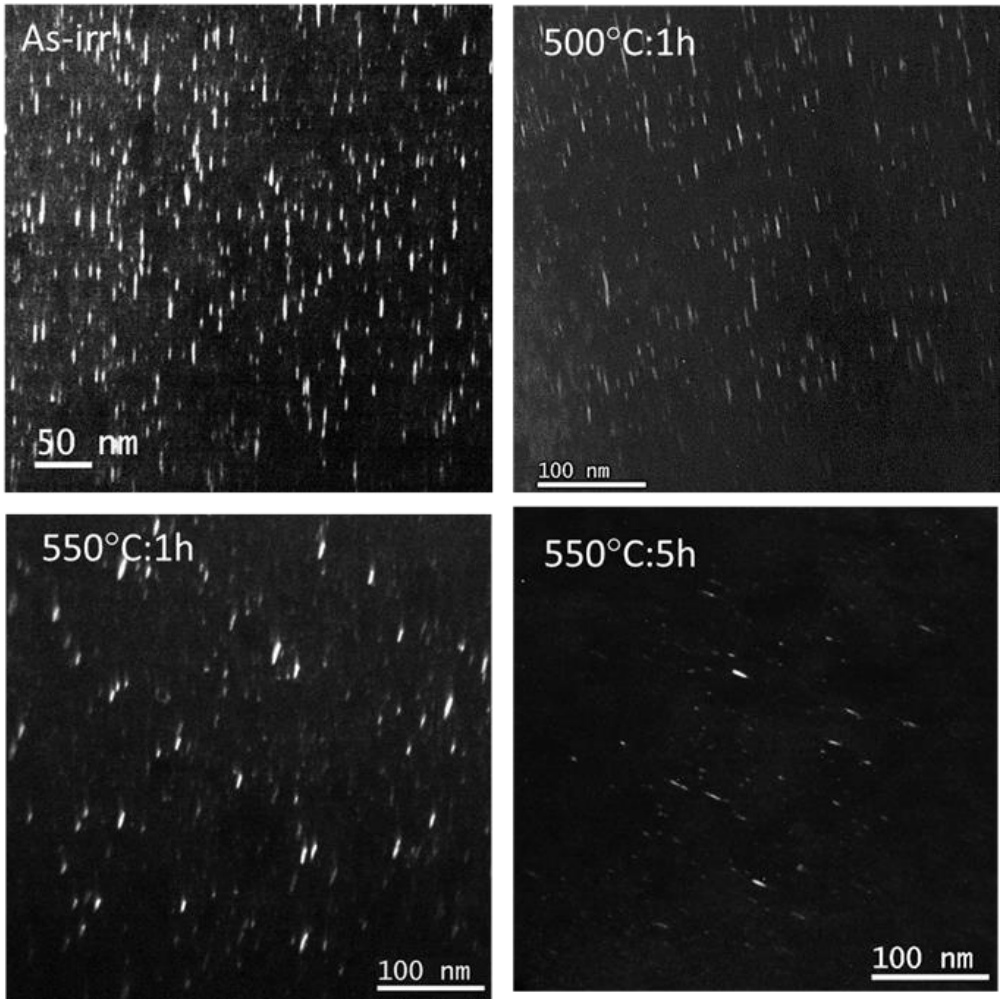

Figure 5.1. Rel-rod dark field TEM image showing the faulted dislocation loops in 304L stainless steel irradiated to 5.9 dpa in BWR after various post-irradiation annealing conditions.

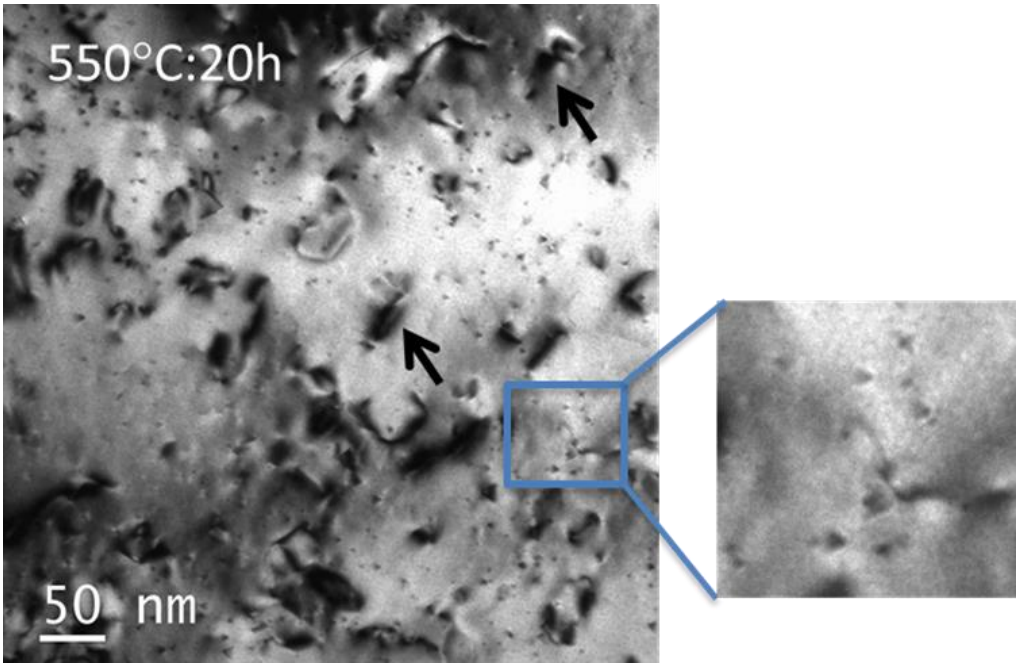

Figure 5.2. Dislocation loops (as indicated by arrows) and small stacking fault tetrahedrons (as shown in the insert) in 304L stainless steel after post-irradiation annealing at 550°C: 20 h.

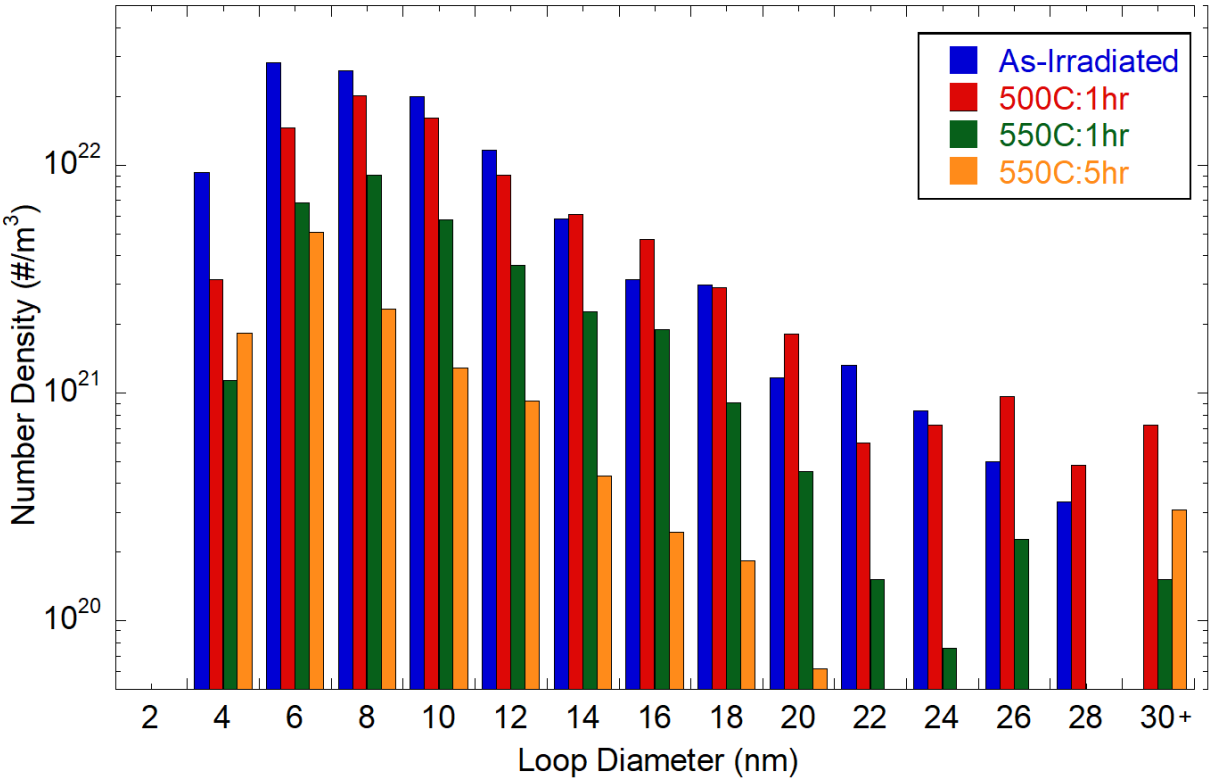

Figure 5.3. Comparison of size distribution of faulted dislocation loops in 304L SS irradiated to 5.9 dpa in BWR and after various post-irradiation annealing conditions.

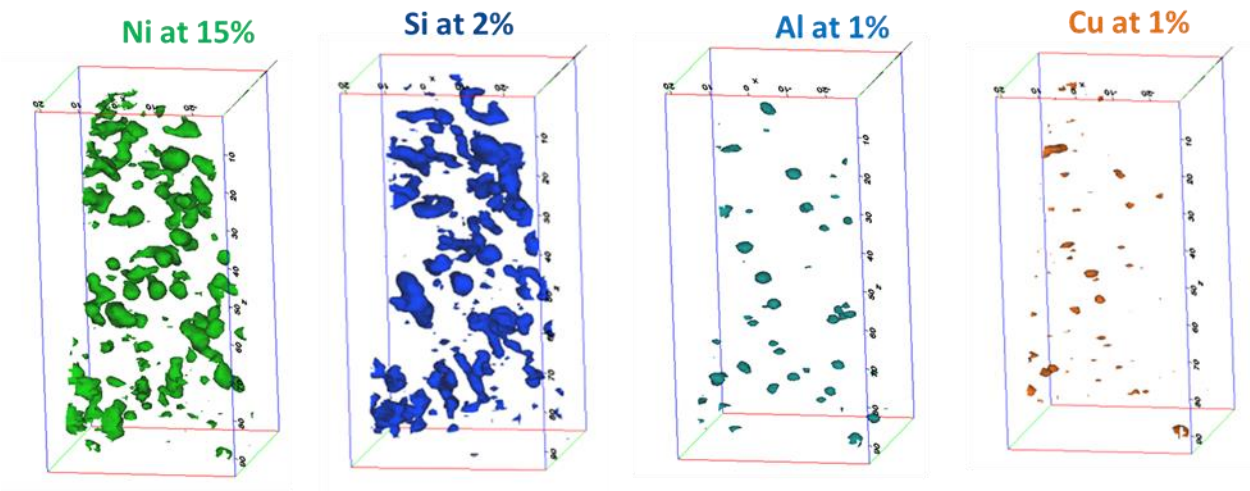

Figure 5.4. Ni-Si and Al-Cu clusters as observed in 304L stainless steel irradiated to 5.9 dpa in BWR. Clusters are shown using isoconcentration surface plots from APT atom maps.

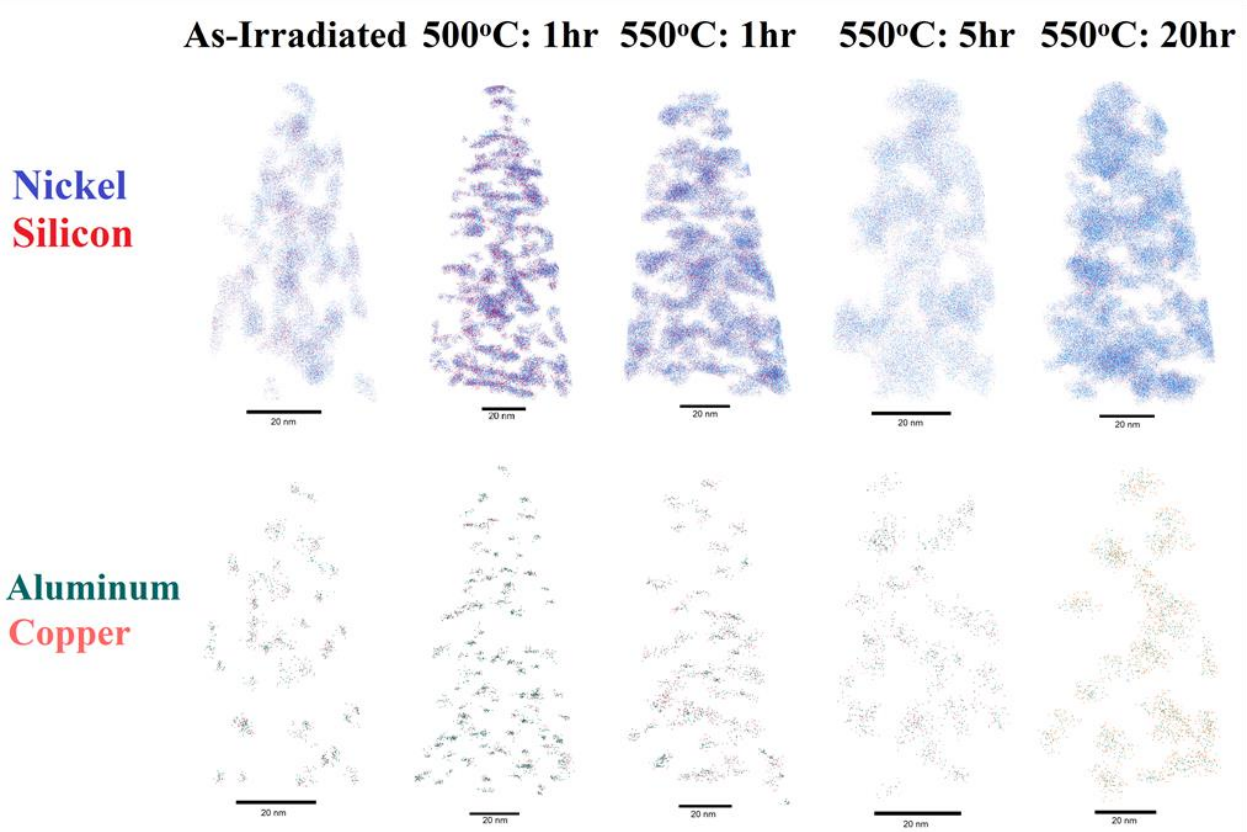

Figure 5.5. Evolution of Ni-Si and Al-Cu clusters in 304L stainless steel irradiated to 5.9 dpa in BWR after various post-irradiation annealing conditions. All scale bars are 20 nm.

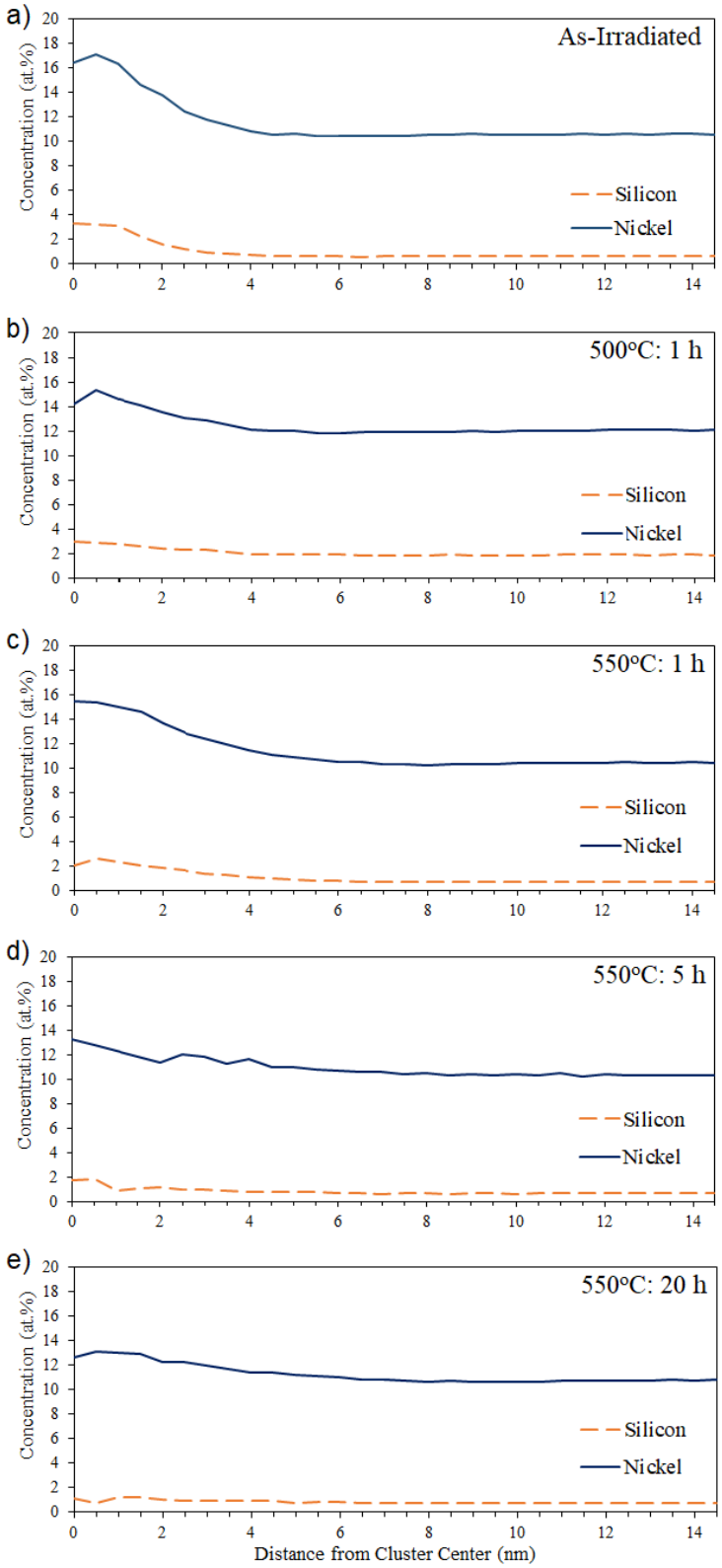

Figure 5.6. Normalized radial concentration profiles for all the Ni-Si solute clusters characterized by APT: a) as-irradiated, b) 500°C: 1 h, c) 550°C: 1 h, d) 550°C: 5 h, e) 550°C: 20 h,

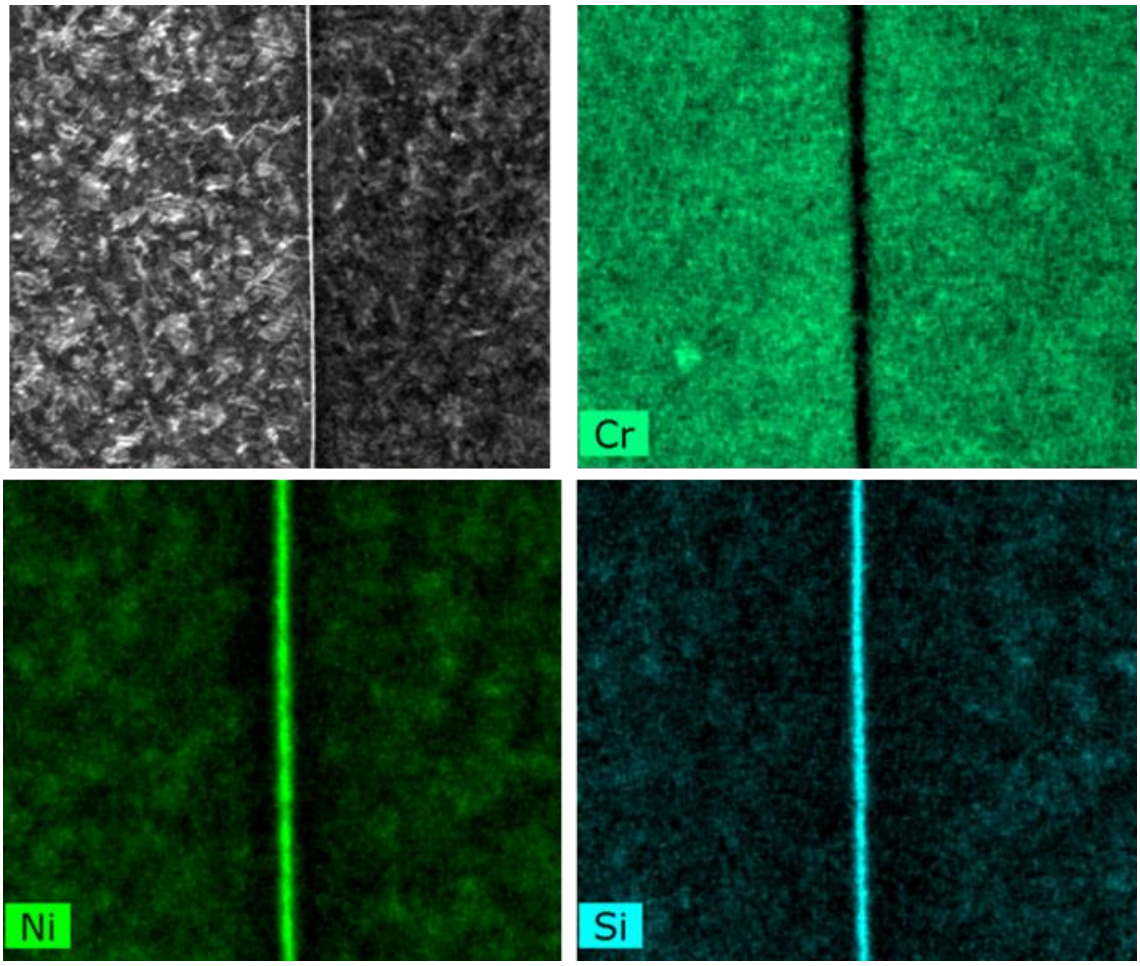

Figure 5.7. Radiation-induced segregation in 304L stainless steel irradiated to 5.9 dpa in BWR as revealed by ChemiSTEM image. Depletion of Cr and enrichment of Ni and Si are evident.

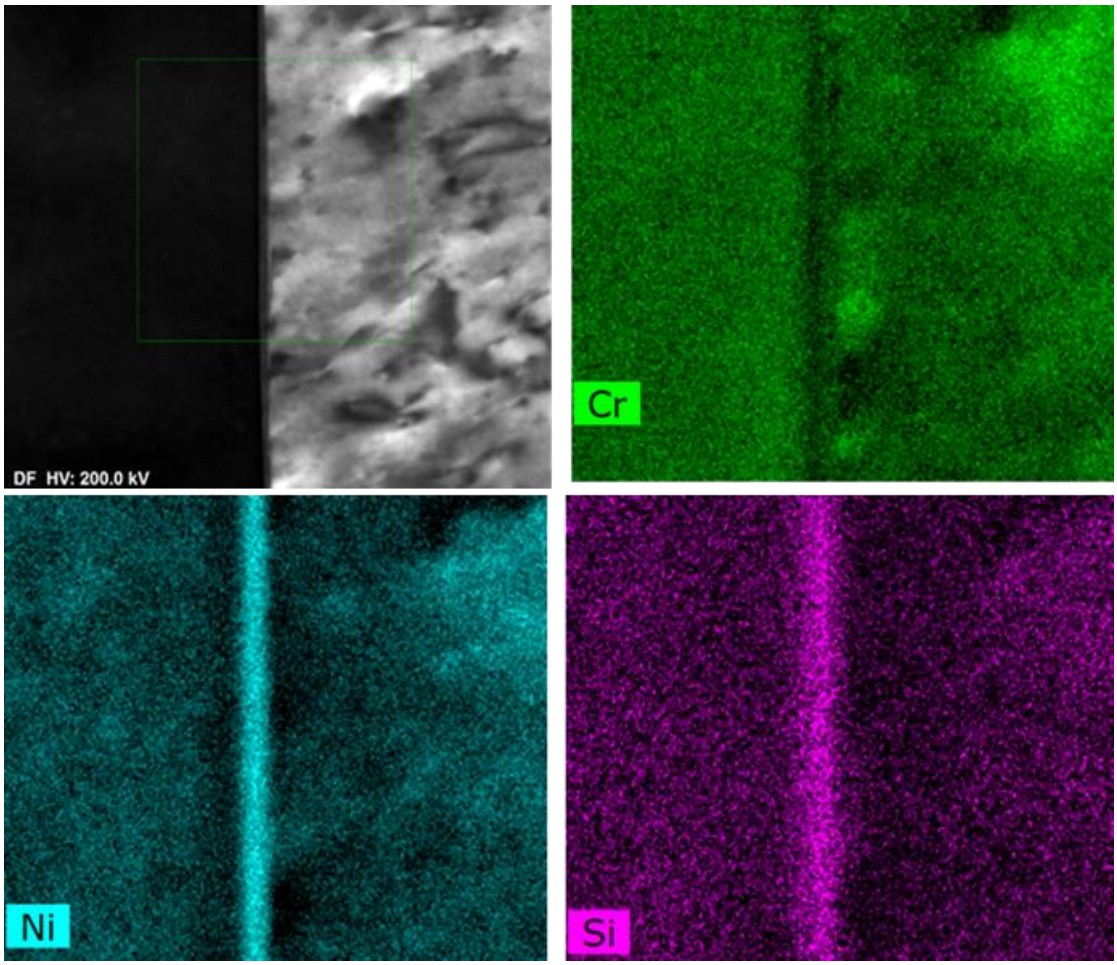

Figure 5.8. Radiation-induced segregation in 304L stainless steel irradiated to 5.9 dpa in BWR and post-irradiation annealing at 550°C: 20 h as revealed by ChemiSTEM image. Depletion of Cr and enrichment of Ni and Si are still evident.

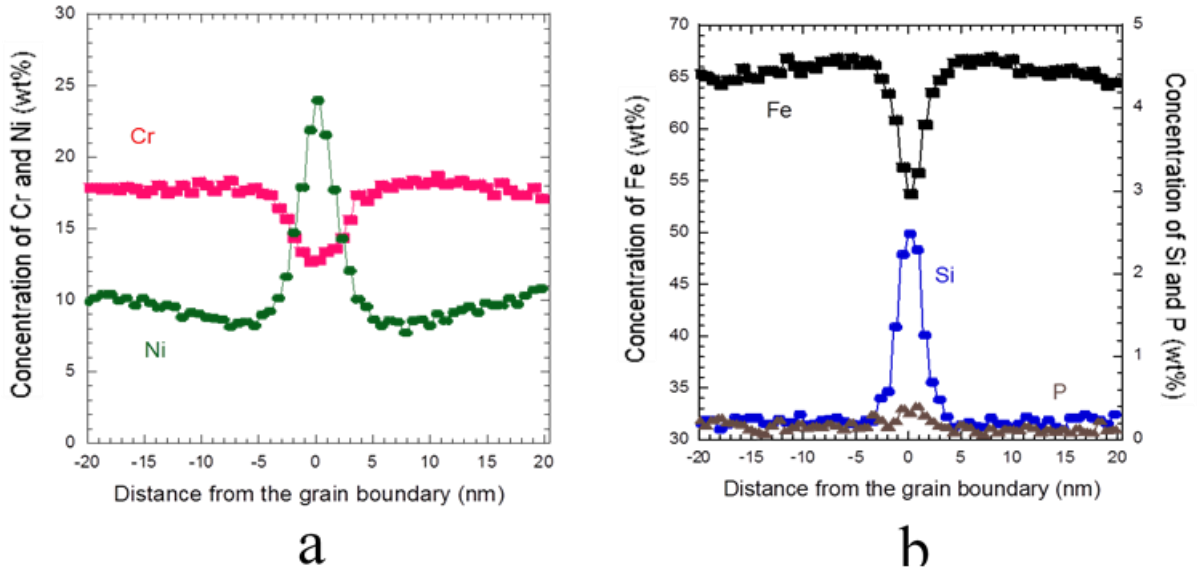

Figure 5.9. Composition profile across the grain boundary in 304L stainless steel irradiated to 5.9 dpa in BWR for (a) Ni and Cr, and (b) Fe, Si and P.

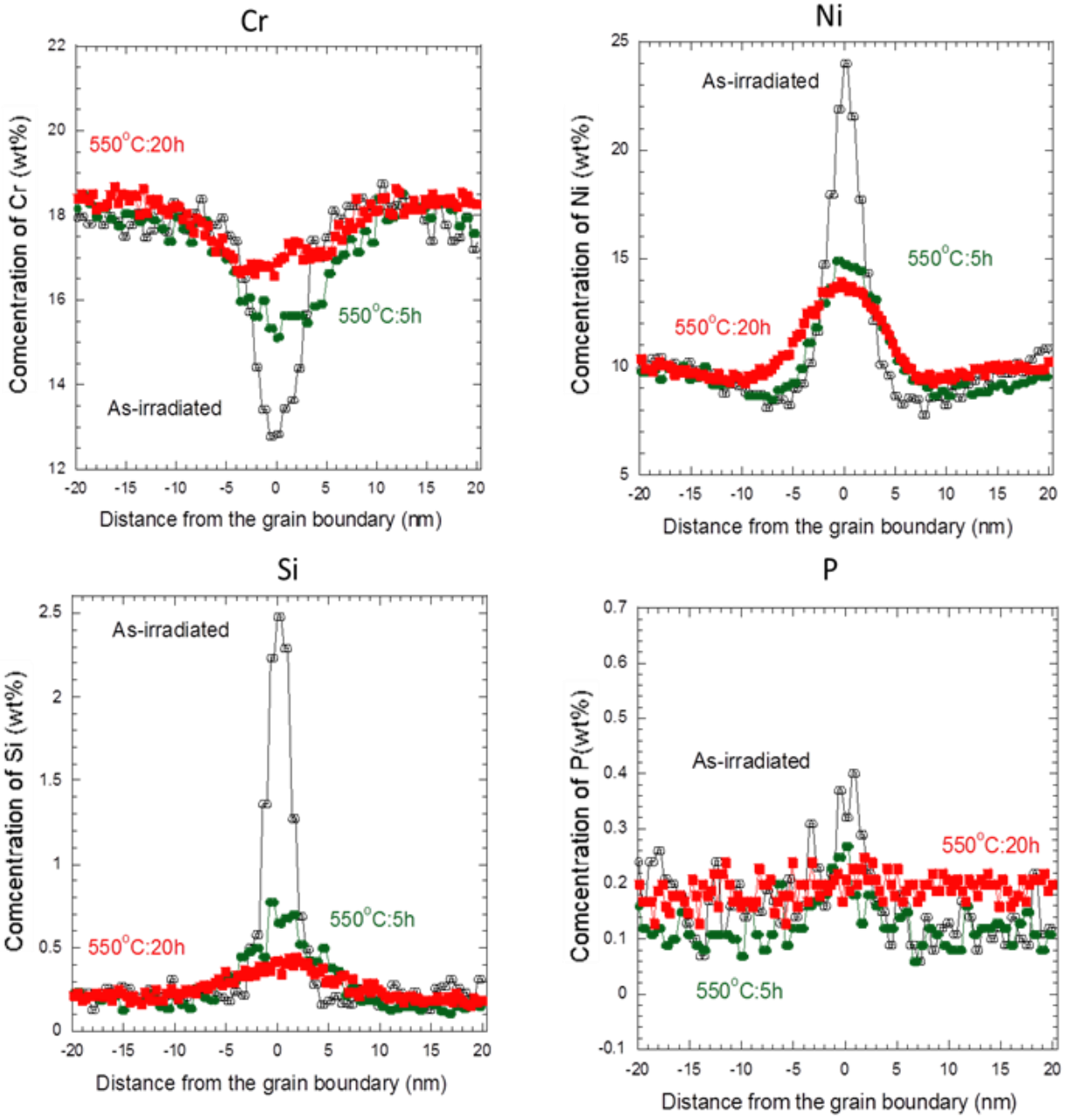

Figure 5.10. Effect of post-irradiation annealing on the segregation profiles of Cr, Ni, Si, and P in 304L stainless steel irradiated to 5.9 dpa in BWR.

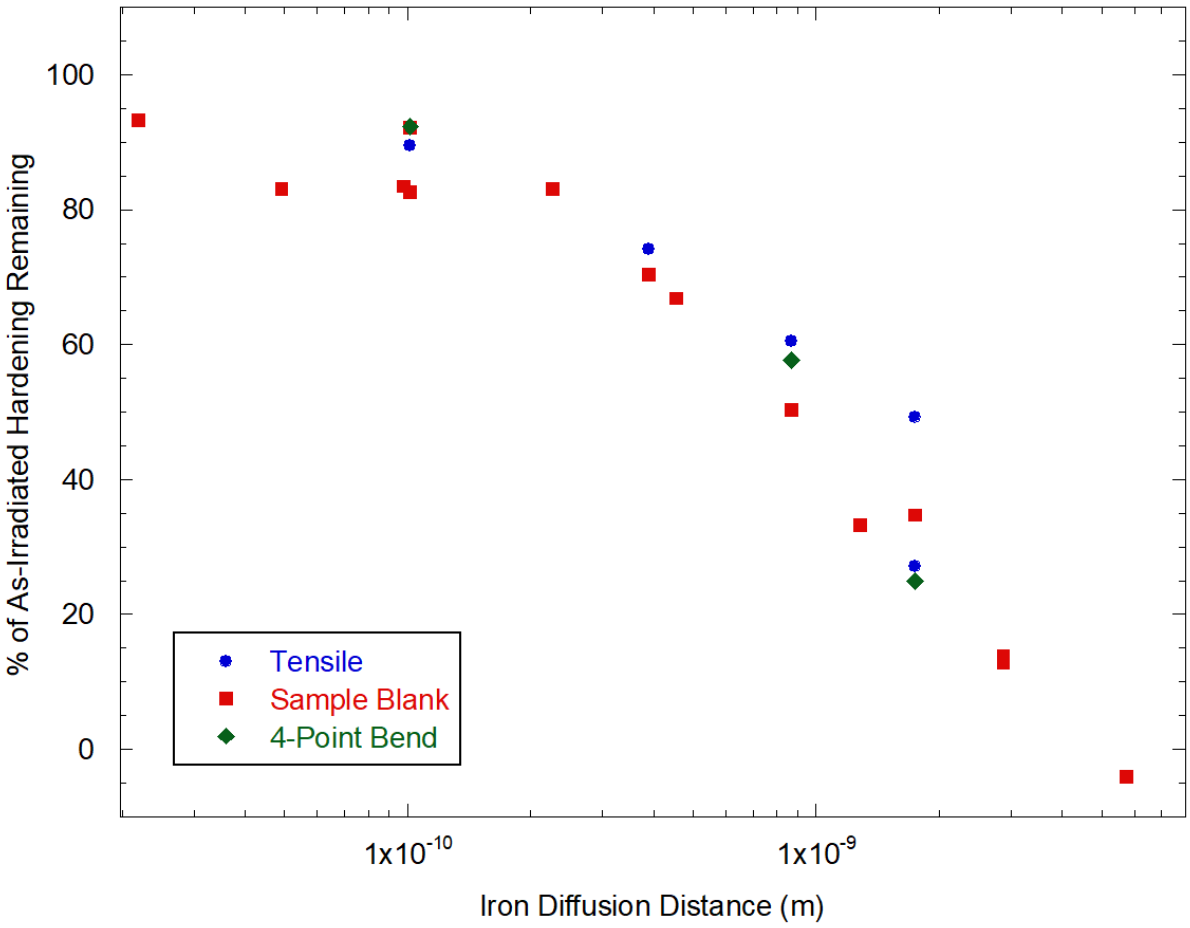

Figure 5.11. Comparison of the residual hardening following PIA treatments for the varying specimen types.

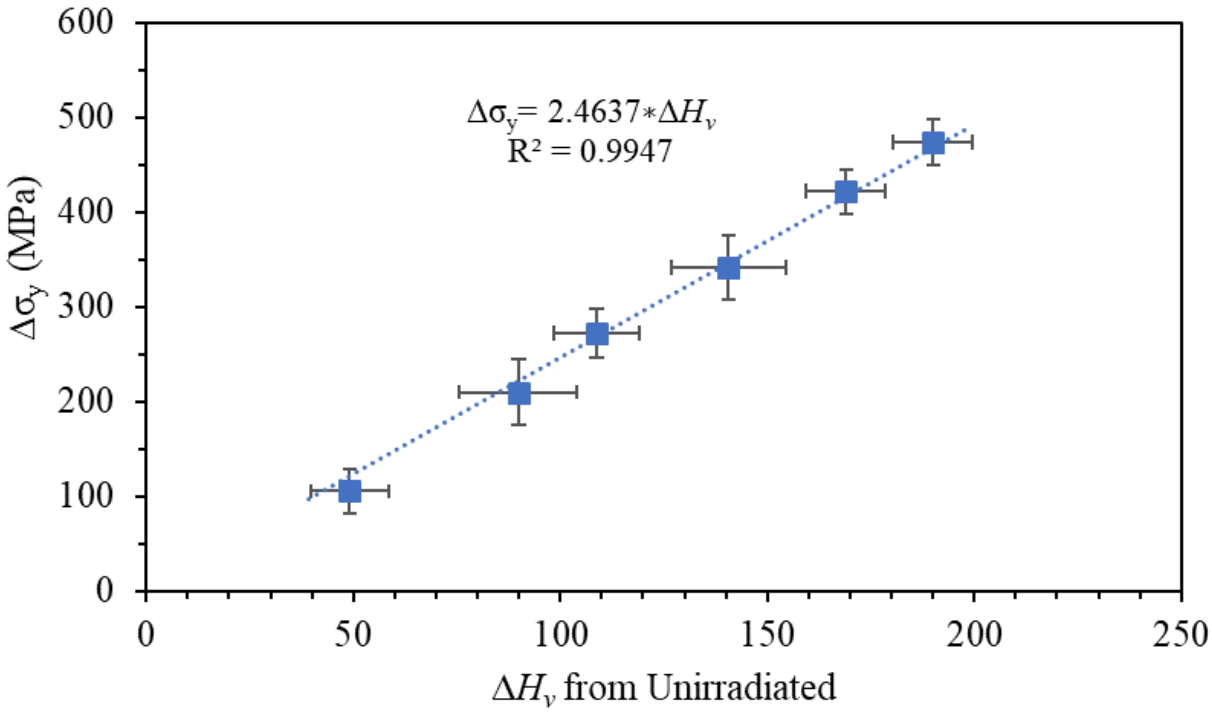

Figure 5.12. Comparison between the measured change in yield stress and the change in hardness from the base unirradiated condition (σ_y = 211.5 MPa, H_v = 157.95) used to predict the yield stress.

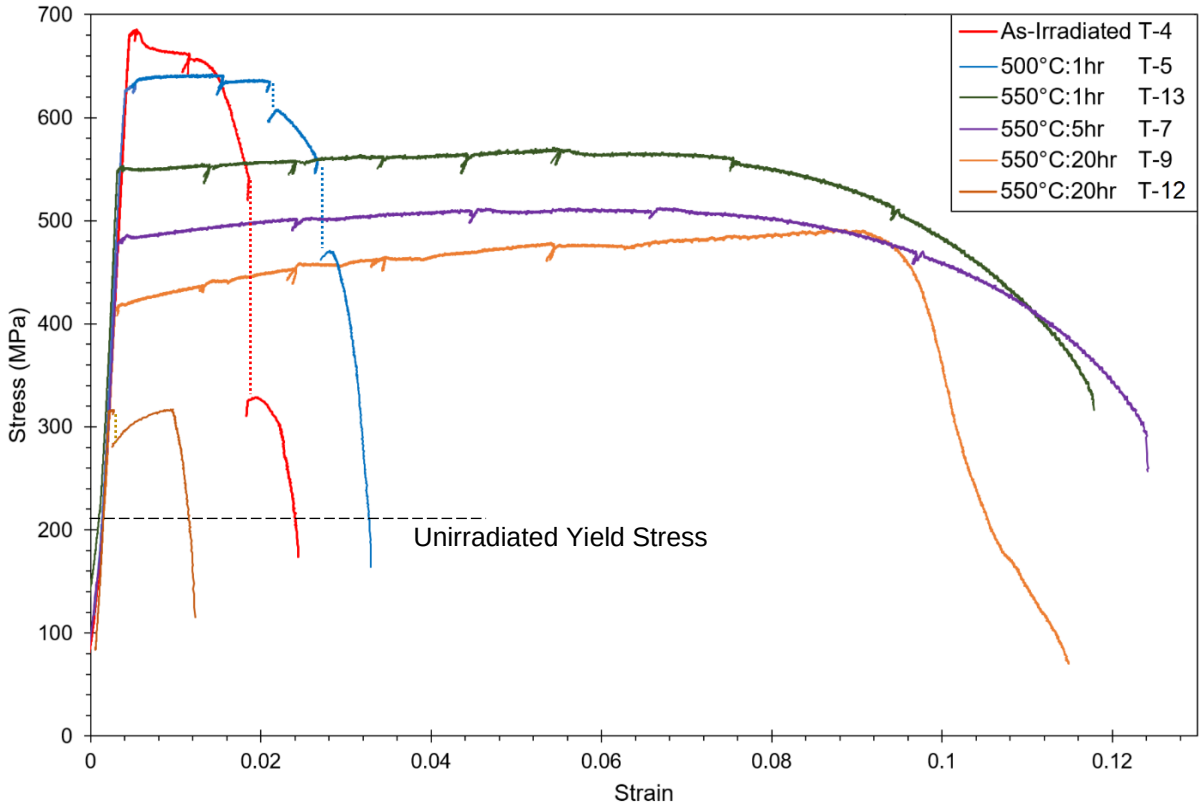

Figure 5.13. Change in the stress strain behavior because of specific annealing treatments: 500°C: 1 h, 550°C: 1 h, 550°C: 5 h, and 550°C: 20 h. Note the large difference in behavior between the two 550°C: 20 h specimens, T-9 and T-12.

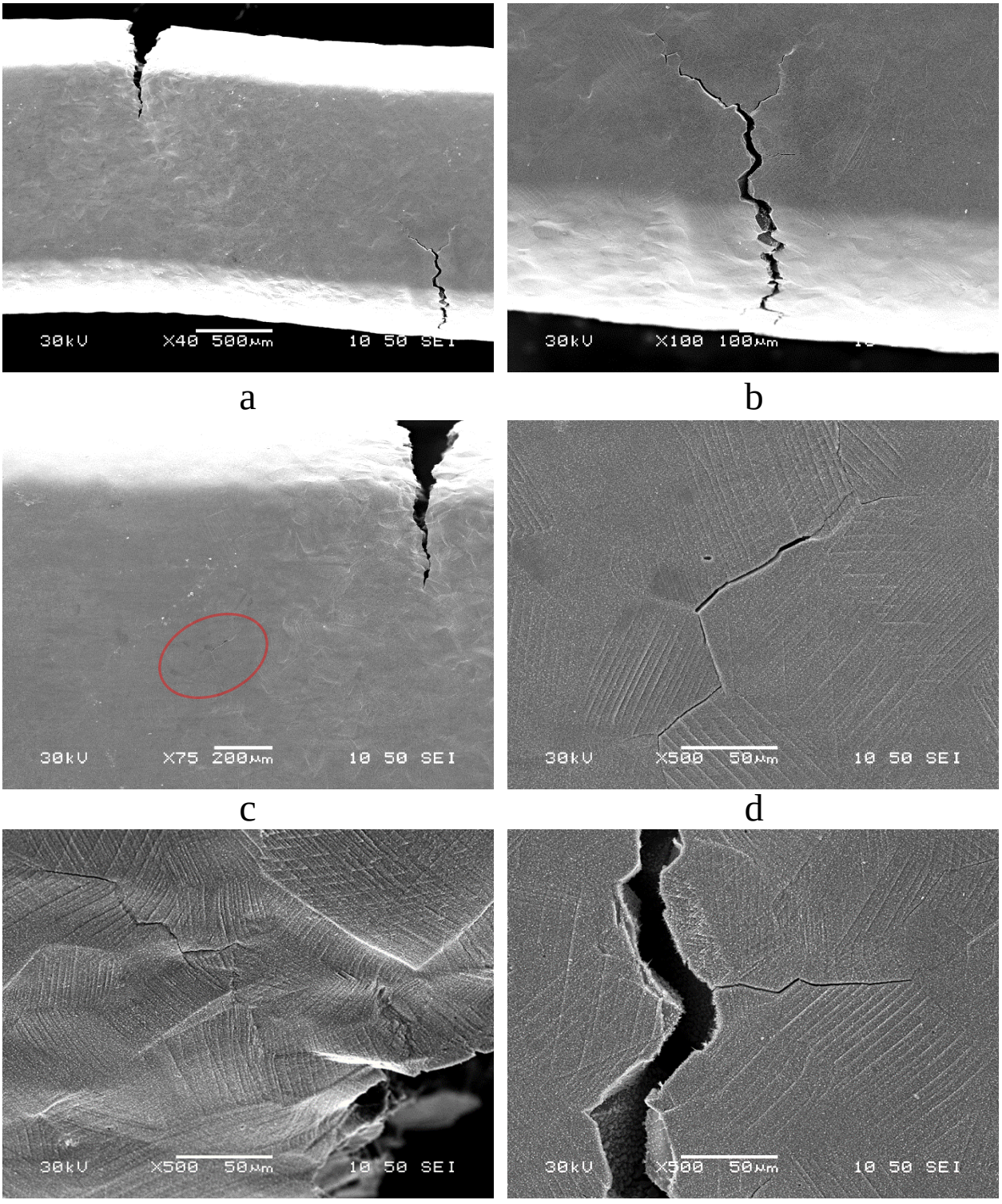

Figure 5.14. Crack initiation in T-4 (as-irradiated) at 1.51% ε_p: a) an overview of the primary and secondary cracks, b) closer view of the secondary crack, c) location of a tertiary crack, d) higher magnification view of tertiary crack, e) and f) images of auxiliary cracks near the primary and secondary cracks.

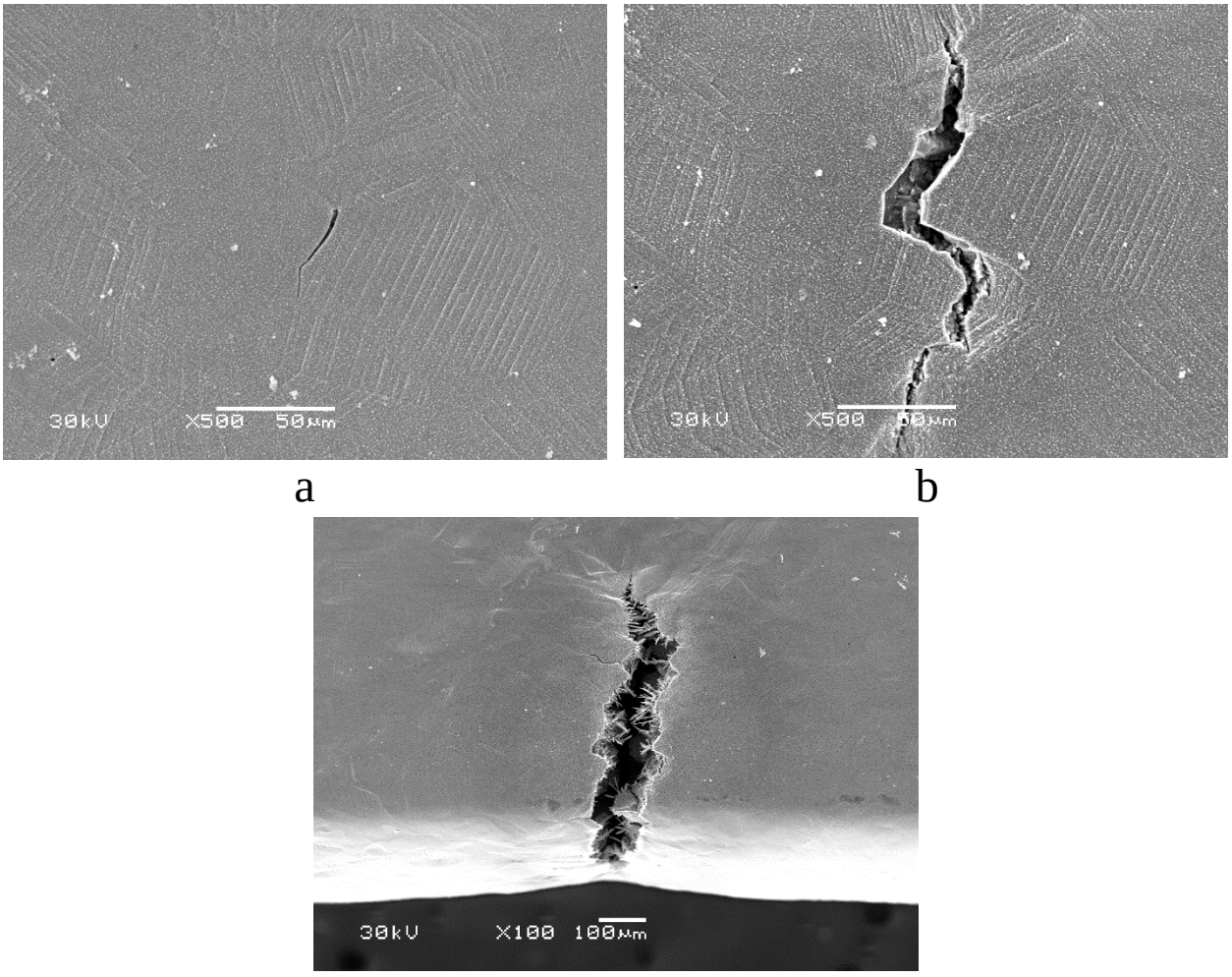

Figure 5.15. Crack initiation in T-5 (500°C: 1 h): a) initiation site identified at 1.10% ε_p, b) crack growth after 1.63% ε_p, c) additional crack growth at 2.11% ε_p, no further crack initiation sites were observed.

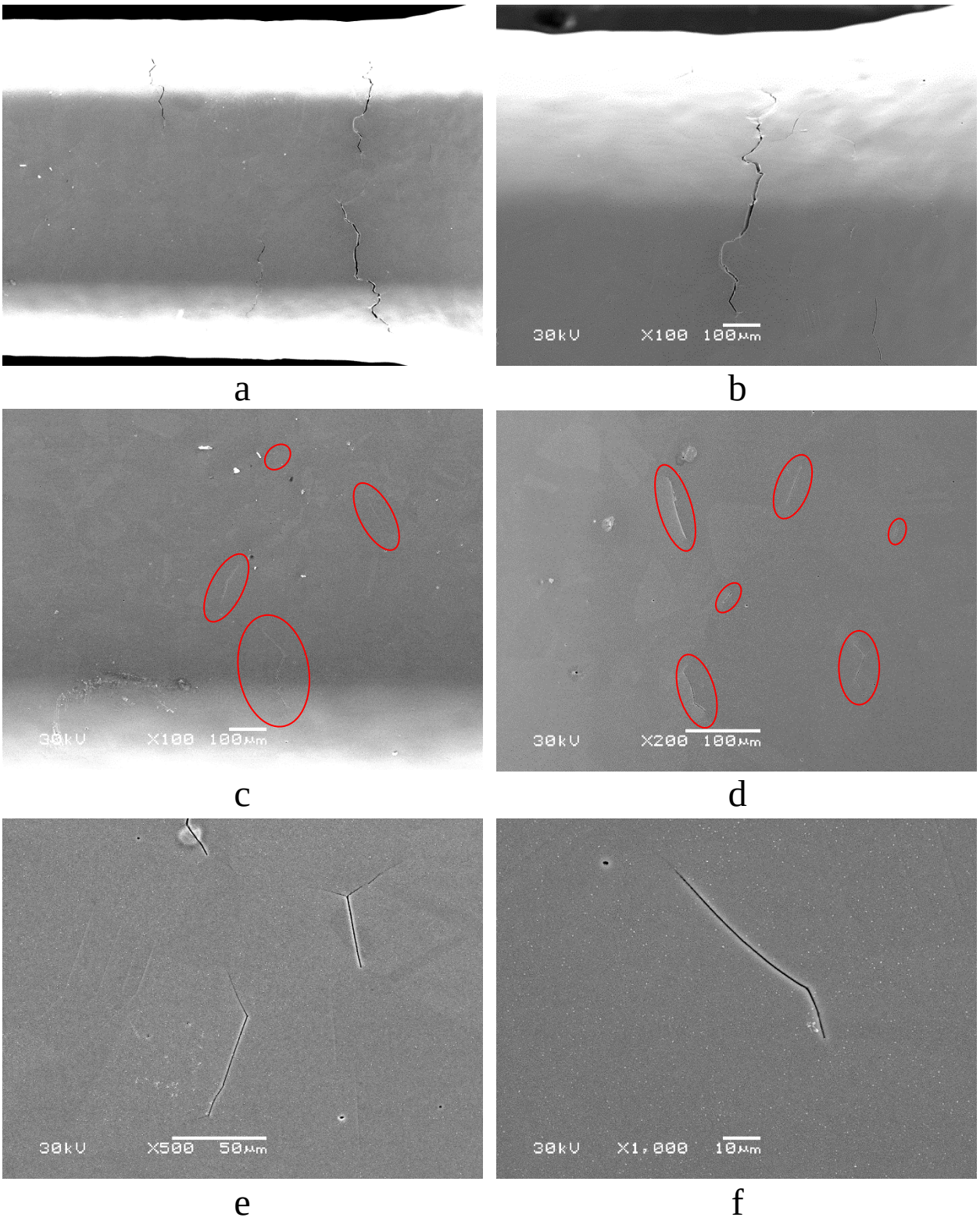

Figure 5.16. Cracking in T-12 (550ºC: 20 h) at 0.17% ε_p: a) Overview of the highest region of crack initiation, b) higher magnification view of a larger crack, c) and d) overview of regions with multiple small crack initiation sites circled in red, e) and f) higher magnification view of crack initiation sites.

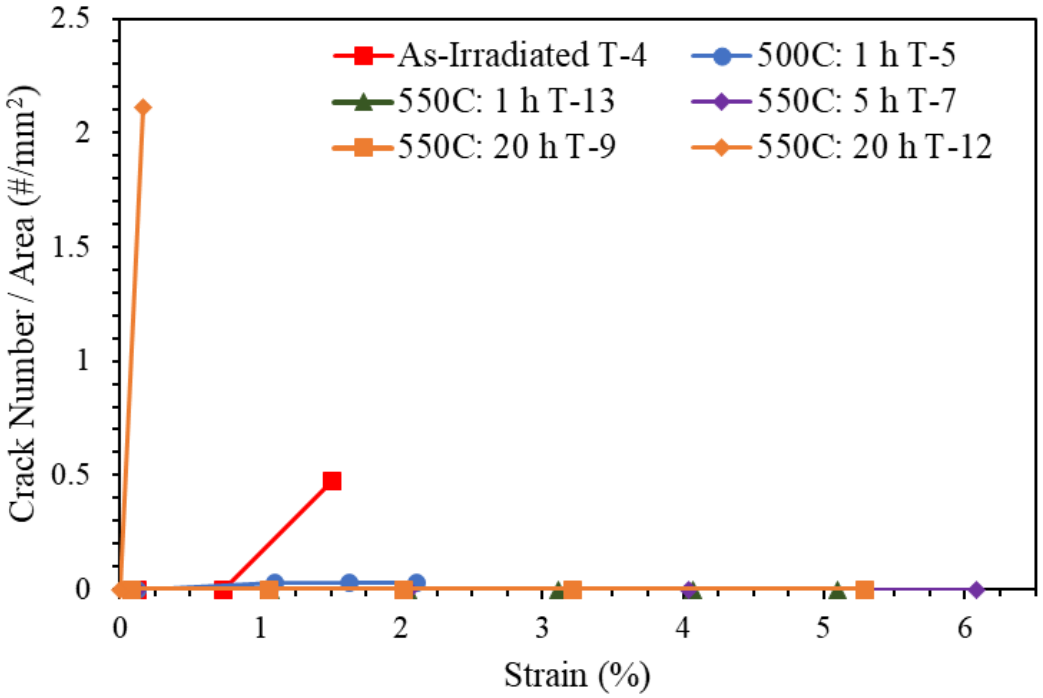

Figure 5.17. Crack number density as a function of annealing condition and bulk specimen strain for the tensile specimens.

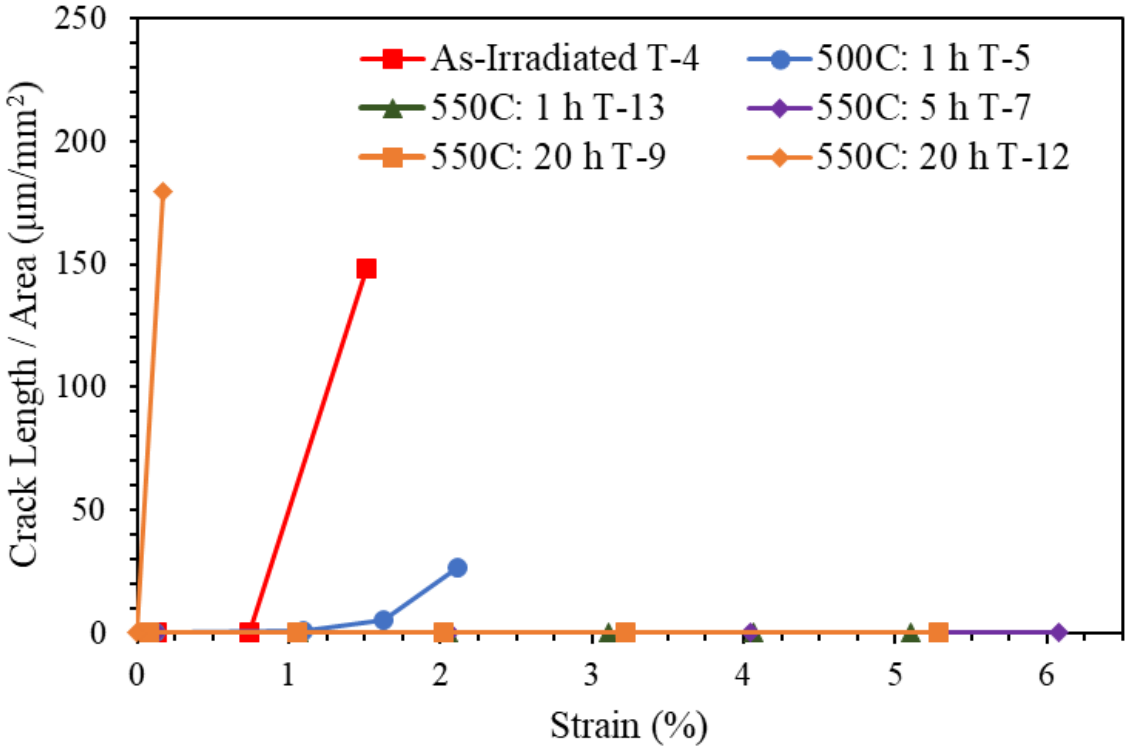

Figure 5.18. Total crack length density on the specimen surface as a function of the annealing condition and bulk specimen strain for the tensile specimens.

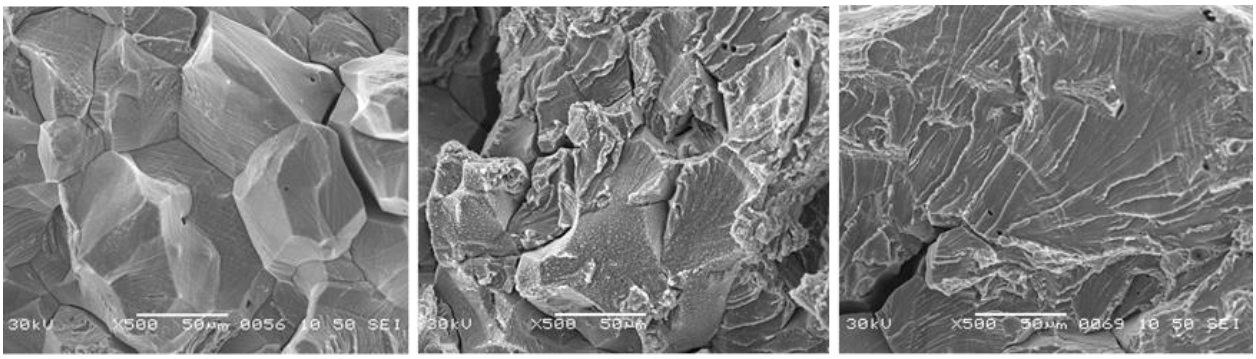

a b c

Figure 5.19. Example images from the T-5 (PIA 500°C: 1 h) specimen of the three primary modes of failure that were observed during the crack growth of the as-irradiated and PIA specimens: a) intergranular, b) mixed intergranular-transgranular, c) transgranular.

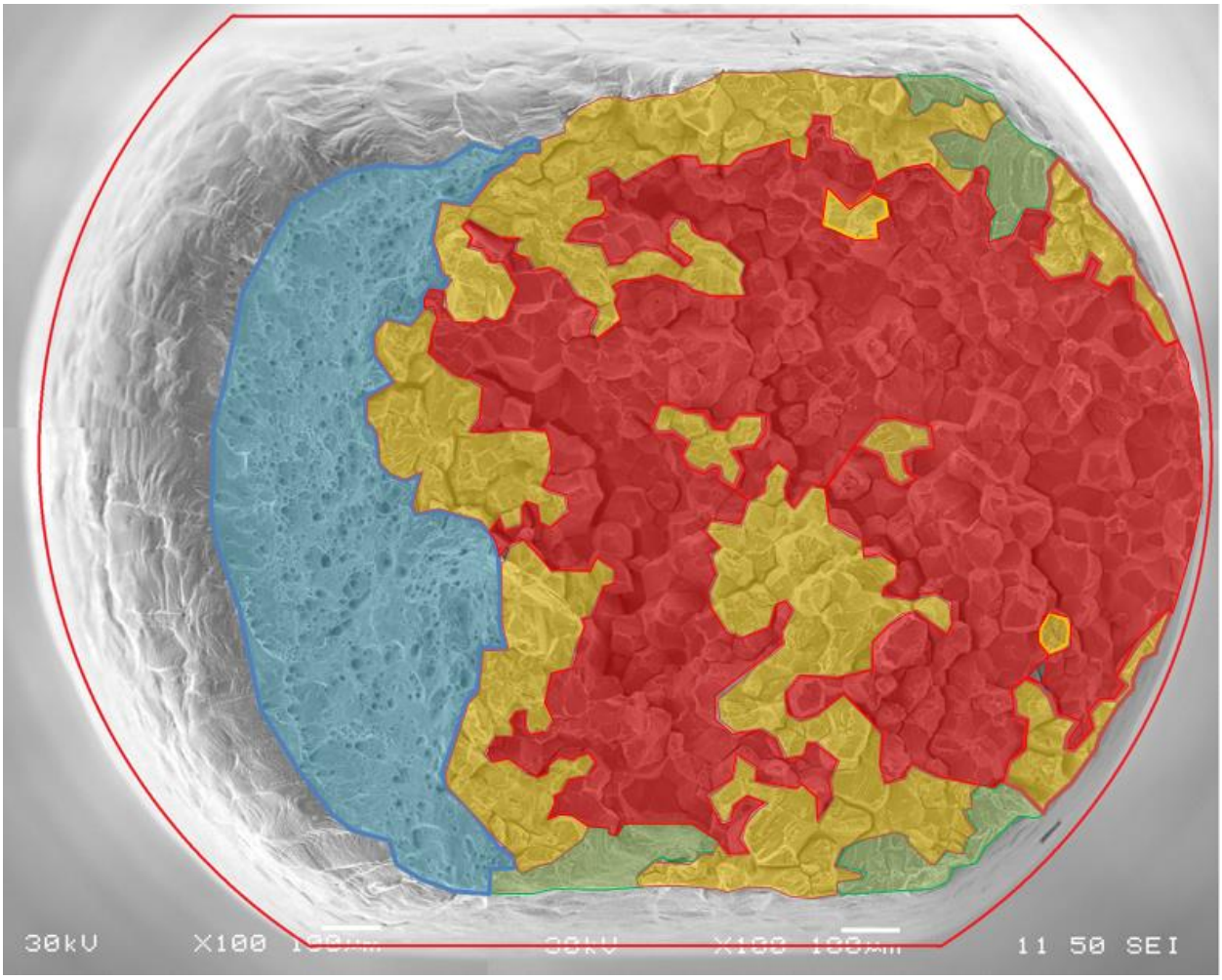

Figure 5.20. Final fracture surface of the CERT tensile specimen: T-4, as-irradiated. Red is utilized to represent areas of intergranular failure, while green shows regions of transgranular propagation. Orange represents mixed IG/TG, while blue is ductile fracture. The outer red ring displays the original cross section of the specimen.

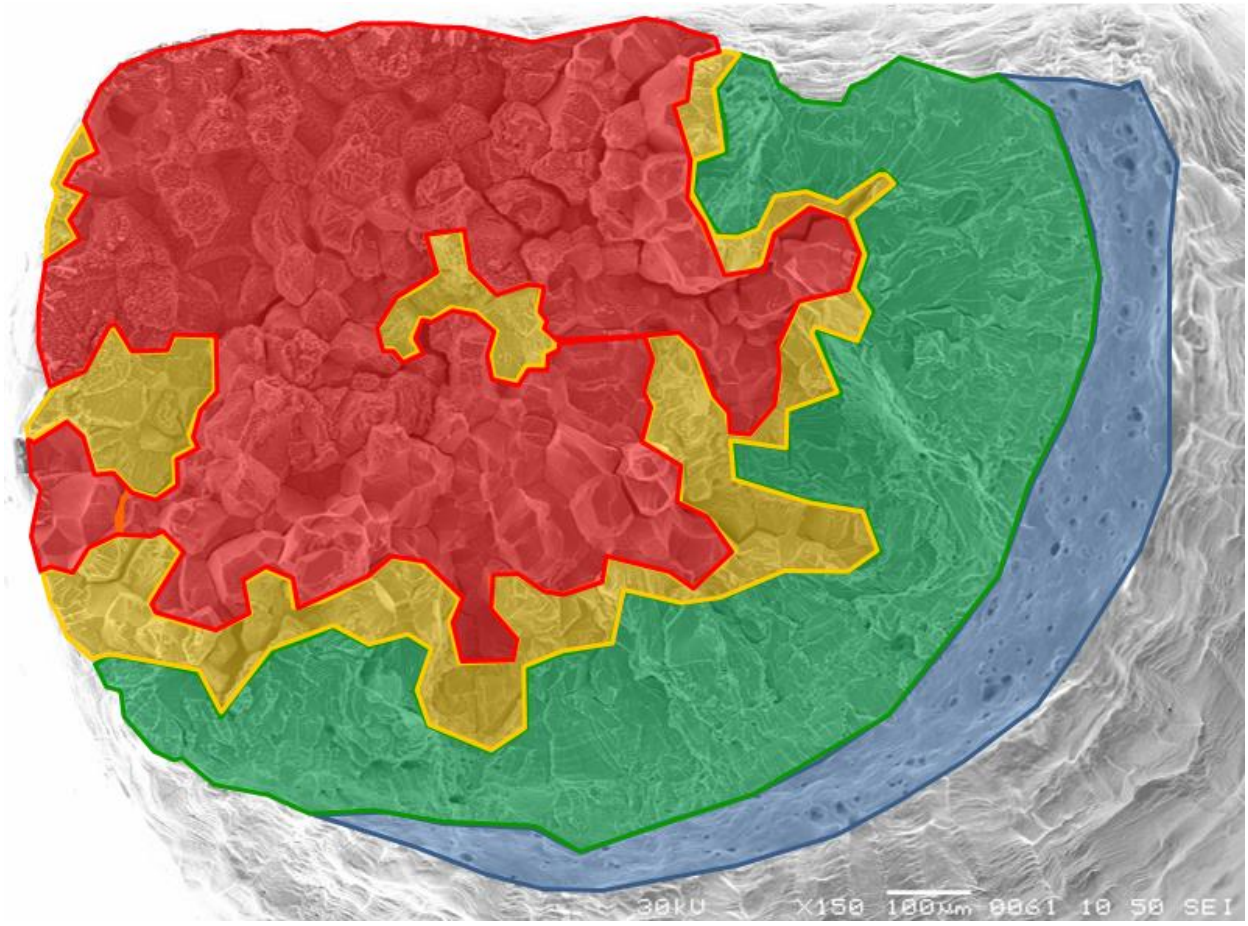

Figure 5.21. Final fracture surface of the CERT tensile specimen: T-5, 500°C: 1 h. Red is utilized to represent areas of intergranular failure, while green shows regions of transgranular propagation. Orange represents mixed IG/TG, while blue is ductile fracture.

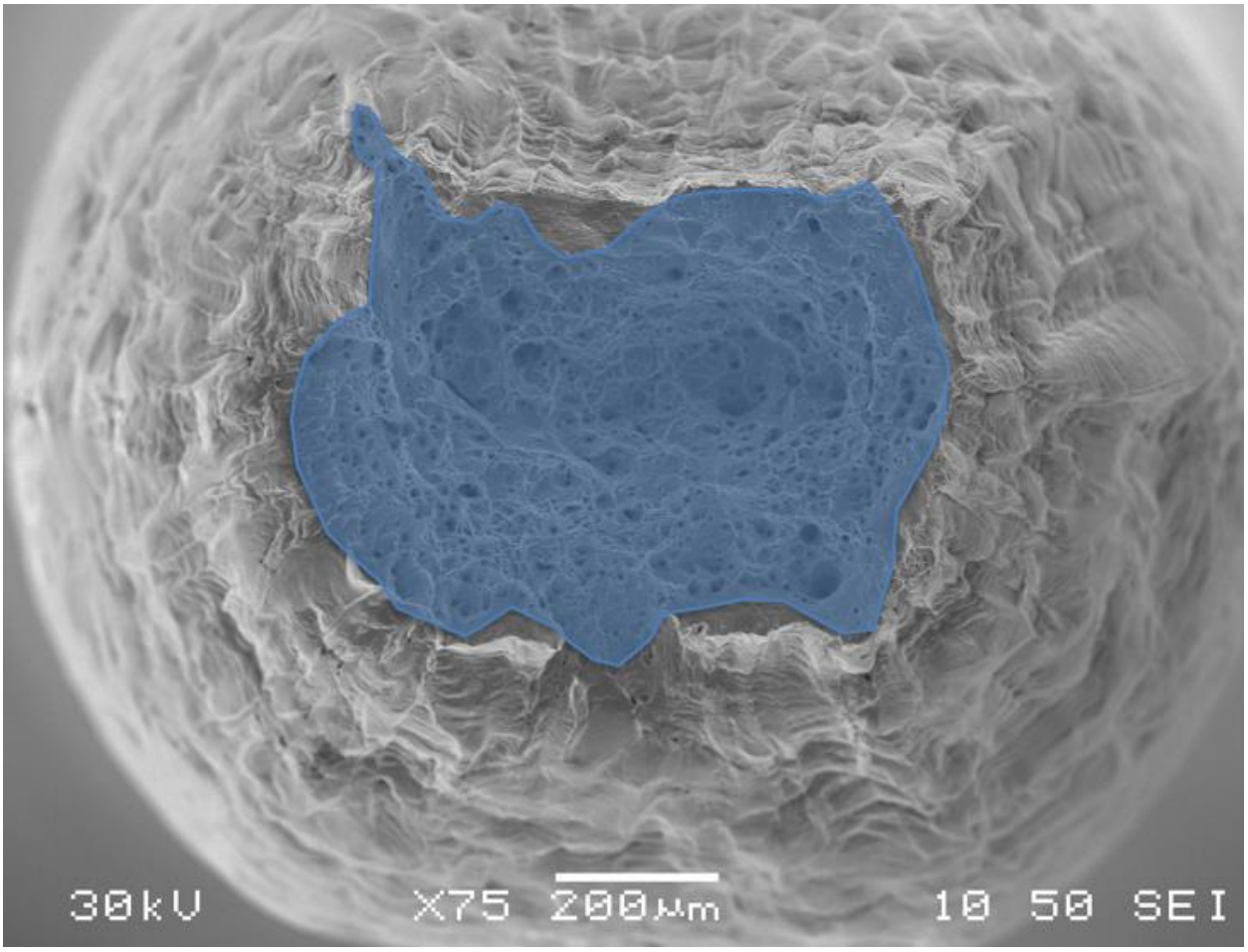

Figure 5.22. Final fracture surface of the CERT tensile specimen: T-13, 550^{o}C: 1 h. Red is utilized to represent areas of intergranular failure, while green shows regions of transgranular propagation. Orange represents mixed IG/TG, while blue is ductile fracture.

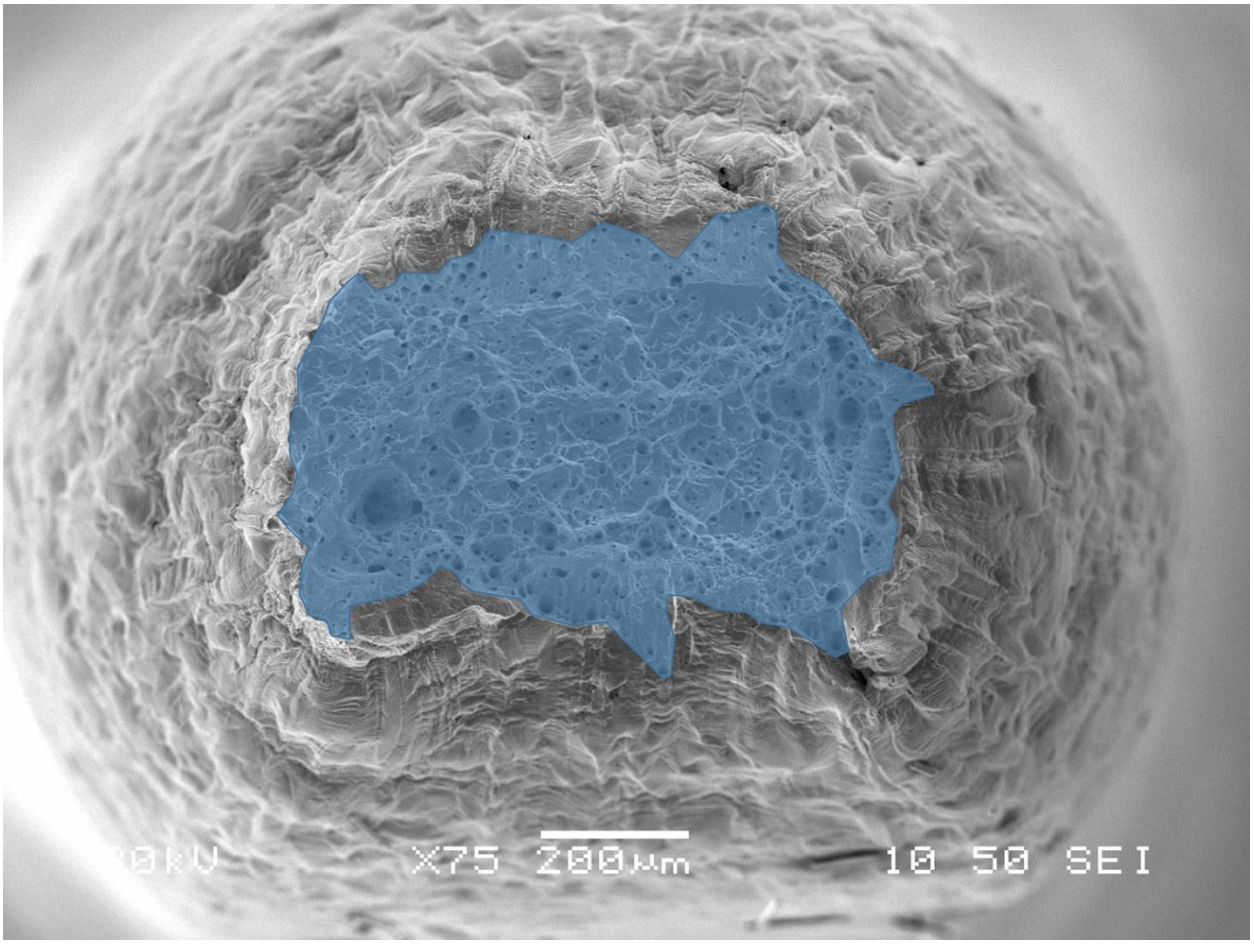

Figure 5.23. Final fracture surface of the CERT tensile specimen: T-7, 550°C: 5 h. Red is utilized to represent areas of intergranular failure, while green shows regions of transgranular propagation. Orange represents mixed IG/TG, while blue is ductile fracture.

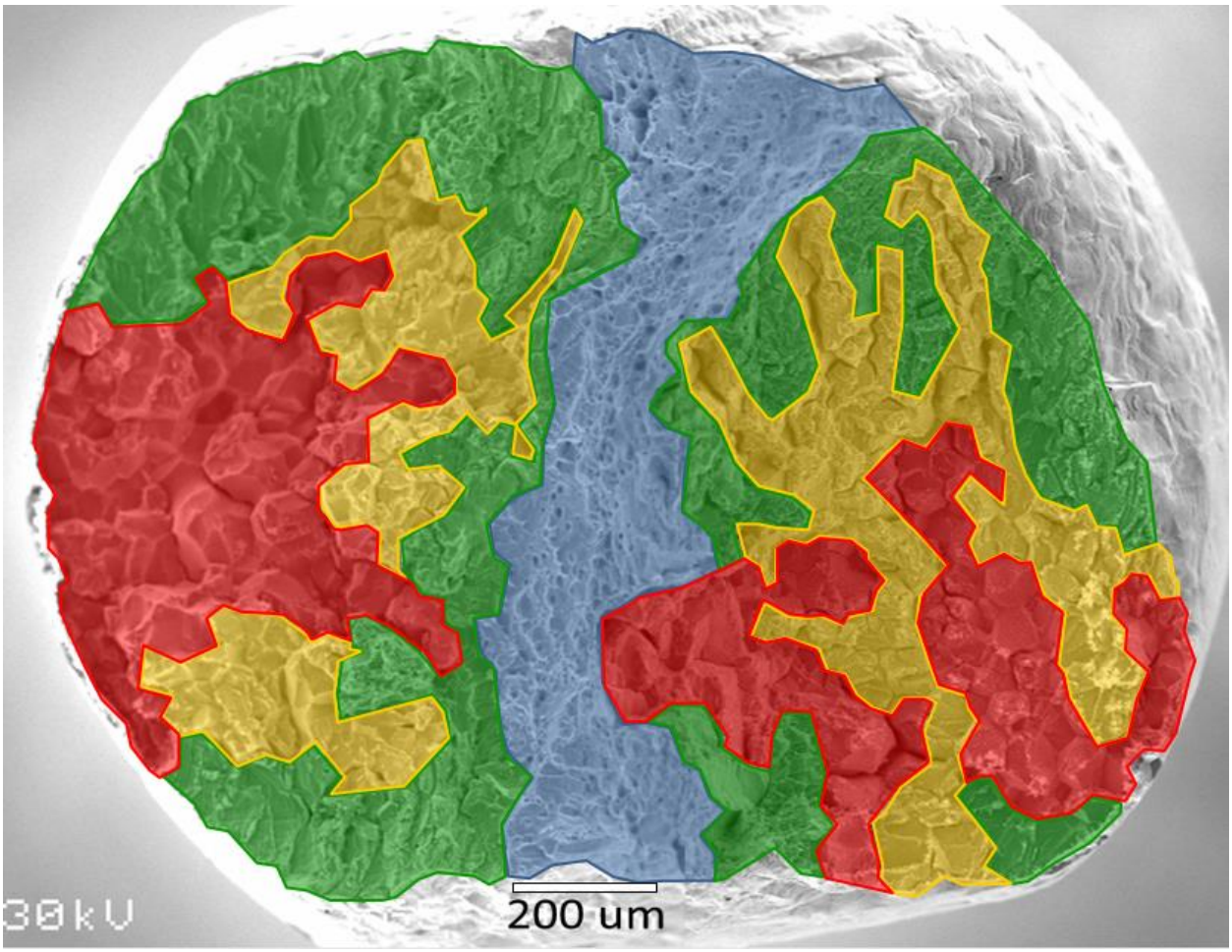

Figure 5.24. Final fracture surface of the CERT tensile specimen: T-9, 550^{o}C: 20 h. Red is utilized to represent areas of intergranular failure, while green shows regions of transgranular propagation. Orange represents mixed IG/TG, while blue is ductile fracture.

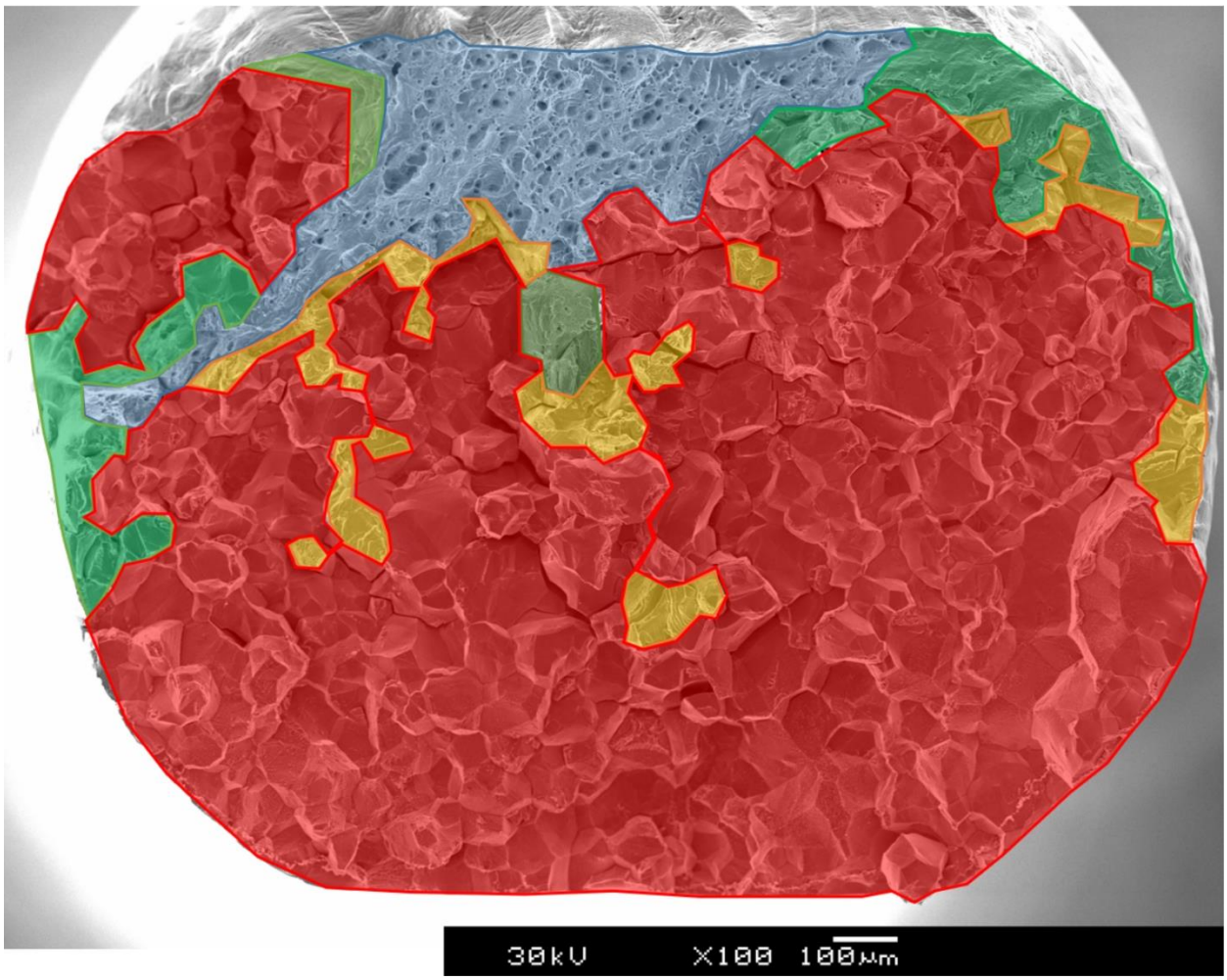

Figure 5.25. Final fracture surface of the CERT tensile specimen: T-12, 550ºC: 20 h. Red is utilized to represent areas of intergranular failure, while green shows regions of transgranular propagation. Orange represents mixed IG/TG, while blue is ductile fracture.

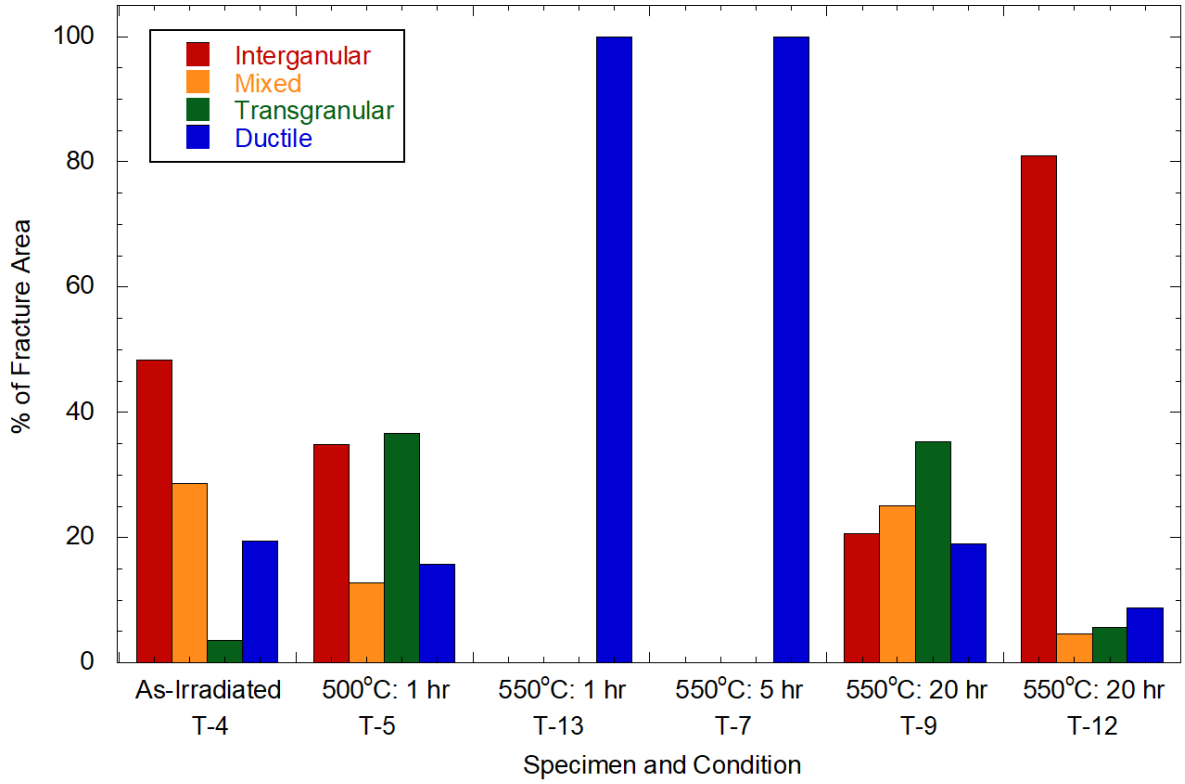

Figure 5.26. Change in the fracture morphology of the as-irradiated, PIA: 500°C: 1 h, PIA: 550°C: 1, 5, and 20 h conditions.

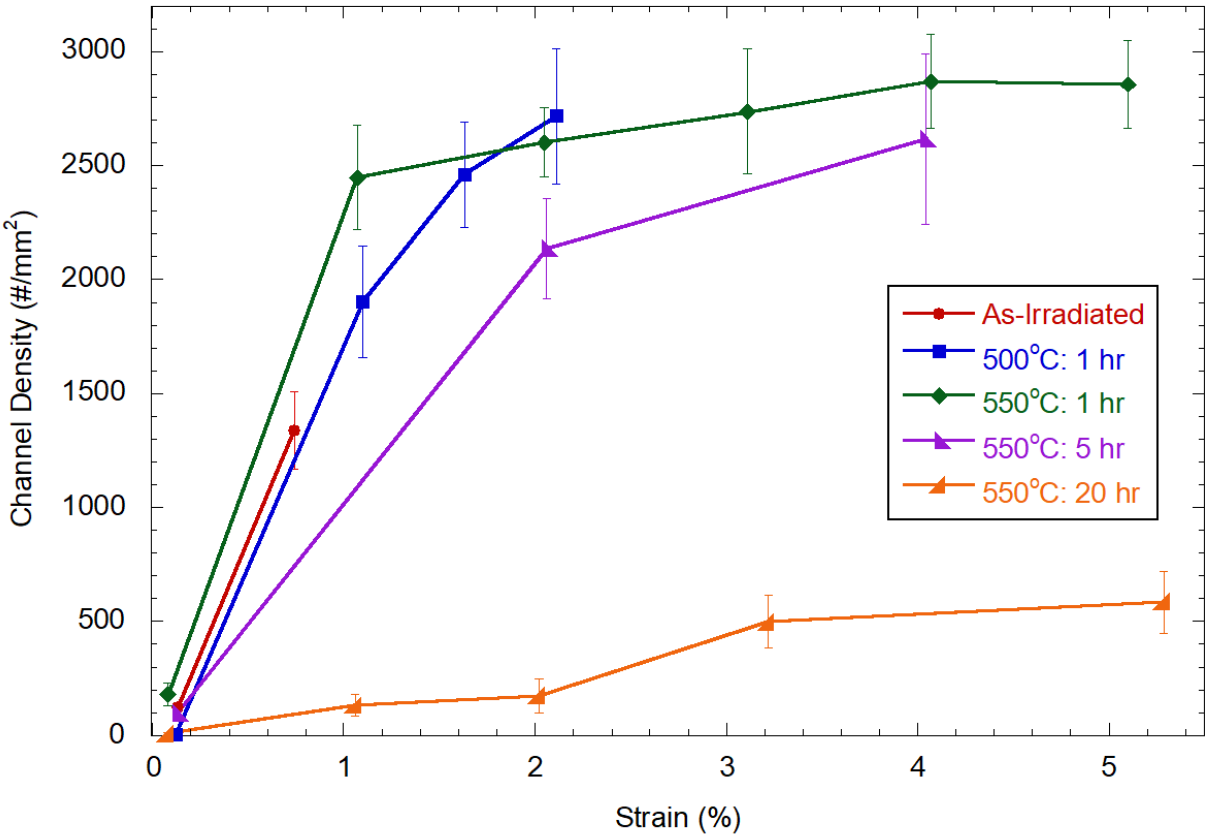

Figure 5.27. Change in the dislocation channel density of the failure region in response to increasing plastic strain, prior to crack growth or specimen necking.

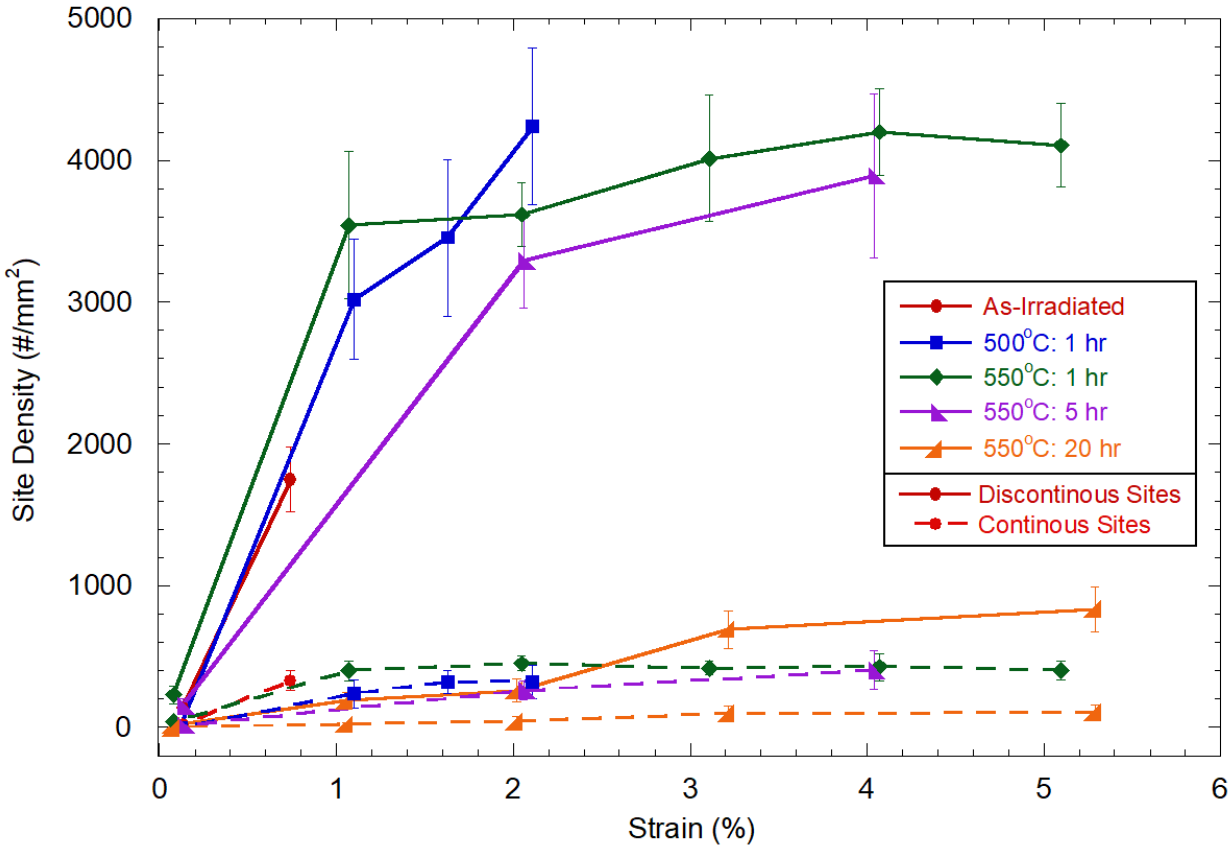

Figure 5.28. Change in the grain boundary-dislocation channel interaction site density of the failure region in response to increasing plastic strain.

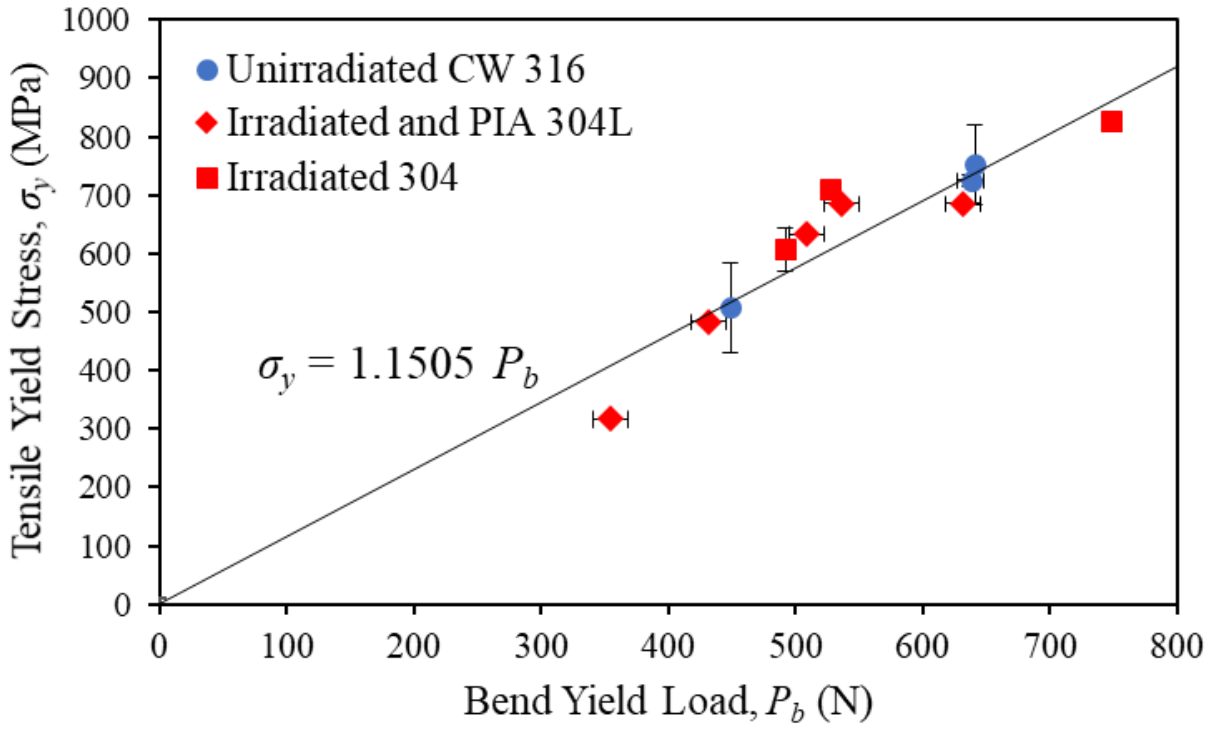

Figure 5.29. Comparison between the yield load in 4-point bend experiments and the tensile yield stress. The red diamonds represent data from this research.

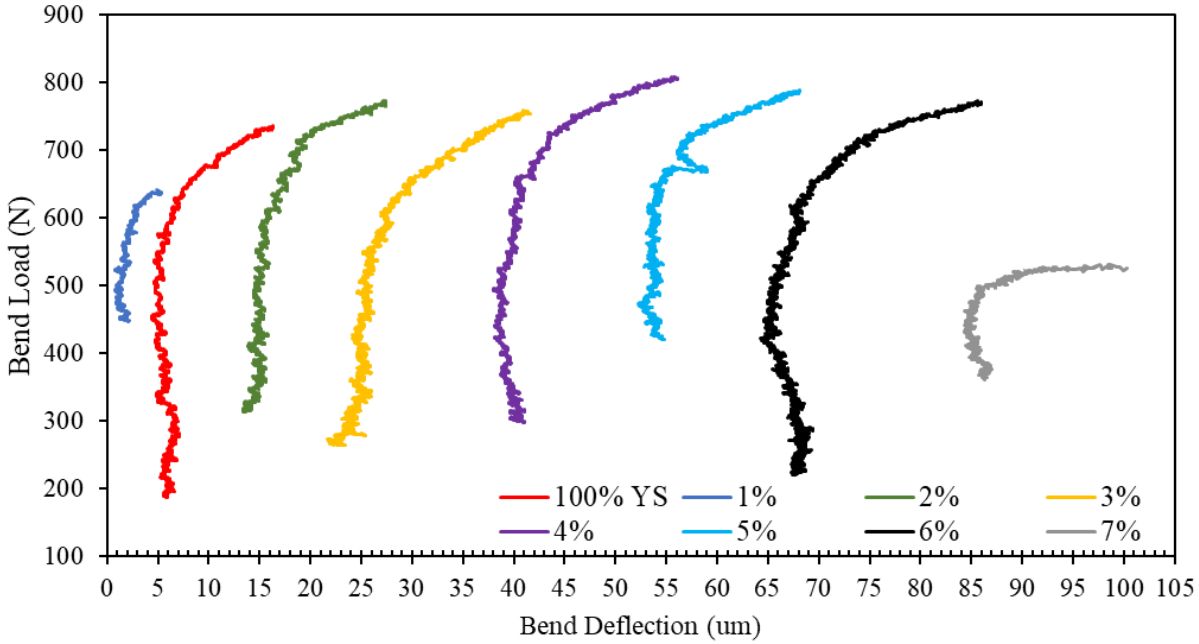

Figure 5.30. Load-deflection curves for the 4-B (as-irradiated) bend specimen over multiple straining increments. Nearly all curves showed an apparent strain hardening which was not present in the next increment.

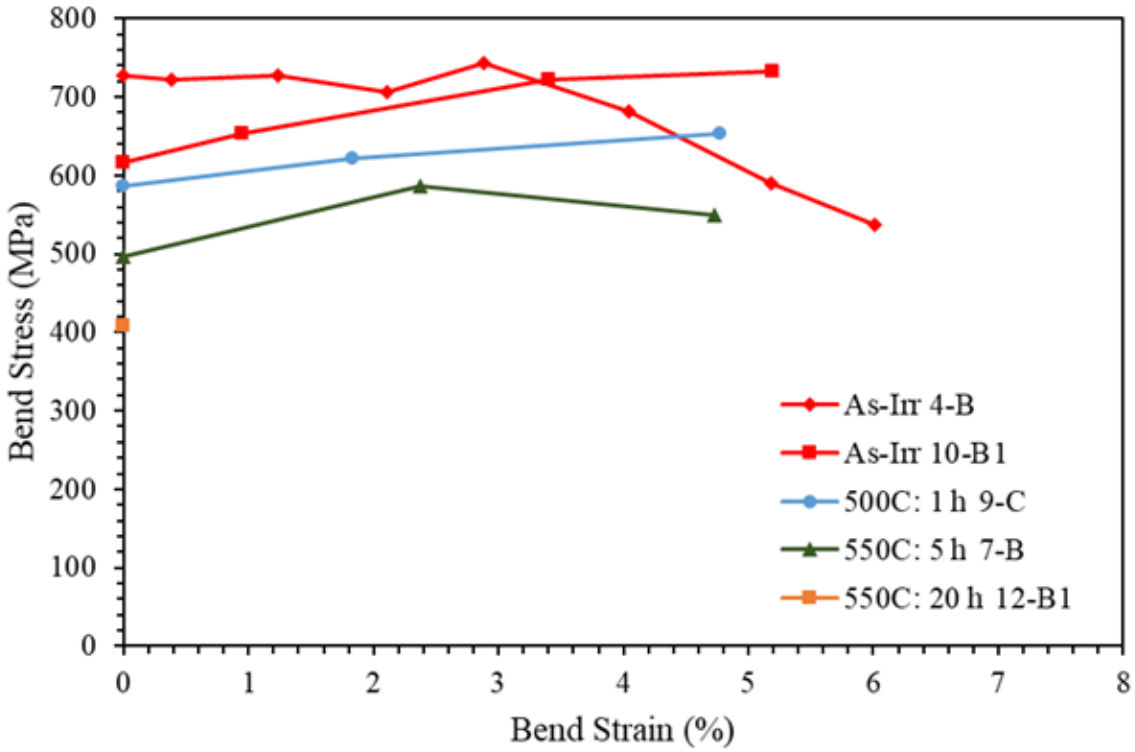

Figure 5.31. Evolution of the 4-point bend increment yield stress with increased strain for the as-irradiated and PIA conditions.

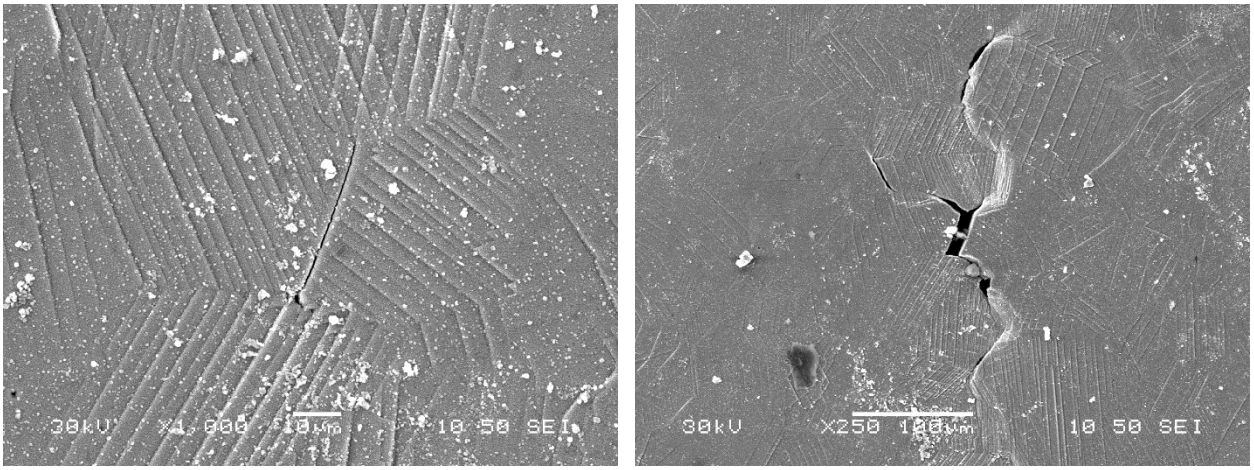

a b

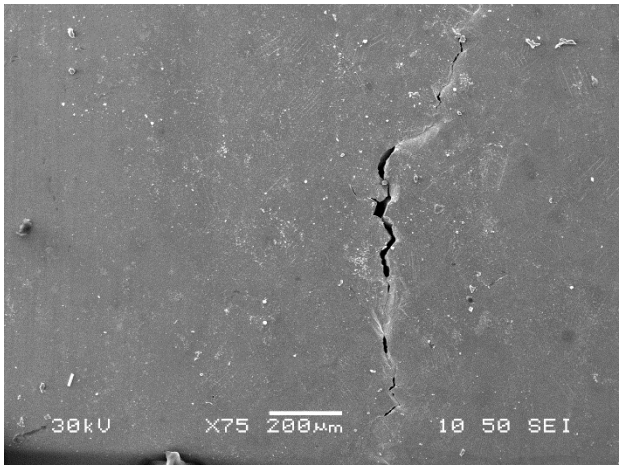

c

Figure 5.32. Crack initiation and growth for the 4-B (as-irradiated) bend specimen: a) initial site of crack initiation after 5.18 ε_p, crack growth, b) crack growth of initial site after 6.01 ε_p, c) further crack extension at 7.25 ε_p. Additional crack initiation sites were observed to the front or sides of the crack front, many of which were integrated into the crack as it grew.

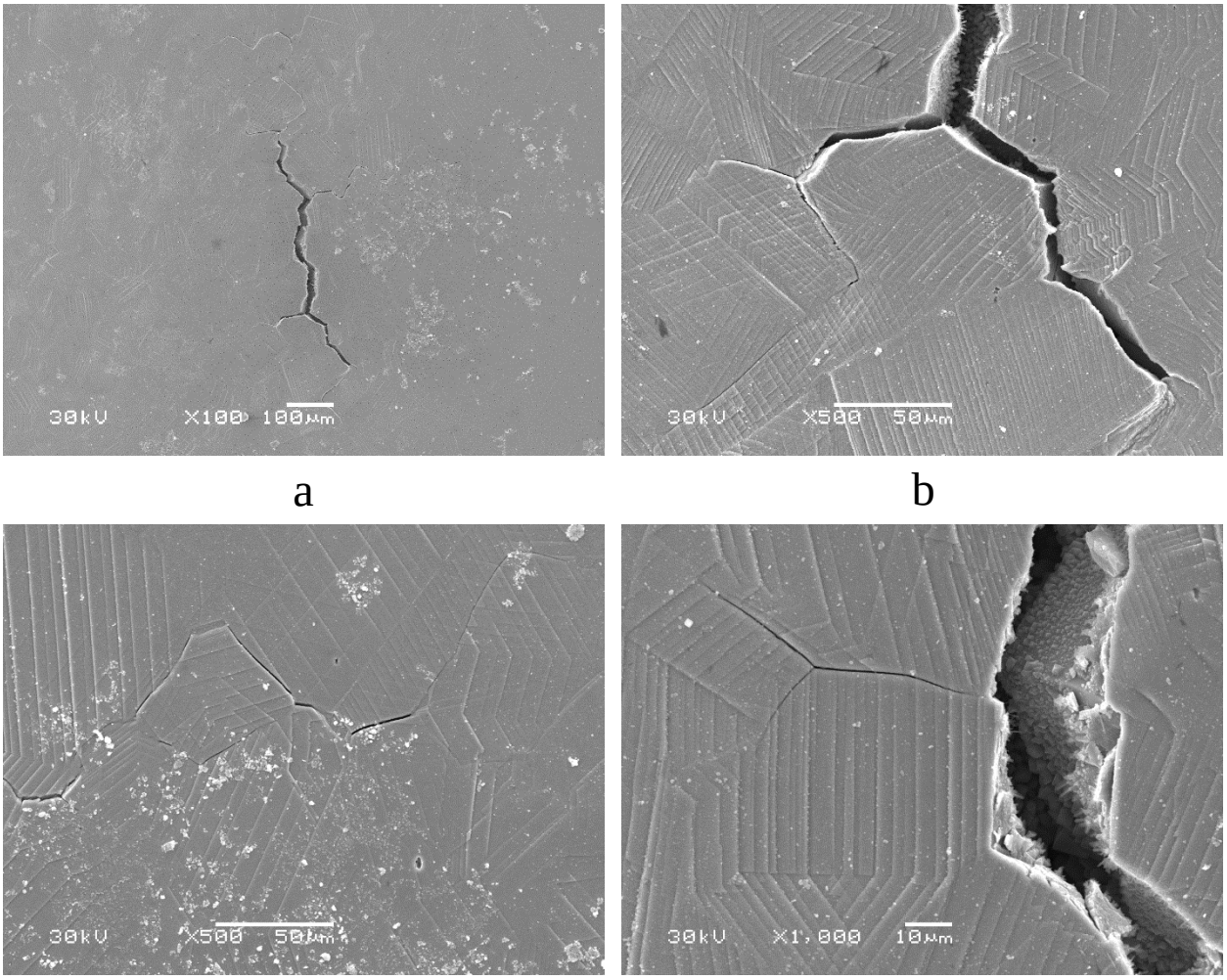

Figure 5.33. Crack initiation and growth for the 10-B1 (as-irradiated) bend specimen at 10.77 ε_p: a) overview of the crack, b) higher magnification of the lower crack fork, c) and d) images of auxiliary cracks to the sides of the primary crack propagation

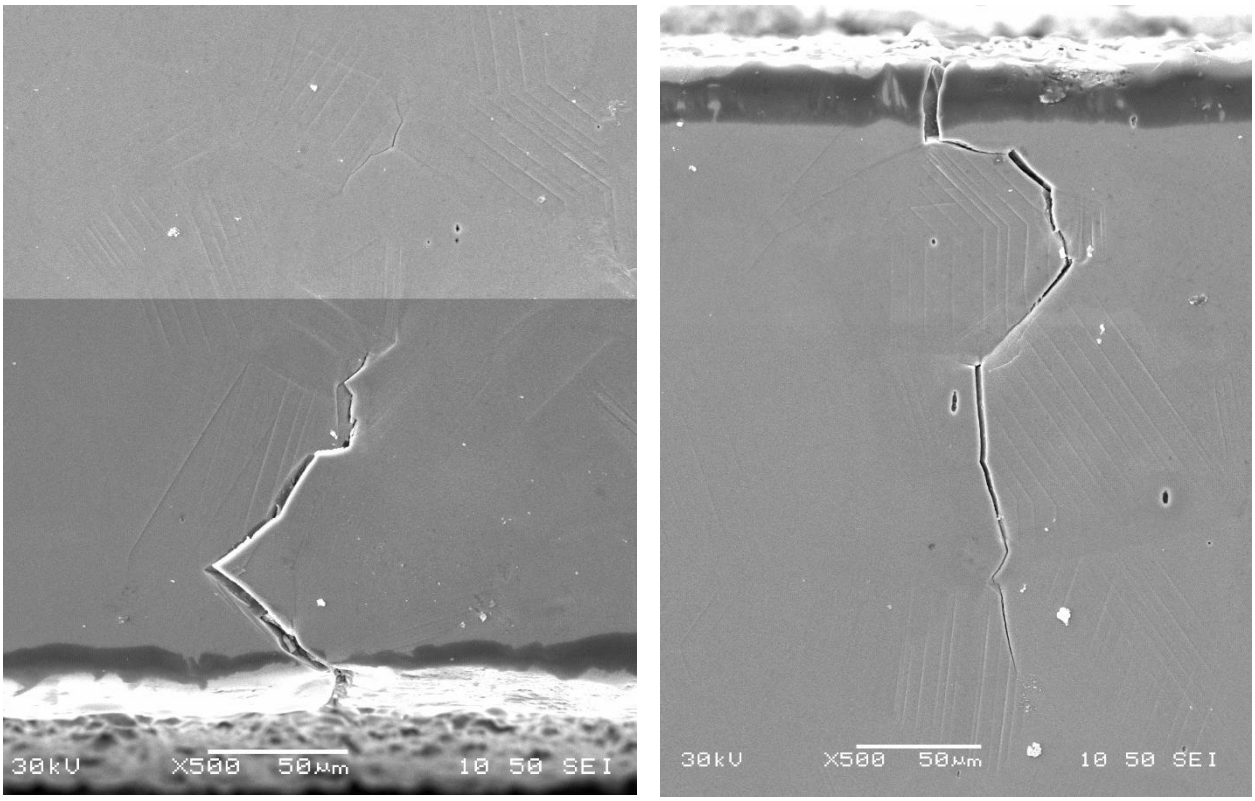

a b

Figure 5.34. Crack initiation and growth for the 12-B1 (550^{o}C: 20 h) bend specimen at 1.83 ε_p: a) crack initiation and growth near the bottom edge, b) crack initiation and growth near the top edge of the specimen. Note that both crack initiations appeared to be associated with the specimen edge.

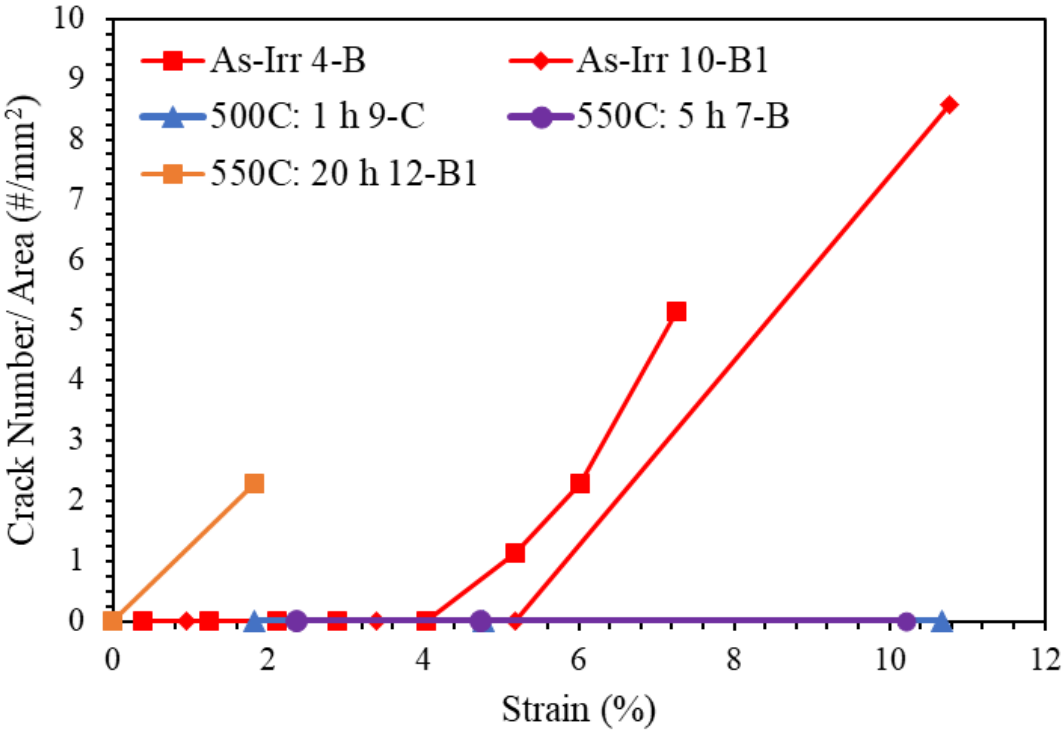

Figure 5.35. Crack number density as a function of strain and annealing condition for the 4-point bend specimens.

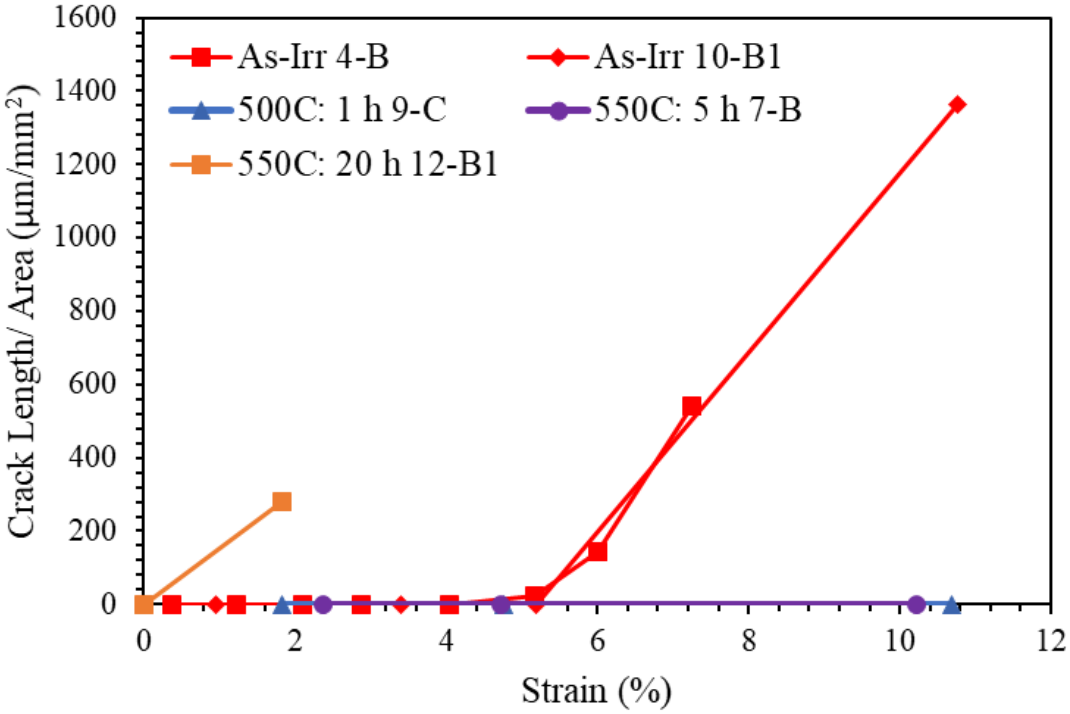

Figure 5.36. Total crack length density as a function of annealing condition and strain for the 4-point bend specimens.

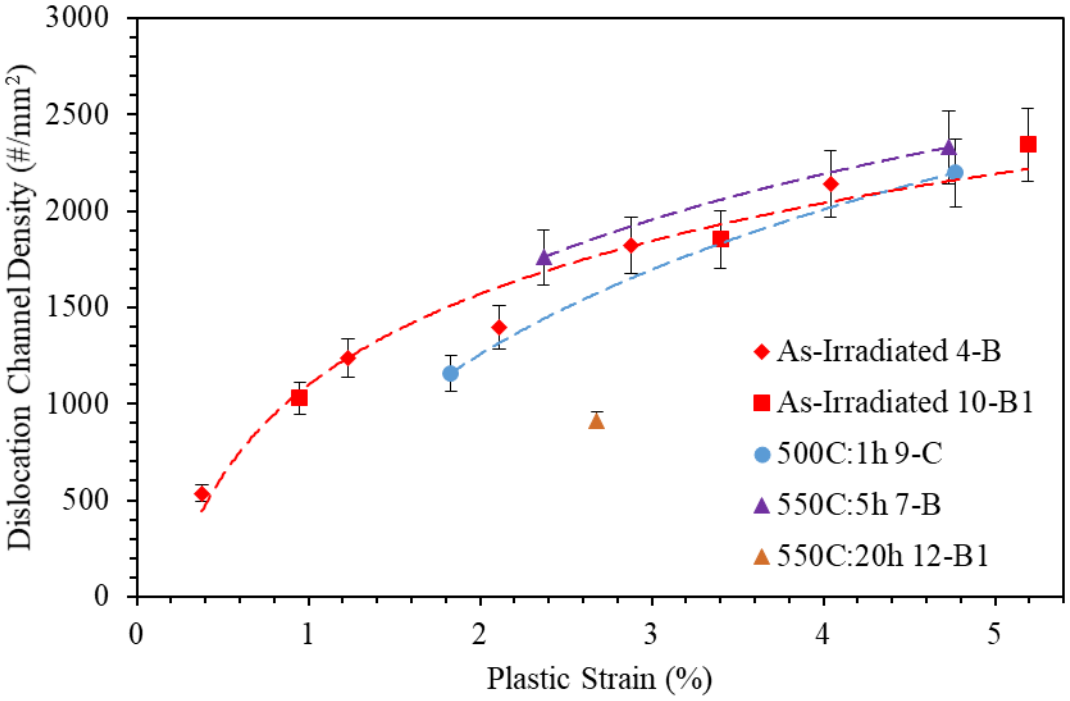

Figure 5.37. Dislocation channel density as a function of strain and annealing condition for the 4-point bend specimens.

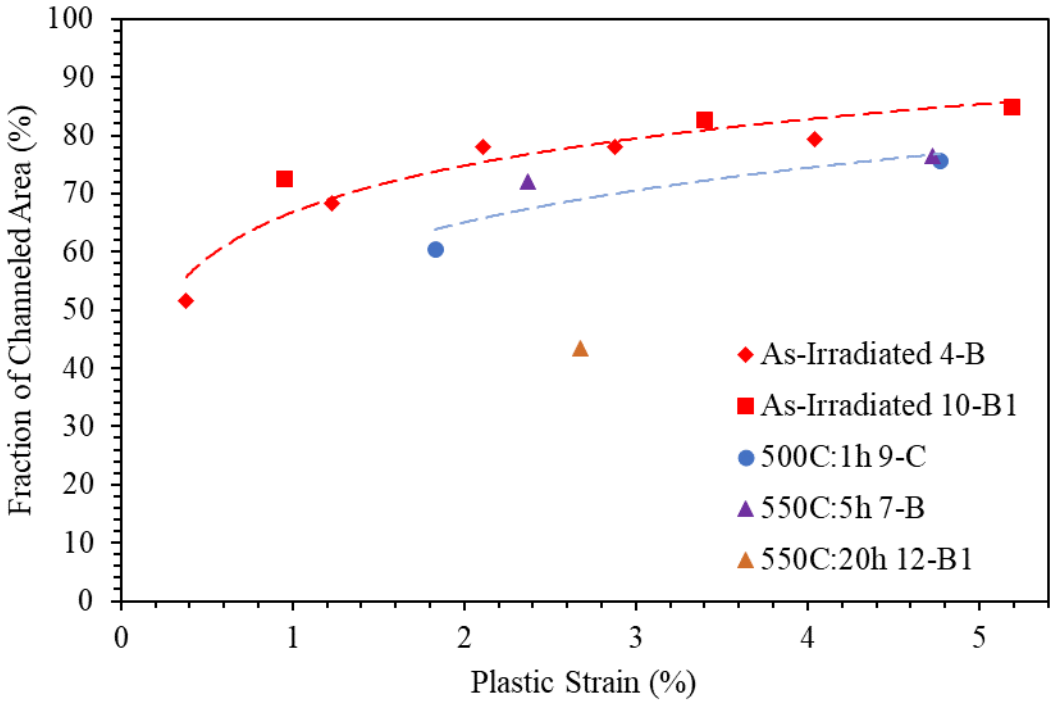

Figure 5.38. Fraction of channeled area as a function of strain and annealing condition for the 4-point bend specimens.

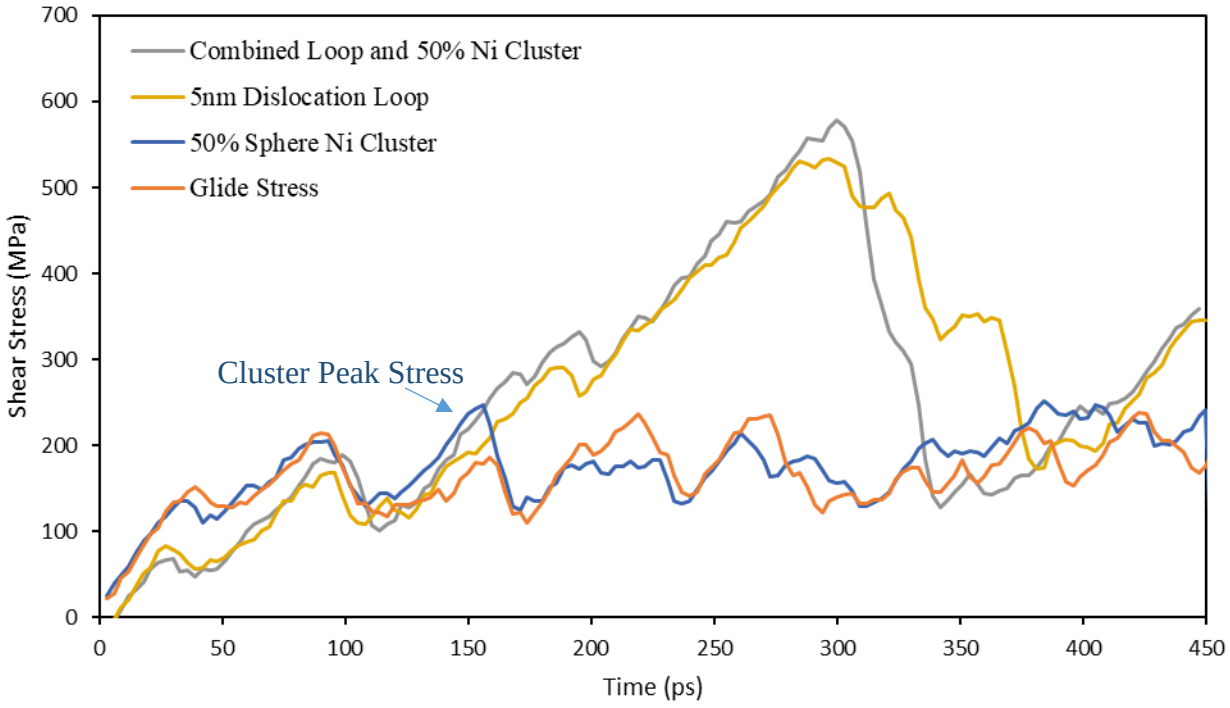

Figure 5.39. Comparison of the shear stress-strain curves for the dislocation interaction with varying defects. Dislocation loop obstacles are both in the $[1\bar{1}1]$ orientation.

CHAPTER 6 - DISCUSSION

In this section, results obtained from the characterization of irradiated microstructure, CERT tensile experiments, and four-point bend experiments following PIA will be discussed. Prior to discussing the resultant IASCC susceptibility, the effect of the thermal annealing treatments on the irradiated microstructure will first be discussed, followed by the relationship between the irradiation-induced defects and the bulk hardening of the material, a relation determined by the obstacle strengths of individual defects. A brief discussion on the evolution of the localized deformation and IASCC susceptibility with PIA will follow, culminating in a determination of the processes responsible for the mitigation of IASCC susceptibility after PIA treatments.

6.1 Thermal Annealing of the Irradiated Microstructure

During annealing irradiation-induced clusters can change in size and density through the diffusion of thermally-induced vacancies; the rate at which this occurs is determined by the vacancy supersaturation in the bulk and at the defect. For a faulted dislocation loop this supersaturation is determined by line tension and stacking fault energy, as well as the normal component of an applied stress, if present. For a void the vacancy supersaturation would result from the surface tension [170]. Solute enhanced defects, such as solute clusters or grain boundary RIS, will not see much vacancy supersaturation as these defects do not significantly influence the free energy of the system; instead their behavior under annealing is expected to simply result from solute diffusion as predicted by Fick's laws.

6.1.1 Dislocation Loops

The resultant behavior for dislocation loops under annealing will not only depend on the vacancy supersaturation, but also availability of sources and sinks for the thermally-induced vacancies. If sufficient external sources and sinks are available outside of the dislocation loop

population, then each defect will behave as though it were in isolation, resulting in a faulted interstitial loop shrinking in size due to vacancy adsorption [170]:

$$dr_l/dt = -(2D_{at})\left\{1 - \exp\left[-\left(\frac{U}{br_l} + \frac{\Gamma}{b}\right)\frac{b^3}{kT}\right]\right\}, \quad (6.1)$$

where r_l is the radius of the dislocation loop, D_{at} is the atomic self-diffusion coefficient, U is the dislocation line energy, b is the Burgers vector, Γ is the stacking fault energy, k is the Boltzmann constant, and T is the annealing temperature [170]. However, if no external sources and sinks are available, then diffusion can only occur between different loops in the population, and the total number of vacancies must be conserved [170]. This situation will lead to the coarsening of the dislocation loop population, where smaller loops will decrease in size, while the larger loops will grow [170], such that:

$$dr_l/dt = \left(\frac{2D_{at}}{b}\right)\exp\left[-\left(\frac{\Gamma b^2}{kT}\right)\right]\left\{\exp\left[-\left(\frac{Ub^2}{r_l kT}\right)\right] - \exp\left[-\left(\frac{Ub^2}{\dot{r}_l kT}\right)\right]\right\}, \quad (6.2)$$

where $\dot{r}_l$ is the average radius of the entire dislocation loop population, and the other parameters are the same as in Eqn. 6.1. A comparison of these two extreme cases is shown in Figure 6.1 and Figure 6.2 [170] for the dissolution and coarsening behavior, respectively, whereas in an actual irradiated material a combination of both methods will likely be observed, especially if there is an exchange of vacancies between multiple defect types. Note that while faulted dislocation loops are sessile, and thus cannot glide, they may still move through dislocation climb [197–199]. During annealing treatments, dislocation climb will occur more readily, particularly for smaller loops and thus faulted loops on parallel slip planes may coalesce, allowing for another method of loop coarsening during annealing [198].

While determining the exact annealing behavior of the dislocation loop population in the examined 304L stainless steel is not easily completed, we can at least verify that the experimentally observed behavior falls within the theoretical predictions of dissolution (Eq. 6.1) and coarsening (Eq. 6.2). Normalizing the dislocation loop population by its total dislocation line length is a straightforward method of comparing the experimental results to the theoretical predictions. This comparison is completed in Figure 6.3, using the characterized loop population of the as-irradiated condition and some of the parameters listed in Table 6.1. The self-diffusion coefficient for the calculation assumed a Fe-12Ni-20Cr composition, as was used in the MD simulations, and was 1.14 x 10^{-3} nm/s for a temperature of 550°C. It must be noted however, that dislocation loops

cannot grow through coarsening indefinitely. As a faulted dislocation loop grows, it will eventually encounter either network dislocations or other dislocation loops [19]; this, combined with their high free energy, will cause faulted dislocation loops to unfault into perfect loops as they grow in size through coarsening. As such, a modified coarsening curve is also shown in Figure 6.3, where a maximum loop diameter of 40 nm is set as the unfaulting limit. Note that the step-like nature of this curve is due to the large decrease in the total loop line length when a 40 nm diameter loop unfaults, and thus is removed from the population. While an unfaulting size of 40 nm was selected to match the theoretical maximum dislocation loop size at 550^{o}C: 1 h, i.e. where loop coarsening was first observed, increasing or decreasing the unfaulting size limit, will simply shift the onset of the unfaulting curve to higher or lower iron diffusion distances, respectively.

In Figure 6.3, the experimentally measured loop population clearly falls within the two extremes of full dissolution and coarsening, for the corresponding temperature conditions. Based on the characterized loop populations, it is evident that most of the loop population is annealed through a dissolution mechanism, though a substantial portion, ~10%, displays a coarsening response under annealing. This behavior is confirmed by the size distributions of the loop populations after annealing, as shown in Figure 5.3. Here it can be observed that with increased annealing the bulk of the size distribution moves to progressively smaller sizes, as predicted by the dissolution behavior shown in Figure 6.1, while select loops are observed to grown with annealing, as indicative of a coarsening behavior. Thus, the experimentally characterized dislocation loop populations exhibited a partial behavior of both dissolution and coarsening under the annealing treatments and was contained between the theoretical boundaries of a pure dissolution or coarsening behavior.

6.1.2 Solute Clusters

The resultant behavior for solute clusters under annealing will not only depend on the concentration of thermally-induced vacancies, but also on the gradient of solute concentration as predicted by Fick's laws of diffusion. The initial concentrations of the solute clusters for this simulation, were obtained from the radial concentration profiles of the nickel-silicon clusters of the as-irradiated condition, shown in Figure 5.6. This concentration profile then underwent a simulated 1D diffusion in accordance with Fick's second law, such that:

$$\frac{dC}{dt} = D\frac{d^2C}{dr^2}\,, \tag{6.3}$$

which was then integrated for the selected annealing time and temperature, for the multicomponent diffusion of iron, nickel, and chromium, though a radial diffusion equation may have been more appropriate. The required parameters to determine the diffusion coefficients of iron, nickel, and chromium are listed in Table 6.1. The simulated nickel concentration profile at annealing conditions of 500ºC: 1 h, 550ºC: 1, 5 and 20 h, are compared to the experimentally measured radial nickel concentration profiles for these conditions in Figure 6.4. A comparison of the iron and chromium profiles displayed similar degrees of accuracy. From Figure 6.4, a good agreement between the simulated and measured concentration profiles is observed, despite some of the simplifications of the simulation, such as assuming a 1D diffusion for a 3D defect, thus confirming that the dissolution of the solute clusters following annealing is primarily driven by the concentration gradients present in the solute clusters. A similar diffusion behavior is expected for the annealing of the radiation-induced segregation (RIS) at the grain boundary, as shown in prior work by Busby *et al.* [57,161].

6.2 Relation Between the Irradiated Microstructure and Irradiation Hardening

Under irradiation austenitic stainless steels experience a sharp increase in hardness and yield stress as the irradiation dose increases. This increase in strength is attributed to the emergence of the irradiation-induced defect population, and their role in impeding the movement of mobile dislocations. There have been many methods used in literature to relate the increase in material strength to the irradiated microstructure [79,82–85], but the dispersed barrier hardening model (DBH), Eqn. 2.4, is one of the earliest and most used of such models. It must be noted that the DBH model is itself derived from the classical equation for the increased shear stress required for a dislocation to cross a square lattice of obstacles [200]:

$$\Delta\tau = \mu b\, cos\,(\emptyset_c/2)/(L-d)\,, \tag{6.4}$$

where L-d is the effective obstacle spacing and is roughly equivalent to $(N_x d_x)^{-1/2}$ for a three-dimensional array, while $\emptyset_c$ is the critical breaking angle for the dislocation. As such the effective barrier strengths of various obstacles have been experimentally measured for various materials and irradiation conditions [43,77,78,84], though with a fair degree of variability. Fits to dislocation

loops have provided obstacle strengths between 0.2-0.5 [78,84], while solute clusters are often less, between 0.1-0.3 [43,84].

6.2.1 Dispersed Barrier Hardening Model Assuming Independent Loop and Cluster Populations

The obstacle strengths of the radiation-induced microstructure, namely dislocation loops, Ni-Si solute clusters, and Al-Cu solute clusters, were calculated from the characterized defect populations using the DBH model shown in Equation 2.4. The sizes, *d*, and densities, *N*, of the irradiation defects required to calculate the effective obstacle spacing were reported earlier in Table 5.1-5.3, while the increase in yield stress, $\Delta\sigma_y$, was calculated from the measured irradiation hardening, ΔH_v, of the characterized sample blank specimens in Table 5.5 and the conversion factor of 2.46 determined for this material in Figure 5.12, as well as necessary constants listed in Table 6.1. The resultant values were then fit using a multi-variable regression analysis in Microsoft Excel™ using both the simple summation, Eqn. 2.5, and root-square-sum (RSS), Eqn. 2.6, methods of combining the strengthening components of multiple defect types. The resultant fits for the obstacle strength, α, for each defect type is listed in Table 6.2.

The obstacle strength was calculated under three separate conditions. The first condition fit the entire data set, however, the anomalous density of Al-Cu solute clusters at the 550ºC: 5 hr condition, as seen in Table 5.3, was expected to adversely affect the calculation, leading to a fitting of a negative obstacle strength for the Al-Cu clusters under the RSS summation method. As such a second fitting was completed, excluding the 550ºC: 5 h condition. This fitting process led to a negative obstacle strength for the Al-Cu clusters via both the simple and RSS summation methods. Based on the results of the prior two fitting conditions, it was concluded that the strengthening contribution of the Al-Cu clusters was negligible, most likely due to their slight volume fractions of ~0.05%. As such a third fitting was completed, excluding the Al-Cu solute cluster populations; this fitting seemed the most appropriate providing an obstacle strength of 0.096 and 0.073 for dislocation loops and solute clusters, respectively, via the simple summation, and 0.190 and 0.076 for dislocation loops and solute clusters, respectively, via the RSS summation method. Across the examined conditions, the simple summation strength fits matched the measured strengthening with an average variance of 10.0 ± 8.1 MPa, while the RSS strength fits had an average variance of 3.7 ± 7.8 MPa. As the RSS summation method more accurately matched the measured strengthening and is most applicable to barriers with similar strengths, it was decided that this summation method

was most appropriate. The calculated obstacle strength of 0.190 for the faulted dislocation loops is quite similar to the range of 0.2-0.5 [78,84] often reported in literature. It should be noted that many of these early studies calculated the obstacle strength assuming that only dislocation loops contributed to the hardening, as such the strengthening contribution of any other microstructural defects, such as solute clusters, would have been attributed to the loop population, hence increasing the calculated obstacle strength. The calculated obstacle strength for solute clusters, 0.076 is also lower than the range for solute cluster populations in irradiated stainless steel, which varies between 0.1-0.3 [43,84]. One reason for this discrepancy may be the difficulty of distinguishing between solute clusters and precipitates when utilizing certain analysis methods for irradiated alloys, such as APT [43]. Including populations of precipitates, which are expected to be much stronger barriers to dislocation movement than solute clusters would lead to higher obstacle strength.

Using the calculated obstacle strengths of dislocation loops and Ni-Si solute clusters, a calculation of the predicted strengthening from these independent defect populations through the DBH model with an RSS combination was compared to the measured strengthening in Table 6.3 and displayed visually in Figure 6.5. It should be clarified that the relative contributions of strengthening from both the independent solute clusters and dislocation loops in Figure 6.5 are shown as a proportion of the $\Delta\sigma_y{}^2$ for each defect type as an RSS method was used to determine the total strengthening from the defects. As expected, a good comparison is observed between the predicted and measured strengthening, especially given the degree of error in the fitting parameters, thus validating the calculated fits. It can also be seen in Figure 6.5 that the dislocation loops are the dominate strengthening defect in the as-irradiated condition, but the contribution from the Ni-Si clusters overcomes that of the dislocation loops by annealing at 550^{o}C: 1 h and becomes the only hardening feature after 550^{o}C: 20 h.

6.2.2 Molecular Dynamics Simulations of Irradiation Defects

While the calculation of the obstacle strength from fits to experimental measurements may demonstrate a difference in the strengths of different irradiation-induced defects, these estimates do not examine the underlying cause of the obstacle strengths, while also ignoring the possible correlation between irradiation defects, such as that between solute clusters and dislocation loops.

As such, molecular dynamics (MD) simulations were conducted to more precisely measure the obstacle strength of different defect types and their respective contribution to the overall material hardness.

6.2.2.1 Calculation of Obstacle Strength

To calculate the obstacle strength for of each of the examined defect types, a modified version of Eqn. 6.4 was utilized:

$$\alpha = \frac{\Delta\tau(L-d)}{\mu b} \quad , \tag{6.5}$$

where α is the unitless obstacle strength between 0-1, $\Delta\tau$ is the increase in shear stress from the obstacle array taken as the difference between the peak shear stress and the friction stress, L is the obstacle spacing, 21.5 nm for this simulation, d is the obstacle diameter, and μ and b are the shear modulus and Burgers vector, 77 GPa and 2.48 x 10^{-10} m, respectively, as listed in Table 6.1. For solute clusters, d was simply the diameter of the cluster and for dislocation loops, an effective obstacle size, d_{eff}, was used to account for the effect of orientation with respect to the mobile edge dislocation, Figure 6.6. While the orientations of $[1\bar{1}1]$ and $[\bar{1}11]$ have similar effective loop diameters which increase with the obstacle size, the effective size of a loop in the $[\bar{1}\bar{1}1]$ orientation remains constant at ~0.8 nm regardless of the obstacle size, due to its edge-on orientation with the edge dislocation. These values of d_{eff} were used in Eqn. 6.5 in place of d. As most of the obstacle strength for the combined solute cluster-dislocation loop defects came from the dislocation loops, the same d_{eff} was used when calculating the obstacle strength for these compound defects. The calculated obstacle strength for each of the examined defects is given in Table 6.4 along with the propagated errors from the peak shear stresses. Recall that, due to the enhanced strain rates in the MD simulations and hence a limitation of diffusion-related processes such as climb, the simulated obstacle strengths are probably enhanced as compared to slower strain rates, though the effect is presumed to be minimal.

6.2.2.2 Interstitial Faulted Dislocation Loop Defects

The obstacle strength for dislocation loops, and the effect of obstacle size and orientation are shown in Figure 6.7. It is evident that the obstacle strength of dislocation loops of the $[\bar{1}\bar{1}1]$

orientation remains constant despite increasing obstacle size. As shown in Figure 6.6, the $[\bar{1}\bar{1}1]$ loop orientation is edge-on with respect to the direction of the mobile edge dislocation; due to this orientation these loops were generally sheared by the edge dislocation rather than bypassed through a super job or adsorption interaction as was commonly observed for loops of the $[1\bar{1}1]$ and $[\bar{1}11]$ orientations. This shearing interaction thus required a threshold shear stress to initiate but was not affected by the loop size. The obstacle strength for loops of the $[1\bar{1}1]$ and $[\bar{1}11]$ orientations increased with increasing loop diameter, though loops of the $[1\bar{1}1]$ orientation were noticeably stronger than those of the $[\bar{1}11]$ orientation, particularly at smaller loop diameters. Figure 6.7 also includes the average obstacle strength for all three examined orientations with increasing loop diameter. The average increase in obstacle strength with diameter for all the observed loop orientations displayed a $\sqrt{d}$ dependence as shown in Figure 6.8. This implies that the generalized obstacle strength for a random population of dislocation loops: $\alpha_L = \alpha_{o,L}\sqrt{d}$, where $\alpha_{o,L}$ is about 0.094 $nm^{-1/2}$.

6.2.2.3 Solute Cluster Defects

The obstacle strength of solute clusters, and the effect of obstacle size and solute concentration are shown in Figure 6.9. Clusters below a diameter of 4 nm had a sharp decrease in the measured obstacle strength; it is believed that these smaller clusters lacked the required surface area to be a consistently effective barrier to the mobile edge dislocation. The increase in the obstacle strength with solute concentration, i.e. increased nickel content for this study, displayed a $\sqrt{\Delta \mathrm{Ni}}$ dependence as shown in Figure 6.10, implying that the generalized obstacle strength for a random population of solute clusters: $\alpha_c = \alpha_{o,c}\sqrt{\Delta \mathrm{Ni}}$, where $\alpha_{o,c}$ is about 0.099. This dependence on solute content agrees with prior literature on solution strengthening for low concentrations of substitutional solutes [201–203].

6.2.2.4 Combined Solute Cluster-Dislocation Loop Defects

The obstacle strength for the combined solute cluster-dislocation loop defects, α_{c+L}, are compared to the strengths of their independent dislocation loops and solute clusters in Figure 6.11. Figure 6.11a shows the relative change in the obstacle strength as a function of solute concentration

of the spherical cluster. The increase in the obstacle strength of the cluster-loop defect with increasing solute concentration is only slightly larger than that for the solute cluster alone. Figure 6.11b displays the change in the obstacle strength as a function of the diameter of the defects. Again, the obstacle strength of the combined cluster-loop defect increases with defect diameter and is only slightly larger than that of the dislocation loop alone and approximately equal to the sum of the loop and cluster obstacle strengths. Figure 6.11c shows the change in the obstacle strengths when accounting for the orientation of the dislocation loop. While the obstacle strength of the cluster-loop combined defect is approximately the summation of that of the solute cluster and dislocation loop for the orientations of $[1\bar{1}1]$ and $[\bar{1}11]$, a large divergence is observed for the $[\bar{1}\bar{1}1]$ loop orientation, such that α for the cluster-loop compound defect is weaker than α for the dislocation loop. A closer examination of the dislocation interaction with the $[\bar{1}\bar{1}1]$ cluster-loop defect revealed no clear differences from the interaction of the dislocation with an independent $[\bar{1}\bar{1}1]$ loop; the loop did not unfault and the edge dislocation bypassed the loop through a shearing mechanism. As both an independent solute cluster and a $[\bar{1}\bar{1}1]$ loop is bypassed through a shearing mechanism, it is suspected that their combination led to a synergistic reaction allowing for an easier initiation of the shear process, hence the lower peak stresses and obstacle strength.

The obstacle strength of the combined cluster-loop defect depends heavily on the obstacle strength of its individual components, such that $\alpha_{c+L} = \alpha_L + X \cdot \alpha_c$, where X is a fractional value of the solute cluster strength. An RSS approach was also examined in comparing the obstacle strengths, however, as $\sqrt{{\alpha_L}^2 + {\alpha_c}^2} \approx \alpha_L$, a linear sum was a more accurate representation. The determined value for X, for each examined loop and cluster combination is listed in Table 6.4. When comparing the fractional cluster strength, X, with cluster size, X is seen to vary from 1.05, 0.54, and 0.69 for diameters of 3, 5, and 7 nm, respectively, at a solute concentration of 50 at.% Ni and loop orientation of $[1\bar{1}1]$. These values are relatively the same when considering the error ranges, though the higher value at 3 nm, suggests a slightly higher strengthening effect when solute clusters are combined with smaller dislocation loops. When comparing the fractional cluster strength, X, with solute concentration, X is seen to vary from 0.37, 0.54, and 0.58 for nickel concentrations of 25, 50, and 75 at.%, respectively, at a diameter of 5 nm and loop orientation of $[1\bar{1}1]$. Again, these fractional strengths are relatively the same, though a lower cluster concentration provides less of a strengthening effect. Overall, both obstacle size and solute concentration seem to have a rather negligible effect on the fractional cluster strength, at least at

the examined $[1\bar{1}1]$ loop orientation. However, large variations in the fractional strength are observed when examining different loop orientations. While the $[1\bar{1}1]$ and $[\bar{1}11]$ orientations have similar values at 0.54 and 0.65, respectively, the fractional strength for the $[\bar{1}\bar{1}1]$ loop orientation was much different at -0.71, as the combined cluster-loop defect was weaker than an independent dislocation loop. To best represent a random distribution of loop orientations, the fractional strength was averaged over the three loop orientations, for an average fractional strength of 0.16, that is: $\alpha_{c+L} = \alpha_L + 0.16 \cdot \alpha_c$, as a generalized equation.

This result for the average obstacle strength for a random population of a combined cluster-loop defect is only slightly increased as compared to that of a random population of dislocation loops, primarily due to the weakening observed at the $[\bar{1}\bar{1}1]$ loop orientation. However, it must be reminded that these results are reflective of an increased nickel solute concentration, an element which is expected to have relatively minor synergy with a dislocation loop. Other solute elements, such as silicon, may have more of a synergistic effect, though this is beyond the scope of this thesis research.

6.2.3 Relation between MD Simulations and Experimental Results

The dislocation loop sizes used in the MD simulations are slightly smaller than those observed in the irradiated material examined in this study, Table 5.1, due to constraints on the simulation box size. The average diameter of the dislocation loops in this study varied between 8.0-9.6 nm, with an average size of 8.7 nm across all the examined conditions. Based on the identified trend with loop size from the MD simulations, $\alpha_L = \alpha_{o,L}\sqrt{d}$, an average obstacle strength of 0.277 would be anticipated. This obstacle strength is somewhat higher than the experimental fits using the DBH model for this study, which had a fitted obstacle strength of 0.190 for the dislocation loop population. While the precise reason for this variance in loop strength as measured by both methodologies is not known, it is likely due to either the time and spatial limitations of the MD simulations or the simplifications inherent to the DBH model.

It must be noted that the solute concentrations used in the MD simulations were higher than those observed in the irradiated material via APT. The higher solute concentrations were utilized to provide a statistically valid variation between the measured solute concentrations. The APT analysis on the nickel-silicon solute clusters in the as-irradiated found an increased concentration

of 6.1 and 2.6 at.% for ΔNi and ΔSi, respectively, or a total Δsolute of 8.7 at.% in at the core region of the clusters. This value falls short of the lowest ΔNi of 12 at.% used in this study but is not surprising given that the ternary Fe-Ni-Cr potential was not able to accommodate the addition of silicon on the cluster strength, which will likely be substantial. Therefore, approximations were made by comparing the Ni-Si bond strength relative to that of Ni-Ni. To complete this approximation, it was assumed that the relative difference in bond strength is the same as the relative difference in bond dissociation energies. Results on bond dissociation energies show an energy of 225 kJ/mol for a Ni-Ni bond compared to 318 kJ/mol for a Ni-Si bond [204], or a strength increase of 41%. Using a replacement ratio of ~30%, which corresponds to concentrations in the Ni-Si clusters yields a strength increase of ~12% assuming that the bond strengths of Si-Cr and Si-Fe increase the same relative amount as compared to Ni-Cr and Ni-Fe bonds as data for these bond dissociation energies were not available. Including the approximate strengthening effect from silicon: $\alpha_c = 1.12 \cdot \alpha_{o,c}\sqrt{\Delta\text{solute}}$, solute clusters with a chemistry identified in this thesis research should have an obstacle strength of ~0.032. This obstacle strength for solute clusters is less than half of the value of 0.076 obtained using the DBH model for solute cluster populations in the as-irradiated and annealed conditions, though the absolute difference in obstacle strength is less than that present in the dislocation loops. One possible reason for this discrepancy may be additional synergistic effects from silicon, as it is suspected that the earlier approximation based on bond strengths fails to encompass the full contribution of this solute to the cluster strength.

Utilizing the obstacle strengths for independent dislocation loops and solute clusters obtained via the MD simulations, a calculation of the predicted strengthening from the characterized microstructure using the DBH model with an RSS combination was completed, as shown in Figure 6.12. In Figure 6.12, the proportional contribution, i.e. $\Delta{\sigma_y}^2$, of each defect type to the total predicted strengthening is identified. When utilizing the obstacle strengths measured from the MD simulations, a large discrepancy from the experimentally measured strengthening is observed, particularly at low and high annealing conditions. At low annealing conditions, i.e. as-irradiated and 500°C: 1 h, the higher obstacle strength of the dislocation loops leads to an over prediction of the strengthening due to the higher density of dislocation loops characterized in those conditions. At high annealing conditions, such as 550°C: 20 h, we see instead an underestimation of the total strengthening as the dislocation loops have been fully removed, and the lower obstacle strength of the solute clusters. Overall, the obstacle strengths determined by the MD simulations

of independent dislocation loops and solute clusters, due not match with the experimentally observed strengthening when utilizing the DBH model, though it is not clear if this discrepancy results from limitations in the MD simulations, simplifications of the DBH model, or a partial responsibility of both.

The MD simulations of a combined defect of a solute cluster and a dislocation loop listed in Table 6.4 observed an average obstacle strength of 0.279, though this was seen to fluctuate with obstacle size, loop orientation, and solute concentration. This strength of the combined defect was observed to be proportional to the strengths of the independent loop and cluster, such that $\alpha_{c+L} = \alpha_L + X \cdot \alpha_c$, where X = 0.16 for a population with a random loop orientation. Based on the predicted obstacle strengths of dislocation loops and solute clusters of the experimentally observed microstructure, 0.277 and 0.032, respectively, a combined cluster-loop defect would have an obstacle strength of ~0.282. To better understand the effect of that a combined cluster-loop defect may have on the overall strengthening of a material, a calculation was made assuming that all the experimentally observed dislocation loops were instead combined cluster-loop defects. Assuming a combination of one cluster per loop, due to their similar sizes, the density of dislocation loops was subtracted from the density of solute clusters at each annealing condition, to reflect their participation in the combined defect; no change in the average size of solute clusters population was assumed. As the experimentally measured density of solute clusters is higher than that of dislocation loops, the remaining solute clusters not on loops were considered as separate defects and contributed to the overall strengthening with an RSS combination. A graphical representation of the total strengthening is shown in Figure 6.13, where the relative proportion of the strengthening from either the combine cluster-loop defects and the independent solute clusters is identified. As compared to the case of independent loops and clusters (Figure 6.12) there is a negligible difference in the total strengthening as the slight increase in the strength of the combined cluster-loop obstacle, as compared to the strength of an independent dislocation loop, is offset by the decrease in the density of independent solute clusters. This data shows that the strengthening predicted by a completely independent population of dislocation loops and solute clusters is very similar to that predicted for a population containing some fraction of combined cluster-loop defects, thus implying that combined cluster-loop defects will not affect the strengthening of a material beyond that of the individual defects.

Overall, there was a consistency between the obstacle strengths of solute clusters and dislocation loops as measured from MD simulations and fit to the characterized microstructure through the DBH model. Both methods showed comparable trends in that the strength of dislocation loops was much higher than that of the solute clusters. These variances in obstacle strengths between both methodologies can be easily attributed the time and spatial limitations of the MD simulations or the simplifications inherent to the DBH model. In this manner, the MD simulations helped to both validate the obstacle strengths predicted by the DBH model and provide a better understanding of the effect of obstacle size, loop orientation, and solute concentration on the resultant obstacle strength. Finally, the MD simulations were able to demonstrate that a full population of combined cluster-loop defects, would have a negligible impact on the predicted strengthening of a material as compared to a population of independent solute clusters and dislocation loops.

6.3 Evolution of Localized Deformation with PIA

The localized deformation present in the as-irradiated and annealed conditions was characterized through multiple methods in the CERT and four-point bend specimens. The localized deformation was examined based on the bulk dislocation channel density, density of both discontinuous and continuous channel-grain boundary intersection sites, and the average channel spacing for the tensile specimens. The four-point bend specimens were characterized based on the bulk dislocation channel density, average dislocation channel spacing, and the fraction of channeled surface area. Overall, no statistically significant variations were observed in the bulk dislocation channel density, shown in Figure 6.14, for the as-irradiated condition and annealing conditions: 500^{o}C: 1 h, 550^{o}C: 1 and 5 h for both the four-point bend and CERT specimens. A significant change in the bulk dislocation channel density was observed after an annealing treatment of 550^{o}C: 20 h. This characterization also shows that the density of dislocation channels increased rapidly at low levels of strain, before leveling off at higher strains; indicating that a majority of the dislocation channels were formed between 0-2% plastic strain. It should be remembered that the bulk dislocation channel density is an average over the entire examined surface and includes many grains which did not display dislocation channel formation. However, by dividing the bulk channel density by the fraction of channeled area, a measurement of the

average channel density in grains with dislocation channels would be determined. Unlike the bulk channel density, this average dislocation channel density in grains with channeling was observed to largely increase with annealing, at least over the limited conditions where both measurements were made.

The examination of the dislocation channel-grain boundary interaction sites in the CERT specimens revealed both that most of all dislocation channel-grain boundary intersection sites were discontinuous in nature, and the density of such sites changes relative to the overall density of dislocation channels, as shown in Table 5.11. Furthermore, it was noted that the ratio of discontinuous to continuous interaction sites remained relatively constant in response to both strain and annealing treatments, in Table 5.11. While it has been previously established that discontinuous channel-grain boundary intersection sites are preferred sites for IASCC crack initiation [7,149] due to their enhanced local stresses [148], the fact that the ratio of discontinuous to continuous interaction sites remains constant with annealing treatments implies that the mitigation of IASCC susceptibility with PIA treatments is not due to an increase in the ease of slip transfer across grain boundaries.

Channel spacing is observed to decrease monotonically with plastic strain. There is no significant difference in the average channel spacing between CERT and 4-point bend samples for each annealing condition when compared based on local plastic strain, as in Figure 6.15. The trend lines shown in Figure 6.15 are fit to the data from Table 5.11 and Table 5.15 for each annealing condition, regardless of the specimen type. With regards to the annealing condition, a clear decrease in channel spacing is present following annealing treatment at 500^{o}C: 1 h and 550^{o}C: 1 h, though no further decreases in channel spacing are observed following annealing treatments of 550^{o}C: 5 and 20 h. As there was no statistical variation in the average channel spacing between the specimens annealed at 550^{o}C:1, 5, and 20 h, the measurements for these specimens were fit with a single curve in Figure 6.15. With regards to strain, the average channel spacing was observed to decrease with increasing plastic strain, regardless of the annealing condition. This is due to the initiation of new dislocation channels to accommodate the increased strain.

Finally, the localized deformation in the four-point bend specimens was also characterized by the fraction of channeled area, as shown in Figure 5.38. This characterization shows that the fraction of channeled area increased rapidly at low levels of strain, before leveling off at higher strains. This is reflective of the initiation of dislocations in new grains as strain increases, until

~85% of grains contain channels in the as-irradiated condition at 5% plastic strain. Annealing treatments of 500°C: 1 h and 550°C: 5 h were observed to decrease the fraction of channeled area by ~10% as compared to the as-irradiated conditions. This implies that roughly 50% as many grains were able to accommodate the applied strain without forming dislocation channels after these annealing conditions as compared to the as-irradiated condition. A further reduction in the fraction of channeled area was observed after annealing at 550°C: 20 h, however, this is difficult to validate as it consists of a singular data point.

6.3.1 Dependence of the Localized Deformation on the Irradiated Microstructure

The degree of localized deformation, including channel spacing, has been previously linked to the irradiated microstructure in proton-irradiated 300-series steels, and was shown to primarily depend on the dislocation loop density [100]. Thus, it is worth examining the relation between the irradiated microstructure and the localized deformation, which was best characterized by the average channel spacings shown in Figure 6.15, and their changes under annealing treatments. The strengthening from the Ni-Si solute clusters, shown in Table 6.3, decreased to only ~90% of the as-irradiated condition after annealing up to 550°C: 1 h, by which point all reduction in the average channel spacing had occurred. Therefore, the comparison between the average channel spacing and the irradiated microstructure will focus on the dislocation loop population, previously listed in Table 5.1, which was observed to significantly change under annealing. After annealing at 500°C: 1 h, the dislocation density and average channel spacing similarly dropped to ~75% of the as-irradiated condition. However, during annealing at 550°C, the faulted dislocation loop population continued to decrease to ~30% of as-irradiated density after 550°C: 1 h and full removal after 550°C: 20 h. Meanwhile, the average channel spacing stabilized to ~65% of the as-irradiated condition after 550°C: 1 h and did not change with further annealing at 550°C: 5 and 20 h. While the changes in dislocation channel spacing and dislocation loop density matched well up to 500°C: 1 h, their behaviors began to diverge at higher annealing treatments, suggesting that the two measurements are not directly correlated.

One explanation for this divergence is that the evolution of the localized deformation under annealing is not fully captured by the measurement of average channel spacing. The reduction in the dislocation loop population matched quite well with average channel spacing up to 550°C: 1

h, however, the negligible changes in channel spacing with increased annealing treatments suggests a minimum channel spacing of ~4-5 μm. Thus, rather than visibly reducing the channel spacing, further annealing resulted in a decrease in the fraction of channeled area, which is another indication of homogenization of the applied strain. This is particularly evident in the bend specimen at 550°C: 20 h, which had only ~50% of channeled area as compared to similarly strained specimens in the as-irradiated condition. Also, since the Ni-Si clusters controlled the hardening at these longer heat treatments, the channel spacing will be dictated by their size distribution rather than that of the loops. This demonstrates that the relationship between the irradiated microstructure and localized deformation is quite complex and a more in-depth characterization will be needed before it can be fully understood.

6.3.2 Consistency between CERT and Four-Point Bend Test Results

The localized deformation in CERT and four-point bend experiments had an overlapping characterization in both the dislocation channel density and average dislocation channel spacing and IASCC susceptibility following PIA treatments. The bulk dislocation channel density on the specimen surface showed similar values and trends between both the tensile and four-point bend specimens with local plastic strain as shown in Figure 6.14, though it must be noted that neither specimen type displayed an obvious response to the annealing treatments. Unlike the dislocation channel density, the average dislocation channel spacing displayed a clear change in response to the annealing treatments in both the CERT and 4-point bend specimens, as shown in Figure 6.15. This behavior confirms that the localized deformation in both the CERT and 4-point bend specimens developed in the same manner with applied strain. Due to its measurable change with annealing treatments, and its measurement in both the tensile and four-point bend specimens, the average dislocation channel spacing was selected to best quantify the changes in the localized deformation with PIA, and its relation to the mitigation of IASCC susceptibility.

6.4 Mitigation of IASCC Susceptibility

The mitigation of IASCC susceptibility of the tensile specimens from this study are compared to several similar PIA neutron-irradiated austenitic stainless steels in Figure 6.16

[77,78,167,171]. IASCC susceptibility is assessed by comparing the fraction of intergranular fracture after annealing relative to the as-irradiated condition. The annealing conditions are normalized based on iron diffusion distance (d), which is calculated as $d = \sqrt{Dt}$, where t is the annealing time, D is the iron self-diffusion coefficient given by $D = D_o \exp(-Q/kT)$, and T is the annealing temperature, k the Boltzmann constant, Q the migration energy: 2.95 eV, and D_o equals 4.9 x 10^{-5} m^2/s [78]. There is a good comparison between the prior literature data and the results from this study, except for the 550°C: 20 h samples. The results match particularly well with the data from Jacobs *et al.* [171] who also used 304L SS with similar irradiation dose, and water chemistry, i.e. BWR-NWC. These experiments by Jacobs also displayed a large variation in IASCC susceptibility around annealing at 500°C: 1 h.

6.4.1 Susceptibility of the 550°C:20 h Treatment

A clear discrepancy in IASCC behavior was observed for the specimens annealed at 550°C: 20 h in both CERT and four-point bend experiments. Despite full mitigation of IASCC by 1 h at 550°C, all the specimens annealed at 550°C: 20 h showed very high susceptibility to crack initiation. Cracks appeared to be related to grain boundary etching that occurred following the electropolishing procedure, as shown in Figure 6.17. In fact, cracks occurred preferentially at the etched grain boundaries leading to an extremely high degree of intergranular fracture of the T-12 tensile specimen: ~165% that of the as-irradiated condition. Similarly-etched grain boundaries were identified on the sides of the 12-B1 bend specimen, which were directly correlated with the location of crack initiation in that specimen.

A lift out taken near one of the etched grain boundary sites of the T-12 (550°C: 20 h) tensile specimen was characterized using an FEI Talos F200, analytical TEM-STEM optimized for X-ray spectroscopy in the LAMDA laboratory by Dr. Phil Edmundson at Oak Ridge National Laboratory [205]. Energy-dispersive X-ray spectroscopy (EDS) maps taken along the edge-on grain boundary revealed the formation of chromium-rich precipitates on the grain boundary and a corresponding depletion of chromium at the grain boundary, Figure 6.18. Figure 6.19 shows a comparison of the chromium concentration in this grain boundary [205] compared to chromium RIS in the previously examined grain boundaries for the as-irradiated and 550°C: 5 h conditions. The deep and comparatively wide chromium depletion profile is indicative of the onset of sensitization caused

by the precipitation of chromium carbides at the grain boundary [206]. Since the 304L alloy was used in the solution annealed condition, and no grain boundary carbides were observed in any condition besides the 550°C: 20 h condition, it is concluded that this heat treatment resulted in precipitation of carbides and the consequent chromium depletion. That this heat treatment was sufficient to initiate sensitization was verified by the small fraction of grains displaying precipitation and etching during electropolishing. The low bulk concentration of carbon in this heat is just outside of the precipitation zone in the industry-standard time-temperature-sensitization curves (Figure 2.2) for an annealing treatment of 550°C:20 h, but earlier work by Katsura *et al.* [167] suggests that irradiated alloys may be more susceptible to sensitization than their unirradiated counterparts. Based on the evidence provided, it was concluded that the specimens annealed at 550°C: 20 h underwent some degree of sensitization, which severely enhanced the susceptibility to IGSCC. As such, this annealing condition is excluded from the following discussion of processes controlling IASCC mitigation with PIA.

6.4.2 Consistency between CERT and Four-Point Bend Test Results

CERT and four-point bend experiments displayed similar behaviors with regard to the IASCC susceptibility following PIA treatments, but some variations were observed, as shown in Figure 6.20. There are two primary differences between CERT and four-point bend specimens that may cause differences in the extent of cracking: through-thickness stress state and effective surface area. The through-thickness stress state in a tensile experiment permits cracks that initiate on the surface to grow inward into the specimen. For a four-point bend specimen, the gradient in stress from tensile on the examination surface to compressive stress on the opposite side causes crack propagation to be confined to the surface. The effect of this phenomenon can be observed in Figure 6.20 when comparing the as-irradiated T-4 CERT specimen and four-point bend specimens: 4-B and 10-B1. While all examined specimens were initiated between 4-6% local strain, the two bend specimens showed a self-consistent but higher crack length density with strain as compared to the CERT specimen. This difference is due to most of the crack advancement in the CERT specimen being into the specimen, rather than along the surface, whereas the stress gradient in the four-point bend specimens limits their advancement to the tensile surface.

The second consideration is the effective surface area of the specimen, the four-point bend specimens are much smaller than the tensile specimens, having an examination area of ~1.5 mm^2 compared the ~35 mm^2 of an entire tensile gage length. Considering only the necked region of the tensile specimen, where all crack initiation occurred in the examined specimens, the average examination area is still ~8-9 mm^2. This means that the tensile specimens have an effective examination area of at least five times that of a four-point bend specimen. For the case of the tensile specimen, T-5, where only a single crack initiation site was identified, it can be inferred that the equivalent bend specimen, 9-C, would have a less than 20% chance of having an identical site within its examination area. As such, the small size of four-point bend specimens limits their applicability in examining materials conditions with a relatively low chance of crack initiation.

6.5 Processes Responsible for the Mitigation of IASCC Susceptibility with PIA

The IASCC susceptibility as measured by both crack length per unit area ($\mu m/mm^2$) and the percent intergranular fracture (%IG) in four-point bend and CERT experiments, respectively, along with other factors that may affect the observed cracking susceptibility are plotted in Figure 6.21. The IASCC susceptibility decreased rapidly with annealing treatments, to a value of ~70% of the as-irradiated condition after 500°C: 1 h and full mitigation after 550°C: 1 h for the CERT specimens, while cracking in the four-point bend test was fully removed by 500°C: 1h. The irradiation hardening and increase in yield stress, assuming an unirradiated yield stress of 211 MPa, were observed to similarly decrease with the extent of annealing. However, this occurred at a much slower rate than that of the IASCC mitigation, with both values at ~70% of their as-irradiated state after annealing at 550°C: 1 h. The defect populations of dislocation loops and Ni-Si solute clusters from Table 5.1 and Table 5.2 are normalized on the basis of $\sqrt{Nd}$, which is representative of their effect as obstacles to mobile dislocations. Compared to the as-irradiated condition, the $\sqrt{Nd}$ for dislocation loops decreased to ~90% after annealing at 500°C: 1 h and to ~55% after 550°C: 1 h. Meanwhile the decrease in $\sqrt{Nd}$ for solute clusters was much slower at higher temperatures, remaining at ~90% after the 550°C: 1 h annealing treatment. While the data of chromium RIS, Table 5.4, was not available for the 500°C: 1 h and 550°C: 1 h conditions, ~60% of the as-irradiated chromium segregation was remaining after 550°C: 5 h, suggesting that at least that much segregation, and likely more based on previous literature [78,132], was remaining when

IASCC was fully mitigated. The annealing of silicon RIS was much faster, decreasing to ~16% and to ~6% of the as-irradiated state after annealing treatments of 550^{o}C: 5 and 20 h, respectively. However, as IASCC is known to occur in silicon-free alloys [126], its role could be to enhance the susceptibility relative to higher purity alloys. Furthermore, the segregation data for the most critical annealing conditions, 500^{o}C: 1 h and 550^{o}C: 1 h, are not available, thus it is difficult to determine the exact silicon or chromium segregation when IASCC was fully mitigated, and thus the precise role that it may have played as well. The change in the average dislocation channel spacing with annealing was calculated by the trend lines shown in Figure 6.15 at 2% plastic strain, but it should be noted that only slight variations, i.e. <5%, were observed in the relative average channel spacing between 2 and 10% plastic strain. As the trend in average channel spacing is the same for the 550^{o}C: 1, 5, and 20 h annealing conditions, they share the same value as compared to the as-irradiated conditions.

While all the examined features decrease with increasing annealing treatments, none were observed to decrease in the exact same way (or rate) as the IASCC susceptibility, as measured by either the CERT or four-point bend specimens. More specifically most of the examined features have minimal changes after annealing at 500^{o}C: 1 h, where the largest change in IASCC mitigation occurred. Unlike the other examined features, the average dislocation channel spacing, displayed a similar shape as the IASCC mitigation in that it decreased rapidly after annealing at 500^{o}C: 1 h and 550^{o}C: 1 h, and remained constant thereafter. Furthermore, 70% of the total reduction occurred after annealing at 500^{o}C: 1 h and full reduction occurred after 550^{o}C: 1 h, similar to the average IASCC mitigation from both the CERT and four-point bend experiments, i.e. ~65% reduction after 500^{o}C: 1 h and 100% after 550^{o}C: 1 h. The desegregation of silicon from the grain boundaries displayed the second-best correlation with the removal of IASCC susceptibility, decreasing to 16% of the as-irradiated condition after annealing at 550^{o}C: 5 h. As silicon has been previously shown to significantly enhance crack growth rate in similar alloys [134–136], it is worth discussing the possible role that the grain boundary silicon may have had in this study.

6.5.1 Role of Localized Deformation in Mitigating IASCC Susceptibility

Of all the features examined, the decrease in the average channel spacing with annealing displayed the best correlation with the mitigation of IASCC susceptibility following annealing

treatments. However, correlation does not necessarily imply causation, thus it is important to verify that this observation fits with our current understanding of IASCC initiation. Recent studies of the crack initiation in irradiated austenitic stainless steels have shown an increasing relevance of the role of localized deformation in the IASCC susceptibility and crack initiation [4,6,7,147,207]. These studies have shown that grain boundaries that are intersected by discontinuous dislocation channels have a higher fraction of crack initiation, as compared to boundaries that transmit strain between adjacent grains [7], and that this enhanced cracking fraction is likely due to the high tensile stress at these intersections [147,148]. This increase in stress has been linked to the pile-up of dislocations at the grain boundary after moving through the dislocation channel. It has also been observed that there is a pseudo-threshold ("pseudo" as the value may be specific to environment, alloy composition, etc.) level of stress required to initiate cracks [147,148]. It should also be noted that triple junctions had a similarly high cracking fraction as these sites also experience high local stresses [7]. From this perspective it is important to analyze how the observed changes in the localized deformation following PIA treatments, may have led to the mitigation of IASCC susceptibility.

Figure 6.15 clearly shows that the average dislocation channel spacing decreases with both increased strain and the extent of annealing. The decrease in average channel spacing with increasing strain is due to the formation of new channels as the total strain in the specimen is increased. The decrease in spacing with the extent of annealing is likely related to the removal of dislocation barriers, thus enabling the initiation of additional channels at lower strains. As a prior study by Jiao *et al.* [21] has shown, in the irradiated state, most of strain is confined to the dislocation channels and for the same strain, a higher channel density results in fewer dislocations per channel and therefore, lower stress concentration at the grain boundary [148]. This is in addition to the fact that following annealing, even grains that display channel formation will be more likely to accommodate some of the strain in a homogeneous manner outside of the dislocation channels, further reducing the pile-up in channels.

Also indicated in Figure 6.15 is the plastic strain at which crack initiation was first identified. In both the as-irradiated and the 500^{o}C: 1h cases, this value was ~5%. Note that the high plastic strains for crack initiation for two of the as-irradiated specimens are slightly misleading as both specimens displayed a large degree of crack initiation during that strain increment and are suspected to have initiated much earlier. This requirement of a significant plastic strain for IASCC

crack initiation suggests that a build-up to a pseudo-threshold stress through dislocation pile-up may have been required. The smaller channel spacing and reduced IASCC susceptibility of the 550^{o}C annealed specimens further supports this reasoning. While additional dislocation channels form under increased strain, these new channels will not reduce the amount of dislocations piled-up in the preexisting channels, nor will the further strain in the grain be confined to just these new channels. As the annealing treatments cause the formation of additional dislocation channels at lower strains, these additional channels will more evenly distribute the stresses from the pile-up dislocations, presumably keeping this below the threshold stress required for crack initiation.

The agreement between the behavior of the IASCC susceptibility and the dislocation channel spacing matches with the present picture of crack initiation due to a critical local stress, most commonly achieved by the increased stresses at dislocation channel-grain boundary intersections [148]. However, it is important to examine the crack initiation sites in this study to determine if they are consistent with the occurrence of discontinuous dislocation channels. In this study, four of the examined specimens: T-4, 4-B, 10-B1, and T-5, displayed IASCC crack initiation. The T-4 (as-irradiated) tensile specimen displayed a large degree of crack initiation and advancement in a singular strain increment, hence the location of the first crack initiation site was not identifiable. The 10-B1 (as-irradiated) specimen also displayed an appreciable amount of crack initiation and advancement in a single increment, however, as this was a four-point bend specimen, the crack growth was limited, and the initiation location was able to be identified to a reasonable degree.

Figure 6.22 displays the location of crack initiation for the 4-B (as-irradiated) bend specimen that occurred between strains of 4.04% and 5.18%. From these images the crack clearly nucleated on a boundary with discontinuous channels impinging from both adjacent grains. Figure 6.23 displays the location of crack initiation for the 10-B1 (as-irradiated) bend specimen. As mentioned before this specimen exhibited a large degree of crack advancement, however, the most probable crack ignition location was identified by both the crack opening and changes in the localized deformation. The incremental straining of this specimen allowed the location to be examined for both the increment prior to initiation at 5.19% plastic strain, Figure 6.23a, and after initiation at 10.77% strain, Figure 6.23b. As discussed earlier the average channel spacing decreased with increased strain, while it is also known that the advancement of a crack will created a local stress/strain field as it advances. By comparing the relative changes in the localized

deformation in grains beside which the crack advanced, the crack was determined to have most likely initiated along one of the two grain boundaries between the two white arrows shown in Figure 6.23b, as the neighboring grains to these boundaries showed the least increase in dislocation channels. An examination of these boundaries reveals that the lower boundary had impinging discontinuous channels, while the upper boundary had channels running parallel to the boundary. While these discontinuous channels were not impinging directly on the grain boundary, their proximity to the triple junctions may have enhanced the stress state at those locations. As such, while the initiation location is not precisely known, the most probable location is a boundary at which discontinuous channels impinge.

Figure 6.24 displays the location of crack initiation for the T-5 (500^{o}C: 1 h) tensile specimen; due to the incremental straining the location was examined for both the increment prior to initiation at 1.21% local plastic strain, Figure 6.24a, and after initiation at 5.47% local strain, Figure 6.24b. This crack initiation site is particularly interesting as no defining features are present following the increment prior to initiation. Based on the crack opening, it is presumed that the crack initiated at the upper triple junction, where the white arrow is pointing. Like the upper boundary in the 10-B1 bend specimen, this triple junction appears to have discontinuous channels intersecting near the grain boundaries.

6.5.2 Role of Silicon Segregation in the Mitigation of IASCC Susceptibility

While the decreased dislocation channel spacing with PIA treatments explains a mitigation of IASCC through a reduced likelihood of crack initiation, it must be remembered that IASCC is not solely dependent on a stress [149], but also corrosion. The role of silicon in the corrosion of stainless steels has been previously established, with an increased silicon content being closely linked to an enhanced grain boundary corrosion in simulated BWR-HWC environments [134–136]. This enhanced corrosion is theoretically linked to an increased dissolution rate of silicon oxide at the grain boundary in relation to the environmental overpotential, which is in turn affected by the silicon content as shown in Equation 2.8. This study observed a rapid reduction of the grain boundary silicon concentration following annealing treatments, displaying the next best correlation with the mitigation of IASCC susceptibility following localized deformation (Figure

6.21). As such, it is worth discussing the possible role that silicon segregation may have in IASCC mitigation, either through the crack initiation event or in the later propagation of an initiated crack.

During exposure to high temperature water, silicon is readily oxidized to SiO_2 which then dissolves [136]. As such, an increased silicon concentration at a grain boundary may increase the likelihood of crack initiation by increasing both the amount of SiO_2 present at the grain boundary as well as its dissolution rate. Such dissolution has been clearly documented by Lou *et al.* [136] where the Si-rich oxides were dissolved from the grain boundaries, leaving an observable etching along the boundary and increasing the likelihood of crack initiation. As this dissolution rate would be controlled by the overpotential, we would expect a greater etching from SiO_2 dissolution in the as-irradiated condition, which had the highest grain boundary silicon concentration, as compared to the annealed specimens. However, no appreciable grain boundary etching was observed in either the as-irradiated nor annealed conditions, as shown in Figure 6.22 and Figure 6.23, suggesting that grain boundary SiO_2 dissolution did not play a significant role in the crack initiation observed in this study. This negligible response to silicon content is likely due to the large overpotential present in the simulated BWR-NWC environment. The difference in overpotential between the as-irradiated and 550^{o}C: 20 h conditions due to silicon concentration is ~20 mV_{SHE} from Equation 2.8, as compared to the overpotential created by the environment, ~1200 mV_{SHE}; thus, its influence on corrosion is not observed.

The second consideration is the possible role of grain boundary silicon on the crack propagation rate; for this study any enhancement of crack growth would be most reflected in the %IG of the fracture surface of the tensile specimens. Fortunately, there exist several studies which examined the effect of silicon content on crack growth rate [134–136]. While tensile specimens are quite different from the compact tension specimens used in those studies, it can be assumed that the dependence of the crack propagation rate on the environment and silicon concentration should be consistent between both specimen types. The work by Li *et al.* [134] and Andresen *et al.* [135] demonstrated a clear increase in the crack growth rate with increasing silicon concentration in an BWR-HWC water environment, however, no significant variations in crack growth rate were observed in a BWR-NWC environment. This lack of response under NWC conditions is explained by the environmental conditions at the crack tip. As the oxygen in the water reacts with silicon to form an oxide, the potential of the water is reduced, thus reducing the overpotential and the dissolution rate of the resultant SiO_2. While the overpotential should still

increase with increasing silicon concentration in accordance to Equation 2.8, an increased silicon concentration would lead to increased oxidation, and hence a further reduction of the water potential in the crack tip. These shifts in the overpotential balance under NWC conditions, leading to a relatively constant crack growth rate, irrespective of the silicon content. Based on these studies, we would not expect the crack growth in our tensile specimens to have been significantly changed by the differential grain boundary silicon content between our as-irradiated and annealed specimens, and the observed differences in intergranular fracture are instead related to a decrease in the stress intensity at the crack tip due to a reduced strength after annealing.

The results of this thesis work have confirmed a connection between IASCC crack initiation and localized deformation, or more precisely the high local stresses that may result from discontinuous dislocation channels impinging on a grain boundary [148]. Post-irradiation annealing caused a reduction in the average channel spacing in both CERT and four-point bend tests, presumably due to the easier formation of independent dislocation channels at lower plastic strains. This decrease in spacing resulted in an increased homogenization of deformation and reduced pile-up stresses in the channel-grain boundary intersection. A closer investigation of the crack initiation locations in this study revealed that all initiation sites were related to high stress locations, by virtue of discontinuous channels impinging on the grain boundary or a triple junctions. However, it must be remembered that IASCC is not solely dependent on a stress, thus corrosion-based phenomenon must also be considered. Silicon de-segregation displayed the next best relation to the mitigation of IASCC susceptibility with PIA (Figure 6.21) of all the examined features in this study. While this result is consistent with prior studies on the role of silicon in increasing corrosion, no direct evidence was identified in this research work, confirming that the role of silicon may be limited to more of an enhancement of IASCC susceptibility, rather than the underlying cause. The results of this thesis research are consistent with the prior research regarding the role of discontinuous channels in IASCC susceptibility, being the mostly closely related factor with the mitigation of IASCC under PIA treatments.

Table 6.1. Parameters used for the dislocation loop and solute cluster annealing simulations [57,80,208].

Parameter	Notation	Value
Lattice Constant	a	3.5146 Å
Burgers Vector	b	0.2485 nm
Stacking Fault Energy	Γ	0.018 N/m
Shear Modulus	μ	76 GPa
Taylor Factor	M	3.06
Dislocation Line Energy	U ($\mu b^2/2$)	2.35 x 10^{-9} N
Vacancy Jump Frequency: Fe	ω_{Fe}	2.7 x 10^{13} s^{-1}
Vacancy Jump Frequency: Cr	ω_{Cr}	4.7 x 10^{13} s^{-1}
Vacancy Jump Frequency: Ni	ω_{Ni}	1.5 x 10^{13} s^{-1}
Vacancy Correlation Factor: Fe	$F_{Fe,v}$	0.785
Vacancy Correlation Factor: Cr	$F_{Cr,v}$	0.668
Vacancy Correlation Factor: Ni	$F_{Ni,v}$	0.872
Vacancy Migration Energy for Pure Fe	$E_{v,m}^{Fe}$	1.28 eV
Vacancy Migration Energy for Pure Cr	$E_{v,m}^{Cr}$	0.97 eV
Vacancy Migration Energy for Pure Ni	$E_{v,m}^{Ni}$	1.04 eV
Vacancy Formation Energy for Pure Fe	$E_{v,f}^{Fe}$	1.40 eV
Vacancy Formation Energy for Pure Cr	$E_{v,f}^{Cr}$	1.60 eV
Vacancy Formation Energy for Pure Ni	$E_{v,f}^{Ni}$	1.79 eV
Recombination Volume	Z	12

Table 6.2. Fitting of obstacle strengths for the characterized dislocation loops, Ni-Si clusters and Al-Cu clusters based on DBH model, assuming either a simple summation or root-sum-square (RSS) combination.

Fitted Conditions	Summation Method	Fitted α Value		
		Dislocation Loop	Ni-Si Cluster	Al-Cu Cluster
All Conditions	Summation	0.107 ± 0.025	0.056 ± 0.027	0.016 ± 0.024
Exclude 550°C: 5 h		0.076 ± 0.038	0.125 ± 0.070	-0.062 ± 0.003
All, but no Al-Cu		0.096 ± 0.017	0.073 ± 0.006	--
All Conditions	RSS	0.172 ± 0.050	0.095 ± 0.030	-0.056 ± 0.028
Exclude 550°C: 5 h		0.155 ± 0.051	0.121 ± 0.038	-0.111 ± 0.045
All, but no Al-Cu		0.190 ± 0.043	0.076 ± 0.030	--

Table 6.3. Irradiation strengthening determined from the measured hardening and an estimated starting yield strength of 212 MPa, $\Delta\sigma_{y,Hv,}$ along with the estimated contribution of the microstructure to the change in yield stress using the DBH model and an RSS combination, $\Delta\sigma_{y,\ DBH}$, of dislocation loops, $\Delta\sigma_{y,\ loop}$, and Ni-Si solute clusters, $\Delta\sigma_{y,\ Ni\text{-}Si}$.

Annealing Condition	$\Delta\sigma_{y,\ Hv}$ (MPa)	$\Delta\sigma_{y,\ DBH}$ (MPa)	$\Delta\sigma_{y,\ loop}$ (MPa)	$\Delta\sigma_{y,\ Ni\text{-}Si}$ (MPa)
As-Irradiated	448.5	433.0	333.9	275.7
500°C: 1 h	370.3	393.6	308.8	244.0
550°C: 1 h	319.1	307.6	187.1	244.1
550°C: 5 h	222.8	236.3	110.9	208.7
550°C: 20 h	153.5	168.6	0	168.6

Table 6.4. Compilation of the examined defect types, sizes, solute concentration, and loop orientations from the MD simulations and their calculated obstacle strengths. Also included is the fractional strength of the solute cluster added to the combined defect structure, as compared to the strength of an independent dislocation loop.

Obstacle Type	Loop Orientation/ Cluster Shape	Diameter (nm)	Nickel (at.%)	Obstacle Strength (α)	Fractional Cluster Strength (X)
None	Friction Stress	--	12	--	--
Dislocation Loop	$[1\bar{1}1]$	3	12	0.212 ± 0.009	--
		5	12	0.301 ± 0.015	--
		7	12	0.330 ± 0.012	--
	$[\bar{1}\bar{1}1]$	3	12	0.195 ± 0.043	--
		5	12	0.184 ± 0.084	--
		7	12	0.176 ± 0.086	--
	$[\bar{1}11]$	3	12	0.124 ± 0.027	--
		5	12	0.160 ± 0.039	--
		7	12	0.273 ± 0.043	--
Solute Cluster	Spherical	3	50	0.043 ± 0.013	--
		4	50	0.062 ± 0.019	--
		5	25	0.034 ± 0.018	--
			50	0.067 ± 0.019	--
			75	0.079 ± 0.016	--
		6	50	0.063 ± 0.019	--
		7	25	0.038 ± 0.016	--
			50	0.058 ± 0.010	--
			75	0.078 ± 0.016	--
Loop-Cluster Combined Defect	$[1\bar{1}1]$ + Spherical	3	50	0.257 ± 0.033	1.05 ± 0.30
		5	25	0.310 ± 0.013	0.36 ± 0.52
			50	0.338 ± 0.025	0.54 ± 0.29
			75	0.341 ± 0.016	0.58 ± 0.20
		7	50	0.370 ± 0.020	0.69 ± 0.17
	$[\bar{1}\bar{1}1]$ + Spherical	5	50	0.136 ± 0.051	-0.71 ± 0.29
	$[\bar{1}11]$ + Spherical	5	50	0.203 ± 0.021	0.65 ± 0.29

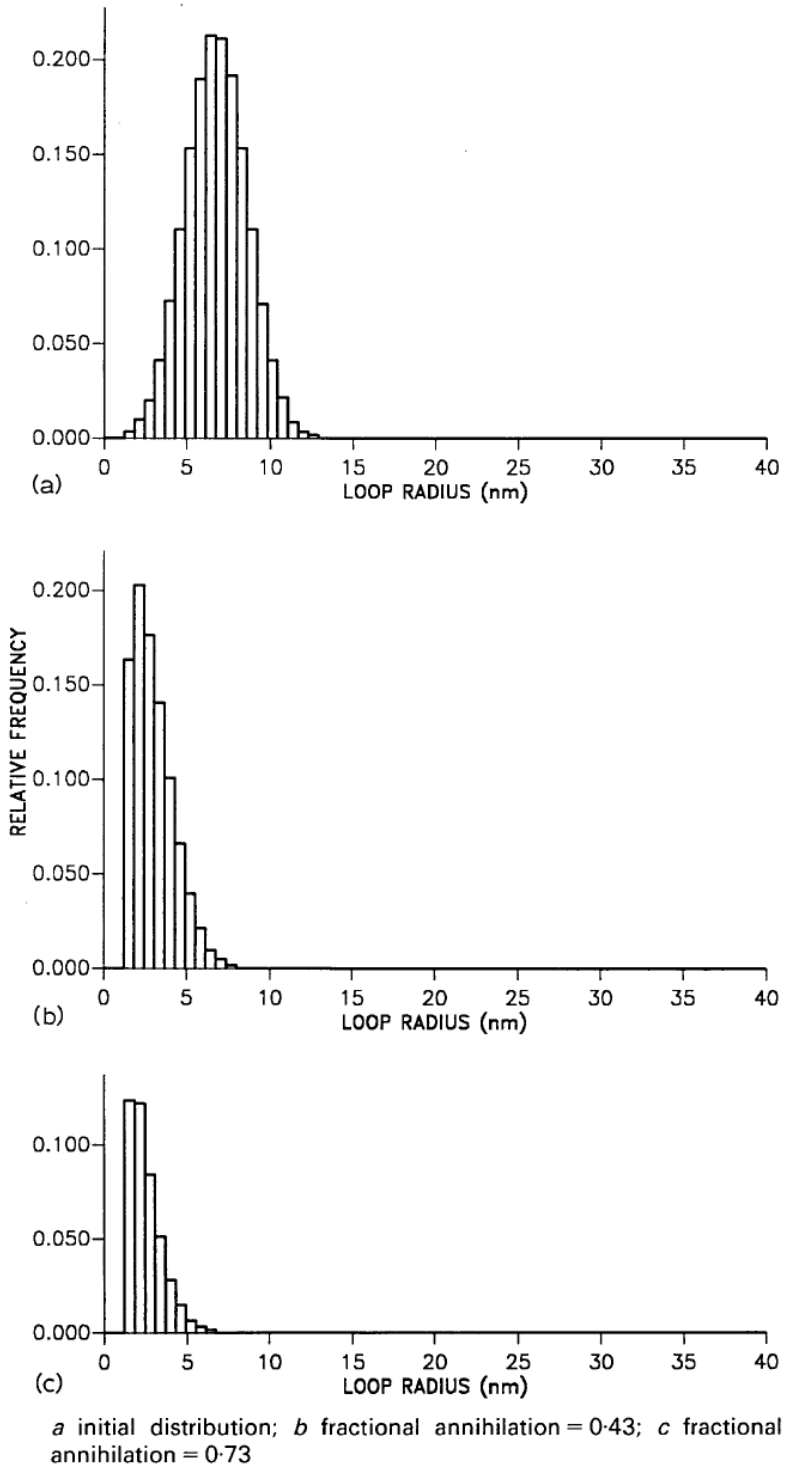

a initial distribution; *b* fractional annihilation = 0·43; *c* fractional annihilation = 0·73

Figure 6.1. Calculation of the annealing behavior of a population of faulted dislocation loops where abundant external sources and sinks are present. A clear dissolution of the loop population is observed [170].

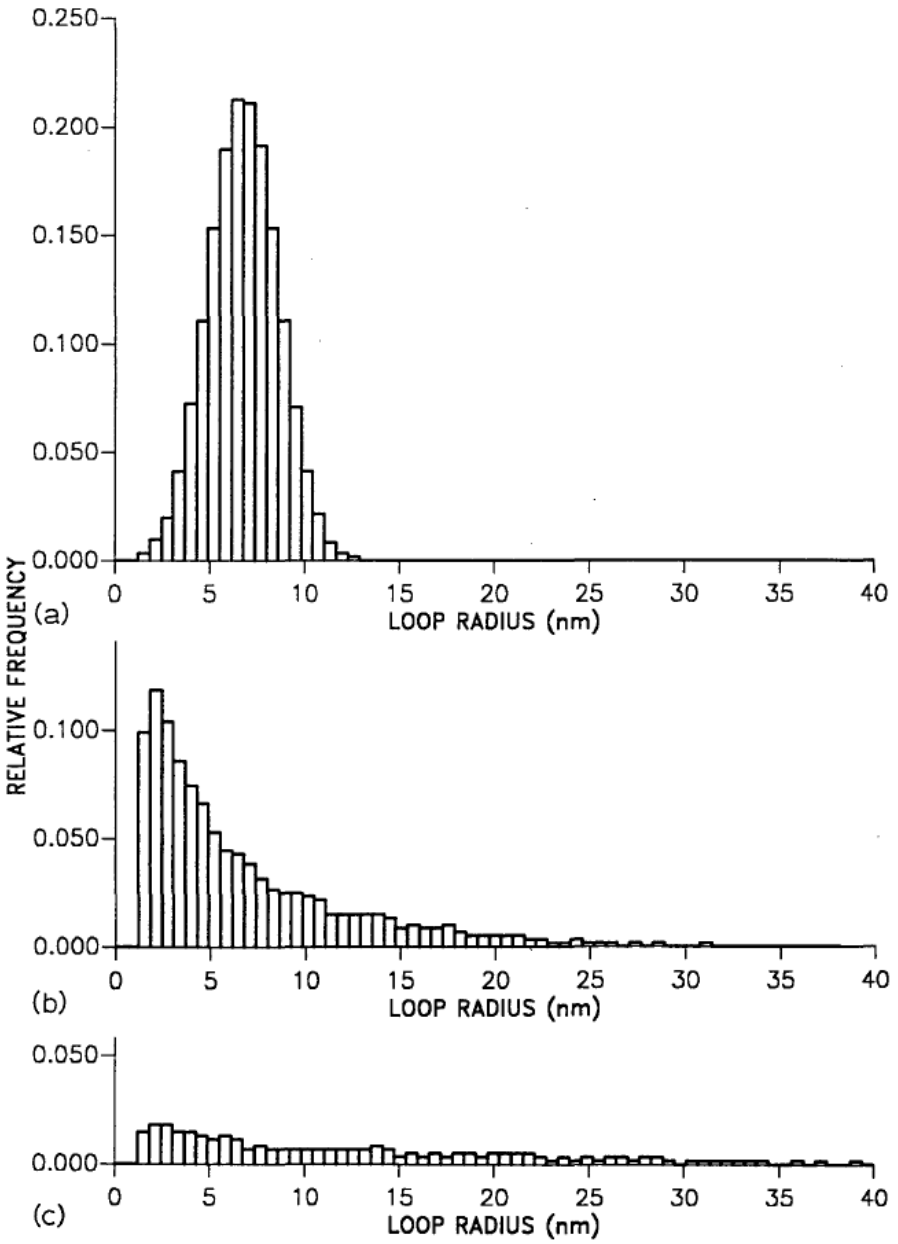

a initial distribution; *b* fractional annihilation = 0·44; *c* fractional annihilation = 0·8

Figure 6.2. Calculation of the annealing behavior of a population of faulted dislocation loops where no external sources and sinks are present. A clear coarsening of the loop population is observed [170].

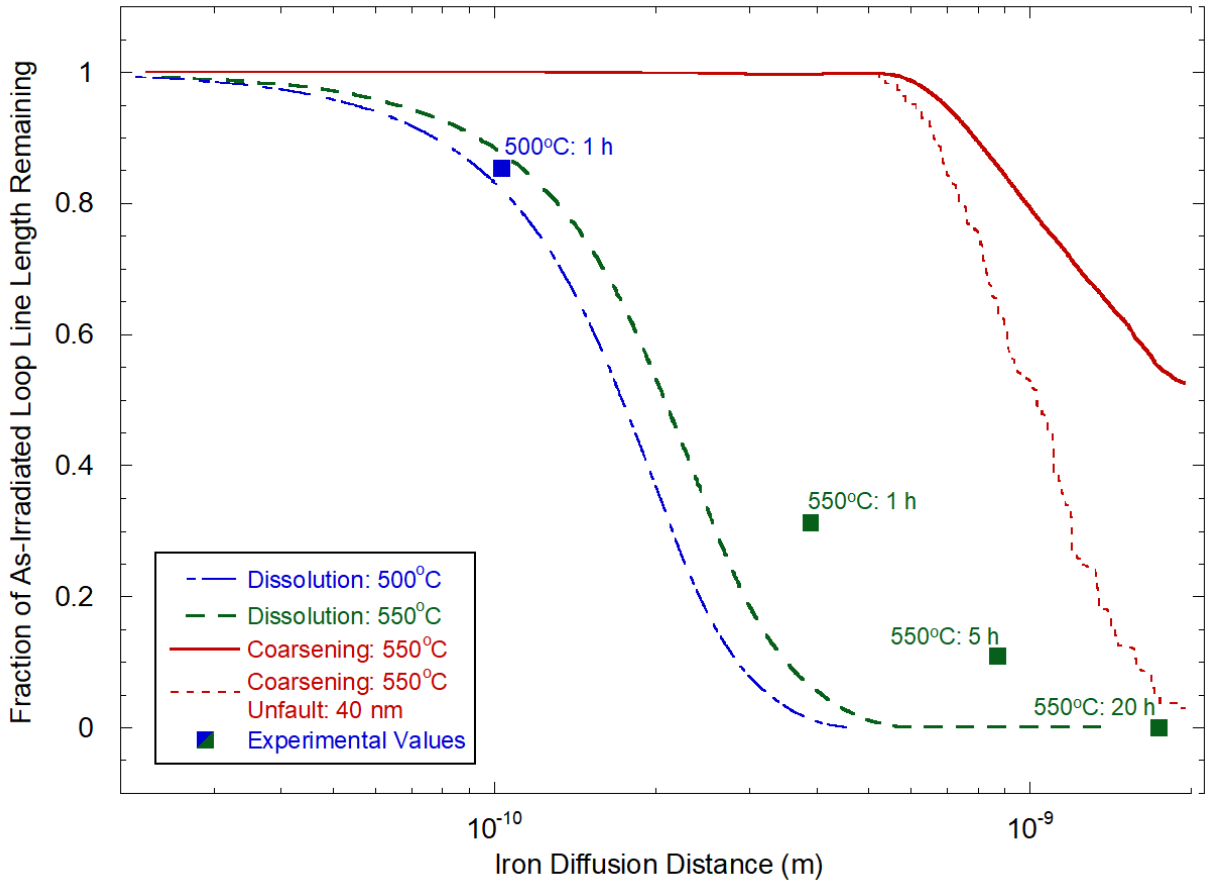

Figure 6.3. Comparison of the predicted dislocation loop annealing for both pure loop dissolution and coarsening and the experimentally measured populations. Also compared is the effect of adding a maximum loop diameter for unfaulting due to loop coarsening.

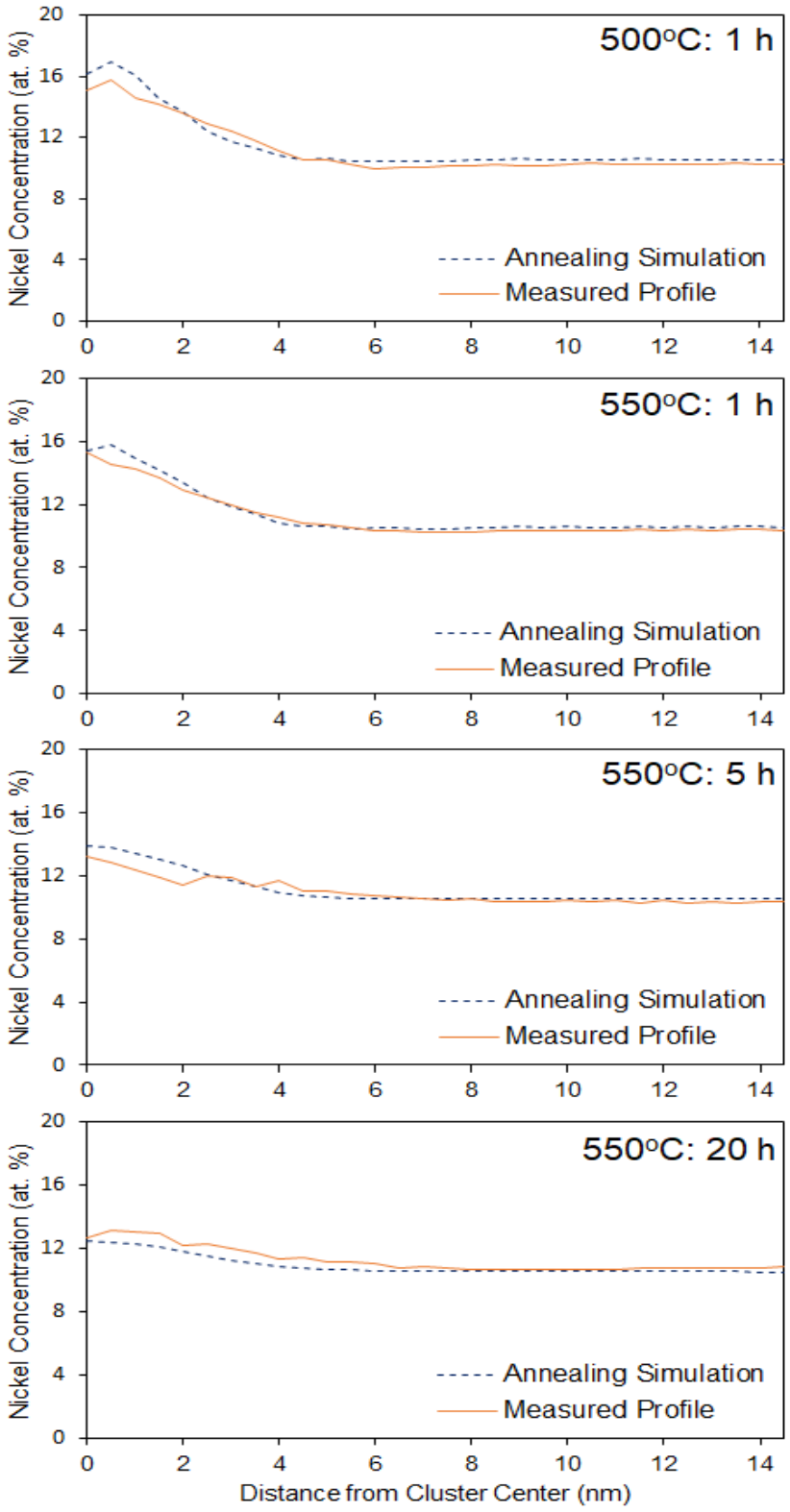

Figure 6.4. Comparison of the simulated nickel diffusion under annealing and that measured by the APT characterization of the solute clusters.

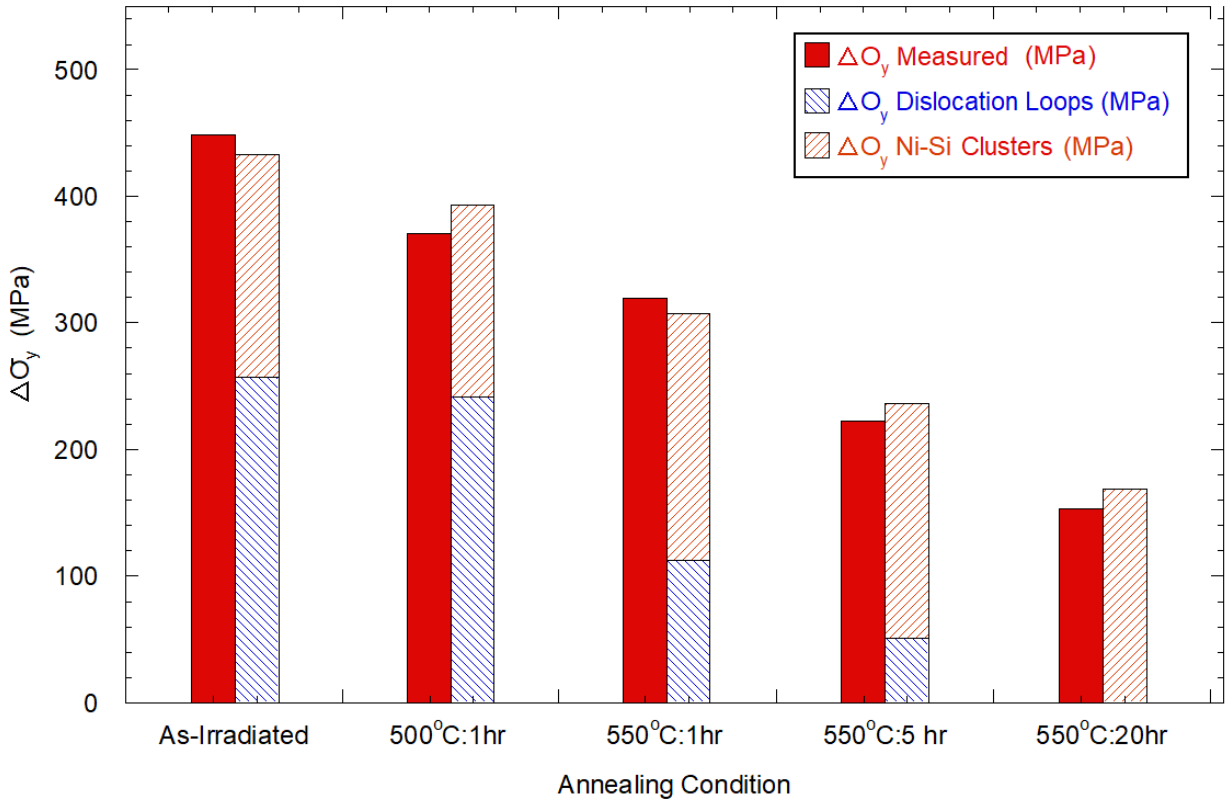

Figure 6.5. Comparison of the measured irradiation strengthening and the predicted strengthening from a population of dislocation loop and solute cluster defects, based on the obstacle strengths determined by the fitting of the DBH model. The fractional contribution of the dislocation loops and solute clusters to the overall strengthening is represented by their relative bar height.

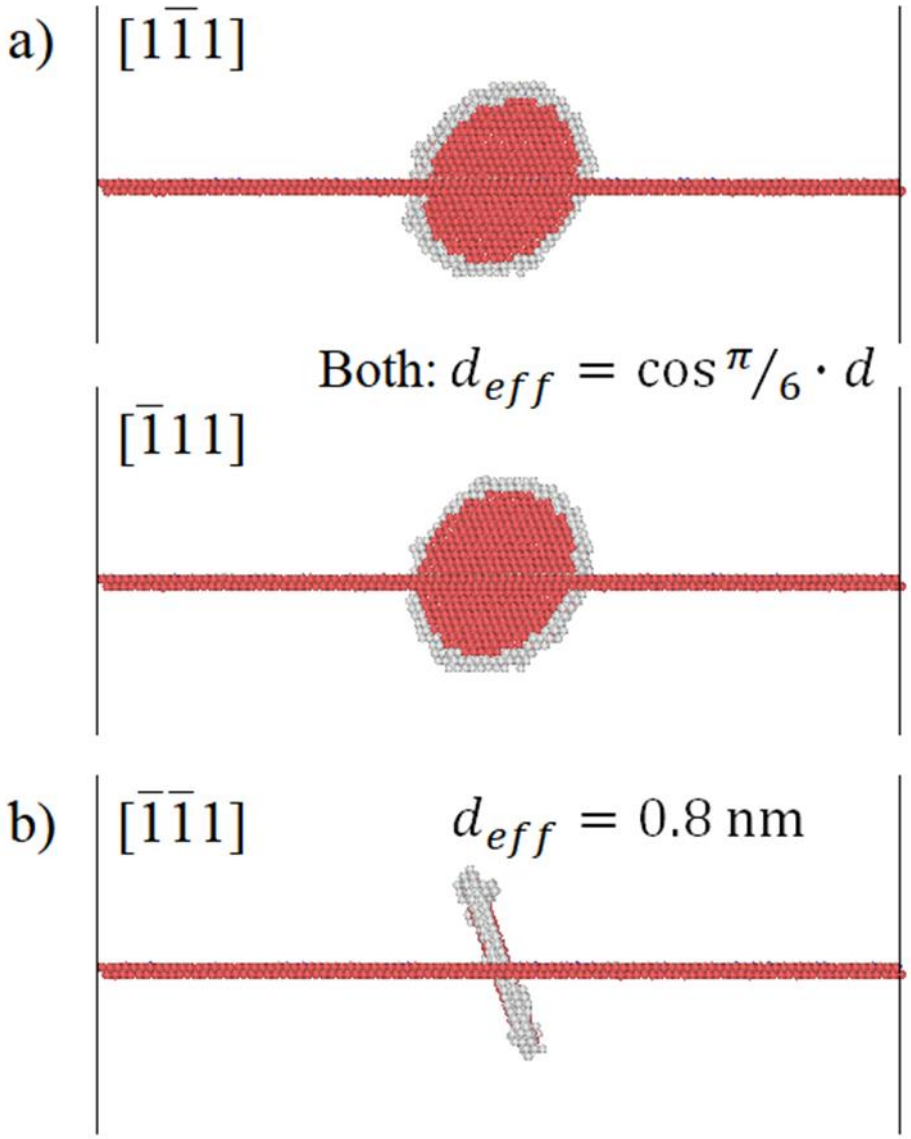

Figure 6.6. Depiction of the effective diameter, d_{eff}, of the different loop orientations with respect to the direction of the mobile $[\bar{1}10]$ edge dislocation: a) $[1\bar{1}1]$ and $[\bar{1}11]$ b) $[\bar{1}\bar{1}1]$

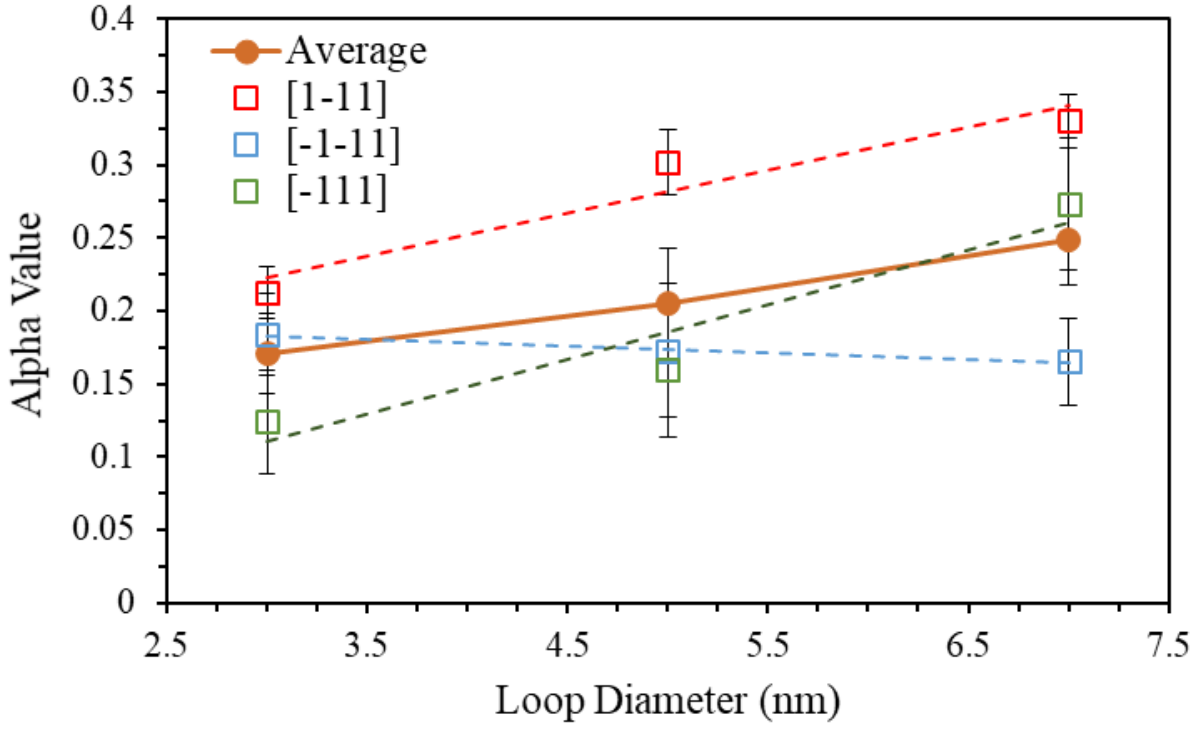

Figure 6.7. Comparison of the calculated obstacle strength, α, for each of the dislocation loop sizes and orientations. Also included is the average strength of the three examined orientations.

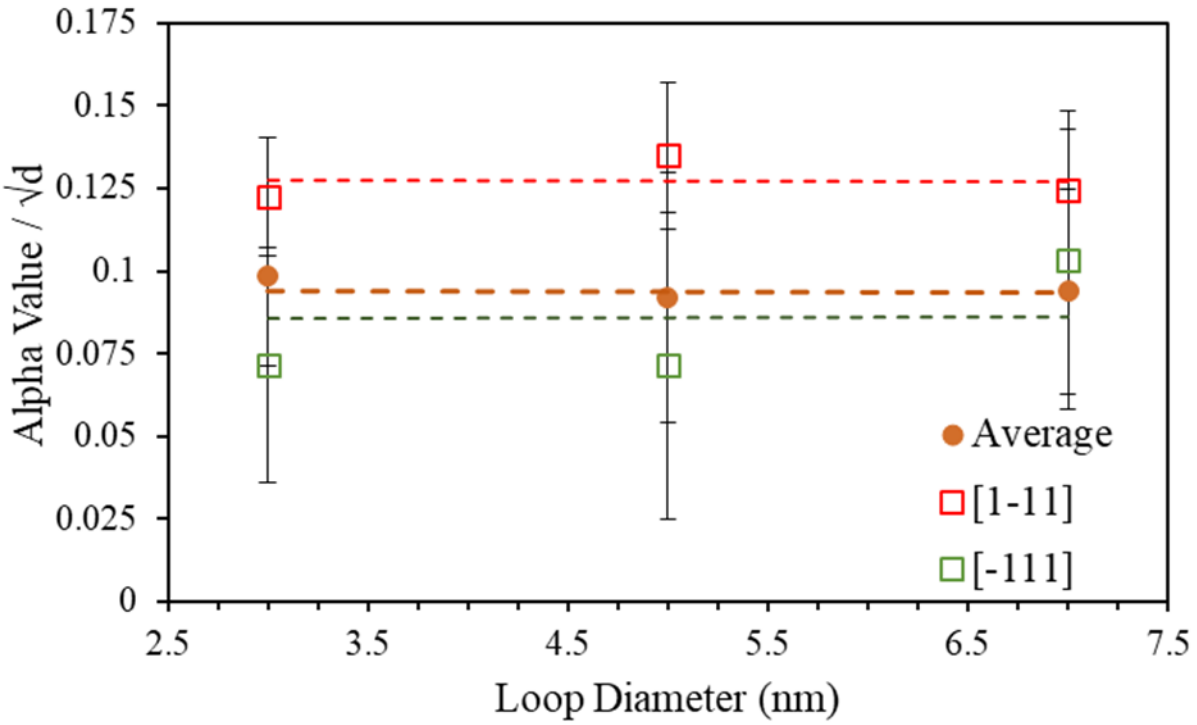

Figure 6.8. Examination of the obstacle strength, α, divided by the $\sqrt{d}$ for the average loop strength and the orientations which increased with loop diameter

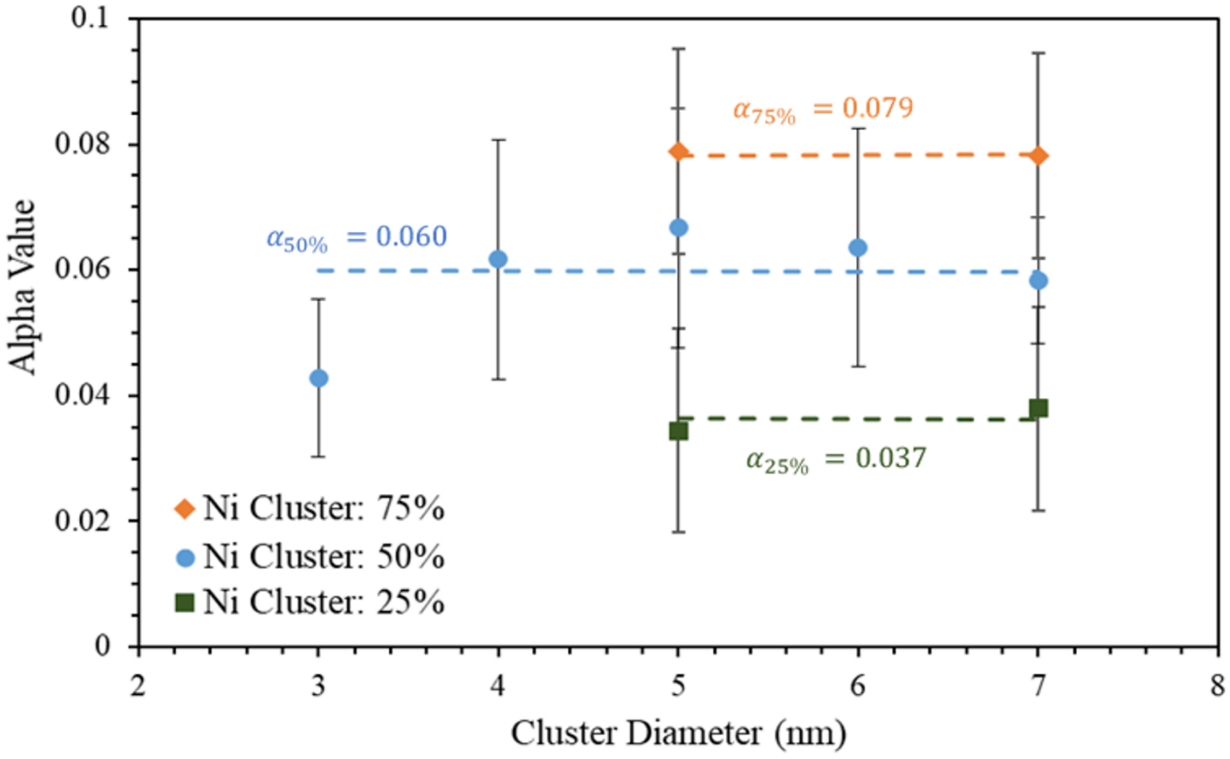

Figure 6.9. Comparison of the calculated obstacle strength, α, for each of the examined solute cluster sizes and solute concentrations.

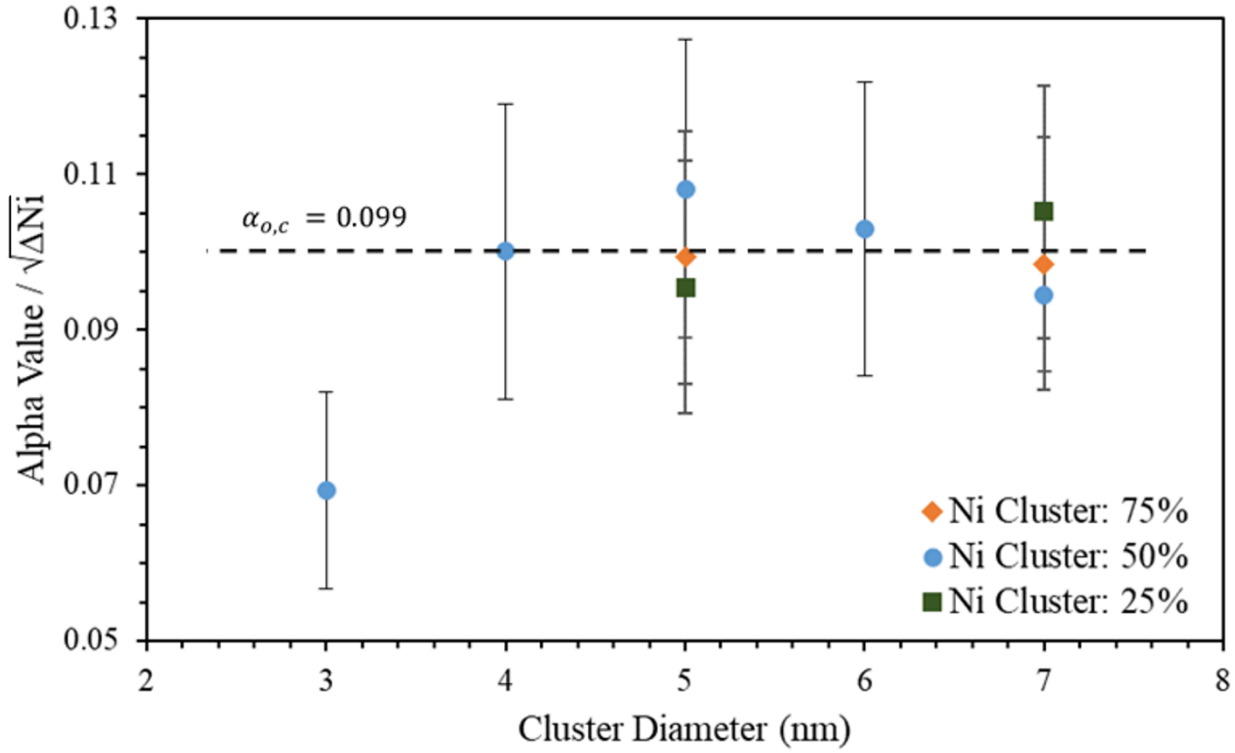

Figure 6.10. Examination of the obstacle strength, α, divided by the $\sqrt{\Delta Ni}$ for the solute clusters. The increase in strength with solute concentration is proportional to the $\sqrt{\Delta Ni}$.

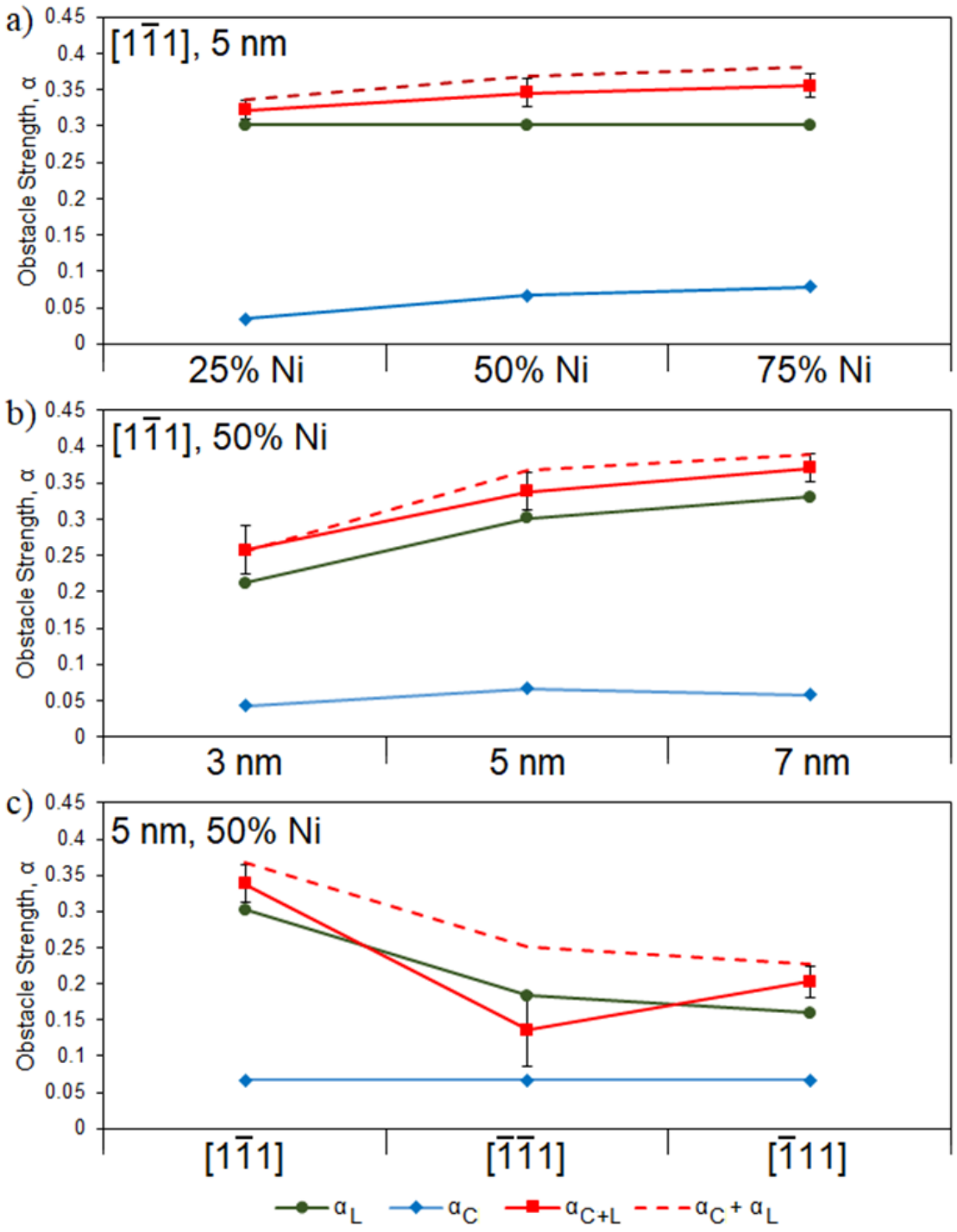

Figure 6.11. Comparison of the measured obstacle strength of the combined cluster-loop defects with the strength of independent dislocation loops and solute clusters. a) change in strength with solute concentration, b) change in strength with defect size, c) change in strength with loop orientation.

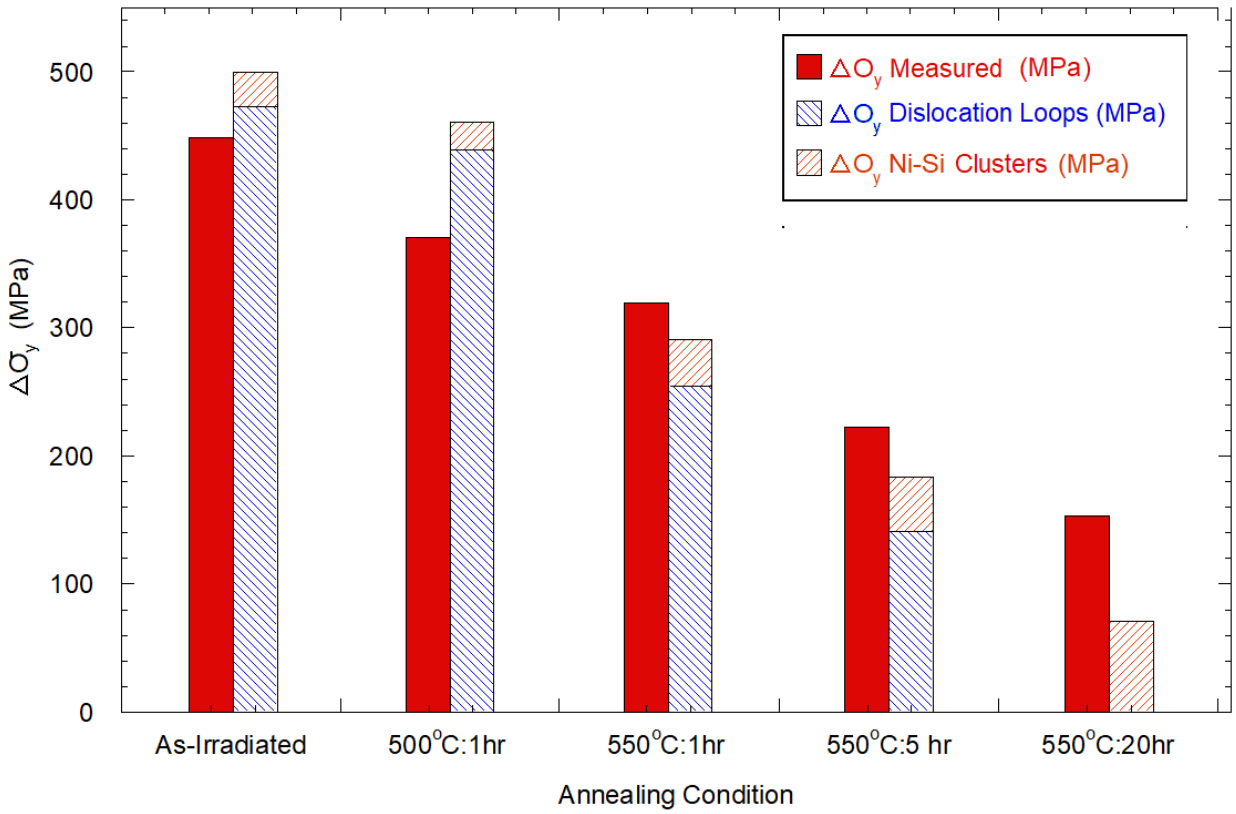

Figure 6.12. Comparison of the measured irradiation strengthening and the predicted strengthening from a population of dislocation loop and solute cluster defects, based on the obstacle strengths determined by the MD simulations. The fractional contribution of the dislocation loops and solute clusters to the overall strengthening is represented by their relative bar height.

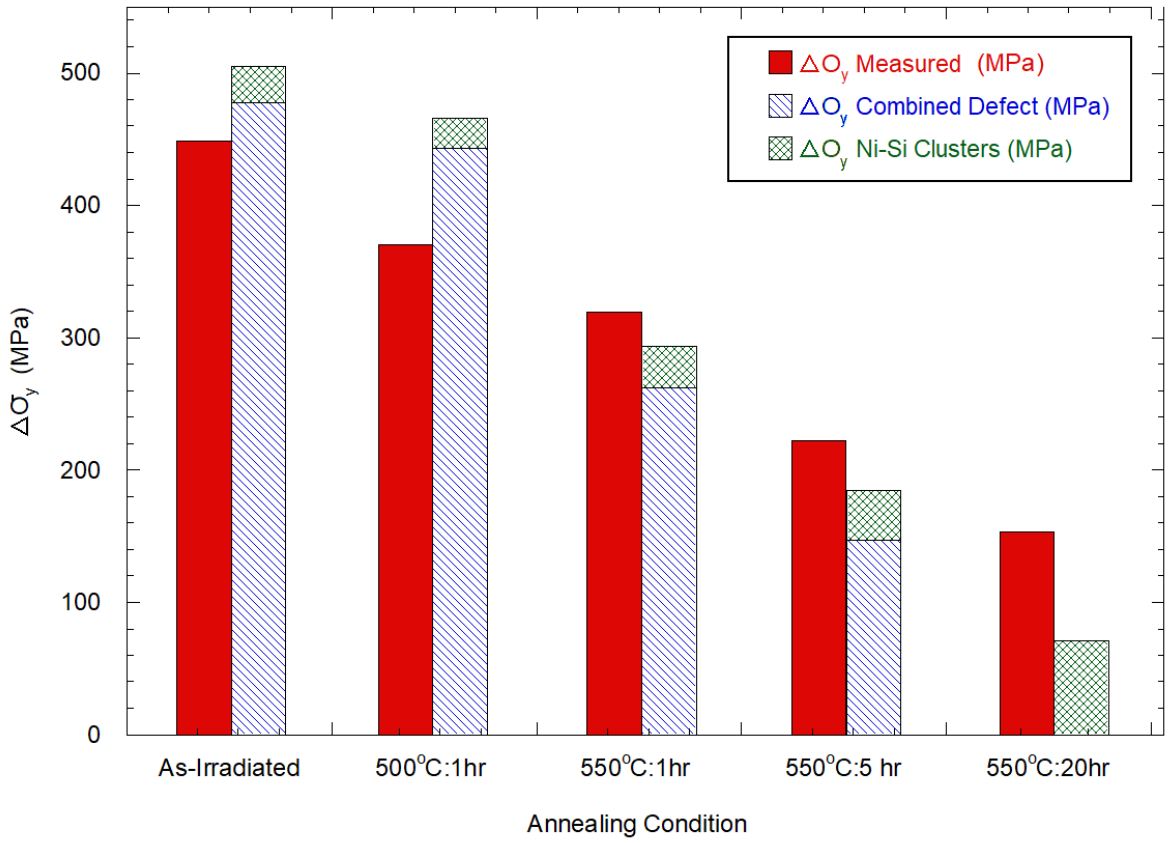

Figure 6.13. Comparison of the measured irradiation strengthening and the predicted strengthening from a population of combined cluster-loop defects and the remaining solute clusters, based on the obstacle strengths determined by the MD simulations. The fractional contribution of the combined defects and solute clusters to the overall strengthening is represented by their relative bar height.

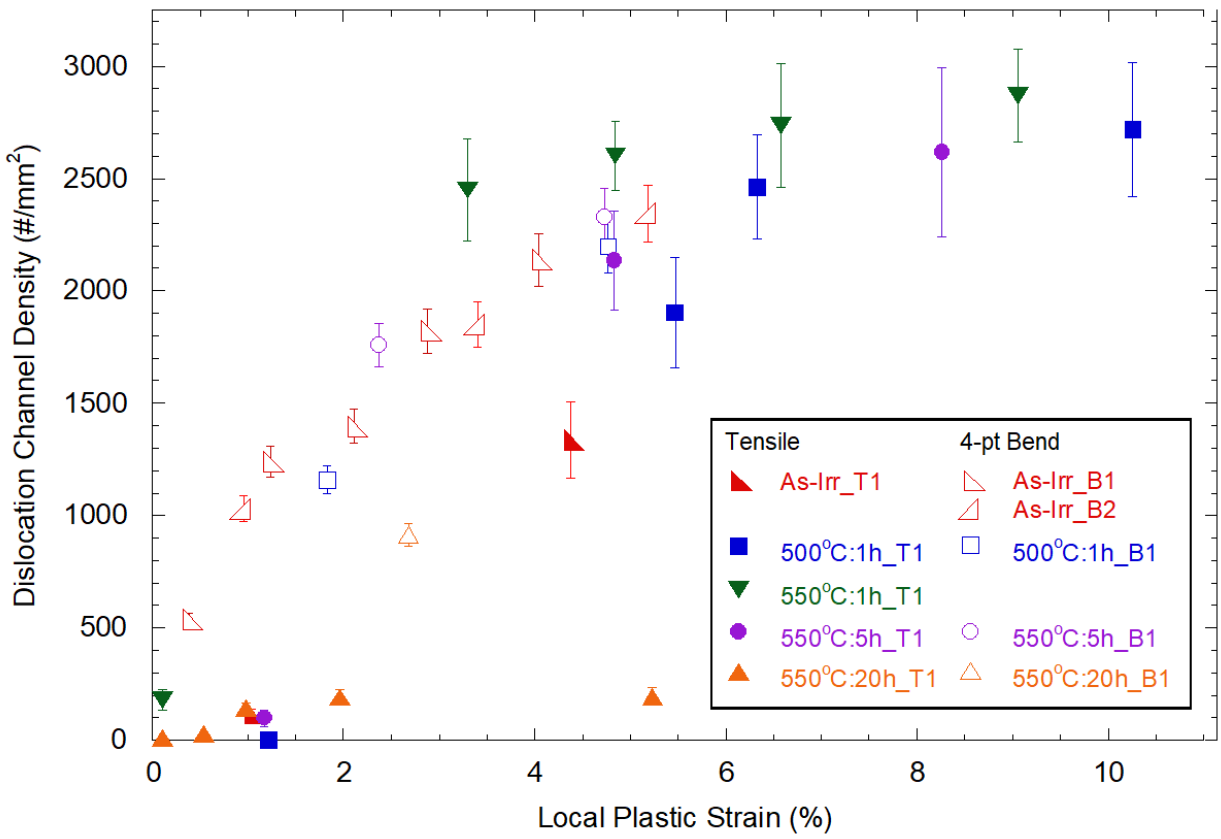

Figure 6.14. Comparison of the bulk dislocation channel density for the tensile and bend experiments.

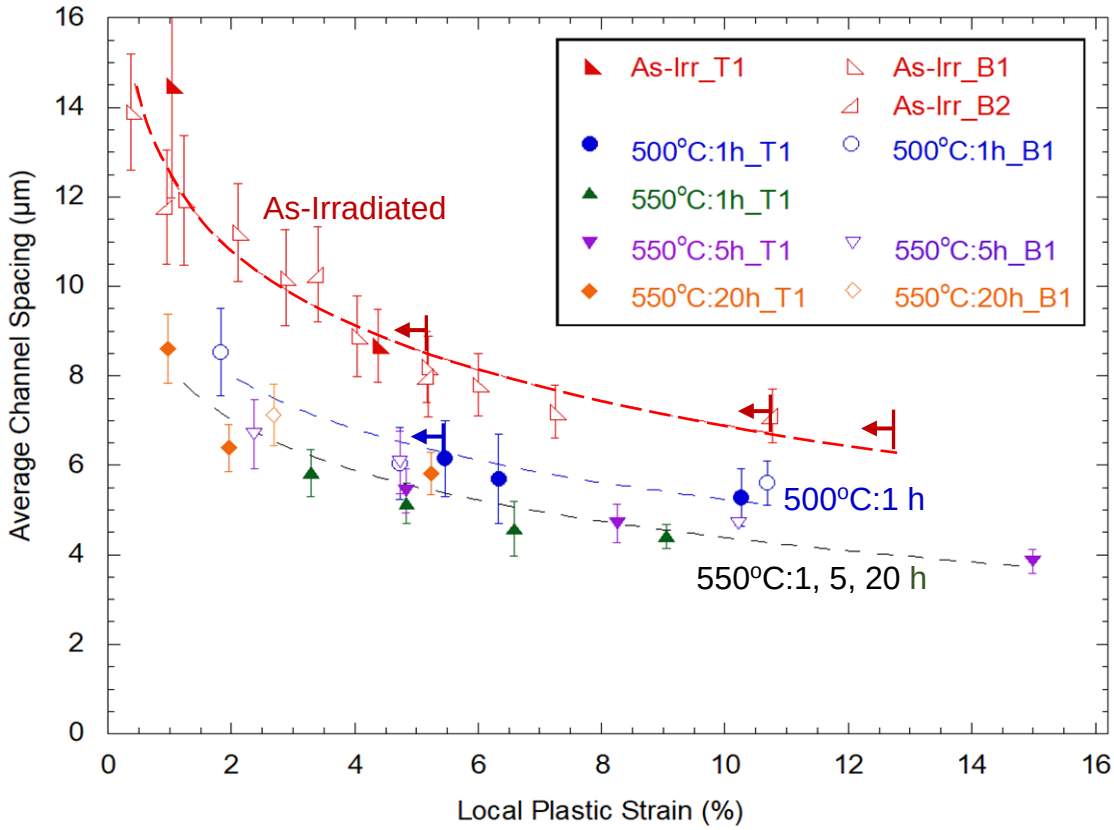

Figure 6.15. Comparison of the average channel spacing for the tensile and bend experiments. Vertical lines denote the maximum value of plastic strain at which IASCC crack initiation was first observed.

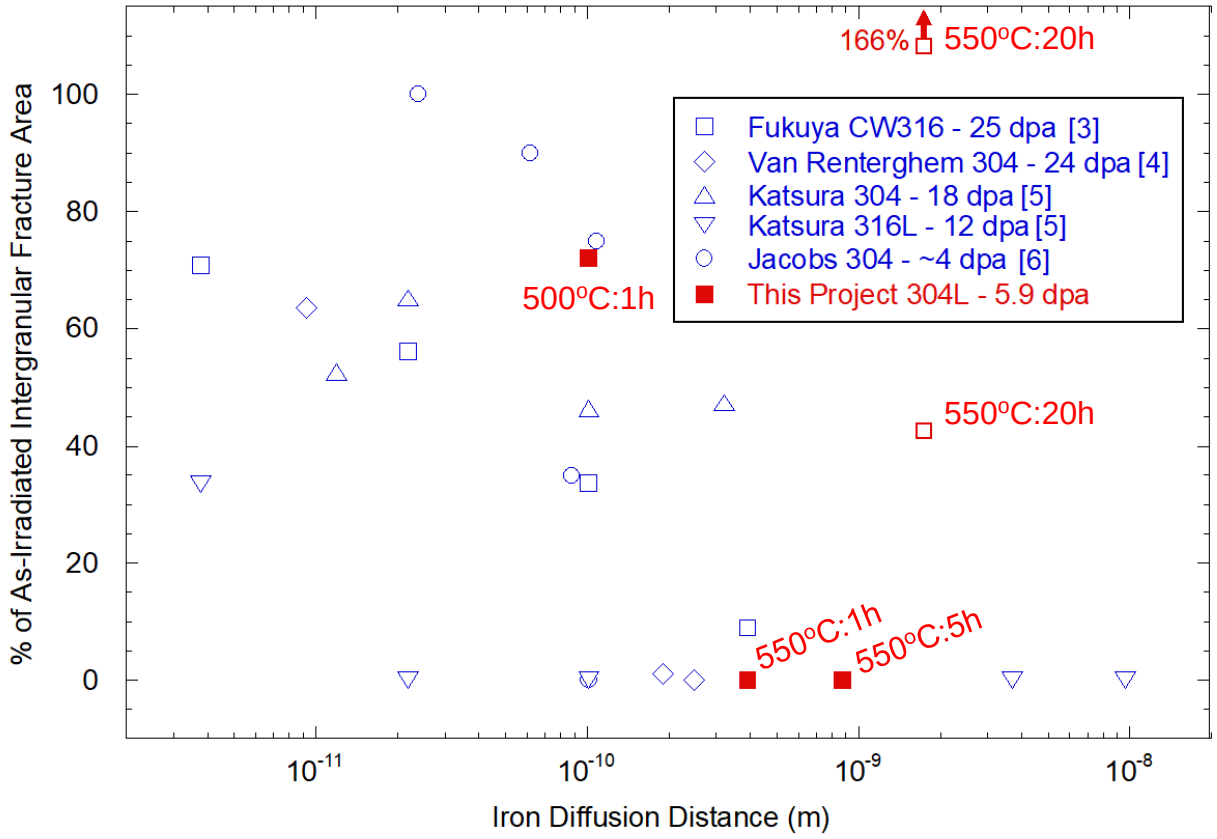

Figure 6.16. Comparison of the observed mitigation of IASCC susceptibility following PIA for this study, as compared to previous literature studies on neutron-irradiated austenitic stainless steels.

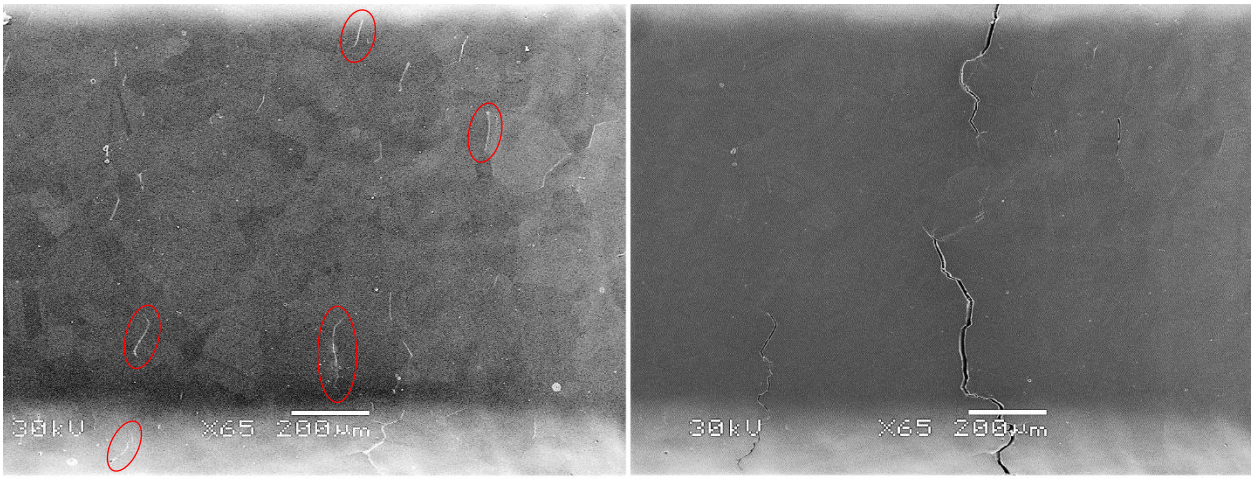

a) b)

Figure 6.17. Image of the gage of the T-12 (550ºC:20h) tensile specimen: a) post-electropolish, but prior to straining, b) same region after straining to 0.11% bulk stain. Circled in red are some of the locations which displayed etching after the electropolish and crack initiation after straining.

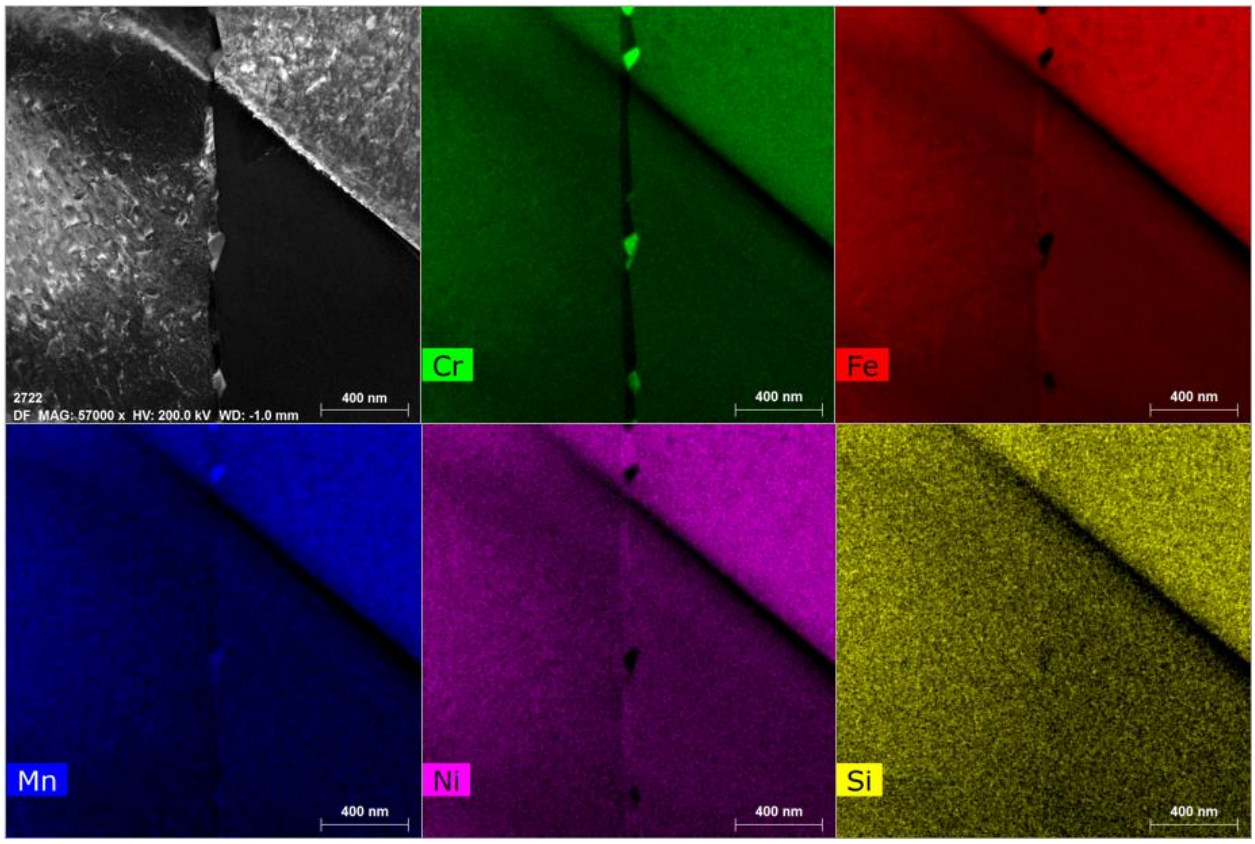

Figure 6.18. Images of the sensitization present near an etched grain boundary site. Chromium precipitation is evident along the grain boundary [205].

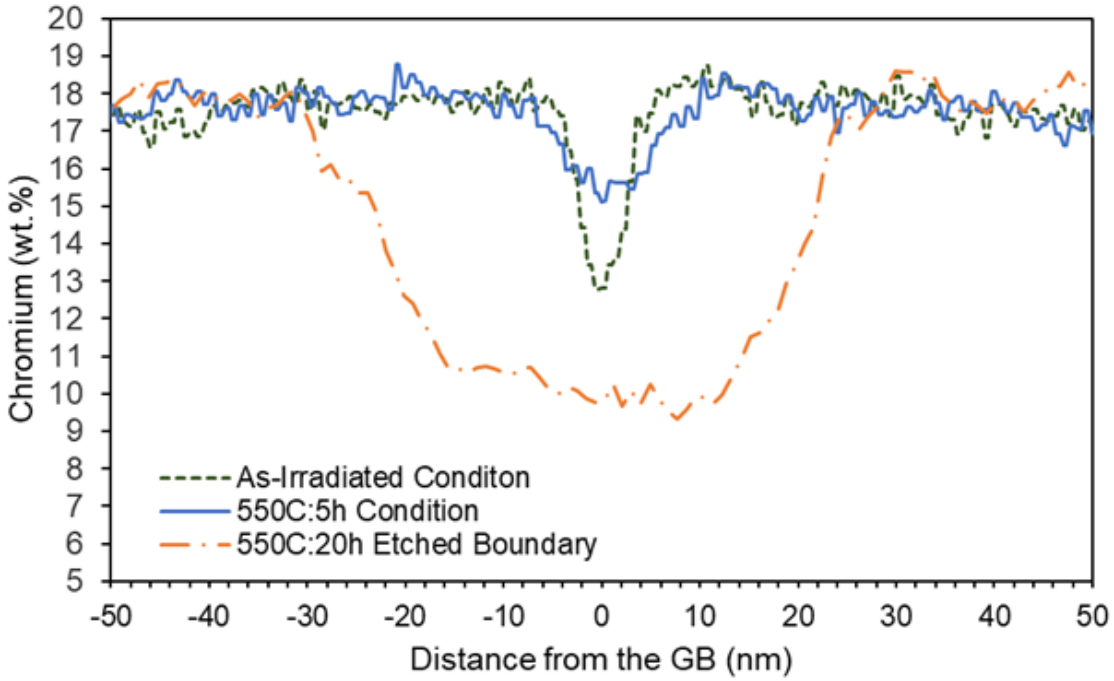

Figure 6.19. Comparison of the grain boundary chromium concentration between the as-irradiated and 550ºC: 5 h conditions and the grain boundary that displayed etching and chromium precipitation after 550ºC: 20 h.

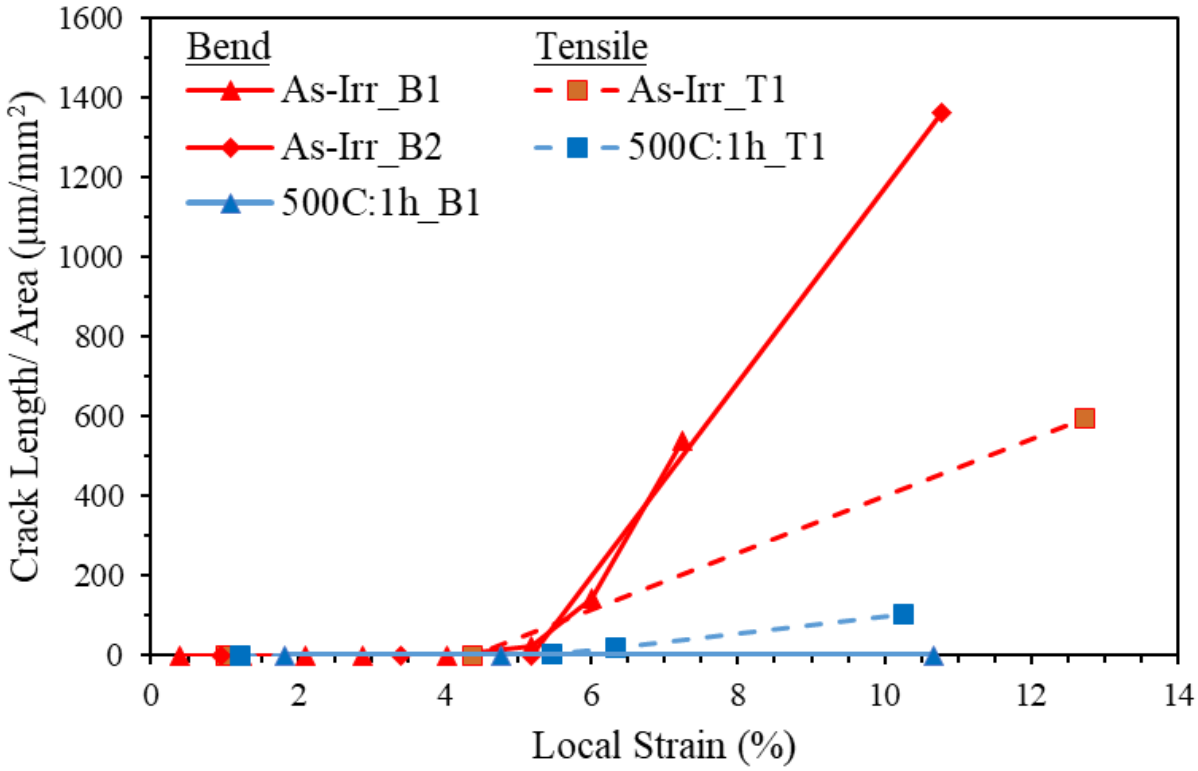

Figure 6.20. Change in the crack length density in response to local plastic strain and annealing condition for the tensile and bend experiments.

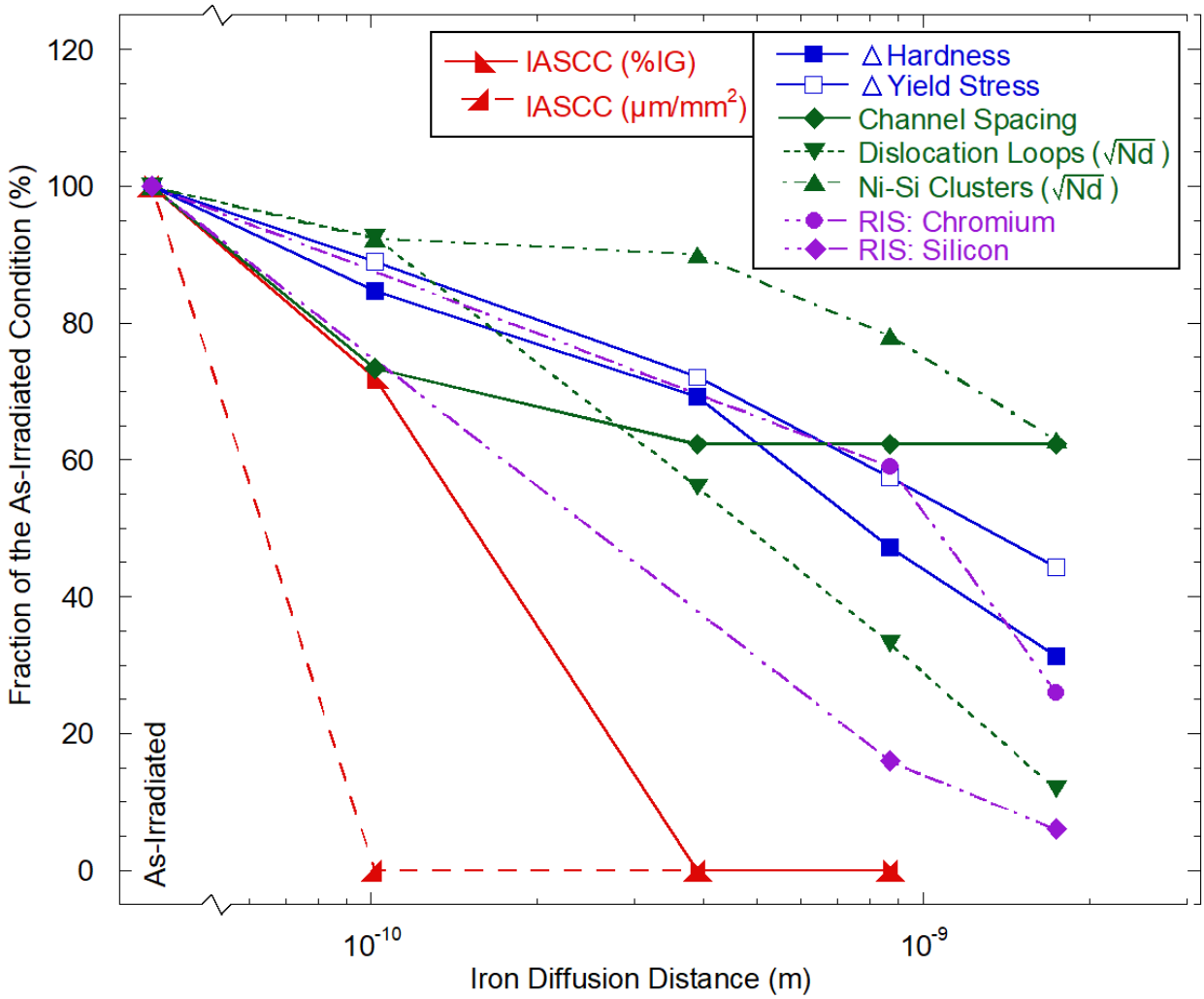

Figure 6.21. Comparison of the observed IASCC susceptibility and various irradiation induced features of the material.

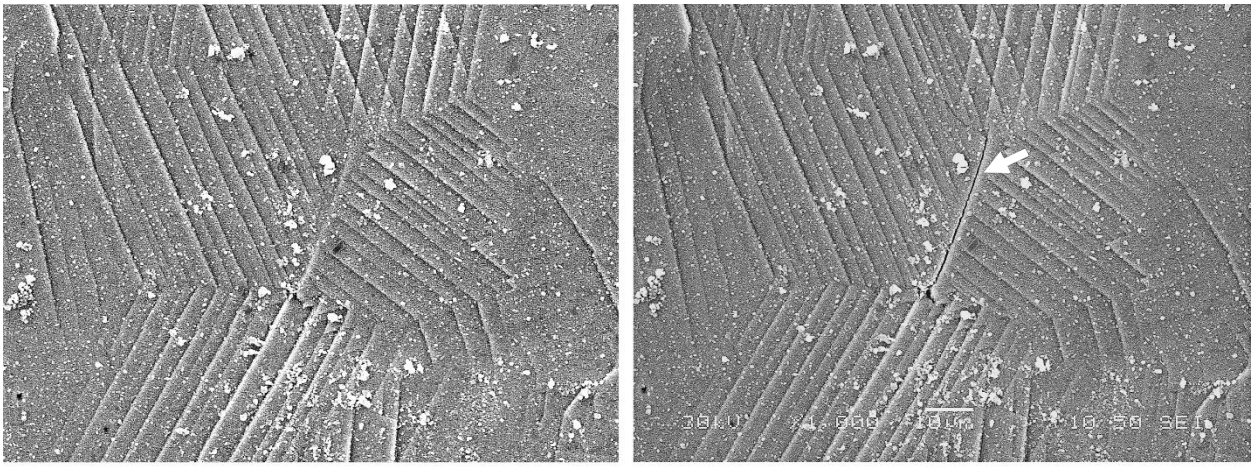

a) b)

Figure 6.22. Examination of the crack initiation site in the as-irradiated 4-B bend specimen: a) site prior to initiation, ~4%; b) crack initiation site, ~5%. Arrow points to the crack created between the two strain increments. Stress direction is horizontal in both images.

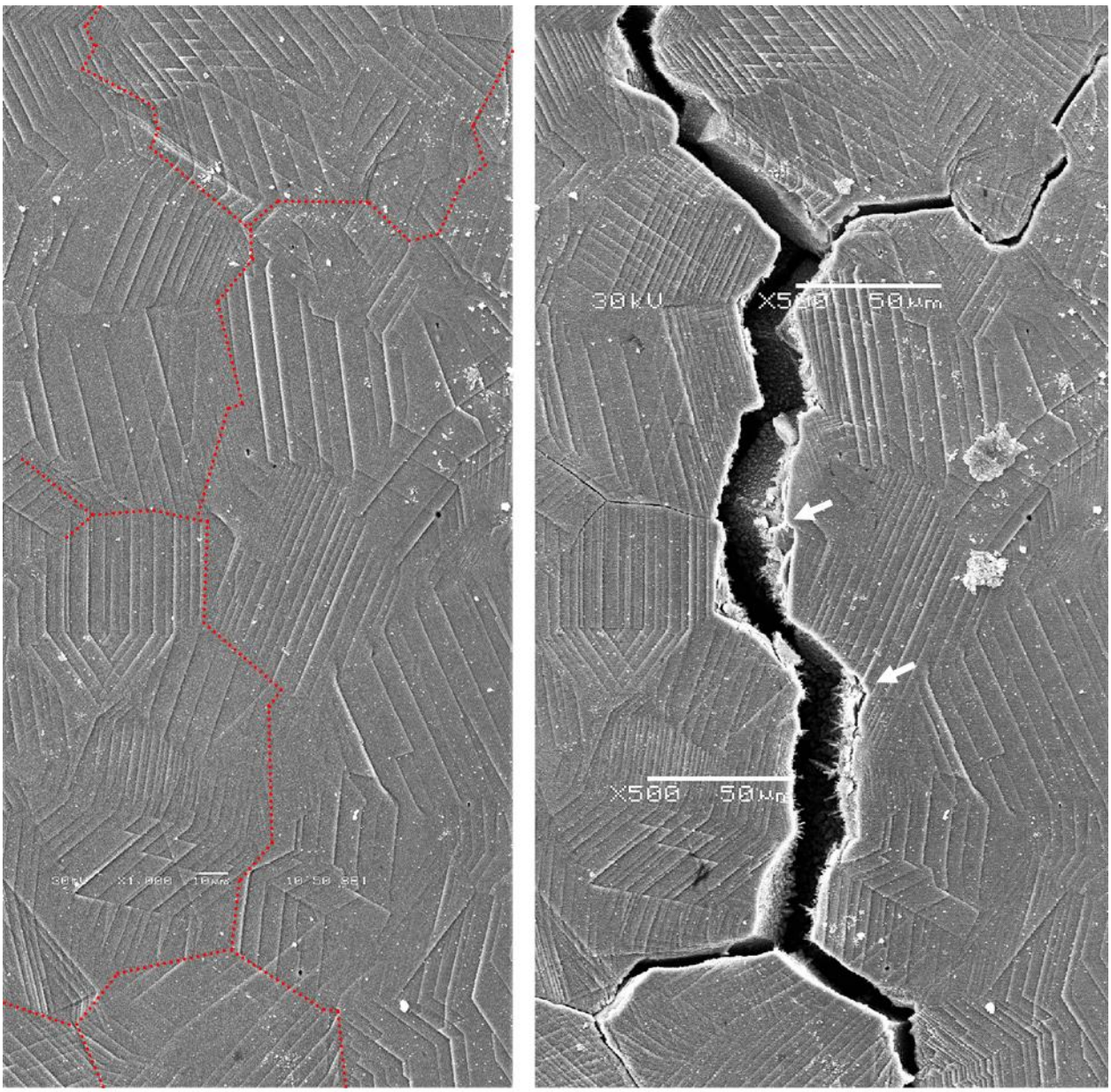

a) b)

Figure 6.23. Examination of the crack initiation site in the as-irradiated 10-B1 bend specimen: a) site prior to initiation, ~5%; b) crack initiation site, ~10%. Arrows indicate the range of grain boundaries between which the crack was believed to first initiate, based on the crack opening and the relative change in localized deformation. Stress direction is horizontal in both images.

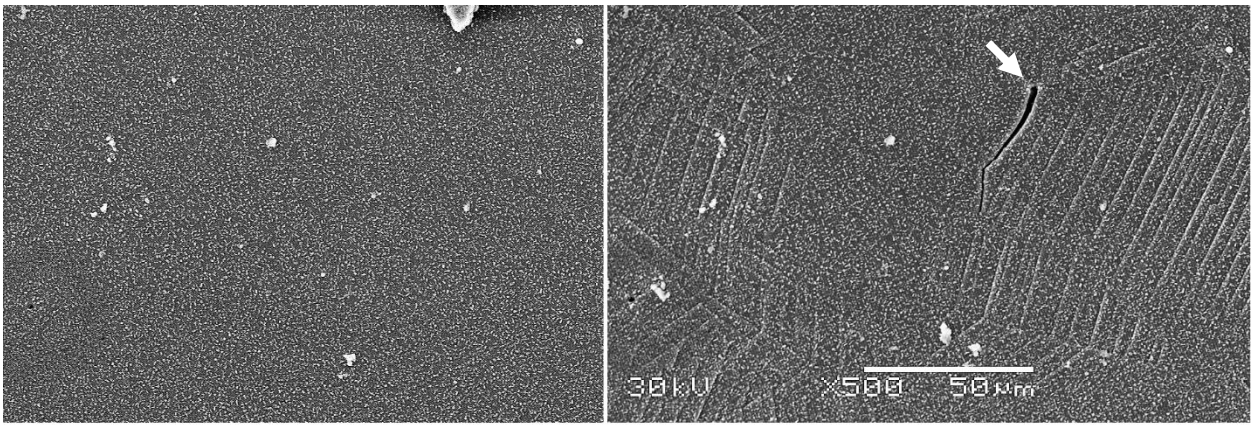

a) b)

Figure 6.24. Examination of the crack initiation site in the T-5 (500°C:1 h) tensile specimen: a) site after the strain increment prior to initiation, 1.21% local plastic strain; b) crack initiation site, 5.47% local plastic strain. The arrow points to the crack created between the two strain increments; stress direction is horizontal in both images.

CHAPTER 7 - CONCLUSIONS

The effect of post-irradiation annealing (PIA) on the irradiation-induced microstructure, localized deformation morphology, and mitigation of IASCC susceptibility was determined for a 304L austenitic stainless steel neutron-irradiated to 5.9 dpa.

- Annihilation of dislocation loops with annealing was vacancy diffusion-controlled and demonstrated a mixed dissolution and coarsening behavior. PIA at 550^{o}C:20 h was sufficient to remove all of the faulted dislocation loops; this annihilation of dislocation loops as a function of iron diffusion distance agrees with prior literature.
- Ni-Si and Al-Cu clusters were observed in the as-irradiated condition and decreased in density, while increasing in size with PIA treatments. The increase in cluster size was due to the diffusion of solutes away from the higher concentration core of the cluster and matched the theoretical Fick's diffusion of solutes.
- Irradiation resulted in significant depletion of Cr and enrichment of Si and Ni at the grain boundaries. Significant recovery of Cr and Ni at the grain boundary was observed after PIA at 550^{o}C: 5 h but neither Cr nor Ni was fully recovered after 550^{o}C: 20 h. Grain boundary Si recovered faster than Ni, which is consistent with the annealing behavior of Ni-Si clusters.
- Decreases in the irradiation strengthening with PIA treatments reflected the changes in the size and density of the dislocation loop and solute cluster populations, as predicted by the dispersed barrier hardening (DBH) model.
- Fits to the characterized microstructure using the DBH model seemed to underpredict the strength of dislocation loops, while overpredicting the obstacle strength of solute cluster defects as compared to the completed MD simulations, though the obtained strength values were relatively similar.

- MD simulations of a combined cluster-loop defect demonstrated only a slight strengthening as compared to independent loops when examining a random loop orientation. A full population of combined defects has a negligible effect on the bulk strengthening as compared to a population of independent loops and clusters.
- Localized deformation, as characterized by the average dislocation channel spacing, decreased in response to PIA treatments up to 550°C: 1 h, with the largest decrease occurring after 500°C: 1 h. Further annealing after 550°C: 1 h reduced the fraction of grains with dislocation channels rather than the average channel spacing.
- IASCC susceptibility decreased with increasing annealing time and temperature. Full mitigation was observed after PIA at 550°C: 1 h for CERT specimens, while 500°C: 1 h was sufficient to remove all susceptibility in four-point bend specimens. The mitigation of IASCC with PIA agrees with prior literature data on similar neutron-irradiated austenitic stainless steels.
- An increase in cracking susceptibly was observed after annealing treatments of 550°C: 20 h due to the sensitization of select grain boundaries. As such, this annealing condition was removed from consideration in regard to IASCC.
- Both CERT and four-point bend experiments displayed an identical change in the localized deformation with annealing and a similar mitigation of IASCC susceptibility. This confirms that the results of four-point bend experiments are consistent with traditional tensile straining when assessing IASCC susceptibility and localized deformation.
- The mitigation of IASCC susceptibility with PIA was related to the decrease in the average dislocation channel spacing and is consistent with a process in which crack initiation is controlled in part by the high tensile stress at discontinuous dislocation channel-grain boundary intersections.

CHAPTER 8 - FUTURE WORK

This research concluded that the key process responsible for the removal of IASCC susceptibility of a 304L austenitic stainless steel irradiated to 5.9 dpa with PIA treatments was the decrease in localized deformation for the examined crack initiation. Despite the importance of this result, additional research could provide further insight into several areas.

1) Two compounding issues when studying neutron-irradiated material is the low availability of material and the large variation in IASCC susceptibility observed with slight changes in experimental variables, such as alloy heat, dose rate and type, and test environment. Together these issues create a wide array of literature results (Figure 2.34) while repeatability experiments are a rare occurrence, thus making it difficult to present a conclusion to the entire research field. While the 304L material used in this thesis research displayed a mitigation of IASCC under PIA due to a decrease in localized deformation, this process must be verified through both repeatability experiments on this material and similar experiments on other irradiated alloys, before this process of IASCC mitigation can be considered applicable to all irradiated austenitic stainless steels.

2) The primary objective in the selection of annealing conditions for this research was to bound the annealing conditions at which full IASCC susceptibility was removed. For this material, full IASCC mitigation was achieved between the treatments of 500^{o}C: 1 h and 550^{o}C: 1 h for the tensile experiments, while 500^{o}C: 1 h was not susceptible in the four-point bend specimens. As these results suggest that 500^{o}C: 1 h very close to the mitigation limit experimenting on similar annealing conditions, i.e. 500^{o}C: 15 min to 500^{o}C: 10 h, for this irradiated alloy could lend a better examination of the exact state of the material when IASCC susceptibility is fully mitigated. An important part of this further examination would a measurement of the grain boundary segregation at these annealing treatments, an analysis which was missing from the research presented in this thesis.

3) As a part of this research, MD simulations were utilized to examine the obstacle strengths of dislocation loops and solute clusters. In this research, the strength of the solute clusters calculated via the simulations were much less than the fits gained through applying the DBH model to the measured strengthening. The primary reason for this discrepancy is the absence of silicon from the simulation, due to the lack of suitable potentials. As the development of a quaternary Fe-Ni-Cr-Si potential has not been completed, an adjustment of obstacle strength based on relative bond strengths of silicon was attempted in this study. However, a more through estimate of the effect of silicon could be attempted, including the mechanical aspects, such as the enhancement from a differing shear modulus.

4) Prior research has clearly shown that the localized deformation should be dependent on the irradiated microstructure. However, in this study the changes in the localized deformation were not directly correlated with changes in either the dislocation loop or solute cluster populations, instead suggesting a shift in the relationship between the microstructure and localized deformation under continued annealing treatments, i.e. first causing a reduction in the average channels spacing up to 550^{o}C: 1 h, while reducing the fraction of grains with channeling at higher annealing treatments. As such, a more detailed examination of irradiated material should be conducted to determine the precise relationship between the irradiated microstructure and the localized deformation, and their subsequent evolution under PIA treatments.

5) This research stipulated that the observed reduction in the IASCC susceptibility following the PIA was linked to the similar reduction of the average channel spacing. Proposing that an increased number of channels would better distribute the dislocations, thus lowering the pile-up stress in each individual channel which has been previously linked to crack initiation [149]. This predicted reduction in stress, however, is theoretical as actual values of the average pile-up stresses before and after annealing treatments were not measured in this research. As such, quantifying the precise changes in pile-up stresses with the adjustment of the localized deformation is critical in verifying its precise role in crack initiation.

6) While this study focused on the use of PIA to study the processes behind the mitigation of IASCC, there is a desire to utilize PIA as a method to mitigate IASCC in the reactor core internals of current reactors. However, despite the success of these treatments, there are still many concerns which must be addressed before PIA treatments can be applied in this manner. One concern in close relation to this thesis research is the sensitization of steels during the PIA

treatments. While sensitization has been well studied for unirradiated steels, this knowledge is not directly applicable to irradiated materials, as indicated by the observed sensitization after the 550^{o}C:20 h annealing treatment. While this enhanced sensitization is likely related to the segregation of elements to grain boundaries during irradiation, more research work must be completed to better understand the risks of sensitization during annealing treatments on irradiated austenitic stainless steels.

APPENDIX

Below is the complete LAMMPS input script that was used to complete the MD simulations in this study. In the presented form, the input script will create a rectangular prism of FCC atoms with a centered edge dislocation at an atomic concentration of Fe-20Cr-12Ni, in conjunction with the ternary EAM potential by Bonny *et al* [191]. All obstacle types are currently commented out (a line beginning with # for LAMMPS) but can be added as desired by uncommenting the specified lines of code.

```
# Richard and Justin's LAMMPS input file for an FCC lattice oriented for the dislocation slip
# problem under controlled shear strain using static minimization and/or MD.
# 3/14/17
#
# The basic geometry for this problem is taken from work by Wirth and Bacon/Osetsky/Rodney.
#
# The direction of applied shear strain on the box surface is tauZX, added by displacing
# the top and bottom Z planes in the +/- X direction. Edge dislocations (with line length
# along Y) move parallel to B=X. Screw dislocations (with line length l=B=X) move in the
# Y direction. The cell is periodic in X and Y with free surfaces in Z. The top and bottom
# several layers of Z are held fixed as displacement control grips.
#
# Step 1 is to create and populate the lattice
# Step 2 is to remove atoms to create 2 missing 1/2 planes, they are (-1  1 -2) planes
#                   perpendicular to X, below the Z mid-planes
# Step 3 is to assign regions for the top and bottom grip sections, and put them into a group
# Step 4 is to establish the group inside the free moving cell for computes/thermo
# Step 5 is typically done along the Burgers vector is to squeeze the box to match
#       the average number of planes, above and below the core, and achieve 0 net stress.
# Step 6 minimize the cell with no external transactions
#
# From this point, the strain may be applied to the system in increments either by displacement
# or force control. Note that unless a barrier is present, the edge dislocation will want
# to glide continously under shear, so there is no converged solution in minimization

# Basic setup of units and dimension and style
# Metal in 3D with periodic boundary in X and Y
# Assume cell fairly cubical, so split processors accordingly.
```

```
units                   metal
dimension               3
newton                  on
processors              * * *
boundary                p p s
atom_style              atomic

# Assign variables to determine what defect geometry to make in this cell
# set these!
# crystal lattice types  0=hcp/zr, 1=fcc/Ni
# dislocation types are         0=edge, 1=screw
# obstacle types are            0=void, 1=int loops
# ... note all these variables are in lattice units.
 variable xltype                equal 1
 variable dislocation   equal 0
 variable obstacle              equal 1
# ... note all these variables in lattice units.
 variable halfx                 equal 50
 variable halfy                 equal 25
 variable halfz                 equal 15
 variable obsx0                         equal 0
 variable obsy0                         equal 0
 variable aloopdy               equal 3.9
 variable aloopdz               equal 3.9
# ... note all these variables are in box units of Angstroms
 variable obsr                  equal 25
# If doing an intersitial loop, specify the rotation vector which is the
# Z axis of the lab frame, which is then rotated into the CS of the dislocation
# problem becomes
 variable Zx                    equal 0.0
 variable Zy                    equal 0.8164965809
 variable Zz                    equal 0.5773502692
# Then we specify the rotation axis in degrees, which depending on where you
# want the loop to point should be 0.0, 90.0, 180.0, or 270.0
 variable theta                 equal 180.0

# Variable changes added for Solute Cluster creation
# thetarad and obsrlo are only used to create a ring of solute around a loop
 variable thetarad                      equal ${theta}/180.0*3.14159
 variable obsrlo                        equal ${obsr}-1.0
 variable obsrhi                        equal ${obsr}

# Generally I read my computational cell from a precomputed file, but for this
# simple problem, LAMMPS can easily generate the perfect lattice internally.
# The fcc lattice described above has x = a1, y = a1*sqrt(3), z = a1*sqrt(6)
```

```
# with a1 (nearest neighbor distance) = a0/sqrt(2), a0 being the conventional cubic cell
# lattice constant
# Basis atoms are at   (0,     0,     0)
#                      (1/2,   1/2,   0)
#                      (0,     2/3,   1/3)
#                      (1/2,   1/6,   1/3)
#                      (0,     1/3,   2/3)
#                      (1/2,   5/6,   2/3)
# relative to each period vector.

        print 'Simulation is on FCC cell...'
        variable a0 equal 3.5146
        variable a1x equal ${a0}/1.41421356237
        variable a2y equal ${a1x}*1.73205080757
        variable a3z equal ${a0}*1.73205080757
        variable burgers equal ${a1x}
        lattice custom 1.0                                                  &
         a1          ${a1x}          0.0             0.0                    &
         a2          0.0             ${a2y}          0.0                    &
         a3          0.0             0.0             ${a3z}                 &
         basis  0.0                  0.0             0.0                    &
         basis  0.5                  0.5             0.0                    &
         basis  0.0          0.66666666667   0.33333333333                  &
         basis  0.5          0.16666666667   0.33333333333                  &
         basis  0.0          0.33333333333   0.66666666667                  &
         basis  0.5          0.83333333333   0.66666666667

# Obviously we can make the computational box any size that we need.
# 20x20x20 cells x 4 atoms/cell = 32000
# We need an odd cell for the screw dislocation.....

# Activate the below section if a screw dislocation is desired
#if "${dislocation} == 1" then                                              &
#"region mybox prism -${halfx} ${halfx} -${halfy} ${halfy} -${halfz} ${halfz} 0.5 0.0 0.0
units lattice" &
#else                                                                       &

region mybox block -${halfx} ${halfx} -${halfy} ${halfy} -${halfz} ${halfz} units lattice

create_box 3 mybox
create_atoms 1 box

# This section of the code should be exectuted in order to construct an obstacle....
# type 0 is void, type 1 is an interstitial loop
# any other type makes no obstacle at all
#
```

```
# Do this before making dislocations which move the lattice points

#Add the below section if a Dislocation Loop Obstacle is desired
#print 'FCC Loop Obstacle'
#region loop cylinder z 0.0 0.0 ${obsr} -0.5 0.5 units box
#create_atoms 2 region loop
#group loop type 2
#set type 2 type 1
#variable obsx0a equal ${obsx0}*${a1x}
#variable obsy0a equal ${obsy0}*${a2y}
#print 'FCC Loop Obstacle3'
#displace_atoms loop rotate 0.0 0.0 0.0 ${Zx} ${Zy} ${Zz} ${theta} units box
#displace_atoms loop move ${obsx0}+0.5 ${obsy0}+0.5 0.5 units lattice

#Add the below section if a Solute Ring on a Dislocation Loop is desired
#print 'FCC Solute Obstacle'
#region solute1 cylinder z 0.0 0.0 ${obsrhi} -5.5 5.5 rotate v_thetarad 0.0 0.0 0.0 ${Zx} ${Zy}
${Zz} units box
#group cluster1 region solute1
#region solute2 cylinder z 0.0 0.0 ${obsrlo} -5.5 5.5 rotate v_thetarad 0.0 0.0 0.0 ${Zx} ${Zy}
${Zz} units box
#group cluster2 region solute2
#group cluster subtract cluster1 cluster2

# This section adds a spherical zone which can later be enhanced in solute concentration
print 'FCC Solute Obstacle1'
region solute1 sphere 0.0 0.0 0.0 ${obsrhi} units box
group cluster1 region solute1


# This section of code should be executed to construct the dislocation
# type 0 is edge, type 1 is screw
# any other type specified makes no dislocation at all
#
#if "${dislocation} == 0"                                then

print 'Edge Dislocation'
variable edgem equal -${halfx}+3.25
variable edger equal ${edgem}+0.3
variable edgel equal ${edgem}-0.3
region edgebottom block ${edgel} ${edger} INF INF INF 0.0 units lattice
delete_atoms region edgebottom
region leftbottom block INF ${edgem} INF INF INF 0.0 units lattice
region rightbottom block ${edgem} INF INF INF INF 0.0 units lattice
variable xmid equal ${edgem}*${burgers}
variable halfB equal 0.5*${burgers}
```

```
variable myD equal 0.75*${burgers}
variable leftd equal ${halfx}-${myD}+${xmid}
variable rightd equal ${halfx}-${myD}-${xmid}
variable newxleft atom x+${halfB}*(x+${halfx})/${leftd}
variable newxright atom x-${halfB}*(${halfB}-x)/${rightd}
set region leftbottom x v_newxleft
set region rightbottom x v_newxright

# Add the below section if a screw dislocation is desired
#elif "${dislocation} == 1"
#print 'Screw Dislocation'
#variable newx atom x+0.5*${burgers}*atan2(y,z)/PI
#set atom * x v_newx

# Create regions for the upper and lower (in Z) slabs that will be used as grips
region upperslab block INF INF INF INF ${halfz}-1.0 INF units lattice
region lowerslab block INF INF INF INF INF -${halfz}+1.0 units lattice
group uppers region upperslab
group lowers region lowerslab
group bothslabs region upperslab
group bothslabs region lowerslab
group insides subtract all bothslabs

# This section applies change_box to adjust the cell for periodicity of either
# The edge or screw - different changes.

if "${dislocation} == 0"                                then
        &
"change_box all x delta 0.5 -0.5 remap units lattice"


# Section to change to Fe-Ni-Cr alloy (68%-12%-20at%)
# Random seeds can be changed to adjust the randomized matrix
set group all type/fraction 2 0.320 6545
group notFe type 2
set group notFe type/fraction 3 0.625 4528
group notFeNi type 3

#Add the below section if a solute cluster obstacle is desired
# Cluster Ni Concentration: 25% = 0.148, 50% = 0.432, 75% = 0.716, as 12% Ni base
#set group cluster1 type/fraction 2 0.432 8553
#group clusteratom type 2

# Forcefield Settings section
#Fe-Cr-Ni alloy
pair_style eam/alloy
```

```
pair_coeff * * FeNiCr.eam.alloy Fe Ni Cr

# Run control parameters for time intergration
neighbor        0.3 bin
neigh_modify    delay 5
timestep        0.001
run_style       verlet
min_style       cg

# Establish computes to get the pe and press of just the inside atoms
compute PE all pe/atom
compute STRESS all stress/atom NULL
compute insidepe insides reduce sum c_PE
compute insidestress insides reduce sum c_STRESS[1] c_STRESS[2] c_STRESS[3]
c_STRESS[4] c_STRESS[5] c_STRESS[6]

# Calculations for total stresses in each direction including shear
variable myvol equal lx*ly*(2.0*(${halfz}-1))*${a3z}
variable sxx equal (c_insidestress[1]/${myvol})
variable syy equal (c_insidestress[2]/${myvol})
variable szz equal (c_insidestress[3]/${myvol})
variable sxy equal (c_insidestress[4]/${myvol})
variable sxz equal (c_insidestress[5]/${myvol})
variable syz equal (c_insidestress[6]/${myvol})

thermo 1000
thermo_style custom temp v_sxx v_syy v_szz v_sxy v_sxz v_syz
thermo_modify flush yes

# Minimization of the cell with no applied strain to relax internal lattice. The top and bottom
# slab atoms are fixed to move only in the Z plane. Once the cell has relaxed, ALL forces on
# these atoms need to be turned off to apply strain control on each step

fix holdlower lowers setforce 0.0 0.0 0.0
fix holdupper uppers setforce 0.0 0.0 0.0

dump 1 all custom 1000000 myMin.* id type xu yu zu c_PE c_STRESS[1] c_STRESS[2]
c_STRESS[3] c_STRESS[4] c_STRESS[5] c_STRESS[6]

fix holdallz all setforce NULL NULL 0.0

minimize  1.0E-13  1.0E-13  5000  50000

# Starting from the minimized structure, do some molecular dynamics
# First equilibrate to 300K
```

```
unfix holdallz

reset_timestep 0
undump 1
dump 1 all custom 1000000 myEquil.* id type xu yu zu c_PE c_STRESS[1] c_STRESS[2]
c_STRESS[3] c_STRESS[4] c_STRESS[5] c_STRESS[6]

velocity insides create 300.0 988157
fix 1 insides npt temp 300.0 300.0 0.1 x 0.0 0.0 1.0 y 0.0 0.0 1.0
run 20000

# Now got to NVE and turn on stress
reset_timestep 0
unfix 1
undump 1
dump 1 all custom 25000 myDyn.* id type xu yu zu c_PE c_STRESS[1] c_STRESS[2]
c_STRESS[3] c_STRESS[4] c_STRESS[5] c_STRESS[6]
dump 2 cluster1 custom 25000 myLoop.* id type xu yu zu c_PE c_STRESS[1] c_STRESS[2]
c_STRESS[3] c_STRESS[4] c_STRESS[5] c_STRESS[6]

fix 1 all nve
velocity uppers set 2.0E-3 0.0 0.0
velocity lowers set -2.0E-3 0.0 0.0

# Creation of a seperate file of the desired shear stress in the XZ direction
fix data all print 3000 "${sxz}" append Stress_xz_1.dat

run 450000
```

REFERENCES

[1] Nuclear Power in the USA, World Nucl. Assoc. (2018). http://www.world-nuclear.org/information-library/country-profiles/countries-t-z/usa-nuclear-power.aspx.

[2] G. Was, Y. Ashida, P. Andresen, Irradiation assisted stress corrosion cracking, Corros. Rev. 29 (2011) 7–49. doi:10.1515/CORRREV.2011.020.

[3] K. Fukuya, Current understanding of radiation-induced degradation in light water reactor structural materials, J. Nucl. Sci. Technol. 50 (2013) 213–254.

[4] Z. Jiao, G. Was, Localized deformation and IASCC initiation in austenitic stainless steels, J. Nucl. Mater. 382 (2008) 203–209. doi:10.1016/j.jnucmat.2008.08.032.

[5] M. McMurtrey, G. Was, Quantification of Stress and Strain States at Dislocation Channel-Grain Boundary Intersections and their Relation to IASCC in Austenitic Steels, in: Proc. 16th Int. Conf. Environ. Degrad. Mater. Nucl. Power Syst. React., 2014.

[6] M. McMurtrey, G. Was, B. Cui, I. Robertson, L. Smith, D. Farkas, Strain localization at dislocation channel-grain boundary intersections in irradiated stainless steel, Int. J. Plast. 56 (2014) 219–231. doi:10.1016/j.ijplas.2014.01.001.

[7] M. McMurtrey, B. Cui, I. Robertson, D. Farkas, G. Was, Mechanism of dislocation channel-induced irradiation assisted stress corrosion crack initiation in austenitic stainless steel, Curr. Opin. Solid State Mater. Sci. 19 (2015) 305–314. doi:10.1016/j.cossms.2015.04.001.

[8] Z. Jiao, G. Was, Impact of localized deformation on IASCC in austenitic stainless steels, J. Nucl. Mater. 408 (2011) 246–256. doi:10.1016/j.jnucmat.2010.10.087.

[9] M. McMurtrey, G. Was, L. Patrick, D. Farkas, Relationship between localized strain and

irradiation assisted stress corrosion cracking in an austenitic alloy, Mater. Sci. Eng. A. 528 (2011) 3730–3740. doi:10.1016/j.msea.2011.01.073.

[10] H. Nishioka, K. Fukuya, K. Fujii, T. Torimaru, IASCC Initiation in Highly Irradiated Stainless Steels under Uniaxial Constant Load Conditions, J. Nucl. Sci. Technol. 45 (2008) 1072–1077.

[11] K. Stephenson, G. Was, Relationship Between Dislocation Channeling and IASCC in Neutron Irradiated Stainless Steel, in: 16th Int. Conf. Environ. Degrad., 2013.

[12] K. Stephenson, G. Was, Crack initiation behavior of neutron irradiated model and commercial stainless steels in high temperature water, 2013.

[13] K. Stephenson, G. Was, Development of a Novel SCC Test for Isolating Crack Initiation in Neutron Irradiated Stainless Steel, in: 17th Int. Conf. Environ. Degrad., 2015.

[14] M. Mcguire, Austenitic Stainless Steels, in: Stainl. Steels Des. Eng., 2008: pp. 69–78. doi:http://dx.doi.org/10.1016/B0-08-043152-6/00081-4.

[15] G. Was, P. Andresen, Irradiation-Assisted Stress-Corrosion Cracking in Austenitic Alloys, JOM. (1992) 8–13.

[16] A. Tekin, J. Martin, B. Senior, Grain Boundary Sensitization and Desensitization during the Ageing of 316L(N) Austenitic Stainless Steels, J. Mater. Sci. 26 (1991) 2458–2466.

[17] R. Singh, Stainless Steels, in: Appl. Weld. Eng. Process. Codes, Stand., 2012: pp. 65–73. doi:10.1016/B978-0-12-391916-8.00008-X.

[18] R. Desu, H. Krishnamurthy, B. Aditya, A. Gupta, S. Singh, Mechanical Properties of Austenitic Stainless Steel 304L and 316L at Elevated Temperatures, J. Mater. Res. Technol. 5 (2015) 13–20. doi:10.1016/j.jmrt.2015.04.001.

[19] G. Was, Fundamentals of Radiation Materials Science, 2007.

[20] J. Lu, L. Hultman, E. Holmström, K. Antonsson, M. Grehk, W. Li, et al., Stacking fault energies in austenitic stainless steels, Acta Mater. 111 (2016) 39–46. doi:10.1016/j.actamat.2016.03.042.

[21] T. Byun, E. Lee, J. Hunn, Plastic deformation in 316LN stainless steel - Characterization of deformation microstructures, J. Nucl. Mater. 321 (2003) 29–39. doi:10.1016/S0022-3115(03)00195-8.

[22] E. Lee, T. Byun, J. Hunn, M. Yoo, K. Farrell, L. Mansur, On the origin of deformation microstructures in austenitic stainless steel: Part I - Microstructures, Acta Mater. 49 (2001) 3269–3276. doi:10.1016/S1359-6454(01)00193-8.

[23] T. Miura, K. Fujii, K. Fukuya, Y. Ito, Characterization of deformation structure in ion-irradiated stainless steels, J. Nucl. Mater. 386–388 (2009) 210–213. doi:10.1016/j.jnucmat.2008.12.093.

[24] T. Byun, On the stress dependence of partial dislocation separation and deformation microstructure in austenitic stainless steels, Acta Mater. 51 (2003) 3063–3071. doi:10.1016/S1359-6454(03)00117-4.

[25] E. Lee, P. Maziasz, A. Rowcliffe, Structure and composition of phases occurring in austenitic stainless steels in thermal and irradiation environments, in: Symp. Irradiat. Phase Stab., 1980.

[26] E. Lee, M. Yoo, T. Byun, J. Hunn, K. Farrell, L. Mansur, On the origin of deformation microstructures in austenitic stainless steel: Part II - Mechanisms, Acta Mater. 49 (2001) 3277–3287. doi:10.1016/S1359-6454(01)00193-8.

[27] G. Taylor, Plastic Strain in Metals, J. Inst. Met. 62 (1938) 307–325. doi:not found.

[28] M. Kamaya, Y. Kawamura, T. Kitamura, Three-dimensional local stress analysis on grain boundaries in polycrystalline material, Int. J. Solids Struct. 44 (2007) 3267–3277. doi:10.1016/j.ijsolstr.2006.09.020.

[29] R. Carter, D. Damcott, M. Atzmon, G. Was, S. Bruemmer, E. Kenik, Quantitative analysis of radiation-induced grain-boundary segregation measurements, J. Nucl. Mater. 211 (1994) 70–84. doi:10.1016/0022-3115(94)90282-8.

[30] G. Was, T. Allen, J. Busby, J. Gan, D. Damcott, D. Carter, et al., Microchemistry and microstructure of proton-irradiated austenitic alloys: toward an understanding of

irradiation effects in LWR core components, J. Nucl. Mater. 270 (1999) 96–114. http://www.sciencedirect.com/science/article/pii/S0022311598008976 (accessed August 17, 2012).

[31] T. Allen, J. Cole, G. Was, E. Kenik, Radiation-induced Segregation and the Relationship to Physical Properties in Irradiated Austenitic Alloys, in: Natl. Soc. Black Phys. Conf. Procedings, 2008.

[32] E. Kenik, T. Inazumi, G. Bell, Radiation-induced grain boundary segregation and sensitization of a neutron-irradiated austenitic stainless steel, J. Nucl. Mater. 183 (1991) 145–153.

[33] D. Damcott, T. Allen, G. Was, Dependence of radiation-induced segregation on dose, temperature and alloy composition in austenitic alloys, J. Nucl. Mater. 225 (1995) 97–107. doi:10.1016/0022-3115(94)00690-3.

[34] T. Toyama, Y. Nozawa, W. Van Renterghem, Y. Matsukawa, M. Hatakeyama, Y. Nagai, et al., Grain boundary segregation in neutron-irradiated 304 stainless steel studied by atom probe tomography, J. Nucl. Mater. 425 (2012) 71–75. doi:10.1016/j.jnucmat.2011.11.072.

[35] P. Okamoto, H. Wiedersich, Segregation of Alloying Elements to Free Surfaces During Irradiation, J. Nucl. Mater. 53 (1974) 336–345.

[36] S. Bruemmer, E. Simonen, P. Scott, P. Andresen, G. Was, J. Nelson, Radiation-induced material changes and susceptibility to intergranular failure of light-water-reactor core internals, J. Nucl. Mater. 274 (1999) 299–314. doi:10.1016/S0022-3115(99)00075-6.

[37] T. Allen, J. Cole, N. Dietz, Y. Wang, G. Was, E. Kenik, The Effect of Bulk Composition on Swelling and Radiation-Induced Segregation in Austenitic Alloys, in: MRS 2000 Fall Meet., 2000.

[38] D. Edwards, E. Simonen, S. Bruemmer, Radiation-Induced Segregation Behavior in Austenitic Stainless Steels: Fast Reactor versus Light Water Reactor Irradiations, in: 13th Int. Conf. Environ. Degrad. Mater. Nucl. Power Syst., 2007: pp. 1–17.

[39] A. Etienne, B. Radiguet, N. Cunningham, G. Odette, P. Pareige, Atomic scale

investigation of radiation-induced segregation in austenitic stainless steels, J. Nucl. Mater. 406 (2010) 244–250. doi:10.1016/j.jnucmat.2010.08.043.

[40] Z. Jiao, G. Was, P. Chou, An atom probe tomography study of proton-irradiated austenitic stainless steels, in: 14th Int. Conf. Environ. Degrad. Mater. Nucl. Power Syst., 2009: pp. 1240–1247.

[41] P. Pareige, A. Etienne, B. Radiguet, Experimental atomic scale investigation of irradiation effects in CW 316SS and UFG-CW 316SS, J. Nucl. Mater. 389 (2009) 259–264. doi:10.1016/j.jnucmat.2009.02.009.

[42] Y. Chen, P. Chou, E. Marquis, Quantitative atom probe tomography characterization of microstructures in a proton irradiated 304 stainless steel, J. Nucl. Mater. 451 (2014) 130–136. doi:10.1016/j.jnucmat.2014.03.034.

[43] T. Toyama, Y. Nozawa, W. Van Renterghem, Y. Matsukawa, M. Hatakeyama, Y. Nagai, et al., Irradiation-induced precipitates in a neutron irradiated 304 stainless steel studied by three-dimensional atom probe, J. Nucl. Mater. 418 (2011) 62–68. doi:10.1016/j.jnucmat.2011.07.027.

[44] A. Volgin, C. Pokor, B. Radiguet, P. Pareige, A. Gentils, F. Fortuna, et al., Understanding of solute clustering under ion irradiation in austenitic stainless steels, in: JTT Nucl. Fe Alloy. Model. Exp., 2012.

[45] Z. Jiao, G. Was, Novel features of radiation-induced segregation and radiation-induced precipitation in austenitic stainless steels, Acta Mater. 59 (2011) 1220–1238. doi:10.1016/j.actamat.2010.10.055.

[46] R. Krummeich, P. Pareige, J. Massoud, S. Jumel, Solute cluster formation in austenitic and ferritic alloys under ion irradiation: a three-dimensional atom probe characterization, Surf. Interface Anal. 36 (2004) 575–580. doi:10.1002/sia.1704.

[47] Z. Jiao, J. Hesterberg, G. Was, Effect of post-irradiation annealing on the irradiated microstructure of neutron-irradiated 304L stainless steel, J. Nucl. Mater. 500 (2018) 220–234. doi:10.1016/j.jnucmat.2017.12.030.

[48] S. Zinkle, P. Maziasz, R. Stoller, Dose dependence of the microstructural evolution in neutron-irradiated austenitic Stainless steel, J. Nucl. Mater. 206 (1993) 266–286.

[49] P. Maziasz, Formation and Stability of Radiation-Induced Phases in Neutron-Irradiated Austenitic and Ferritic Steels, J. Nucl. Mater. 169 (1989) 95–115.

[50] V. Pechenkin, G. Epov, The influence of radiation-induced segregation on precipitate stability in austenitic steels, J. Nucl. Mater. 207 (1993) 303–312.

[51] M. Butt, P. Feltham, Review Solid-solution hardening, J. Mater. Sci. 28 (1993) 2557–2576.

[52] H. Sieurin, J. Zander, R. Sandström, Modelling solid solution hardening in stainless steels, Mater. Sci. Eng. A. 415 (2006) 66–71. doi:10.1016/j.msea.2005.09.031.

[53] J. Hyde, G. Sha, E. Marquis, A. Morley, K. Wilford, T. Williams, A comparison of the structure of solute clusters formed during thermal ageing and irradiation., Ultramicroscopy. 111 (2011) 664–71. doi:10.1016/j.ultramic.2010.12.030.

[54] G. Was, J. Busby, Role of irradiated microstructure and microchemistry in irradiation-assisted stress corrosion cracking, Philos. Mag. 85 (2005) 443–465. doi:10.1080/02678370412331320224.

[55] T. Shoji, S. Suzuki, K. Raja, Current status and future of IASCC research, J. Nucl. Mater. 258–263 (1998) 241–251. doi:10.1016/S0022-3115(98)00304-3.

[56] D. Edwards, E. Simonen, F. Garner, L. Greenwood, B. Oliver, S. Bruemmer, Influence of irradiation temperature and dose gradients on the microstructural evolution in neutron-irradiated 316SS, J. Nucl. Mater. 317 (2003) 32–45. doi:10.1016/S0022-3115(03)00003-5.

[57] J. Busby, Isolation of the Role of Radiation-Induced Segregation in Irradiation-Assisted Stress Corrosion Cracking of Proton-Irradiated Austenitic Stainless Steels, 2001.

[58] R. Stoller, Primary damage formation in irradiated materials, JOM. 48 (1996) 23–27. doi:10.1007/BF03223261.

[59] J. Busby, M. Sowa, G. Was, E. Kenik, The Role of Fine Defect Clusters in Irradiation-

Assisted Stress Corrosion Cracking of Proton-Irradiated 304 Stainless Stress, J. ASTM Int. 1 (2004) 78–91.

[60] J. Busby, M. Sowa, G. Was, E. Simonen, Post-irradiation annealing of small defect clusters, Philos. Mag. 85 (2005) 609–617. doi:10.1080/02678370412331320071.

[61] S. Bruemmer, J. Cole, E. Simonen, Microstructural Evolution, Localized Deformation and Intergranular Stress Corrosion Cracking of Irradiated Stainless Steels, Corrosion. (1997).

[62] N. Yoshida, Q. Xu, H. Watanabe, T. Muroga, M. Kiritani, Low dose fission neutron irradiation on P- and Ti-modified austenitic alloys with improved temperature control, J. Nucl. Mater. 194 (1992) 1114–1118.

[63] H. Kawanishi, S. Ishino, Characterization of microstructure at 673 K in neutron-irradiated Fe-16Ni-15Cr with the addition of C, Ti and Nb, J. Nucl. Mater. 179–181 (1991) 534–537. doi:10.1016/0022-3115(91)90143-U.

[64] N. Shigenaka, T. Hashimoto, M. Fuse, Effects of alloying elements (MO , Si) in an austenitic stainless steel on dislocation loop nucleation under ion irradiation, J. Nucl. Mater. 207 (1993) 46–52.

[65] F. Garner, E. Simonen, B. Oliver, L. Greenwood, M. Grossbeck, W. Wolfer, et al., Retention of hydrogen in fcc metals irradiated at temperatures leading to high densities of bubbles or voids, J. Nucl. Mater. 356 (2006) 122–135. doi:10.1016/j.jnucmat.2006.05.023.

[66] O. Chopra, A. Rao, A Review of Irradiation Effects on LWR Core Internals Materials - Neutron Embrittlement, Void Swelling, and Irradiation Creep, 2011.

[67] T. Allen, J. Cole, C. Trybus, D. Porter, H. Tsai, F. Garner, et al., The effect of dose rate on the response of austenitic stainless steels to neutron radiation, J. Nucl. Mater. 348 (2006) 148–164. doi:10.1016/j.jnucmat.2005.09.011.

[68] S. Porollo, S. Shulepin, Y. V Konobeev, F. Garner, Influence of silicon on swelling and microstructure in Russian austenitic stainless steel EI-847 irradiated to high neutron doses, J. Nucl. Mater. 378 (2008) 17–24. doi:10.1016/j.jnucmat.2008.03.027.

[69] V. Neustroev, F. Garner, Severe embrittlement of neutron irradiated austenitic steels arising from high void swelling, J. Nucl. Mater. 386–388 (2009) 157–160. doi:10.1016/j.jnucmat.2008.12.077.

[70] G. Dobmann, S. Korshunov, M. Kroening, Y. V Martynenko, I. Skorlupkin, A. Surkov, Helium and radiation defect accumulation in metals under stress, Vacuum. 82 (2008) 856–866. doi:10.1016/j.vacuum.2008.01.044.

[71] H. Chung, Assessment of Void Swelling in Austenitic Stainless Steel Core Internals, 2006.

[72] F. Garner, M. Toloczko, B. Sencer, Comparison of swelling and irradiation creep behavior of fcc-austenitic and bcc-ferritic/martensitic alloys at high neutron exposure, J. Nucl. Mater. 276 (2000) 123–142. doi:10.1016/S0022-3115(99)00225-1.

[73] P. Wilkes, Phase stability under irradiation - a review of theory and experiment, J. Nucl. Mater. 83 (1979) 166–175.

[74] N. Sekimura, T. Zama, H. Kawanishi, S. Ishino, Precipitate stability in austenitic stainless steels during heavy ion irradiation, J. Nucl. Mater. 143 (1986) 771–775.

[75] C. Cawthorne, C. Brown, The occurrence of an ordered fcc phase in neutron irradiated M316 stainless steel, J. Nucl. Mater. 66 (1977) 201–202.

[76] A. Kuramoto, T. Toyama, T. Takeuchi, Y. Nagai, M. Hasegawa, T. Yoshiie, et al., Post-irradiation annealing behavior of microstructure and hardening of a reactor pressure vessel steel studied by positron annihilation and atom probe tomography, J. Nucl. Mater. 425 (2012) 65–70. doi:10.1016/j.jnucmat.2011.10.019.

[77] W. Van Renterghem, A. Al Mazouzi, S. Van Dyck, Influence of post irradiation annealing on the mechanical properties and defect structure of AISI 304 steel, J. Nucl. Mater. 413 (2011) 95–102. doi:10.1016/j.jnucmat.2011.04.006.

[78] K. Fukuya, M. Nakano, K. Fujii, T. Torimaru, Y. Kitsunai, Separation of Microstructural and Microchemical Effects in Irradiation Assisted Stress Corrosion Cracking using Post-irradiation Annealing, J. Nucl. Sci. Technol. 41 (2004) 1218–1227.

doi:10.1080/18811248.2004.9726351.

[79] A. Seeger, On the theory of radiation damage and radiation hardening, in: Proc. 2nd United Nations Int. Conf. Peac. Uses At. Energy Vol. 6, 1958: p. 250. doi:10.1007/BF03223261.

[80] R. Stoller, S. Zinkle, On the relationship between uniaxial yield strength and resolved shear stress in polycrystalline materials, J. Nucl. Mater. 283 (2000) 349–352.

[81] J. Bishop, R. Hill, A theoretical derivation of the plastic properties of a polycrystalline face-centred metal, London, Edinburgh, Dublin Philos. Mag. J. Sci. 42 (1951) 1298–1307. doi:10.1080/14786444108561385.

[82] D. Bacon, U. Kocks, R. Scattergood, The effect of dislocation self-interaction on the orowan stress, Philos. Mag. 28 (1973) 1241–1263. doi:10.1080/14786437308227997.

[83] T. Yamamoto, G. Odette, P. Hosemann, E. Marquis, D. Bhattacharyya, IRP Task 3: Microstructure-Property Modelling, 2016.

[84] F. Bergner, C. Pareige, M. Hernández-Mayoral, L. Malerba, C. Heintze, Application of a three-feature dispersed-barrier hardening model to neutron-irradiated Fe – Cr model alloys, J. Nucl. Mater. 448 (2014) 96–102. doi:10.1016/j.jnucmat.2014.01.024.

[85] L. Tan, J. Busby, Formulating the strength factor α for improved predictability of radiation hardening, J. Nucl. Mater. 465 (2015) 724–730. doi:10.1016/j.jnucmat.2015.07.009.

[86] M. Starink, S. Wang, The thermodynamics of and strengthening due to co-clusters: General theory and application to the case of Al-Cu-Mg alloys, Acta Mater. 57 (2009) 2376–2389. doi:10.1016/j.actamat.2009.01.021.

[87] D. Edwards, B. Singh, Evolution of cleared channels in neutron-irradiated pure copper as a function of tensile strain, J. Nucl. Mater. 329–333 (2004) 1072–1077. doi:10.1016/j.jnucmat.2004.04.022.

[88] M. Gussev, K. Field, J. Busby, Deformation localization and dislocation channel dynamics in neutron-irradiated austenitic stainless steels, J. Nucl. Mater. 460 (2015) 139–

152. doi:10.1016/j.jnucmat.2015.02.008.

[89] K. Farrell, T. Byun, N. Hashimoto, Mapping Flow Localization Processes in Deformation of Irradiated Reactor Structural Alloys - Final Report, 2003.

[90] K. Farrell, T. Byun, N. Hashimoto, Deformation mode maps for tensile deformation of neutron-irradiated structural alloys, J. Nucl. Mater. 335 (2004) 471–486. doi:10.1016/j.jnucmat.2004.08.006.

[91] Y. Matsukawa, M. Briceño, I. Robertson, Combining in situ transmission electron microscopy and molecular dynamics computer simulations to reveal the interaction mechanisms of dislocations with stacking-fault tetrahedron in nuclear materials., Microsc. Res. Tech. 72 (2009) 284–92. doi:10.1002/jemt.20681.

[92] Y. Matsukawa, Y. Osetsky, R. Stoller, S. Zinkle, The collapse of stacking-fault tetrahedra by interaction with gliding dislocations, Mater. Sci. Eng. A. 400–401 (2005) 366–369. doi:10.1016/j.msea.2005.01.063.

[93] Y. Matsukawa, G. Liu, In situ TEM study on elastic interaction between a prismatic loop and a gliding dislocation, J. Nucl. Mater. 425 (2012) 54–59. doi:10.1016/j.jnucmat.2011.12.001.

[94] Z. Jiao, M. McMurtrey, G. Was, Strain-induced precipitate dissolution in an irradiated austenitic alloy, Scr. Mater. 65 (2011) 159–162. doi:10.1016/j.scriptamat.2011.04.003.

[95] G. Was, D. Farkas, I. Robertson, Micromechanics of dislocation channeling in intergranular stress corrosion crack nucleation, Curr. Opin. Solid State Mater. Sci. 16 (2012) 134–142. doi:10.1016/j.cossms.2012.03.003.

[96] T. Tanno, A. Hasegawa, S. Sasaki, S. Nogami, M. Satou, Evaluation of localized deformation at low strain levels in austenitic stainless steel irradiated by proton, in: 14th Int. Conf. Environ. Degrad. Mater. Nucl. Power Syst., 2009: pp. 1289–1293.

[97] P. Evrard, M. Sauzay, Modelling of the effect of dislocation channel on intergranular microcrack nucleation in pre-irradiated austenitic stainless steels during low strain rate tensile loading, J. Nucl. Mater. 405 (2010) 83–94. doi:10.1016/j.jnucmat.2010.06.006.

[98] B. Cui, J. Kacher, M. McMurtrey, G. Was, I. Robertson, Influence of irradiation damage on slip transfer across grain boundaries, Acta Mater. 65 (2014) 150–160. doi:10.1016/j.actamat.2013.11.033.

[99] T. Byun, N. Hashimoto, K. Farrell, Deformation mode map of irradiated 316 stainless steel in true stress-dose space, J. Nucl. Mater. 351 (2006) 303–315. doi:10.1016/j.jnucmat.2006.02.033.

[100] Z. Jiao, G. Was, The role of irradiated microstructure in the localized deformation of austenitic stainless steels, J. Nucl. Mater. 407 (2010) 34–43. doi:10.1016/j.jnucmat.2010.07.006.

[101] N. Hashimoto, T. Byun, K. Farrell, Microstructural analysis of deformation in neutron-irradiated fcc materials, J. Nucl. Mater. 351 (2006) 295–302. doi:10.1016/j.jnucmat.2006.02.032.

[102] N. Hashimoto, S. Zinkle, A. Rowcliffe, J. Robertson, S. Jitsukawa, Deformation mechanisms in 316 stainless steel irradiated at 60C and 330C, J. Nucl. Mater. 283–287 (2000) 528–534. doi:10.1016/S0022-3115(00)00087-8.

[103] H. Nishioka, K. Fukuya, K. Fujii, Y. Kitsunai, Deformation structure in highly irradiated stainless steels, J. Nucl. …. 45 (2008) 274–287. http://www.tandfonline.com/doi/abs/10.1080/18811248.2008.9711437 (accessed July 31, 2012).

[104] K. Stephenson, The Role of Dislocation Channeling in IASCC Initiation of Neutron Irradiated Austenitic Stainless Steel, 2016.

[105] K. Fukuya, H. Nishioka, K. Fujii, T. Miura, T. Torimaru, An EBSD examination of SUS316 stainless steel irradiated to 73dpa and deformed at 593K, J. Nucl. Mater. 417 (2011) 958–962. doi:10.1016/j.jnucmat.2010.12.301.

[106] E. Kenik, R. Jones, G. Bell, Irradiation-assisted stress corrosion cracking, J. Nucl. Mater. 215 (1994) 52–59. http://www.osti.gov/energycitations/product.biblio.jsp?osti_id=7010172 (accessed July

31, 2012).

[107] F. Ford, B. Gordon, R. Horn, Corrosion in Boiling Water Reactors, ASM Handb. Corros. Environ. Ind. 13C (2006) 341–361.

[108] B. Gordon, Introduction to Corrosion in the Nuclear Power Industry, ASM Handb. Corros. Environ. Ind. 13C (2006) 339–340.

[109] P. Scott, A review of irradiation assisted stress corrosion cracking, J. Nucl. Mater. 211 (1994) 101–122. http://www.sciencedirect.com/science/article/pii/0022311594903603 (accessed July 31, 2012).

[110] H. Christensen, Effect of water radiolysis on corrosion in nuclear reactors, Radiat. Phys. Chem. 18 (1981) 147–158. http://www.sciencedirect.com/science/article/pii/0146572481900728 (accessed March 7, 2013).

[111] S. Le Caër, Water Radiolysis: Influence of Oxide Surfaces on H2 Production under Ionizing Radiation, Water. 3 (2011) 235–253. doi:10.3390/w3010235.

[112] A. Turnbull, M. Psaila-Dombrowski, A Review of Electrochemistry of Relevance to Environment-Assisted Cracking in Light Water Reactors, Corros. Sci. 33 (1992) 1925–1966.

[113] J. Busby, Water Chemistry Overview, in: NERS 522 Lect., 2013.

[114] Y. Kim, Effect of Variations in Boiling Water Reactor Water Chemistry on Type 304 Stainless Steel Electrochemical Corrosion Potential, Corrosion. 58 (2002) 208–215.

[115] C. Lin, Y. Kim, L. Niedrach, K. Ramp, Electrochemical Corrosion Potential Models for Boiling-Water Reactor Applications, Corrosion. 52 (1996) 618–625.

[116] Y. Kim, Electrochemical Mitigation of Intergranular Stress Corrosion Cracking in Boiling Water Reactors, Corrosion. 61 (2005) 889–894. doi:10.5006/1.3280658.

[117] K. Fukuya, M. Nakano, Role of radiation-induced grain boundary segregation in irradiation assisted stress corrosion cracking, J. Nucl. …. (2004) 37–41.

http://www.tandfonline.com/doi/abs/10.1080/18811248.2004.9715522 (accessed August 1, 2012).

[118] T. Fukumura, T. Terachi, K. Arioka, Influence of water chemistry on IGSCC growth rate of SUS316 under Simulated PWR Primary Water, in: Symp. Water Chem. Corros. Nucl. Power Plants Asia, 2007.

[119] J. Pongpuak, The Effects of Boric Acid on Corrosion of Steels in Simulated Pressurized Water Reactor Primary Coolant, 2006.

[120] W. Pearl, S. Sawochka, S. Choi, Evaluation of Field Applications of Boric Acid in PWR Steam Generators, 1984.

[121] S. Garcia, Capturing 30 years of BWR ECP experience, Nucl. Eng. Int. (2012) 14–16.

[122] A. Ramar, P. Grundler, V. Karastoyanov, I. Günther-Leopold, S. Abolhassani-Dadras, N. Kivel, et al., Effect of Pt injection rate on corrosion potential and Pt distribution on stainless steel under simulated boiling water reactor conditions, Corros. Eng. Sci. Technol. 47 (2012) 489–497. doi:10.1179/1743278212Y.0000000031.

[123] G. Was, P. Andresen, Stress Corrosion Cracking Behavior of Alloys in Aggressive Nuclear Reactor Core Environments, Corrosion. 63 (2007) 19–45.

[124] T. Tsukada, Y. Miwa, H. Nakajima, Stress corrosion cracking of neutron irradiated type 304 stainless steels, in: 7th Int. Conf. Environ. Degrad. Mater. Nucl. Power Syst., 1995: pp. 1009–1019.

[125] I. Ioka, Y. Ishijima, K. Usami, N. Sakuraba, Y. Kato, K. Kiuchi, Radiation hardening and IASCC susceptibility of extra high purity austenitic stainless steel, J. Nucl. Mater. 417 (2011) 887–891. doi:10.1016/j.jnucmat.2010.12.154.

[126] J. Cookson, R. Carter, D. Damcott, M. Atzmon, G. Was, Irradiation assisted stress corrosion cracking of controlled purity 304L stainless steels, J. Nucl. Mater. 202 (1993) 104–121.

[127] A. Jenssen, L. Ljungberg, Irradiation assisted stress corrosion cracking post irradiation

CERT tests of stainles steels in a BWR test loop, in: 7th Int. Conf. Environ. Degrad. Mater. Nucl. Power Syst., 1995: pp. 1043–1053.

[128] M. Kodama, J. Morisawa, S. Nishimura, K. Asano, S. Shima, K. Nakata, Stress corrosion cracking and intergranular corrosion of austenitic stainless steels irradiated at 323 K, J. Nucl. Mater. 212–215 (1994) 1509–1514. doi:10.1016/0022-3115(94)91080-4.

[129] R. Smith, W. Geng, C. Geller, R. Wu, A. Freeman, The Effect of Li, He, and Ca on Grain Boundary Cohesive Strength in Ni, Scr. Mater. 43 (2000) 957–961.

[130] J. Cole, T. Allen, G. Was, R. Dropek, E. Kenik, The Influence of Pre-irradiation Heat Treatments on Thermal Non-Equilibrium and Radiation-induced Segregation Behavior in Model Austenitic Stainless Steel Alloys, in: Symp. Eff. Radiat. Mater., 2003.

[131] A. Etienne, B. Radiguet, N. Cunningham, G. Odette, R. Valiev, P. Pareige, Comparison of radiation-induced segregation in ultrafine-grained and conventional 316 austenitic stainless steels., Ultramicroscopy. 111 (2011) 659–63. doi:10.1016/j.ultramic.2010.12.026.

[132] J. Busby, G. Was, E. Kenik, Isolating the effect of radiation-induced segregation in irradiation-assisted stress corrosion cracking of austenitic stainless steels, J. Nucl. Mater. 302 (2002) 20–40. doi:10.1016/S0022-3115(02)00719-5.

[133] J. Isselin, R. Kasada, A. Kimura, Work Hardening , Sensitization , and Potential Effects on the Susceptibility to Crack Initiation of 316L Stainless Steel in BWR Environment, J. Nucl. Sci. Technol. 48 (2011) 1462–1470.

[134] G. Li, Y. Kaneshima, T. Shoji, Effects of Impurities on Environmentally Assisted Crack Growth of Solution-Annealed Austenitic Steels in Primary Water at 325°C, Corros. Sci. (2000) 460–469.

[135] P. Andresen, M. Morra, Effects of Si on SCC of Irradiatied and Uniradiated Stainless Steels and Nickel Alloys, Corrosion. (2005) 1–22.

[136] X. Lou, P. Andresen, R. Rebak, Oxide Inclusions in Laser Additive Manufactured Stainless Steel and their Effects on Impact Toughness and Stress Corrosion Cracking

Behavior, J. Nucl. Mater. 499 (2018) 182–190. doi:10.1016/j.jnucmat.2017.11.036.

[137] A. Roine, Outokumpu HSC Chemistry 6.0, (2002).

[138] H. Chung, W. Shack, Irradiation-Assisted Stress Corrosion Cracking Behavior of Austenitic Stainless Steels Applicable to LWR Core Internals, 2006.

[139] T. Allen, H. Tsai, J. Cole, T. Yoshitake, N. Akasaka, T. Donomae, et al., The Effect of Low Dose Rate Irradiation on the Tensile Properties and Microstructure of Austenitic Stainless Steels, in: 2nd Euransian Conf. Nucl. Sci. It's Appl., 2002.

[140] A. Etienne, B. Radiguet, P. Pareige, J. Massoud, C. Pokor, Tomographic atom probe characterization of the microstructure of a cold worked 316 austenitic stainless steel after neutron irradiation, J. Nucl. Mater. 382 (2008) 64–69. doi:10.1016/j.jnucmat.2008.09.015.

[141] M. Hash, J. Busby, G. Was, The effect of hardening source in proton irradiation-assisted stress corrosion cracking of cold worked type 304 stainless steel, in: Eff. Radiat. Mater. 21st Int. Symp., 2004: pp. 92–104.

[142] J. Busby, M. Hash, G. Was, The relationship between hardness and yield stress in irradiated austenitic and ferritic steels, J. Nucl. Mater. 336 (2005) 267–278. doi:10.1016/j.jnucmat.2004.09.024.

[143] Z. Jiao, Y. Chen, J. Hesterberg, E. Marquis, G. Was, Post-Irradiation Annealing in Mitigation of IASCC of Proton-Irradiated Stainless Steel, in: 16th Int. Conf. Environ. Degrad., 2013.

[144] G. Was, M. Atzmon, L. Wang, Isolation of Microstructure in Proton-Irradiated Steels, 2000.

[145] T. Byun, Strain Localization in Irradiated Materials, Nucl. Eng. Technol. 38 (2006) 619–638.

[146] M. Sauzay, K. Bavard, W. Karlsen, TEM observations and finite element modelling of channel deformation in pre-irradiated austenitic stainless steels – Interactions with free surfaces and grain boundaries, J. Nucl. Mater. 406 (2010) 152–165.

doi:10.1016/j.jnucmat.2010.01.027.

[147] D. Johnson, G. Was, Novel technique for quantitative measurement of localized stresses near dislocation channel—Grain boundary interaction sites in irradiated stainless steel, in: Proc. 18th Int. Conf. Environ. Degrad. Mater. Nucl. Power Syst. – Water React., 2018: pp. 1005–1013. doi:10.1007/978-3-319-68454-3.

[148] D. Johnson, B. Kuhr, D. Farkas, G. Was, Quantitative analysis of localized stresses in irradiated stainless steels using high resolution electron backscatter diffraction and molecular dynamics modeling, Scr. Mater. 116 (2016) 87–90. doi:10.1016/j.scriptamat.2016.01.017.

[149] D. Johnson, B. Kuhr, D. Farkas, G. Was, Quantitative Linkage between the Stress at Dislocation Channel-Grain Boundary Interaction Sites and Irradiation Assisted Stress Corrosion Crack Initiation, Acta Mater. (2019). doi:10.1016/j.actamat.2019.02.032.

[150] T. Allen, G. Was, S. Bruemmer, J. Gan, S. Ukai, Design of Radiation-Tolerant Structural Alloys for Generation IV Nuclear Energy Systems, 2005.

[151] E. Kiss, Component Reliability Considerations for New Designs and Extended Operation of Boiling Water Reactor (BWRs), Vol. 1 Plant Oper. Maintenance, Install. Life Cycle; Compon. Reliab. Mater. Issues; Adv. Appl. Nucl. Technol. Codes, Stand. Licens. Regul. Issues. (2008) 717–721. doi:10.1115/ICONE16-48864.

[152] T. Allen, Developing Improved Structural Materials using Proton Irradiation as a Rapid Analysis Tool, 2003.

[153] A. Etienne, B. Radiguet, P. Pareige, Understanding silicon-rich phase precipitation under irradiation in austenitic stainless steels, J. Nucl. Mater. 406 (2010) 251–256. doi:10.1016/j.jnucmat.2010.08.045.

[154] G. Ackland, Controlling radiation damage., Science (80-.). 327 (2010) 1587–8. doi:10.1126/science.1188088.

[155] R. Andrievski, Behavior of Radiation Defects in Nanomaterials, Rev. Adv. Mater. Sci. 29 (2011) 54–67.

[156] Y. Chen, O. Chopra, Y. Yang, W. Shack, B. Alexandreanu, E. Gruber, et al., Crack Growth Rates and Fracture Toughness of Neutron Irradiated Grain-Boundary-Engineered Austenitic Stainless Steels, in: 14th Int. Conf. Environ. Degrad. Mater. Nucl. Power Syst., 2009: pp. 1219–1227.

[157] C. Xu, W. Chen, X. Zhang, Y. Wu, M. Li, Y. Yang, Effects of neutron irradiation and post-irradiation annealing on the microstructure of HT-UPS stainless steel, J. Nucl. Mater. 507 (2018) 188–197. doi:10.1016/j.jnucmat.2018.04.043.

[158] K. Fukuya, M. Nakano, K. Fujii, M. Kodama, T. Torimaru, Effects of Post-irradiation Annealing on Radiation-induced Material Changes and IASCC Susceptibility in PWR-irradiated Stainless Steels, in: 11th Int. Conf. Environ. Degrad. Mater. Nucl. Power Syst., 2003: pp. 1153–1163.

[159] E. Simonen, D. Edwards, S. Bruemmer, Concurrent Annealing Of Vacancy-Type And Interstitial-Type Damage In Neutron Irradiated Stainless Steel, in: Mater. Res. Soc. Symp. Proc. Vol. 650, 2001: pp. 1–6.

[160] E. Simonen, D. Edwards, S. Bruemmer, J. Busby, G. Was, Light-Water Reactor Microstructural Characterization from Post-Irradiation Annealing Behavior, in: 10th Int. Conf. Environ. Degrad. Mater. Nucl. Power Syst., 2002.

[161] J. Busby, G. Was, E. Kenik, Post-Irradiation Annealing of Dislocation Microstructure and Radiation-Induced Segregation in Proton-Irradiated Stainless Steels, MRS Proc. 540 (1998) 495–500. http://journals.cambridge.org/abstract_S1946427400291847 (accessed July 31, 2012).

[162] G. Was, Recent Developments in Understanding Irradiation Assisted Stress Corrosion Cracking, in: 11th Int. Conf. Environ. Degrad. Mater. Nucl. Power Syst., 2003: pp. 965–985.

[163] G. Was, M. Atzmon, L. Wang, J. Busby, Mechanism of Irradiation Assisted Cracking of Core Components in Light Water Reactors, 2003.

[164] J. Cole, T. Allen, Microstructural changes induced by post-irradiation annealing of

neutron-irradiated austenitic stainless steels, J. Nucl. Mater. 283–287 (2000) 329–333. doi:10.1016/S0022-3115(00)00072-6.

[165] J. Chen, P. Jung, M. Rödig, H. Ullmaier, G. Bauer, Ductility recovery in structural materials for spallation targets by post-irradiation annealing, J. Nucl. Mater. 343 (2005) 227–235. doi:10.1016/j.jnucmat.2004.09.076.

[166] K. Asano, R. Katsura, M. Kodama, S. Nishimura, K. Fukuya, K. Nakata, Post-irradiation annealing effects on hardness and intergranular corrosion in type 304 stainless steel, in: 7th Int. Conf. Environ. Degrad. Mater. Nucl. Power Syst., 1995: pp. 1033–1042.

[167] R. Katsura, Y. Ishiyama, N. Yokota, T. Kato, K. Nakata, K. Fukuya, et al., Post-Irradiation Annealing Effect of Austenitic Stainless Steels on IASCC, Corrosion. (1998). http://www.onepetro.org/mslib/servlet/onepetropreview?id=NACE-98132 (accessed July 31, 2012).

[168] A. Jacobs, S. Dumbill, Effects of low-temperature annealing on the microstructure and grain boundary chemistry of irradiated type 304SS and correlations with IASCC resistance, in: 7th Int. Conf. Environ. Degrad. Mater. Nucl. Power Syst., 1995: pp. 1021–1031.

[169] R. Pelli, K. Törrönen, State-of-the-Art Review on Thermal Annealing, 1995.

[170] B. Burton, Theoretical analysis of annealing behaviour of mixed distributions of dislocation loops , voids , and gas bubbles: comparison with annealing behaviour of irradiated reactor component irradiated reactor component, Mater. Sci. Technol. 8 (1992) 602–610. doi:10.1179/mst.1992.8.7.602.

[171] A. Jacobs, G. Wozadlo, G. Gordon, Low-Temperature Annealing: A Process to Mitigate Irradiation-Assisted Stress Corrosion Cracking, Corrosion. 51 (1995) 731–737. doi:10.5006/1.3293549.

[172] A. Jenssen, Machining and Shipment of Specimens from Heat SW – Documentation of Fabricated Specimens, 2013.

[173] N. Soneda, K. Nishida, P. Chou, Characterization of solute atom distribution in grain

interior of neutron-irradiated 304L and 304 stainless steels, 2011.

[174] M. Ayanoglu, A. Motta, Microstructural evolution of the 21Cr32Ni model alloy under irradiation, J. Nucl. Mater. 510 (2018) 297–311. doi:10.1016/j.jnucmat.2018.07.060.

[175] M. Swenson, The Mechanism of Radiation-Induced Nanocluster Evolution in Oxide Dispersion Strengthened and Ferritic-Martensitic Alloys, 2017.

[176] M. Miller, R. Forbes, Atom-Probe Tomography: The Local Electrode Atom Probe, 2014. doi:10.1007/978-1-4899-7430-3.

[177] G. Hollenberg, G. Terwilliger, R. Gordon, Calculation of Stresses and Strains in Four-Point Bending Creep Tests, J. Am. Ceram. Soc. 54 (1971) 196–199.

[178] S. Plimpton, Fast Parallel Algorithms for Short–Range Molecular Dynamics, J. Comput. Phys. 117 (1995) 1–19.

[179] Z. Rong, V. Mohles, D. Bacon, Y. Osetsky, Dislocation dynamics modelling of dislocation–loop interactions in irradiated metals, Philos. Mag. 85 (2005) 171–188. doi:10.1080/14786430412331315644.

[180] J. Shim, D. Kim, W. Jung, Y. Cho, B. Wirth, Atomistic modeling of nanosized Cr precipitate contribution to hardening in an Fe-Cr alloy, J. Nucl. Mater. 386–388 (2009) 56–59. doi:10.1016/j.jnucmat.2008.12.058.

[181] A. Simar, H. Voigt, B. Wirth, Molecular dynamics simulations of dislocation interaction with voids in nickel, Comput. Mater. Sci. 50 (2011) 1811–1817. doi:10.1016/j.commatsci.2011.01.020.

[182] A. Bakaev, D. Terentyev, P. Grigorev, E. Zhurkin, Atomistic simulation of the interaction between mobile edge dislocations and radiation-induced defects in Fe-Ni-Cr austenitic alloys, J. Surf. Investig. X-Ray, Synchrotron Neutron Tech. 8 (2014) 220–228. doi:10.1134/S1027451014020062.

[183] D. Terentyev, A. Bakaev, Interaction of a screw dislocation with Frank loops in Fe-10Ni-20Cr alloy, J. Nucl. Mater. 442 (2013) 208–217. doi:10.1016/j.jnucmat.2013.08.044.

[184] D. Bacon, Y. Osetsky, D. Rodney, Dislocation – Obstacle Interactions at the Atomic Level, in: Dislocations in Solids, Elsevier, 2009: pp. 4–85. doi:10.1016/S1572-4859(09)01501-0.

[185] V. Krasnikov, A. Mayer, Y. Osetsky, D. Bacon, An Atomic-level Model for Studying the Dynamics of Edge Dislocations in Metals Influence of Local Stresses on Motion of Edge Dislocation in Aluminum, Model. Simul. Mater. Sci. Eng. 11 (2003) 427–446. http://iopscience.iop.org/article/10.1088/0965-0393/11/4/302/pdf.

[186] Y. Osetsky, D. Bacon, Atomic-scale mechanisms of void hardening in bcc and fcc metals, Philos. Mag. 90 (2010) 945–961. doi:10.1080/14786430903164580.

[187] Y. Osetsky, D. Bacon, Void and precipitate strengthening in α-iron: What can we learn from atomic-level modelling?, J. Nucl. Mater. 323 (2003) 268–280. doi:10.1016/j.jnucmat.2003.08.028.

[188] D. Terentyev, F. Bergner, Y. Osetsky, Cr segregation on dislocation loops enhances hardening in ferritic Fe-Cr alloys, Acta Mater. 61 (2013) 1444–1453. doi:10.1016/j.actamat.2012.11.021.

[189] Y. Osetsky, D. Bacon, An Atomic-level Model for Studying the Dynamics of Edge Dislocations in Metals, Model. Simul. Mater. Sci. Eng. 11 (2003) 427–446. http://iopscience.iop.org/article/10.1088/0965-0393/11/4/302/pdf.

[190] S. Zhao, Y. Osetsky, Y. Zhang, Atomic-scale dynamics of edge dislocations in Ni and concentrated solid solution NiFe alloys, J. Alloys Compd. 701 (2017) 1003–1008. doi:10.1016/j.jallcom.2017.01.165.

[191] G. Bonny, D. Terentyev, R. Pasianot, S. Poncé, A. Bakaev, Interatomic potential to study plasticity in stainless steels: The FeNiCr model alloy, Model. Simul. Mater. Sci. Eng. 19 (2011). doi:10.1088/0965-0393/19/8/085008.

[192] C. Brandl, P. Derlet, H. Van Swygenhoven, Strain rates in molecular dynamics simulations of nanocrystalline metals, Philos. Mag. 89 (2009) 3465–3475. doi:10.1080/14786430903313690.

[193] Z. Ruan, W. Wu, N. Li, Effects of Strain Rate, Temperature and Grain Size on the Mechanical Properties and Microstructure Evolutions of Polycrystalline Nickel Nanowires : A Molecular Dynamics Simulation, Wuhan Univ. J. Nat. Sci. 23 (2018) 251–258.

[194] S. Hajilar, B. Shafei, T. Cheng, A. Jaramillo-botero, Reactive Molecular Dynamics Simulations to Understand Mechanical Response of Thaumasite under Temperature and Strain Rate Effects, J. Phys. Chem. A. 121 (2017) 4688–4697. doi:10.1021/acs.jpca.7b02824.

[195] A. Stukowski, Visualization and analysis of atomistic simulation data with OVITO – the Open Visualization Tool, Model. Simul. Mater. Sci. Eng. 18 (2010) 7. doi:10.1088/0965-0393/18/1/015012.

[196] G. Was, Fundamentals of Radiation Materials Science, 2007.

[197] D. Hull, D. Bacon, Dislocations in Face-centered Cubic Metals, in: Introd. to Dislocations, 2011: pp. 85–107. doi:10.1016/B978-0-08-096672-4.00005-0.

[198] B. Burton, M. Speight, The coarsening and annihilation kinetics of dislocation loop, Philos. Mag. A. 53 (1986) 385–402. doi:10.1080/01418618608242839.

[199] J. Edington, R. Smallman, Faulted Dislocation Loops in Quenched Aluminium, Philos. Mag. 11 (1965) 1109–1123. doi:10.1080/14786436508224922.

[200] A. Foreman, M. Makin, Dislocation Movement Through Random Arrays of Obstacles, Can. J. Phys. 45 (1967) 511–517.

[201] U. Kocks, Kinetics of Solution Hardening, Metall. Trans. A. 16A (1985) 2109–2129.

[202] O. Ryen, O. Nijs, E. Sjolander, B. Holmedal, H. Ekstrom, E. Nes, Strengthening Mechanisms in Solid Solution Aluminum Alloys, Metall. Mater. Trans. A. 37A (2006) 1999–2006.

[203] R. Labusch, Statistical Theories of Solid Solution Hardening, Acta Metall. 20 (1972) 917–927.

[204] J. Dean, Properties of Atoms, Radicals, and Bonds, in: Lange's Handb. Chem., 1999: p. 4.41.

[205] P. Edmundson, Personal Communication, (2018).

[206] G.S. Was, R.M. Kruger, A Thermodynamic and Kinetic Basis for Understanding Chromium Depletion in Ni-Cr-Fe Alloys, Acta Metall. 33 (1985) 841–854.

[207] K. Stephenson, G. Was, The role of dislocation channeling in IASCC initiation of neutron irradiated stainless steel, J. Nucl. Mater. 481 (2016) 214–225. doi:10.1016/j.jnucmat.2016.09.001.

[208] R. Schramm, R. Reed, Stacking Fault Energies of Seven Commercial Austenitic Stainless Steels, Metall. Trans. A. 6A (1975) 1345.